Wafer Bonding: Mechanics-Based Models and Experiments

by

Kevin T. Turner

B.S., The Johns Hopkins University (1999)
S.M., Massachusetts Institute of Technology (2001)

Submitted to the Department of Mechanical Engineering
in partial fulfillment of the requirements for the degree of

Doctor of Philosophy

at the

MASSACHUSETTS INSTITUTE OF TECHNOLOGY

May 2004

© Massachusetts Institute of Technology MMIV. All Rights Reserved.

Author ____
Department of Mechanical Engineering
7 May 2004

Certified by ____
S. Mark Spearing
Associate Professor of Aeronautics and Astronautics
Thesis Supervisor

Certified by ____
Alexander H. Slocum
Professor of Mechanical Engineering
Thesis Committee Chairman

Certified by ____
Martin A. Schmidt
Professor of Electrical Engineering and Computer Science

Certified by ____
John W. Hutchinson
Abbott and James Lawrence Professor of Engineering, Harvard University

Accepted by ____
Ain A. Sonin
Chairman, Department Committee on Graduate Students

Wafer Bonding: Mechanics-Based Models and Experiments

by

Kevin T. Turner

Submitted to the Department of Mechanical Engineering
on 7 May 2004, in partial fulfillment of the
requirements for the degree of
Doctor of Philosophy

Abstract

Direct wafer bonding has emerged as an important technology in the manufacture of silicon-on-insulator substrates (SOI), microelectromechanical systems (MEMS), and three-dimensional integrated circuits (3D IC's). While the process is currently employed in applications such as these, a lack of knowledge of the basic mechanics of the process has made developing robust processes and preventing process failures extremely challenging. The current work addresses this problem through the development and validation of mechanics-based models that connect the wafer geometry, etch pattern, clamping configuration, and work of adhesion to bonding failure.

An energy-based bonding criterion, which allows the effect of flatness variations and etch patterns to be quantified, is presented and employed to develop analytical and numerical models. Analytical models, based on plate theory, are developed to examine the role of wafer-scale shape variations, etch patterns, and the clamping configuration. Finite element models are developed to verify the analytical models and to evaluate the bonding criterion for wafers with anisotropic elastic properties and arbitrary geometries. Experiments in which silicon substrates with wafer-scale shape variations and etch patterns were bonded demonstrate that the shape and size of the bonded area and the shape of the bonded pair can be predicted using the models developed. The effect of mid-spatial wavelength height variations (nanotopography) on bonding is examined through a combination of modeling and experiments. The experiments and analysis provide a route for characterizing nanotopography and assessing its impact on bonding. The accuracy of the wafer bonded double cantilever beam, which is one method to evaluate the key process parameter of interface toughness, is also examined in the current work.

The results of the modeling and experiments are discussed to provide guidance in process, device, and tool design. The models that are presented may be used to establish tolerances on wafer geometry and to improve process control.

Thesis Supervisor: S. Mark Spearing
Title: Associate Professor of Aeronautics and Astronautics

Acknowledgments

There are many people and organizations that have provided significant assistance in the course of completing the work reported in this thesis. First and foremost, I would like to thank my advisor, Mark Spearing, for providing me with the support, encouragement, and guidance to complete this work. Mark provided me with an enormous amount of freedom and gave me the opportunity to pursue research that I felt was interesting and important. I would also like to thank my committee, Professors John Hutchinson, Marty Schmidt, and Alex Slocum, for providing suggestions, advice, and support along the way. Furthermore, I would like to acknowledge the help of Professors John Dugundji and Michael Thouless, who provided insight and suggestions on portions of the mechanics models presented in this thesis.

While at MIT, I have been lucky to be a member of several groups and labs. Among them are TELAC, MTL, AMSL, and the MHT and microengine programs. The students and staff in these various groups have been a constant source of support throughout this work. In particular, I appreciate the numerous discussions with and suggestions from fellow students. While many have helped, I am especially grateful for the interactions that I have had with Jeremy, DJ, Christine, and Lodewyk over the past five years. Equally important was the support that I have received from numerous staff in these groups. Dave Roberston, Dennis Ward, John Kane, and Bob Bicchieri provided me with significant assistance in developing the experiments, purchasing equipment, and fabricating specimens.

An essential part of the experimental work in this thesis was appropriate metrology. I would like to thank Win Baylies (who Professor Duane Boning introduced me to) for help in arranging measurements at ADE and Zygo. I appreciate the help of Pat Hester at ADE in obtaining wafer shape measurements as well as Maria Robinson at Zygo in measuring wafer nanotopography. The help from ADE and Zygo were both critical to completing this work.

Finally, I would like to thank my friends and family for providing encouragement along the way as well as an occasional escape from my thesis research. Countless people in the groups that I mentioned above have become good friends over the years and have made the hours spent in the lab, fab, and office significantly more enjoyable. I appreciate the friendship and support from all those in the THDA as well as the great friends I lived with at Windsor Road. My parents and brothers have been great throughout this experience and have always supported me. Lastly, but certainly not least, I would like to thank my wife, Kate, for her support, patience, and friendship. I sincerely appreciate her ability to provide a different view on problems that I encountered as well her willingness to proof the drafts of this thesis.

This work was supported by the Cambridge-MIT Institute under [CMI-059/P-IR(FT)MEMS].

Contents

1 Introduction **21**

1.1 Wafer Bonding 21

1.2 Motivation 23

1.3 Objectives 24

1.4 Thesis Scope 25

2 Background and Bonding Criterion **27**

2.1 Wafer Geometry 28

2.2 Review of Wafer Bonding Mechanics 30

2.3 Bonding Criterion 32

3 Wafer Shape Variations and Etch Patterns **37**

3.1 Geometry 37

3.2 Classical Plate Theory 38

3.3 Axisymmetric Finite Element Analysis 42

3.4 Etch Pattern 43

3.4.1 Shallow features 43

3.4.2 Deep features 45

3.5 Results and Discussion 46

3.6 Summary 50

4 Asymmetric Wafer Shape Variations **51**

4.1 Model Overview 52

4.2 Geometry and Finite Element Mesh 53

4.3 Local Calculation of G 56

4.4 Iteration Scheme 57

4.5 Results and Discussion 60

4.5.1 Elastic Anisotropy 60

4.5.2 Asymmetric Wafer Shape . . . 62
4.6 Summary and Limitations . . . 64

5 Clamping **67**
5.1 Free Configuration . . . 68
5.2 Clamped Configuration . . . 71
5.3 Results and Discussion . . . 73
5.3.1 Final Shape . . . 73
5.3.2 Strain Energy Release Rate . . . 75
5.4 Summary . . . 78

6 Experiments **81**
6.1 Approach . . . 81
6.2 Bond Propagation Study . . . 83
6.2.1 Experimental Details . . . 83
6.2.2 Analysis . . . 85
6.2.3 Results and Discussion . . . 85
6.3 Bond Shape Experiments . . . 90
6.3.1 Experimental Details . . . 90
6.3.2 Analysis . . . 90
6.3.3 Results and Discussion . . . 92
6.4 Summary . . . 95

7 Nanotopography **97**
7.1 Background . . . 98
7.2 Modeling . . . 99
7.3 Material and Measurements . . . 102
7.4 Results and Discussion . . . 104
7.5 Summary . . . 111

8 Double Cantilever Specimen **113**
8.1 Background . . . 113
8.2 Specimen Mechanics . . . 115
8.3 Finite Element Model . . . 117
8.4 Results and Discussion . . . 121
8.5 Experimental Validation . . . 124
8.6 Summary . . . 125

9 Conclusions and Recommendations 127
9.1 Summary and Discussion . . . 127
9.2 Conclusions . . . 130
9.3 Recommendations for Future Work . . . 131
9.4 Final Remarks . . . 132

References 133

A Mindlin Plate Analysis 141

B Gravity Deformation 145
B.1 Model . . . 145
B.2 Results . . . 147

C Finite Element Code 149
C.1 Asymmetric Bond Prediction . . . 149
C.2 Bond Pair Shape Prediction . . . 164
C.3 Wafer Bonded Double Cantilever . . . 176

List of Figures

1-1 A miniature gas turbine engine that is fabricated using direct wafer bonding. 23

2-1 Three basic steps in direct wafer bonding. 28
2-2 Types of flatness variations. 29
2-3 Typical force separation curve for two surfaces. 33
2-4 Model bonding system showing change in energy. 34

3-1 Schematic of bonding two bowed wafers. 38
3-2 Different etch patterns considered. 45
3-3 Strain energy accumulation rate as a function of bond position. 47
3-4 Strain energy accumulation rate as function of thickness ratio. 47
3-5 Comparison of methods to calculate strain energy accumulation rate. 49
3-6 Final curvature of bond pair. 49
3-7 Effect of shallow etch patterns. 49
3-8 Comparison of the effect of shallow and deep features. 49

4-1 Shape maps of three 100 mm silicon wafers. 52
4-2 Effective elastic modulus and Poisson's ratio of single crystal silicon in the (100) plane. 53
4-3 Finite element mesh to model asymmetric wafer bonding. 54
4-4 Ideal asymmetric wafer shapes considered. 55
4-5 Overview of numerical model. 59
4-6 Distribution of G along a circular bond front in an asymmetric wafer pair. 60
4-7 Predicted bond fronts in an axisymmetric anisotropic silicon wafer pair. 62
4-8 Effective bonding modulus in the (100) plane of a silicon wafer. 62
4-9 Predicted bond fronts for pairs with asymmetric wafer shape. 63

5-1 Two types of clamping configurations considered. 68
5-2 Schematic of free configuration. 71
5-3 Schematic of clamped configuration. 71

5-4 Final curvature of bond pair for the free and clamped configurations. 75
5-5 Bonding curvature required to obtain a flat bond pair. 75
5-6 Curvature of bonded pair for flat wafers that are bonded while curved. 76
5-7 Strain energy release rate as a function of crack length. 76
5-8 Strain energy release rate in the free and clamped configurations. 77
5-9 Ratio of the strain energy release rates of the free and clamped configuration. 77

6-1 Schematic of the bond propagation experiments. 82
6-2 Schematic of the bond shape experiments. 83
6-3 Fabrication process for bond propagation specimens. 84
6-4 Data reduction process in the propagation experiments. 86
6-5 Time dependence in bond propagation experiments. 87
6-6 IR transmission images of the bond pairs in the bond propagation study. 88
6-7 Summary of work of adhesion values measured in the bond propagation study. . . . 89
6-8 Effect of gravity in the shape experiments. 91
6-9 Analysis process to predict the shape of bonded pairs. 93
6-10 Summary of the wafer shape experiments. 94
6-11 Detail of pair S6 in the shape experiments. 95

7-1 Geometry of the ideal wavy surface considered. 100
7-2 ΔU/ΔA as a function of wavelength and amplitude. 101
7-3 Effect of wafer thickness on ΔU/ΔA. 101
7-4 Filtering process used to isolate nanotopography features. 103
7-5 Comparison of filtering approaches. 104
7-6 Nanotopography measurements of the three wafers. 105
7-7 Power spectral densities of the nanotopography of the three surfaces measured. . . . 106
7-8 Root-mean-square of the nanotopography height variations as a function of wavelength. 107
7-9 Relative $\Delta U/\Delta A$ of the three wafers. 107
7-10 Distribution of surface heights on wafer (B). 108
7-11 Surface plots of the three measured surfaces and the reference surface. 110

8-1 Overview of blade insertion test. 114
8-2 Mixed mode properties of the double cantilever beam. 117
8-3 Finite element mesh of the double cantilever specimen. 119
8-4 Strain energy release rate across a straight crack. 120
8-5 Shape of crack fronts in a (100) silicon wafer pair. 122
8-6 Shape of crack fronts in an isotropic silicon wafer pair. 122

8-7 Difference between G calculated using beam theory and finite element analysis. . . . 123
8-8 Finite element strain energy release rate as a function of crack length. 124
8-9 Comparison of finite element results and experiment. 125

B-1 Schematic of wafer loaded by gravity. 146
B-2 Deflection profiles of a wafer loaded by gravity for different support radii. 147
B-3 Deflection at the center and edge of the wafer as a function of support radius. 147

List of Tables

1.1 Typical wafer bonding processes. 22

4.1 Geometry and work of adhesion values of predictions in Fig. 4-7. 61

6.1 Wafer pairs in bond propagation study. 86
6.2 Wafer pairs in final shape study. 92

7.1 Wafers in nanotopography experiments. 102
7.2 Properties of reference surfaces and corresponding $\Delta U/\Delta A$. 109

B.1 Deflections due to gravity for various standard wafer geometries. 148

Nomenclature

Variables and Constants

a	Crack length (m)
A	Bonded area (m^2)
A_C	Crack area (m^2)
A_T	Total area (m^2)
b	Outer radius of wafer (m)
$\mathbf{B}$	Approximate Jacobian calculated via Broyden update (m)
c	Bond radius (m)
c_a, c_v	Etch fraction (area and volume)
c_o	Radius of center region of spoke pattern (m)
C_t	Taper ratio of spoke, $C_t = s_b/s_o$
$C_{11},\ C_{12},\ C_{44}$	Stiffness coefficients of a cubic material (Pa)
d	Interface gap (m)
D	Plate rigidity (Pa m^3)
$\bar{D}$	Effective plate rigidity for bonding curved substrates (Pa m^3)
E	Young's modulus (Pa)
$\bar{E}$	Plane strain modulus $E = E/(1-\nu^2)$ (Pa)
$\tilde{E}$	Biaxial modulus $E = E/(1-\nu)$ (Pa)
E_{eff}	Effective Young's modulus of a porous material (Pa)
f	Spatial frequency (1/m)
$\mathbf{F}$	Equilibrium function in numerical model
g	Gravitational acceleration (m/s^2)
G	Strain energy release rate or accumulation rate (J/m^2)
$h,\ h_1,\ h_2$	Wafer thickness (m)
K_I, K_{II}	Mode I and Mode II stress intensity factors (N/m$^{3/2}$)
M	Moment per unit length (N)
M_r	Radial moment per unit length (N)

M_θ	Tangential moment per unit length (N)
$N(R)$	Moment dependence on bond radius and Poisson's ratio
p_a, p_v	Fraction of un-etched material (area and volume), p_a=$1 - c_a$, p_v=$1 - c_v$
P	Amplitude of nanotopography features (m)
q	Distributed load acting on plate (Pa)
Q	Shear load per unit length (N/m)
R	Non-dimensional bond radius, $R = c/b$
R_o	Non-dimensional radius of center region of spoke pattern, $R_o = c_o/b$
R_g	Radial extension of gap (m)
$\mathbf{R}$	Vector of bond front radii in asymmetric model (m)
s	Support radius (m)
s_o	Arc length of spoke at edge of central region in the spoke pattern (m)
s_b	Arc length of spoke at edge of wafer in the spoke pattern (m)
$S(f)$	Power spectral density (m^3)
$u_1,\ u_2$	Nodal displacements in finite element model (m)
U_E	Strain energy (J)
U_T	Total system energy (J)
w	Shape of wafer - position of wafer mid-surface (m)
$\bar{w}$	Deflection of wafer (m)
W	Work of adhesion (J/m^2)
W_F	External work (J)
$\mathbf{Y}$	Vector describing crack front position (m)
$\gamma,\ \gamma_1,\ \gamma_2$	Surface energies (J/m^2)
γ_{12}	Interface energy (J/m^2)
Γ	Interface toughness (J/m^2)
δ	Wafer bow or blade thickness (m)
δ_0	Initial spacing of nodes at interface in finite element model (m)
η	Thickness ratio
$\kappa_1,\ \kappa_2,\ \kappa_x,\ \kappa_y,\ \kappa_f$	Curvature of wafers and bond pair (1/m)
λ	Wavelength of nanotopography features (m)
λ_C	Cutoff wavelength of nanotopography features (m)
ν	Poisson's ratio
ν_{eff}	Effective Poisson's ratio of a porous material
ρ	Radius of curvature (m) or density (kg/m^3)
$\rho_1,\ \rho_2$	Radius of curvature of wafer (m)
σ	Stress (Pa) or standard deviation of surface heights (m)

Σ	Modulus ratio
Φ	Line element rotation
Ψ	Phase angle (°)
χ	Curvature ratio

Coordinate Systems

r, θ, z	Cylindrical coordinates
x, y, z	Cartesian coordinates

Common Acronyms

3D IC	Three-dimensional integrated circuit
AFM	Atomic force microscope
CMOS	Complementary metal oxide semiconductor
DSP	Double side polished
SOI	Silicon-on-insulator
SSP	Single side polished
VCCT	Virtual crack closure technique

Chapter 1

Introduction

1.1 Wafer Bonding

Wafer bonding has emerged as an important technology in the manufacture of semiconductor substrates, advanced micro- and optoelectronic devices, and microelectromechanical systems (MEMS). Generally speaking, wafer bonding refers to the process of joining multiple, large diameter (50–300 mm), thin (0.4–1.0 mm) substrates. The process adds significant flexibility to the microfabrication tool set and has been coupled with more traditional polishing and microfabrication processes to enable commercial products such as silicon-on-insulator (SOI) substrates [1], microfabricated pressure and inertial sensors [2], and high brightness light emitting diodes (LEDs) [3]. An even larger array of applications are in the research and development stage, including wafer-level packaging schemes for MEMS [2], strained silicon substrates [4], and power-MEMS devices [5]. The range of processes available by which to achieve wafer-level bonding is nearly as broad as the application space, with processes ranging from those that require no intermediate bonding layer, such as direct and anodic bonding, to those with metal (solder/eutectic, thermocompression) and polymer interlayers. Each process has specific attributes, such as processing temperature, surface quality requirements, and bond strength, that have driven their development and dictate the applications that they have been employed in. Table 1.1 lists the more common wafer bonding processes, along with their respective attributes and process requirements.

Direct wafer bonding, the primary focus of this work, is, perhaps, the process that has seen the greatest interest and broadest range of applications of the processes listed in Table 1.1. Direct bonding, also referred to as 'fusion bonding', is a process in which flat and smooth wafers are initially bonded at room temperature via macroscopically short-range surface forces and then annealed at an elevated temperature to strengthen the bond. The process is an attractive joining technology, as it yields bonds with strengths that approach that of the bulk material, are high temperature stable, and do not require an intermediate layer that can cause thermal residual stress and compatibility

Table 1.1: Typical wafer bonding processes.

Bond Process	Required Surface Quality	Processing Temperature	Applied Load	Strength	Ref.
direct	excellent	25-1000°C	none	high	[3, 6]
anodic	good	250-450°C	electric field	high	[7–9]
glass frit	average	≈400°C	low	med	[10, 11]
solder/eutectic	average	310-450°C	low	med	[12, 13]
thermocompression	good	300-350°C	moderate	med	[14]
polymer	poor	200°C	moderate	low	[15, 16]

problems in a traditional CMOS (complementary metal oxide semiconductor) fabrication facility.

The various attributes of direct bonding result in a process that is extremely flexible and one that can be integrated into device manufacture at different points in the process flow. Historically, it has been primarily used as a substrate manufacturing technique to produce SOI and other advanced microelectronic substrates. In the manufacture of these substrates, bonding is typically one of the first steps in the process and is performed prior to any device fabrication. The high temperature stability and material compatibility of the bonding process allows microelectronic devices to be processed on the bonded wafers using traditional integrated circuit fabrication techniques in a standard CMOS fabrication line.

More recently, direct bonding has been pursued in the construction of MEMS and three dimensional integrated circuits (3D IC's). In the fabrication of MEMS, direct wafer bonding is often employed in the middle or at the end of a process to create three-dimensional structures. Pressure sensors are an example where bonding is employed towards the middle of the manufacturing process. In this case, direct wafer bonding is used to create sealed cavities by bonding etched wafers, yielding a substrate that can be subsequently processed to form the sensing and signal conditioning circuitry. An example in which wafer bonding is used as a final joining step, is the MIT microengine that is pictured in Fig. 1-1(a). This device relies on direct bonding to join six wafers that have been micromachined using deep reactive ion etching. The ability to bond multiple processed wafers as a final step allows a complicated network of closed channels and cavities to be fabricated - a feat that would be unattainable with traditional microfabrication techniques alone. Direct bonding is also currently being pursued as a late-stage joining step in the fabrication of 3D IC's. Recent reports of direct bonding without the need for a high-temperature anneal have permitted fully processed logic and memory devices to be joined yielding shorter interconnect lengths and enhanced performance [17].

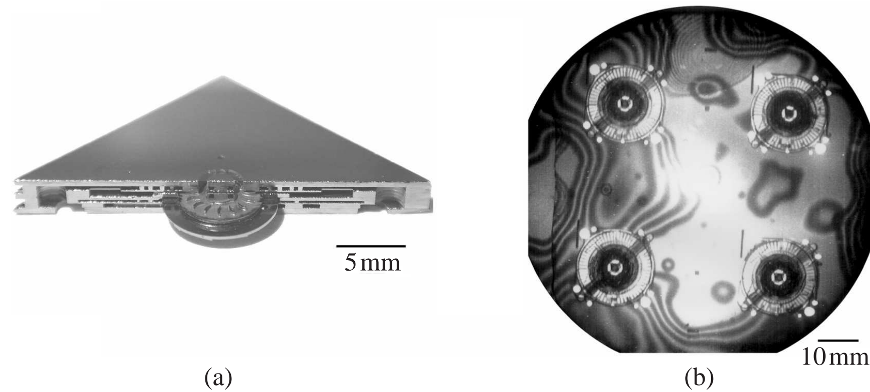

Figure 1-1: A six-wafer miniature gas turbine engine that is fabricated using direct wafer bonding. (a) A cross-section of the device that shows the multi-wafer architecture. (b) An infrared transmission image of a 100 mm bonded wafer set with four devices, in which bonding failed. The fringes and dark regions indicate un-bonded areas [18].

1.2 Motivation

From the examples cited above, it is clear that direct bonding is a powerful process and is of interest for more than the manufacture of SOI substrates, which is the application that originally drove the development of the technology. Direct wafer bonding clearly has practical applications and has the potential to enable a range of new MEMS and three-dimensional integrated circuits. However, as the bonding process has been employed in more advanced applications, such as these, that often require the bonding of multiple processed wafers late in the process sequence, failures during bonding have become more common. An example of a bonding failure that occurred during the fabrication of the MIT microengine is shown in Fig. 1-1(b). There are numerous un-bonded areas across the wafer resulting in zero yield for this wafer set. A key factor in the rise of failures such as those shown in Fig. 1-1(b) is that the majority of the fundamental direct bonding work was done with the aim of producing SOI substrates. SOI fabrication, which typically consists of bonding two standard thickness prime grade silicon wafers that are high quality (smooth, flat, and free of contamination) and unstructured, is by comparison a relatively easy task. As a result, many factors that are important in bonding processes for advanced applications are not fully understood and lead to failure. Among the factors that make direct bonding in the fabrication of MEMS and 3D IC's more difficult than SOI manufacture are,

- Patterning of wafers before bonding. Etching features on the surface is critical in the construction of MEMS, but results in less bonding area and hence a lower total surface energy to drive the bonding process. Furthermore, features on the surface can affect bond propagation and lead to trapped pockets of air at the interface.

- Increased surface roughness and contamination. When wafers are processed significantly prior to bonding, the quality of the surface is often degraded. Increased roughness and contamination reduce the effective surface energy and result in a smaller driving force for the bonding process.

- Wafer scale shape variations. Deposition of residually stressed thin films as well as wafer bonding itself (see Chapter 5) can result in an increase in wafer-scale shape variations such as bow and warp. Larger flatness variations make it more difficult for the wafers to deform to a common shape during the bonding process.

- Multiple wafer bonds. MEMS applications in particular often require the bonding of multiple wafers. This leads to the bonding of thicker pieces, which are stiffer and hence more difficult to bond. Furthermore, multiple bonding steps mean that each step must have high yield in order to achieve a satisfactory overall yield in the final wafer stack.

All of these factors combine to narrow the process window significantly and make the task of developing manufacturable direct bonding processes challenging. While a qualitative idea of the effects of these factors exists, there are very few reports of models that have been verified experimentally and allow for the *quantitative* assessment of these factors. The lack of experimentally validated quantitative models has resulted in processes being developed empirically through an approach that is largely based on trial and error. This has made the task of incorporating direct bonding processes into new complex process flows time consuming and expensive. In order to reduce the 'art' that is required in process development and to ensure that processes are stable and repeatable, an improved understanding of direct bonding is required.

Quantitative models that account for the effects of wafer and surface geometry, etch patterns, and surface chemistry permit more intelligent process, device, and mask design. Furthermore, they allow tolerances to be set on wafer geometry and enable the use of pre-bond metrology for process control. These models along with an improved understanding of the process are essential to reduce process development time and allow for direct bonding to become a competitive manufacturing technology outside the current limited commercial application set.

1.3 Objectives

This work, through a combination of mechanics-based modeling and experiments, seeks to develop models that may be used to facilitate the implementation of wafer bonding processes in emerging applications. Specifically, the objectives of the current work are,

- To develop a general framework and bonding criterion that may be used to assess the effect of wafer geometry, etch patterns, surface chemistry, and machine-wafer interactions in direct

bonding processes. The overall goal is to have a framework that permits bonding success or failure to be predicted.

- To develop an in depth understanding and models of the effect of wafer-scale shape variations (bow and warp) and etch patterns on failure in direct bonding processes. The aim is to develop analytical models that provide first order approximations and insight into the basic behavior and numerical approaches to allow bonding to be assessed for real geometries and etch patterns.
- To develop models that elucidate the effect of clamping and mounting in wafer bonding processes. While the interaction between bonding tools and wafer pairs has previously been ignored, it must be understood to ensure intelligent design of equipment and the development of robust processes.
- To validate experimentally the general bonding criterion and models for wafer shape and clamping effects that are developed. Experimental validation of the models is desired to not only confirm that the models capture the relevant mechanics, but also to demonstrate a route for connecting wafer geometry measurements to bonding success through the models.
- To examine the role of mid-spatial wavelength variations (waviness and nanotopography) in direct bonding processes. The aim is to determine the relative importance of these features in direct bonding through a combination of experiments and modeling.
- To examine the validity of traditional techniques used by the wafer bonding community to assess the interfacial toughness of bonded pairs. As the interfacial fracture energy is an important quantity in understanding failure in bonding processes it is essential to be able to characterize this quantity accurately.

1.4 Thesis Scope

This thesis seeks to address the objectives listed in the previous section in order to develop a knowledge base and set of models that will allow for the development of robust direct wafer bonding processes. The general modeling framework is first described and is followed by the development of models for wafer-shape, etch pattern and clamping effects. Experiments to verify the modeling approach are then detailed. Finally, nanotopography effects in bonding and the measurement of interfacial toughness are examined.

Specifically, in Chapter 2, previous work concerned with the mechanics of direct wafer bonding is reviewed and the general bonding criterion used in this work is introduced. The general framework and bonding criterion are developed and compared to the previous work. In Chapter 3, the effects

of axisymmetric wafer-scale shape variations and etch patterns on direct bonding are examined through the development of an analytical model that implements the bonding criterion described in Chapter 2. The results of the model and practical insights for process design are discussed. A finite element model that extends the analytical model in Chapter 3 to non-axisymmetric cases is presented in Chapter 4. The numerical model is demonstrated and the influence of asymmetries and elastic anisotropy examined. Chapter 5 addresses the effect of wafer clamping and mounting in direct bonding. Analytical models that demonstrate how clamping may effect the final shape of the pair and delamination are developed and practical implications of the results highlighted. Chapter 6 reports experiments that validate the bonding criterion and quantitative process models developed in Chapters 2 through 5. Details regarding the experimental approach, results, and comparison to the models are provided. Chapter 7 addresses the effect of nanotopography in wafer bonding and reports measurements on typical wafers and an analysis to assess the relative importance of these features in direct bonding. Finally, measurement of interfacial toughness using the wafer bonded double cantilever geometry is examined in Chapter 8. Issues associated with the use of the specimen and approaches to improve the accuracy of the method are discussed. The final chapter, Chapter 9, summarizes and discusses the work, reviews the key contributions, and identifies the next steps that should be taken to continue this work.

Portions of the work documented in the thesis have previously been presented in [19–22]

Chapter 2

Background and Bonding Criterion

The basic direct wafer bonding process is shown in Fig. 2-1. The process relies on polishing wafers sufficiently smooth and flat and removing contaminants on the surfaces such that when contacted at room temperature, they may bond via macroscopically short-range surface forces. The bond formed during the room temperature bond step typically consists of weak van der waals and hydrogen bonds and as such a thermal treatment is usually subsequently employed to increase the strength of the interface.

The idea of polishing two brittle materials smooth and flat, such that they will bond when contacted at a room temperature, was established well before the emergence of the microelectronics industry. In the 19th century, as the field of optics emerged, it was realized that smooth glass pieces would bond spontaneously at room temperature [3]. This technique, which became known as 'optical contacting', has been routinely used since then in the construction of optical components. The first reports of direct bonding as a microfabrication technique for joining wafers came more than a century later from two groups in 1986, one at IBM [23] and one at Toshiba [24]. Following these initial reports, significant research on direct wafer bonding began. This research focused on understanding the fundamentals of the process, developing improved surface and thermal treatments, and employing the process to join a range of materials to meet the needs of a diverse set of applications. The literature that documents this work is extensive and the numerous review articles, [3, 25–31], conference proceedings, [32–38], and books, [6, 39] that have been published provide a good picture of the work to this point.

As noted in Chapter 1, while there has been extensive work in this field, there remains a lack of understanding of the basic mechanics of the process. In particular, the factors that determine success or failure in the room temperature bond process have not been thoroughly quantified. The room temperature bond is the step of interest when considering the effect of flatness variations in direct bonding as it is in this step that the bonded area is largely determined. While the thermal

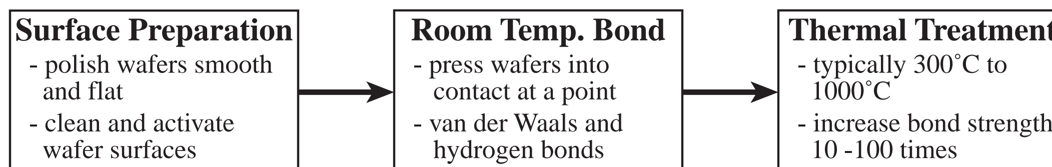

Figure 2-1: Three basic steps in direct wafer bonding.

treatment can strengthen the bond, it is generally recognized that since it is undesirable to apply loads to the wafers during this step, the final bonded area is controlled by the success of the room temperature step. As such, the review of previous work and the modeling in this thesis is restricted to the room temperature bond step.

In this chapter, the range of flatness variations that have an impact on bonding and are typically present on wafers are first outlined. The different types of flatness variations are discussed in terms of the their typical magnitudes and their impact on bonding. Previous work on assessing the role of these flatness variations in causing failures in direct wafer bonding processes is then reviewed. A general modeling framework and bonding criterion, which is the basis of the modeling and experiments in this thesis, is then introduced. The bonding criterion is derived and its connection to previous work in the adhesion of solids and fracture mechanics discussed.

2.1 Wafer Geometry

While manufacturing processes have been developed that yield wafers that are extremely smooth and flat, a range of flatness variations do exist across a typical wafer. As shown in Fig. 2-2, the different types of flatness deviations may be loosely classified into three ranges based on their spatial wavelength. Those with the smallest spatial wavelengths are referred to as roughness, those with mid-spatial wavelengths as waviness or nanotopography, and those that span the wafer, such as bow and warp, are referred to as wafer-scale shape. The exact boundaries that separate these three general types of flatness variations is unclear and numerous definitions may be found in the literature for each. The definitions that are used are often arbitrary and are typically defined as a matter of convenience based on the application or metrology tool. There are several standards which provide some guidance on identifying the different ranges and acquiring and reporting measurements. Among the relevant standards are SEMI M1 [40] and ASTM F 1241 [41] (general terminology); ASTM F 534 [42], ASTM F 1390 [43], and ASTM F 1451 [44] (wafer shape - bow, warp, sori); ASTM F 533 [45] and SEMI M43 [46] (thickness variation and nanotopography); SEMI M40 [47] (roughness). While these standards help in identifying the different ranges, they were not developed

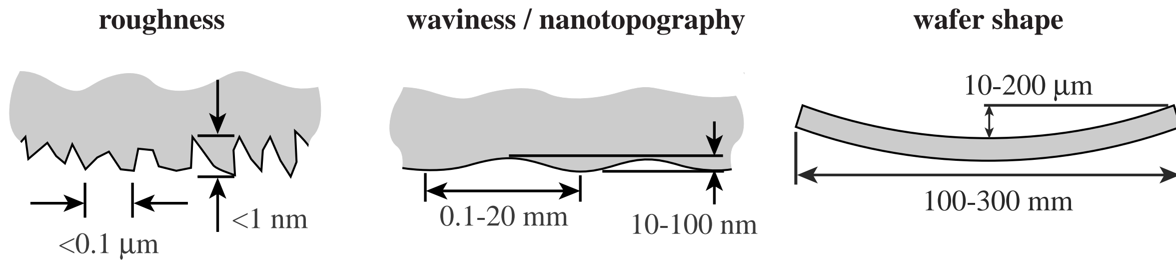

Figure 2-2: Different types of flatness variations on typical wafer. Values shown reflect typical values observed for a silicon wafer.

with bonding in mind and as such do not necessarily suggest metrics that are sufficient to describe the bondability of the wafers.

In terms of direct wafer bonding, it is useful to try to demarcate the boundaries of the different types of flatness variations based on two criteria, 1) the origin of the flatness variation and 2) how it is accommodated during the direct bonding process. Using this classification scheme, the roughness and waviness may be separated from wafer shape based on the consideration that they are a function of the details of the grinding and polishing process, while wafer shape primarily depends on the wafer slicing operation as well as the presence of residually stressed thin films. The roughness and waviness regimes may be separated from one another based on how the features are accommodated during the room-temperature direct bonding process. Long wavelength features, such as surface waviness and wafer-shape, are generally assumed to be accommodated completely through elastic deformation, as failure to do so would result in unacceptably large voids at the interface. On the other hand, surface roughness is not accommodated entirely through elastic deformation, but rather results in a reduction of the real bonded area at the interface.

This approach to defining the different regions is a good strategy for the current work as it not only divides the continuum of flatness variations into to manageable segments whose influence on bonding may be assessed individually, but also separates them based on the origin of the flatness variations. This provides a convenient way not only to identify the flatness variations that prevent bonding, but also permits the prebonding manufacturing steps that must be improved to achieve bonding to be easily identified. The scheme proposed, while well-suited for the current work, does not allow clear limits between the different types of flatness variations to be identified. For example the transition between roughness and waviness is dependent on the elastic properties of the wafers and most likely occurs over some range of spatial wavelengths where there is combination of elastic deformation and reduced contact area during bonding. No attempt was made in this work to identify the boundaries of the different ranges beyond the description given above.

2.2 Review of Wafer Bonding Mechanics

The importance of wafer geometry and its role in determining success in the room temperature step of direct bonding processes has long been recognized. In fact, 50 years prior to the initial reports of direct wafer bonding, Lord Rayleigh performed a systematic study of the joining of glass surfaces brought into 'optical contact' [48]. Rayleigh studied the joining of glass pieces that had been polished smooth and brought into contact at room temperature. Among his conclusions, which were essentially reiterated by wafer bonding researchers later, were that it is essential to keep the surfaces flat and that dust must be excluded from the surfaces to prevent large voids at the interface. Furthermore, Rayleigh noted that thinner pieces of glass are easier to bond and that when contacting a flat plate to a sphere, the bonded area is larger when the radius of the sphere is larger. These simple statements provide some of the key requirements for direct bonding (flat and clean surfaces) and highlight the fact that the large-scale flatness variations are accommodated through elastic deformation (dependence on thickness and radius of curvature).

After the reports of Lasky [23] and Shimbo [24] in 1986 for the joining of semiconductor wafers via direct bonding, several groups addressed the effect of wafer geometry and the elastic deformation that occurs in the direct bonding process. Maszara et al. [49] demonstrated that flatness variations are accommodated through elastic deformation by measuring the elastic strain after bonding using x-ray topography and showing that the strain field had a similar periodicity to measurements of the surface topography. He went on to show that the majority of elastic deformation occurs during the room-temperature bond process and proposed the idea that longer wavelength variations are accommodated through elastic deformation, while fine scale surface roughness features are not.

The first attempt to connect wafer geometry to bonding success was that from Stengl et al., [50] who proposed the idea that a bonding criterion may be established by comparing the strain energy stored in the wafers after bonding to the surface energy available to drive the process. In this initial report and further work by the same group [51–53], simple expressions were developed to compute the total strain energy required to close gaps at the interface that result when wafers with different initial shapes are bonded. They proposed that the total strain energy could be compared to the total surface energy available to determine if the wafers would bond successfully. Expressions were given for the maximum height of the gap, d, that could be closed for two limiting cases,

$$
\begin{aligned}
d &< 1.2\sqrt{\frac{\gamma R_g^4}{\bar{E}h^3}} \qquad R_g > 2h \\
d &< 3.6\sqrt{\frac{\gamma R_g}{\bar{E}}} \qquad R_g < 2h
\end{aligned}
\tag{2.1}
$$

where γ is the surface energy, R_g is the radial extension of the gap, and $\bar{E}$ and h are the plane strain modulus ($\bar{E} = \frac{E}{(1-\nu^2)}$, E, Young's modulus and ν, Poisson's ratio) and thickness of wafers, respectively. These expressions provide insight into the importance of wafer geometry and show

the basic scaling of bonding difficulty with the amplitude and wavelength of the flatness variations as well as wafer thickness and elastic modulus. In particular, the authors noted the importance of wafer thickness when accommodating long wavelength variations and confirmed this experimentally by demonstrating that thicker wafers required improved polishing techniques in order to successfully bond. Yu and Suo [54] later extended this gap closing work and presented a model that allows the strain energy required to deform two sinusoidally varying surfaces to a common shape to be calculated.

In addition to the gap closing work described above, Hong and Bower [55–57] also examined flatness variations accommodated through elastic deformation and reported a model to address the effect of wafer bow in bonding. They derived expressions for the final bow of a bonded pair and a criterion to describe the magnitude of bow that was acceptable. While they reported that reasonable agreement was obtained between their model and experiments, the mechanics used in the model is incorrect. In the model, plate theory was used to predict the bending stresses that develop in the wafer as a result of bonding bowed wafers. They proposed that the bending stresses could be compared to an interface strength to determine if the wafers would bond. The problem with this method is that the bending stresses are parallel to the interface and cannot be equated to the tractions on the interface. As such, the bending stresses cannot be compared to an interface strength, which is presumably defined as a normal stress or shear stress on the interface (the authors did not define what exactly was meant by 'interface strength'). There are similar difficulties with the expression derived for the final shape of the bonded pair in which they theorize that the bending stresses in each wafer must equal one another to satisfy equilibrium. While it is true that equilibrium must be satisfied in the bonded pair, this should be done by balancing the forces and moments on the wafers rather than simply equating the stresses in the two layers. This flawed approach results in an incorrect scaling with wafer thickness in the expression for the final curvature of the pair (they predict a linear dependence on thickness, while it is shown in this work in Chapter 3 that there should be a cubic dependence on thickness).

In addition to the work discussed above that has examined the effect of flatness variations that are accommodated through elastic deformation, there has also been work aimed at understanding the role of surface roughness. Bergh et al. [58] examined the role of roughness by measuring the bonding speed and the fracture surface energy of wafer pairs with different roughness. They attempted to connect these results to measurements on surface roughness obtained with an atomic force microscope (AFM). They demonstrated that a root mean square (rms) value of the roughness does not contain sufficient information to assess bondability as it does not include any information on the spatial wavelength of the roughness. Rather, they suggested that the amplitude spectrum of the surfaces, as obtained via Fourier decomposition, be used to assess the bondability of wafers with different roughness. Gui et al. [59, 60] also acknowledged the importance of including wave-

length information and suggested the use of the surface adhesion parameter, which was originally introduced by Fuller and Tabor [61], to assess the effect of roughness on bonding. The surface adhesion parameter is a non-dimensional quantity that expresses the adhesion of a rough surface as a function of the radius of curvature and standard deviation of the heights of the surface asperities, the elastic modulus of the material, and the surface energy. Gui et al. demonstrated that the bonding behavior could be correlated to the surface adhesion parameter determined from AFM measurements of the surface. Recently, Miki and Spearing [62] examined the effect of roughness and found that the apparent fracture surface energy of room temperature bonded pairs scaled with the bearing ratio of the surface roughness as measured via AFM. This result is consistent with the general statement in Sec. 2.1 that surface roughness primarily leads to a reduced contact area at the interface.

The previous work described in this section provides insight into the mechanics of the room temperature bonding process. While some of the recent work on surface roughness, [60, 62], has made strides in quantitatively connecting surface topography measurements to bondability, the analyses that examine the effect of mid- and long-wavelength flatness variations that are accommodated through elastic deformation only provide an idea of the basic scaling. As there are flatness variations with multiple wavelengths and amplitudes, it is not clear how to employ the expressions given in Eq. (2.1) to quantify the bondability of wafers. Furthermore, the equations were derived by comparing the total strain energy to total surface energy. While this allows the scaling with wafer geometry and elastic properties, to be identified it provides no information about how the bond propagates during the room temperature bond step. As such, it makes it difficult to incorporate the effects of etch patterns and only allows a criterion for bonding or no bonding to be obtained. The limitations of the model to quantify bondability are evident in the lack of comparison to experiments. The comparison to experiments has been limited to demonstrations that thicker wafers require better polishing [52] and that the model suggests that standard prime grade silicon wafers, which usually bond easily, should be bondable [30]. As detailed in Chapter 1 and confirmed by the review of the previous work in this section, there is clearly a need to develop an improved bonding criterion to allow a more quantitative understanding of direct bonding.

2.3 Bonding Criterion

It is well established that the key mechanism in the room temperature contacting step of direct bonding is the formation of weak interatomic bonds, such as van der Waals and hydrogen bonds [6]. These forces which drive the process are short range and their magnitude decreases quickly with increasing distance from the surface. The force-separation curve between two surfaces is expected to have the general form shown in Fig. 2-3. The typical range of the forces is very small and the

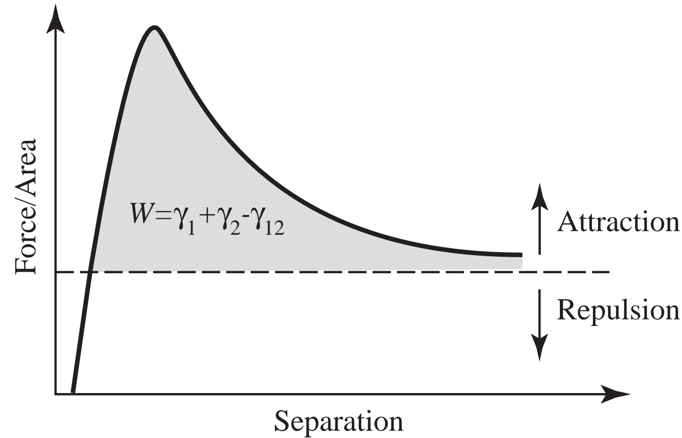

Figure 2-3: A typical force separation curve for two surfaces. The area under the curve is the work of adhesion. The equilibrium separation, the point at which the force switches from repulsive to attractive is small, ≈0.2 nm for van der Waals attraction. The attractive force decreases quickly with increasing distance from the surface, the magnitude of the force drops to a tenth of its maximum at ≈0.6 nm for van der waals attraction [63] (In direct bonding there are additional components to the attractive force at the surface, however the range of the surface forces will be similar to that of the van der waals attraction noted above.)

exact force separation law is typically not known and not readily measured. Given this and the fact that small-scale surface roughness features have a similar length scale to the separation law it is difficult to incorporate the force-separation law in a bonding criterion.

A better approach is to express the driving force for the bonding process as a work of adhesion, W, which is equivalent to the area under the force separation curve as shown in Fig. 2-3. The work of adhesion may be thought of as the energy available to form the bonded interface and can be expressed in terms of the surface energies of the two wafers, γ_1 and γ_2, and the interface energy, γ_{12},

$$W = \gamma_1 + \gamma_2 - \gamma_{12}. \tag{2.2}$$

The work of adhesion has units of energy per unit area.

In order to assess bonding, the work of adhesion can be compared to the strain energy required to deform the wafers to a common shape. Simply comparing the total strain energy to the work of adhesion to predict whether or not bonding will occur, as discussed above, has its limitations. However, if the problem is viewed as one of bond propagation, a better method to compare the work of adhesion to the required strain energy emerges. Direct bonding is typically accomplished by initiating contact at one point from which the bond propagates and 'zips' up the interface. As shown in Fig. 2-4, as the bond propagates, the strain energy in the wafers and the interface energy increase, while the surface energy decreases. The total energy in the system may be expressed as,

$$U_T = U_E + (\gamma_1 + \gamma_2)(A_T - A) + (\gamma_{12})A \tag{2.3}$$

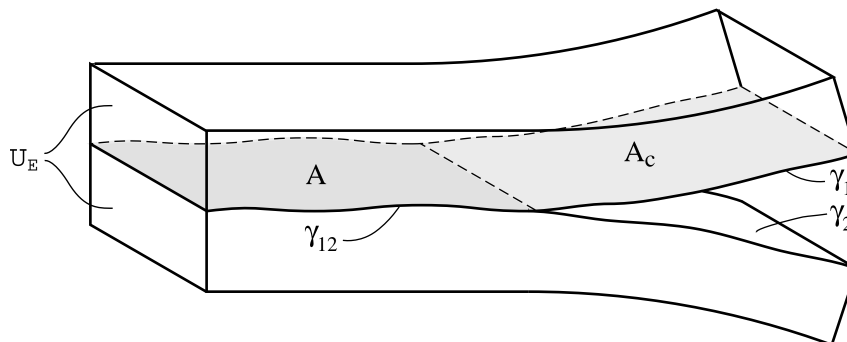

Figure 2-4: Model bonding system showing the change in energy as two surfaces are bonded. The surface energy (γ_1, γ_2) decreases and interface energy (γ_{12}) and strain energy (U_E) increase as the area of the bond, A, increases.

where A is the bonded area, A_T is the total area ($A_T = A + A_C$), and U_E is the strain energy in the wafers and is in general a function of the bonded area. The bond will advance until the system is in equilibrium which occurs when the system energy is minimized,

$$\frac{dU_T}{dA} = 0. \tag{2.4}$$

By differentiating Eq. (2.3), it is seen that for the system shown in Fig. 2-4 this corresponds to,

$$\frac{dU_E}{dA} = W. \tag{2.5}$$

Given this, the bond would be expected to advance when,

$$\frac{dU_E}{dA} < W. \tag{2.6}$$

The term $\frac{dU_E}{dA}$ represents the strain per unit area required to advance the bond, while the work of adhesion represents the energy available to do so. The $\frac{dU_E}{dA}$, which may be thought of as a strain energy accumulation rate, is a function of the wafer geometry, elastic properties, and etch patterns, while the work of adhesion depends on the surface chemistry.

The energy balance approach used in deriving this criterion is analogous to the Griffith energy balance in fracture mechanics [64] and the approach used by Johnson, Kendall and Roberts (JKR) [65] in accounting for adhesion effects during the contact of rubber spheres.

The bonding criterion given in Eq. (2.6) is completely consistent with the Griffith energy balance and the concept of the strain energy release rate [66] used in fracture mechanics. In fracture mechanics, the strain energy release rate, G, is compared to the toughness, Γ, to assess if a crack

will propagate. The criterion for crack propagation is,

$$G > \Gamma. \tag{2.7}$$

The strain energy release rate is defined as the change in the potential energy of the system per unit area of crack advance,

$$G = \frac{d}{dA_c}(W_F - U_E), \tag{2.8}$$

where W_F is the external work, U_E is the strain energy, and A_c is the area of crack. It is seen that when considering the problem of bonding in Fig. 2-4, if the unbonded area, which may be thought of as the area of the crack, $A_c = A_T - A$, is taken as the free variable when minimizing the total system energy [Eq. (2.3) and Eq. (2.4)], the criterion for bond front advance is,

$$-\frac{dU_E}{dA_C} < W. \tag{2.9}$$

This is equivalent to the strain energy release rate [Eq. (2.8)] when there is no change in external work. The strain energy accumulation rate which is defined as the energy accumulated per unit area of bond advance is equivalent to the strain energy release rate which is defined as the energy released per unit area of crack advance,

$$G = \frac{dU_E}{dA} = -\frac{dU_E}{dA_C}. \tag{2.10}$$

The connection between adhesion and fracture has been recognized before and a more formal derivation may be found in [67]. The equivalence between the strain energy release rate and the strain energy accumulation rate is important as it means that the numerous analytical and numerical techniques that have been developed for calculating the strain energy release rate in fracture mechanics problems may be employed to compute the strain energy accumulation rate in bonding problems.

This criterion is general and can be employed to evaluate the effect of a range of flatness deviations that are accommodated through elastic deformation on bonding success. The key to using the criterion is to develop an expression for the strain energy as a function of bond front position. Depending on the nature of the flatness deviation, this may be determined analytically or calculated numerically. In the following chapters, the criterion is evaluated for several cases using analytical models and finite element analysis.

Chapter 3

Wafer Shape Variations and Etch Patterns

Wafer scale shape variations refer to long wavelength variations of the centerline of the wafer. These shape variations, which may arise during the wafer manufacturing process or as a result of the deposition of residually stressed films during device fabrication, can prevent bonding. In this chapter, the effect of axisymmetric wafer-scale shape variations in the bonding of blank and patterned wafers is examined. The analysis in this chapter is limited to the axisymmetric case as it may be addressed analytically and as such provides insight in the basic behavior and essential scaling in direct bonding processes where wafer-scale shape variations are present.

The effect of axisymmetric wafer shape variations and etch patterns is examined in this chapter using the bonding criterion proposed in Chapter 2. First, closed form expressions for the strain energy accumulation rate and final shape of the wafers are developed using classical plate theory. The bonding criterion is then evaluated using an axisymmetric finite element model to validate the plate theory solution and demonstrate implementation of the bonding criterion numerically. Next, the effect of shallow and deep etch features on bonding is considered and integrated with the mechanics models that are developed in the first part of the chapter. Finally, the analytical and finite element models are compared, the model results presented, and practical implications of the results on process and device design discussed.

3.1 Geometry

The geometry considered is illustrated schematically in Fig. 3-1, and assumes that prior to bonding the wafers have the shape of a shallow spherical cap. These wafer-scale shape variations will be referred to as wafer bow. The bow is characterized in terms of the curvature of the substrate, κ, or

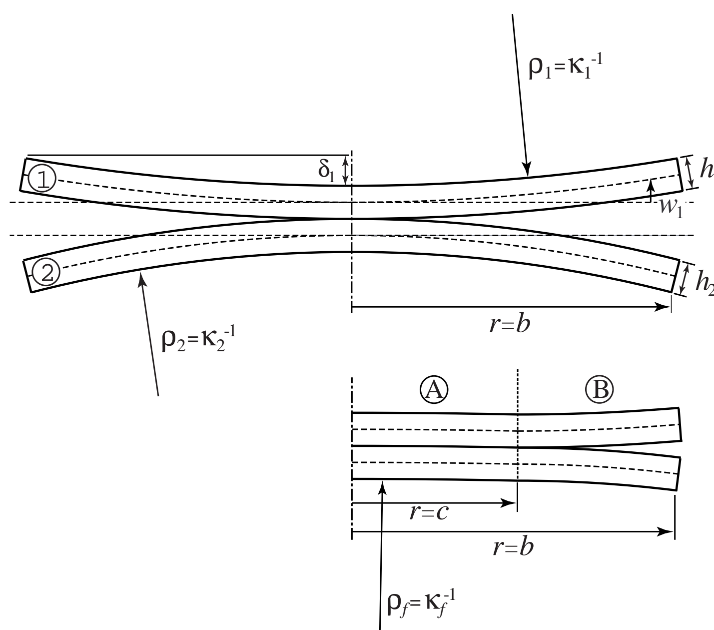

Figure 3-1: Schematic of bonding two bowed wafers showing assumed geometry and notation used. As drawn, κ_1 is a positive curvature and κ_2 is a negative curvature.

the 'bow', denoted as δ in the figure, which is the height difference between the center of the wafer and the edge of the wafer. While highly stressed films can cause large bows, in general, the bow is small compared to the thickness ($\delta \leq \frac{1}{5}h$) and hence small deflections are assumed throughout this analysis.

Figure 3-1 schematically illustrates the process of bonding two bowed wafers. The geometry of the two wafers, denoted 1 and 2, is defined in terms of their curvatures, κ_1 and κ_2, their thicknesses, h_1 and h_2, and their outer diameter, b (it is assumed they both have the same outer diameter). The curvature of either wafer can be negative or positive. As drawn in Fig. 3-1, κ_1 is a positive curvature and κ_2 is negative. The wafers are taken to be isotropic and their elastic behavior is defined in terms of their Young's modulus, E_1 and E_2, and Poisson's ratio, ν_1 and ν_2. Contact between the wafers is initially made at the center and it is assumed that the bond front propagates axisymmetrically outward. The bond front position is denoted as c. As the bond front advances, the wafers deform to a common curvature, κ_f. It should be noted that due to the requirement that contact is initially made at the center, the current analysis is limited to cases where $\kappa_2 < \kappa_1$.

3.2 Classical Plate Theory

As discussed in Chapter 2, in order to assess the bonding criterion, an expression for strain energy as a function of bond front position is required. For the case of bowed wafers, this can be derived

using classical plate theory. The plate is divided into two sections, A and B, as shown in Fig. 3-1, in order to aid in the analysis.

The radius of curvature of the wafers is large, thus the shape of the wafers can be approximated as a parabola. The initial shapes, w_{oi}, of the wafers are given as,

$$w_{oi} = \frac{1}{2\rho_i} r^2 = \frac{1}{2} \kappa_i r^2, \tag{3.1}$$

where the subscript i is used to denote the wafer, either 1 or 2. The shape of the wafers after bonding, w_f, can be expressed in terms of the final curvature or in terms of the initial shape and the deflection, $\bar{w}_i$, of the wafers during the bonding process,

$$w_f = \frac{1}{2} \kappa_f r^2 = w_{oi} + \bar{w}_i. \tag{3.2}$$

In section A of the wafer, the bonded section ($0 \leq r \leq a$), the deflection can be solved for directly from Eqs. (3.1) and (3.2),

$$\bar{w}_{Ai} = \frac{1}{2} (\kappa_f - \kappa_i) r^2. \tag{3.3}$$

Given that it is a plate, the deformation in section A results in stresses and deflection in section B. Using the governing equation for the plate,

$$\frac{d}{dr} \left[\frac{1}{r} \frac{d}{dr} \left(r \frac{d\bar{w}_{Bi}}{dr} \right) \right] = 0. \tag{3.4}$$

and the appropriate boundary conditions,

$$\begin{aligned} \bar{w}_{Ai}|_{r=c} &= \bar{w}_{Bi}|_{r=c} \\ \left.\frac{d\bar{w}_{Ai}}{dr}\right|_{r=c} &= \left.\frac{d\bar{w}_{Bi}}{dr}\right|_{r=c} \\ M_{rBi}|_{r=b} &= 0 \end{aligned} \tag{3.5}$$

where M_r is the radial moment in the plate,

$$M_{ri} = -D_i \left(\frac{d^2\bar{w}_i}{dr^2} + \frac{\nu}{r} \frac{d\bar{w}_i}{dr} \right) \tag{3.6}$$

and D_i is the plate rigidity defined in terms of the elastic modulus, E, Poisson's ratio, ν, and wafer thickness,

$$D_i = \frac{E_i h_i^3}{12(1 - \nu_i^2)}, \tag{3.7}$$

the deflection in section B may be determined. The deflection in section B as a function of bond

front position is,

$$\bar{w}_{Bi} = \frac{1}{2}\frac{c^2(\kappa_f - \kappa_i)}{b^2(1+\nu_i) + c^2(1-\nu_i)}\left\{(1-\nu_i)r^2 + 2(1+\nu_i)b^2\left[\ln\left(\frac{r}{c}\right) + \frac{1}{2}\right]\right\}. \tag{3.8}$$

Note that while the deflections in the two sections of the plate have been determined by considering the displacements during the bonding process, there is a load on the wafers that corresponds to the load that would have to be applied to achieve the specified deflection. The applied load for the current prescribed displacements is a moment at $r = c$, $\Delta M_{ri} = M_{rAi} - M_{rBi}$. In reality, a pure moment cannot be applied at $r = c$ since the bond only provides tractions at the interface. Rather there is a small zone near the bond front advance where the load is transferred via tractions at the interface. This is not captured by the plate theory, but has a small effect on the energy quantities that are of interest in the current work.

The deflection of the wafers as a function of bond front position is fully described by Eqs. (3.3) and (3.8). Using these, the strain energy in each wafer can be calculated directly [68],

$$U_{Ei} = \pi D_i \int_0^b \left[\left(\frac{d^2\bar{w}_i}{dr^2} + \frac{1}{r}\frac{d\bar{w}_i}{dr}\right)^2 - \frac{2(1-\nu_i)}{r}\frac{d\bar{w}_i}{dr}\frac{d^2\bar{w}_i}{dr^2}\right] r dr. \tag{3.9}$$

Applying Eq. (3.9), the strain energy in sections A and B for each wafer are found,

$$U_{Ei}|_A = \frac{\pi}{12}E_i h_i^3(\kappa_f - \kappa_i)^2 \frac{c^2}{1-\nu_i}, \tag{3.10}$$

$$U_{Ei}|_B = \frac{\pi}{12}E_i h_i^3(\kappa_f - \kappa_i)^2 \frac{c^2(b^2 - c^2)}{b^2(1+\nu_i) + c^2(1-\nu_i)}. \tag{3.11}$$

The total strain energy of each wafer, U_{Ei} is the sum of the energy in both sections,

$$U_{Ei} = \frac{\pi}{6}E_i h_i^3(\kappa_f - \kappa_i)^2 \frac{c^2 b^2}{(1-\nu_i)[b^2(1+\nu_i) + c^2(1-\nu_i)]}. \tag{3.12}$$

The quantity of interest for bonding is not the total strain energy, but is the strain energy accumulation rate. The strain energy accumulation rate can be expressed as

$$G_i = \frac{dU_{Ei}}{dA} = \frac{dU_{Ei}}{dc}\frac{dc}{dA} \tag{3.13}$$

for the case of axisymmetric bond front propagation. When the wafers contain no features on the surface that reduce bonding area, the bonding area as a function of bond front position is given as

$$A = \pi c^2, \tag{3.14}$$

and, hence,

$$\frac{dc}{dA} = \frac{1}{2\pi c}. \tag{3.15}$$

Using Eqs. (3.12), (3.13), and (3.15) and defining a non-dimensional parameter, $R = c/b$, that indicates the relative bond front position, the expression for the strain energy accumulation rate in each wafer is written as,

$$G_i = \frac{dU_{Ei}}{dA} = \frac{1}{6}E_i h_i^3(\kappa_f - \kappa_i)^2 \frac{(1+\nu_i)}{(1-\nu_i)} \frac{1}{[(1+\nu_i) + R^2(1-\nu_i)]^2}. \tag{3.16}$$

It is important to recognize that this expression is for one of the wafers in the bonding pair and only accounts for the effect of wafer bow. To compare the strain energy accumulation rate directly to the work of adhesion in order to evaluate whether or not wafers will bond, the strain energy accumulation rates of both bowed wafers and any additional flatness deviations must be accounted for (see methods to account for nanotopography work in Chapter 7 and discussion in Chapter 9 for information on smaller scale flatness variations).

The derivation to this point has assumed that the final curvature, κ_f, is specified. When bonding two wafers with different thicknesses, curvatures, and material properties, the final curvature is in general not known and is determined by equilibrium considerations. The equilibrium curvature that a bonded pair adopts can be calculated by determining the curvature that yields the minimum strain energy. The total strain energy of the system, U_E, is given as the sum of the strain energy in both wafers,

$$U_E(\kappa_f, a) = U_{E1} + U_{E2}. \tag{3.17}$$

For a given bond front position, the curvature that yields the minimum total system energy can be determined from

$$\frac{dU_E}{d\kappa_f} = 0. \tag{3.18}$$

Employing Eqs. (3.12) and (3.17), and solving Eq. (3.18) for κ_f, the equilibrium curvature of the bonded pair is determined,

$$\kappa_f = \frac{\bar{D}_1\kappa_1 + \bar{D}_2\kappa_2}{\bar{D}_1 + \bar{D}_2}, \tag{3.19}$$

where,

$$\bar{D}_i = \frac{E_i h_i^3}{(1-\nu_i)[(1+\nu_i) + R^2(1-\nu_i)]}. \tag{3.20}$$

The equilibrium curvature value is, in general, a function of bond front position, R, which suggests that the curvature is not uniform across the wafer. However, it is important to note that when

$\nu_1 = \nu_2$, Eq. (3.19) is independent of Poisson's ratio and R, and reduces to,

$$\kappa_f|_{\nu_1=\nu_2} = \frac{\Sigma\eta^3\kappa_1 + \kappa_2}{\Sigma\eta^3 + 1}. \tag{3.21}$$

where Σ and η are the moduli and thickness ratios, respectively, $\Sigma = E_1/E_2$, $\eta = h_1/h_2$. It is quite common, for wafers being bonded to have Poisson's ratios that are equal or at the very least close to one another. Thus in many situations, Eq. (3.21) provides a suitable approximation.

The expression given in Eq. (3.21) allows the strain energy accumulation rate for a pair of bowed wafers to be written in terms of their initial curvatures, material properties, and thicknesses. The total strain energy accumulation rate of both wafers is the quantity that is of interest when determining whether or not bowed wafers will bond in this case and is simply the sum of the strain energy accumulation rates of wafers 1 and 2,

$$\frac{dU_E}{dA} = \frac{dU_{E1}}{dA} + \frac{dU_{E2}}{dA}. \tag{3.22}$$

Using Eqs. (3.16), (3.21), and (3.22), the strain energy accumulation rate for the pair is,

$$G = \frac{dU_E}{dA} = \frac{1}{6}\frac{E_1 h_1^3}{1 + \Sigma\eta^3}(\kappa_2 - \kappa_1)^2 \frac{(1+\nu)}{(1-\nu)} \frac{1}{[(1+\nu) + R^2(1-\nu)]^2}. \tag{3.23}$$

This expression, which assumes that the Poisson's ratio of the wafers are equal, gives the strain energy accumulation rate for bonding a pair of bowed wafers in terms of quantities that are either known or are measurable. If wafer bow was the only type of flatness deviation present this quantity can be compared directly to the work of adhesion to predict bonding success.

3.3 Axisymmetric Finite Element Analysis

To verify the analytical derivation of the previous sections and to demonstrate the implementation of the bonding criterion numerically, an axisymmetric finite element model (finite element modeling of non-axisymmetric geometries is discussed in Chapter 4) using the commercial package ABAQUS [69] was constructed of the problem presented in Fig. 3-1. Each wafer was meshed with 800 8-node axisymmetric continuum elements arranged in a rectangular grid with 4 elements through the thickness of the wafer. Displacements were applied at the nodes at the interface to bring the surfaces together. To evaluate the strain energy as a function of interface position, the model was solved multiple times with an increasing number of nodes at the interface being 'bonded' (displaced) in each model run. Strain energy values for each case were recorded and strain energy as a function of bond front position was obtained.

The strain energy accumulation rate was calculated using a numerical differentiation scheme to approximate the derivative of the strain energy with respect to bond area. The strain energy accumulation rate was calculated at bond positions,

$$c = \frac{1}{2}(c_j + c_{j+1}), \tag{3.24}$$

using,

$$\frac{dU_E}{dA} = \frac{U_{j+1} - U_j}{\pi(c_{j+1}^2 - c_j^2)}. \tag{3.25}$$

The subscript, j, denotes the number of nodes displaced at the interface in the finite element analysis and c_j is the bonded length in each finite element run. This approach allows the calculation of strain energy accumulation rate as a function of bond front position.

3.4 Etch Pattern

With the increasing use of direct wafer bonding for micromechanical applications there is a greater need to bond wafers that have been etched. There are a range of features and patterns that may be etched to form mechanical structures such as fluid channels, membranes, and flexures. These features vary in depth and size. In the current work, they are classified into two main groups: shallow and deep features. Shallow features refer to etches that are a few microns deep in a wafer that is hundreds of microns thick, while deep features refer to instances where the etched structures penetrate through an appreciable fraction of the wafer thickness. The present work is limited to features that are etched into the wafers. Thus, the features do not add steps to the surface, but rather remove material from the substrates being bonded.

3.4.1 Shallow features

The sensitivity of the bond process to increased surface roughness means that virtually any areas that have been etched, regardless of depth, will not bond. This fact has been capitalized on in order to bond certain regions selectively [70]. However, it also means that the presence of features may inhibit bonding when not desired. When the features are shallow, the primary effect of the features is to reduce the bonding area and, hence, the energy available to deform the wafers elastically. The fact that very little material is removed means that the stiffness of the wafer is not significantly affected by the presence of shallow features. Thus, the strain energy that is required to deform the wafers does not change appreciably. This effect can be incorporated into the current analysis when calculating the strain energy accumulation rate. In the case of axisymmetric bond front propagation, the bonding criterion is evaluated using Eq. (3.13), where the term dc/dA accounts

for how the bond area changes as a function of bond front position.

The case presented earlier was for blank wafers, where the bonded area is described by $A = \pi c^2$. To demonstrate the effect of reduced bonding area, two types of etch patterns are considered here. None of these patterns represent those required to create practical devices, however they do represent useful bounding cases that illustrate the effect of patterning. The first pattern reflects a randomly distributed arrangement of circular holes and is shown schematically in Fig. 3-2(a). It is assumed that the features are sufficiently small and distributed such that the effect is to reduce the bonding area uniformly. The bonded area is described by

$$A = p_a \pi c^2, \tag{3.26}$$

where p_a is the fraction of bonding area remaining, and may be expressed in terms of the etch area fraction, c_a, as $p_a = 1 - c_a$. The other type of pattern considered in the current work is referred to as the spoke pattern and is designed to demonstrate how a pattern density that changes with radial position affects bonding. The basic geometry is shown in Fig. 3-2(b). The pattern is defined in terms of the radius c_o, the outer radius b, and the taper ratio C_t. The taper ratio is given in terms of the arc length of bonding area at radius c_o, s_o, and the arc length of bonding area at b, s_b. The values of taper ratio, $C_t = s_b/s_o$, are limited to $0 \leq C_t \leq b/c_o$, where the case of $C_t = b/c_o$ corresponds to the case of an un-patterned wafer. Figures 3-2(b)-(d) show spoke patterns with three different taper ratios. The bonding area as a function of bond front position can be written as

$$A = \begin{cases} \pi c^2 & c \leq c_o \\ \pi c_o \left[c_o + (c - c_o) \left(2 - (1 - C_t) \frac{c - c_o}{b - c_o} \right) \right] & c \geq c_o \end{cases} . \tag{3.27}$$

The effect of these different etch patterns is captured in the bonding criterion by the term dc/dA. Evaluating this term for the two cases identified, the strain energy accumulation rate for each can be written in terms of the strain energy accumulation rate of un-patterned wafers, G_{blank}. For a distributed pattern that uniformly reduces the bonding area, as shown in Fig. 3-2(a) the strain energy accumulation rate is given as,

$$G_{distributed} = \frac{1}{p_a} G_{blank}. \tag{3.28}$$

While the distributed etch pattern increases the strain energy accumulation rate equally at any bond front position, the spoke pattern alters the way in which the strain energy accumulation rate varies with radial position. The strain energy accumulation rate for the spoke pattern when $R \geq R_o$ is

$$G_{spoke} = \frac{R}{R_o} \frac{(1 - R_o)}{(1 - R) + C_t (R - R_o)} G_{blank}, \tag{3.29}$$

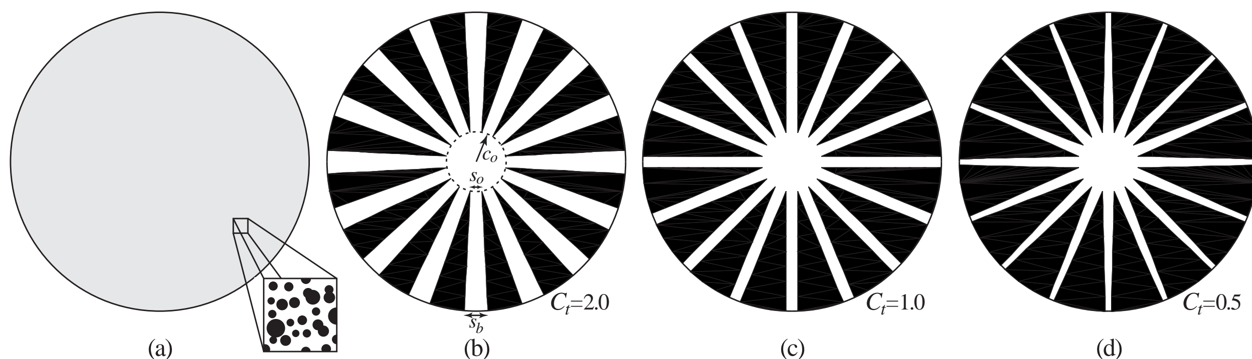

Figure 3-2: Different etch patterns considered in the current work. The black areas indicate etched (non-bonding) regions. (a) An array of small distributed holes resulting in a uniform reduction in bonding area. (b) Spoke pattern showing the geometry definitions. The pattern is defined in terms of c_o and the taper ratio $C_t = s_b/s_o$. Taper ratio of $C_t = 2.0$ is shown. (c) Spoke pattern with $C_t = 1.0$. (d) Spoke pattern with $C_t = 0.5$

.

where $R_o = c_o/b$.

3.4.2 Deep features

While the primary effect of shallow features is to reduce the bonding area, the presence of deep features change the bonding area as well as the stiffness of the wafer. The decrease in the bonding area has the same effect and is incorporated in the model using the approach in the previous section. However, the large removal of material also reduces the stiffness of the wafers and will reduce the strain energy required to deform the wafer, thus making bonding easier. The reduction in stiffness that is caused by cavities obviously depends on the exact pattern. However, to demonstrate the basic effect of deep etched features the etch pattern shown in Fig. 3-2(a) can be considered where the small features are cavities distributed through the thickness of the wafer. For this basic etch pattern, a porous material model can be used to estimate the reduction in modulus with removal of material. Many of the porous material models reported depend on the void size and shape. For the purposes of this work, a model which assumes randomly distributed spherical voids is used. The porous material model employed here is based on numerical simulations where expressions for effective Young's modulus, E_{eff}, and Poisson's ratio, ν_{eff}, were developed through empirical fits to simulation data [71]. The expressions for E_{eff} and ν_{eff} are given as [71],

$$E_{eff} = E \left(\frac{p_v - p_o}{1 - p_o} \right)^m, \tag{3.30}$$

$$\nu_{eff} = \nu + \frac{1 - p_v}{1 - p_1} (\nu_1 - \nu), \tag{3.31}$$

where p_v is the volume fraction of solid material, and p_o, p_1, m, and ν_1 are constants that depend on the pore geometry. For the case of randomly distributed spherical pores, $p_o = 0.182$, $p_1 = 0.160$, $m = 1.65$, and $\nu_1 = 0.221$ [71]. It should be noted that when the Poisson's ratio is near 0.2, which is common for many semiconductor materials, the effective Poisson's ratio does not change significantly with void fraction. Defining the etch volume fraction as $c_v = (1 - p_v)$ and noting that for well distributed holes $c_a = c_v$, the strain energy accumulation rate for deep etched wafers can be written as

$$G_{deep} = \frac{1}{p_v}\left(\frac{p_v - p_o}{1 - p_o}\right)^m G_{blank}. \tag{3.32}$$

This expression incorporates the reduction in stiffness and the reduction in bonding area due to the deep etches. However, it assumes the effective Poisson's ratio does not change as a result of the removal of material.

3.5 Results and Discussion

The strain energy accumulation rate is the quantity that must be considered when predicting whether or not bonding will be successful. If the strain energy accumulation rate exceeds the work of adhesion, bonding will not occur. The normalized strain energy accumulation rate is plotted as a function of the bond front position in Fig. 3-3 using Eq. (3.13). From the plot it is evident that it becomes easier to bond as the bond front approaches the wafer edge. This suggests that for blank wafers, if bonding begins, the bond front will advance to the edge of wafer, assuming that the work of adhesion and curvature are constant across the wafer. The other important point to note from Fig. 3-3 and Eq. (3.13) is the relative influence of the material properties and the geometry of the wafer. It is seen that the strain energy accumulation rate depends linearly on elastic modulus, the square of the curvature, the cube of thickness, and is relatively insensitive to Poisson's ratio in the range of interest. This strong dependence on thickness means that small increases in wafer thickness make it significantly more difficult to bond. Furthermore, the dependence on modulus, suggests that attempts to incorporate stiffer materials, such as SiC or Al_2O_3, will require tighter flatness control than is required when bonding silicon wafers.

This scaling with thickness and modulus is also seen in the total strain energy accumulation rate for a pair of wafers given by Eq. (3.23). The normalized total strain energy accumulation rate for a pair is plotted in Fig. 3-4 as a function of thickness ratio. It has been normalized with respect to the total thickness, thus the plot demonstrates how the relative thickness of the two wafers being bonded affects the strain energy accumulation rate. As is seen in Fig. 3-4, it is hardest to bond when the two wafers being bonded have equal thicknesses. This suggests that it is always desirable to have one wafer that is more compliant when bonding. This clearly has important implications when attempting to use multiple wafer bonding steps to create MEMS structures. For instance, if a

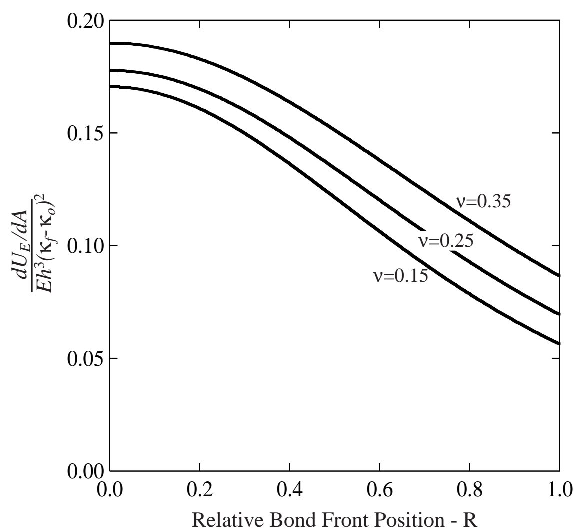

Figure 3-3: Plot of analytical normalized strain energy accumulation rate for common values of Poisson's ratio as a function of relative bond front position.

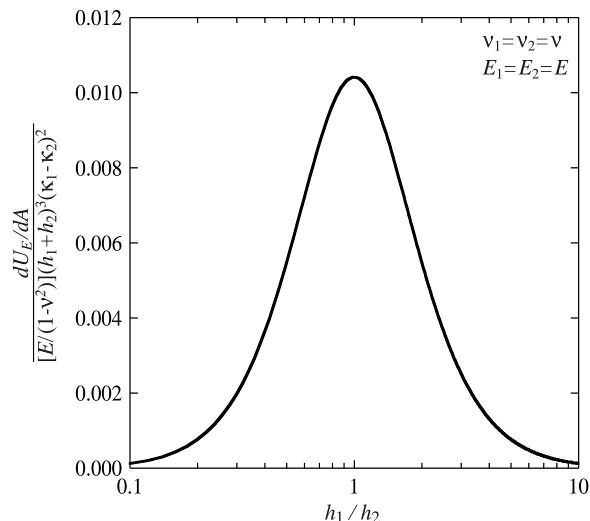

Figure 3-4: Total strain energy accumulation rate (maximum accumulation rate, bond front at $R = 0$) for bonding two bowed wafers as a function of the thickness ratio of the wafers.

six wafer device is to be fabricated, as has been done, [5], it is preferable to add wafers to the stack individually rather than trying to make two three-wafer sub-stacks that then must be bonded.

Another important implication of the result given in Eqs. (3.13) and (3.23) is that the wafer's diameter does not affect their ability to be bond. However, it should be noted that larger diameter wafers are in general thicker, which will increase the strain energy accumulation rate, and imply that bonding will be more difficult. One should also note that Eq. (3.13) is only independent of wafer diameter when expressed in terms of the curvatures (or radii of curvature) of the wafers. If the expression is written in terms of the bow, $\delta_i = \frac{1}{2}b^2\kappa_i$, the strain energy accumulation rate is dependent on wafer diameter. Hence, when comparing acceptable levels of bow on wafers of different diameters it is important to look at the curvature, rather than the more commonly reported bow value.

The analytical results that are shown in Fig. 3-3 are compared to the strain energy accumulation rate calculated via the axisymmetric finite element analysis in Fig. 3-5 for a specific case. In addition, the strain energy accumulation rate calculated using a higher-order Mindlin plate theory (see Appendix A for derivation) is shown for comparison. The parameters in the plot were chosen to approximate a typical case, the bonding of a two equal thickness 100 mm diameter silicon ($E = 150$ GPa and $\nu = 0.2$) wafers with a curvature difference of ($\kappa_1 - \kappa_2 = 0.047$ m^{-1}). The finite element, Mindlin, and classical plate theory results match well at bond radii greater than 15 mm. The deviation between the classical plate theory and the Mindlin and finite element results at short bond front positions is a result of the fact that the classical plate theory does not accurately

capture the stress state when the bond radius is comparable to the wafer thickness. The Mindlin plate theory, which includes a transverse shear term, matches the finite element analysis better at bond lengths less than 15 mm, but is not expected to fully capture the stress-state at very short bond lengths as the assumed state is still relatively simple. From analogous problems in fracture mechanics, it is expected that at very short bond lengths, the strain energy accumulation rate should depend on the square root of the bond radius, thus supporting the trend that the finite element results show. The inability of the classical plate theory to calculate the strain energy release rate accurately at short bond lengths, means that the G is over-predicted by $\approx 10\%$. Despite this deviation at short bond lengths, the classical plate theory solution is still extremely useful as it provides a closed form solution that captures the key scaling and is accurate across the majority of the wafer.

While predicting whether or not bonding will occur is important, it is also critical that the geometry of the wafer pair after bonding can be predicted. This is needed not only to calculate the strain energy accumulation rate for the wafers being bonded, but is also critical if subsequent bonding steps will be performed. Equation (3.21) gives the equilibrium curvature as a function of the material properties and geometry of the wafers. The final curvature of a two wafer stack is plotted for various thickness and modulus ratios in Fig. 3-6. It is clear that the thicker wafer in the pair dominates the final curvature and the modulus ratio only plays an important role when the wafers have similar thicknesses. This result implies that it may be beneficial to measure wafer curvatures prior to bonding and possibly match wafers to minimize the curvature of the bonded pair. This is critical when a process flow involves multiple wafer bonding steps as maintaining flat stacks is essential in preventing bonding failure in the later steps.

Figures 3-7 and 3-8 demonstrate the profound effect that etch features can have on bonding. Figure 3-7 shows the effect of shallow features such as those shown in Figs. 3-2(b)-(d). The strain energy accumulation rate for the spoke pattern (assuming $R_o = 0.2$) for three different taper ratios, $C_t = 0.5$, $C_t = 1.0$, $C_t = 1.0$, was calculated as a function of bond front position using Eq. (3.29). From the plot, it is seen that these etch patterns cause the strain energy accumulation rate to increase as the bond front approaches the wafer edge. This is important because it suggests that it becomes harder to bond as the front advances. Thus, blank wafers that can be bonded may only bond over a certain region once patterned. It should be noted that while these patterns were chosen due to their symmetry, a similar effect could be observed with a wafer where the feature density increases near the edges. The results shown in Fig. 3-8 compare the effect of shallow features to deep features. The results were generated using Eqs. (3.28) and (3.32) and assume small, distributed etched features. It is evident from Fig. 3-8 that while shallow features make it more difficult to bond, wafers with deep features are easier to bond despite the reduction in bonding area. The reduction in stiffness caused by the material removal dominates over the reduction in bonding area.

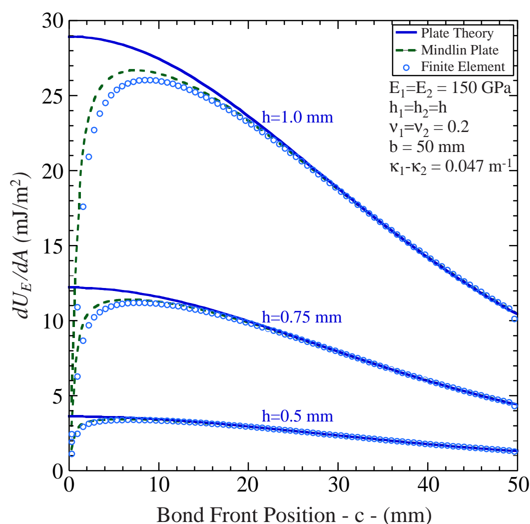

Figure 3-5: Plot of strain energy accumulation rate, comparing classical plate theory, Mindlin plate theory, and finite element results for the specific case of bonding two equal thickness 100 mm diameter wafers, where $E_1 = E_2 = 150$ GPa, $\nu_1 = \nu_2 = 0.2$, and $\kappa_1 - \kappa_2 = 0.047$ m^{-1}.

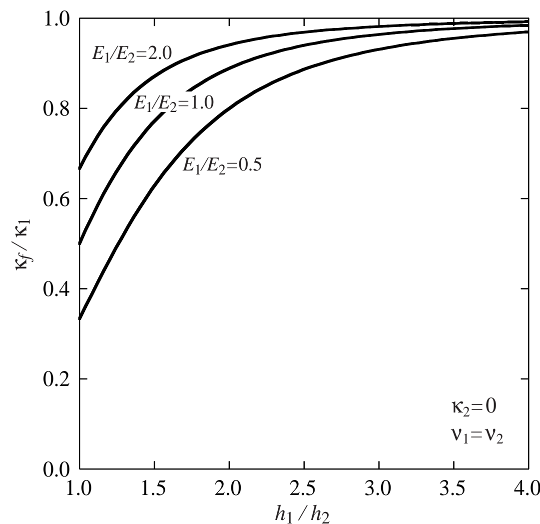

Figure 3-6: The final curvature of a bonded stack given as a function of the thickness ratio and modulus ratio of the two wafers being bonded. One wafer is taken to be flat initially ($\kappa_2 = 0$) and the wafers are assumed to have equal values of Poisson's ratio.

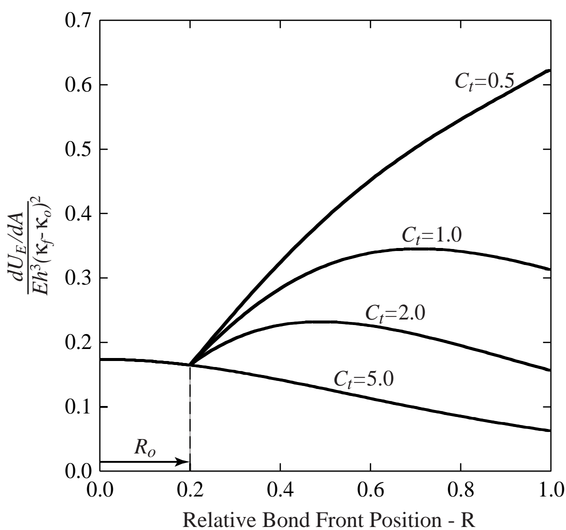

Figure 3-7: Effect of spoke patterns with various taper ratios on strain energy accumulation rate. The case of $C_t = 5.0$ corresponds to the case of blank wafer for $R_o = 0.2$. A decreasing taper ratio increases the strain energy accumulation rate.

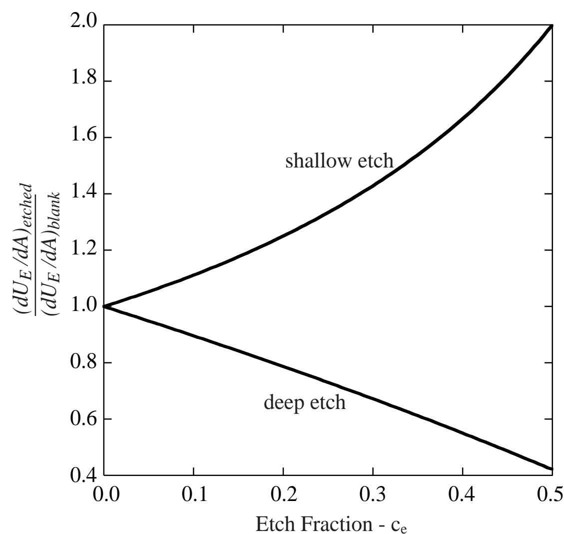

Figure 3-8: The effect of distributed deep and shallow features on strain energy accumulation rate.

These results suggest that the distribution of devices over a wafer can significantly affect the ability to bond the wafers and as such pattern layout should be carefully considered. Furthermore, it may be possible to increase the ability to bond pairs of wafers by removing additional material between devices in order to increase the wafer compliance.

3.6 Summary

The bonding criterion described in Chapter 2 has been implemented to examine the case of bonding bowed wafers with etch patterns. A closed form solution has been developed for the strain energy accumulation rate of bowed wafers and verified using finite element analysis. The results show that, when bonding un-patterned wafers, if the bond front begins to advance it will propagate to the edge of the wafers, since G decreases as bond front advances. However, it was also demonstrated that etched features can alter this situation and, in some cases, it may become more difficult to bond as the bond front approaches the edge. Finally, the effect of deep etched features has been examined and it was demonstrated that their presence may facilitate bonding by lowering the strain energy accumulation rate. The results given demonstrate that intelligent process design and mask layout may help to prevent bonding failure.

Chapter 4

Asymmetric Wafer Shape Variations

In Chapter 3, the bonding criterion described in Chapter 2, was employed to examine the bonding of wafers with axisymmetric wafer-scale shape variations and etch patterns. While the analytical model that was developed in Chapter 3 is useful for understanding the essential mechanics of the process and may be used for first-order assessment of wafer shape effects, the assumptions required to obtain a closed-form solution restrict its applicability. In particular, the model assumes that the wafer shape is axisymmetric and that the material is isotropic. In practice, these assumptions are often not true. While the wafer shape may be axisymmetric after the deposition of a uniform residually stressed thin film, wafer-scale variations that result from patterned stressed films and the manufacturing process (wafer slicing) are typically not axisymmetric. Shape measurements from three virgin prime grade 100 mm silicon wafers, all of which are from the same manufacturing lot, are shown in Fig. 4-1. The wafer-scale shape is clearly not axisymmetric and varies considerably from wafer to wafer. In addition to the asymmetries in wafer shape, bonding processes are often performed between single crystal wafers with anisotropic elastic properties. For example, single crystal silicon wafers, which are the predominant substrate used in direct bonding, have cubic symmetry and as such have elastic properties that vary with direction. The effective elastic modulus and Poisson's ratio in the plane of a (100) silicon wafer as function of direction are shown in Fig. 4-2. The Young's modulus varies from 130-196 GPa and the Poisson's ratio from 0.06-0.28 in the plane and as such may clearly affect bond propagation. Furthermore, etch patterns on device wafers are generally not axisymmetric.

These considerations provide the motivation to develop a model that can be used to assess the bonding of wafers with arbitrary geometries and etch patterns as well anisotropic elastic properties. A numerical model that was developed to accomplish exactly this is described in this chapter. The key elements of the model, including details of the mesh, the local calculation of G, and the iteration scheme that was required are first described. The model is then used to assess the effect

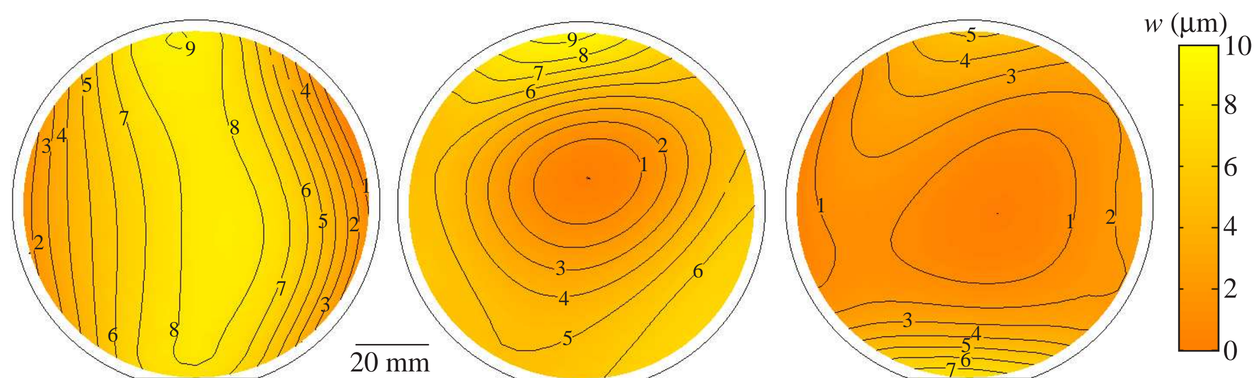

Figure 4-1: Typical shape maps of 100 mm silicon wafers. All wafers are (100) prime grade silicon wafers from a single lot. The contour lines are labeled in microns.

of elastic anisotropy when bonding (100) silicon wafers. The results are compared to the analytical model from the previous chapter and the importance of accounting for elastic anisotropy considered. Finally, the bond front prediction capability of the model is demonstrated for a series of asymmetric test wafers. The bonding of different pairs with varying degrees of asymmetry is examined and the important effects of wafer asymmetry highlighted.

4.1 Model Overview

The primary challenge in developing a model that can accommodate asymmetries is the fact that the shape of the bond front is not known *a priori*. In the axisymmetric case, in which the wafer shape, elastic properties, and etch pattern were all symmetric about the center axis, it was reasonable to assume that the bond front would also be symmetric and hence the bond front was taken to be circular and simply defined by a bond radius, c. However, when an asymmetry is introduced into the model, the bond front, in general, will not be axisymmetric. The shape and size of the bonded area is determined by the equilibrium condition $G = W$, which must be satisfied along the entire front. As such, a model designed to examine wafers with asymmetries must have the capability to calculate G and predict the size and shape of the bond front. The model developed in this work accomplishes this and has three key elements.

- *Three dimensional finite element model.* A finite element model is used to model the elastic deformation of the wafers during the bonding process. A full three dimensional model permits arbitrary geometries and etch patterns as well as elastic anisotropy to be accounted for appropriately. A three dimensional finite element model, while computationally expensive, is essential to include all of the features of interest.

- *Local calculation of G.* The virtual crack closure technique is used to calculate G locally

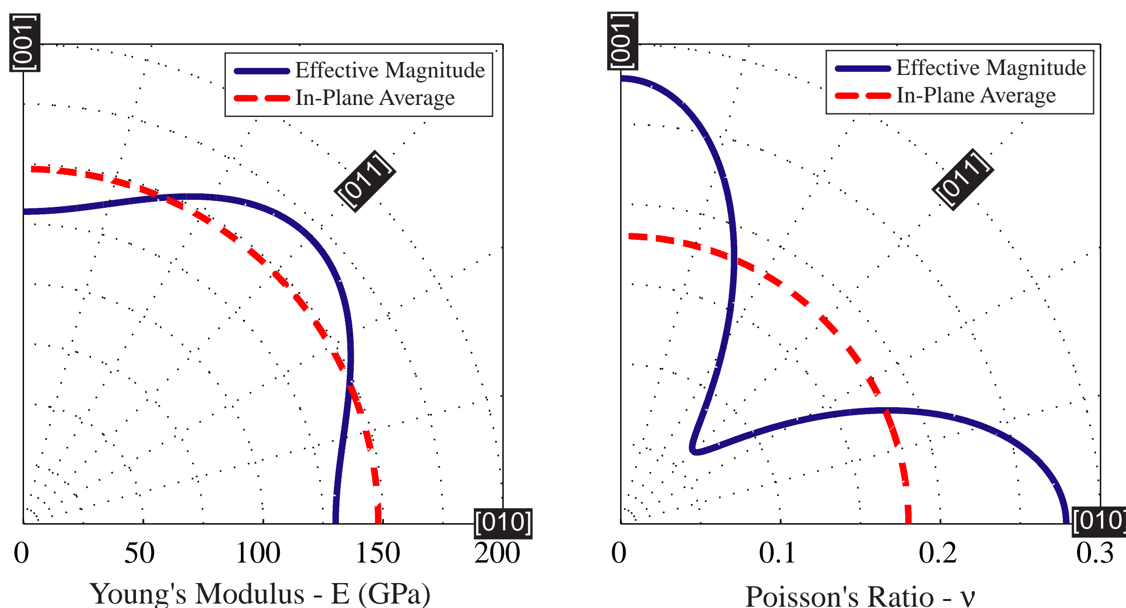

Figure 4-2: Effective elastic modulus and Poisson's ratio of single crystal silicon as a function of direction in the (100) plane calculated from the three elastic constants of silicon. The dashed line indicates the in-plane average values E=148 GPa, ν=0.18.

along the bond front. Equilibrium requires that the strain energy accumulation rate is equal to the work of adhesion along the entire bond front. As such, the strain energy accumulation rate must be calculated locally along the bond front to assess whether or not the front is in equilibrium.

- *Iterative approach.* The shape of the bond front is not known *a priori* and is iterated using a quasi-Newton method to find the equilibrium size and shape. The quasi-Newton method allows the position of the bond front to be systematically changed such that an equilibrium bond front, where $G = W$ along the entire front, may be determined in an efficient fashion.

Each of these three components are described in detail in the following sections.

4.2 Geometry and Finite Element Mesh

The mesh used to examine the bonding of patterned 100 mm wafers is shown in Fig. 4-3. The in-plane geometry is that for a standard (100) 100 mm wafer, a 100 mm diameter with a major flat 32.5 mm long. The minor flat (18 mm long), which (100) wafers typically have oriented 90° (p-type) or 180° (n-type) was not included in the final model as it was shown to not affect the results significantly. The elastic properties were defined as those of single crystal silicon (anisotropic with cubic symmetry C_{11}=165.7 GPa, C_{12}=63.9 GPa, C_{44}=79.6 GPa [72]) and were defined in the model

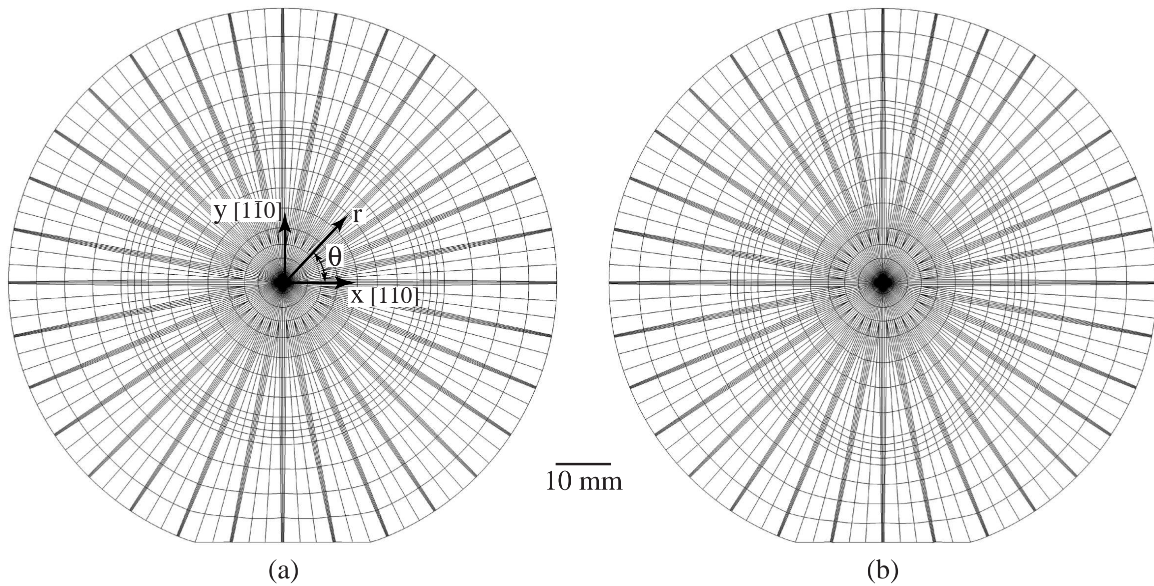

Figure 4-3: Top view of three dimensional finite element mesh used to model the bonding of asymmetric wafers with a spoke pattern at interface. (a) initial mesh (b) final mesh after iteration to obtain $G = W$ along the entire bond front.

such that the [110] direction was parallel to the flat. The etch pattern used in the demonstration version of the model was that of the spoke pattern with $R_o = 0.14$, $C_t = 0.3$ defined in Chapter 2. This pattern was used out of convenience, as the results can easily be compared to the analytical solution in the previous chapter and the pattern was used in the experiments described in Chapter 6. The modeling approach can accommodate asymmetric etch patterns and simply requires that the pattern be defined appropriately when constructing the mesh.

Figure 4-3 only shows the in-plane geometry of the mesh, the out of plane geometry is defined by the wafer thickness and shape (the position of the wafer midplane) at each node. The wafer shapes that are used in this study were defined to provide a range of symmetric and asymmetric geometries. The six wafer shapes that are used are shown in Fig. 4-4. These six wafer shapes provide a range of asymmetries that allow for systematic studies to be conducted using the model. While the asymmetric wafer shapes shown in Fig. 4-4 are defined by a simple mathematical function, more complicated geometries may be examined using the model as well. The model was developed such that wafer shape and thickness data could be imported directly from actual wafer measurements such that geometries like those shown in Fig. 4-1 can be modeled. This functionality is demonstrated in the data reduction of the experiments described in Chapter 6. The model includes both wafers in the bonding pair and the shape and thickness of each are specified independently. In the study in this chapter, the thickness of both wafers are taken to be the same with a thickness of 525 μm, unless otherwise noted.

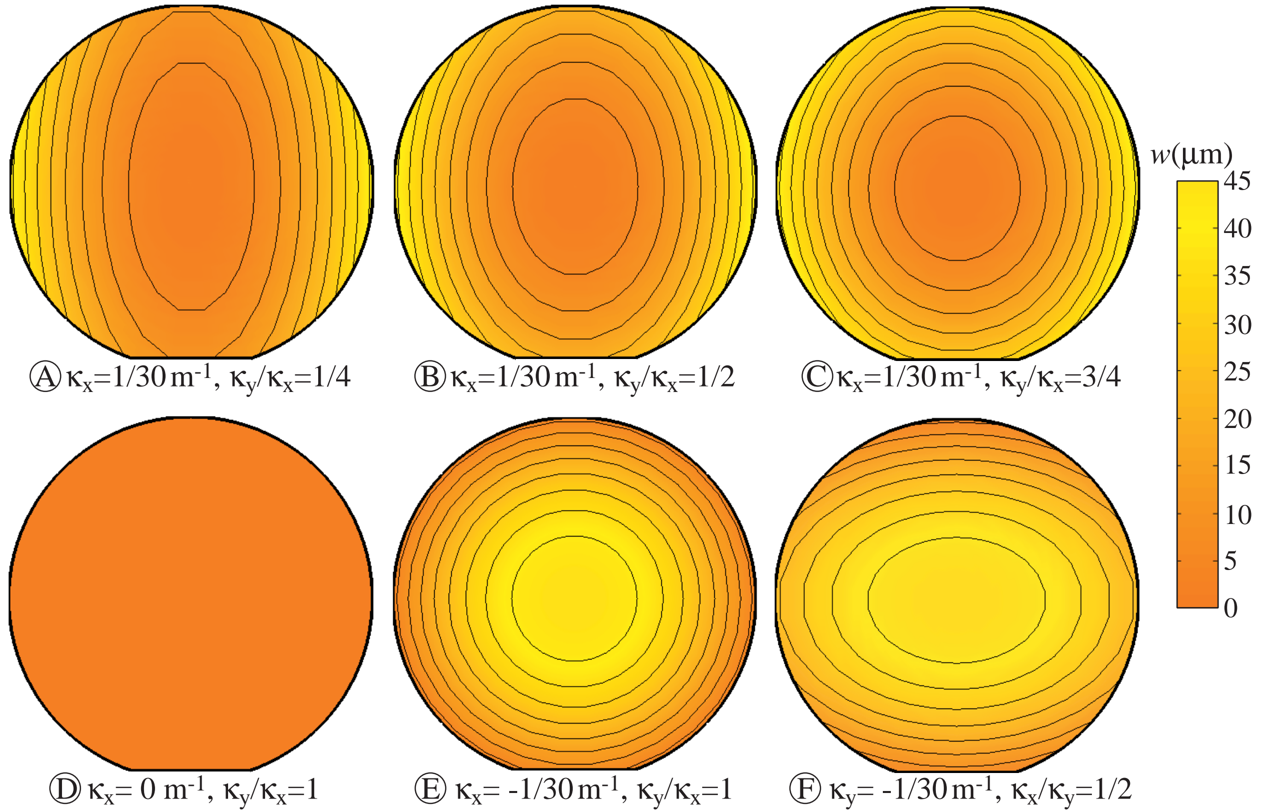

Figure 4-4: Model asymmetric wafer shapes considered in this work, the shapes are defined in terms of the curvature in the x and y directions, κ_x and κ_y. The shape at any point on the surface is defined as $w = \frac{1}{4}r^2[(\kappa_x + \kappa_y) + (\kappa_x - \kappa_y)\cos(2\theta)]$.

The mesh was constructed such that the bond front shape and position were fully described by the radial position of the front at each spoke (i.e 32 spokes means the bond shape is defined by 32 points). Fig. 4-3(a) shows a mesh with a circular bond front, as was often used as the initial guess, while Fig. 4-3(b) shows a mesh after iteration in which the bond front is in equilibrium. The arrangement of the elements in-plane is seen in Fig. 4-3. There are four elements across the width of each spoke and three across the regions between the spokes. The mesh is refined around the bond front in the radial direction. The refined region is 5 mm wide and has four elements perpendicular to the front. In each wafer there are two elements through the thickness. The model was meshed with 20-node continuum solid elements. The mesh geometry described was chosen through a series of convergence studies that ensured that the G values calculated were not a function of the mesh density.

The mesh was generated using a custom MATLAB™ script (included in Appendix C.1) and was exported to and solved with the commercial finite element package ABAQUS™ . The bonding process was modeled by calculating the distance between the two wafer surfaces from the shape

and thickness data and then applying an appropriate displacement to close the gap at the interface. The displacements were applied between corresponding nodes on the opposite wafer surfaces and were specified in a way such that the gap was closed while maintaining a constant reaction force on corresponding nodes on each wafer. This is required as only the total displacement that is needed to close the gap is known and the relative deflection of the two wafers is governed by equilibrium considerations. This is analogous to the method used to determine the final curvature in Chapter 3. In addition to the applied displacements required to bond the wafers, the displacement at the center of the wafers was fixed to represent the wafers being supported on a pin at the center during bonding. This is consistent with the mounting configuration described in Chapter 4. Solving the model yields the stresses and strains at all points in the wafers from which G can be determined.

4.3 Local Calculation of G

The strain energy accumulation rate may be calculated locally along the bond front from the stresses and strains that are obtained using the finite element model. As described in Chapter 2, the strain energy accumulation rate, G, is equivalent to the strain energy release rate, which is a common quantity in fracture mechanics. As such, the strain energy accumulation rate along a bond front may be calculated using approaches similar to those employed in computational fracture mechanics. There are several different approaches that have been developed for calculating G using finite element analysis, including the elemental crack advance method, contour integration (J-Integral), and the virtual crack closure technique (see [73, 74]).

The elemental crack advance method was the method that was used in Chapter 3 to calculate the strain energy accumulation rate in the axisymmetric model. In this method, G is calculated by solving the finite element model two times with two different crack (or bond) lengths. The strain energy accumulation rate is then calculated by dividing the difference in global energy between the two models by the difference in crack area between the two cases. While this technique is straightforward for the axisymmetric case, it is not well suited for the local calculation of G in the current 3-D finite element model. As to obtain the distribution of G along a single bond front using this method the finite element model would have to be solved numerous times with different small incremental bond advances at different locations along the bond front. Other techniques such as contour integration and the virtual crack closure technique provide a better approach for computing the strain energy release rate distribution along a bond front. They permit the strain energy release rate to be computed locally at each node along the front from a single finite element solution.

The virtual crack closure technique (VCCT) was employed in this work to calculate the strain energy accumulation rate. The basic principle of the VCCT is that the strain energy required to

advance the crack may be calculated from the work required to close the crack over a unit area ΔA. The work required to close the crack may be calculated from the reaction forces at the crack tip and the gap between the crack faces at the nodes immediately behind the crack tip. The specific forces and displacements that are included in the calculation depend on the element type. A list of equations for most standard elements can be found in [74]. The equations for the VCCT in [74] and elsewhere in the literature have all been developed for analyzing fracture rather than adhesion problems. As such, in the formulation of the VCCT, G is usually expressed only as a function of the reaction forces and the displacements at the nodes. In fracture analyses the crack faces typically have no separation prior to deformation and as such the sum of the displacements corresponds to the gap that must be closed. However, in the bonding analysis, there is a gap prior to bonding, δ_0 that is determined by the wafer shape. As such when employing the VCCT for adhesion analyses, the displacement term $(u_1 + u_2)$ in the traditional expressions must be replaced by $\delta_0 + (u_1 + u_2)$. The VCCT was chosen over other methods to calculate G locally as it does not require significant mesh refinement around the crack tip and was straightforward to implement for adhesion problems.

The VCCT allows the strain energy accumulation rate to be calculated at each node along the bond front. Thus for the standard mesh geometry used here, where there are 32 spokes each with 9 nodes along the bond front, G is calculated at a total of 288 points along the front. As will be described below, the iteration scheme, that was employed treats each point that G is calculated at as a moveable node. If all 288 nodes were moveable, the iteration process would be computationally expensive and convergence would be difficult. As such an approach was employed in which the G values across each spoke were averaged to a single value for that spoke. The bond front across each spoke was assumed to be straight and as such the size and shape of the front was described by the radial positions at the 32 spokes. This is a simplification, but an acceptable one as the spokes are relatively narrow and 32 points along the bond front allows the overall shape of the bond front to be captured well. The average G value across each spoke is calculated by taking the area weighted average of the G values at the nodes,

$$G_{spoke-avg} = \frac{\sum_{i=1}^{n} G_i \Delta A_i}{\sum_{i=1}^{n} \Delta A_i} \tag{4.1}$$

where i is the node number, n is the total number of nodes across the front on one spoke (9 in this case), and ΔA is the area that was used in each VCCT calculation to determine G.

4.4 Iteration Scheme

The final part of the model is an iteration scheme to allow the shape and size of the bond area to be iterated such that the bond front for which the equilibrium condition, $G = W$, is satisfied along

the entire front, may be determined. As described in the previous section, the bond front is defined by the radial coordinates of the front at each spoke. The strain energy accumulation rate at each spoke, G_i, may be viewed as a non-linear function of the radial coordinates, r_i, of the bond front at all the spokes,

$$G_i = f(r_1, ...r_n) \tag{4.2}$$

where i is the spoke number and n is the total number of spokes. The front is in equilibrium when the strain energy accumulation rate at each spoke is equal to the work of adhesion. This criterion may be written as a non-linear set of equations,

$$\mathbf{F} \equiv \begin{bmatrix} G_1(r_1, ..., r_n)/W - 1 \\ \vdots \\ G_n(r_1, ..., r_n)/W - 1 \end{bmatrix} = \begin{bmatrix} 0 \\ \vdots \\ 0 \end{bmatrix}. \tag{4.3}$$

The vector, $\mathbf{R}$, ($\mathbf{R} = [r_1...r_n]^T$), fully specifies the bond front position. The strain energy accumulation rates at all the spokes may be calculated for a given $\mathbf{R}$ from one finite element solution.

The vector $\mathbf{R}$ that satisfies Eq. (4.3) specifies the bond shape and size at equilibrium and may be solved for iteratively. The approach used here to accomplish this was adapted from [75] and uses a quasi-Newton method to update the bond shape after each iteration. After each iteration, a new bond front position is calculated,

$$\mathbf{R}^{k+1} = \mathbf{R}^k - (\mathbf{B}^k)^{-1}\mathbf{F}^k, \tag{4.4}$$

where k indicates the iteration number. An approximate Jacobian, $\mathbf{B}$, was used and is updated after each iteration using the rank one Broyden update formula,

$$\mathbf{B}^{k+1} = \mathbf{B}^k + \frac{(\mathbf{dF}^k - \mathbf{B}^k\mathbf{dR}^k)(\mathbf{dR}^T)^k}{(\mathbf{dR}^T)^k(\mathbf{dR})^k} \tag{4.5}$$

where,

$$\begin{aligned} \mathbf{dR}^k &= \mathbf{R}^{k+1} - \mathbf{R}^k \\ \mathbf{dF}^k &= \mathbf{F}^{k+1} - \mathbf{F}^k \end{aligned} . \tag{4.6}$$

The iteration scheme calculates the new bond front position based on the previous position of the front, the difference between G and the specified work of adhesion, and the approximate Jacobian. Given that G may vary significantly along the bond front and the exact Jacobian is not being used, it is likely that Eq. (4.4) may predict a new bond front that would not be physically possible (i.e outside the boundary of the wafer) or cause significant mesh distortion. To prevent this, the radial shifts, ($\Delta\mathbf{R} = \mathbf{R}^{k+1} - \mathbf{R}^k$), that are predicted in each iteration are checked to

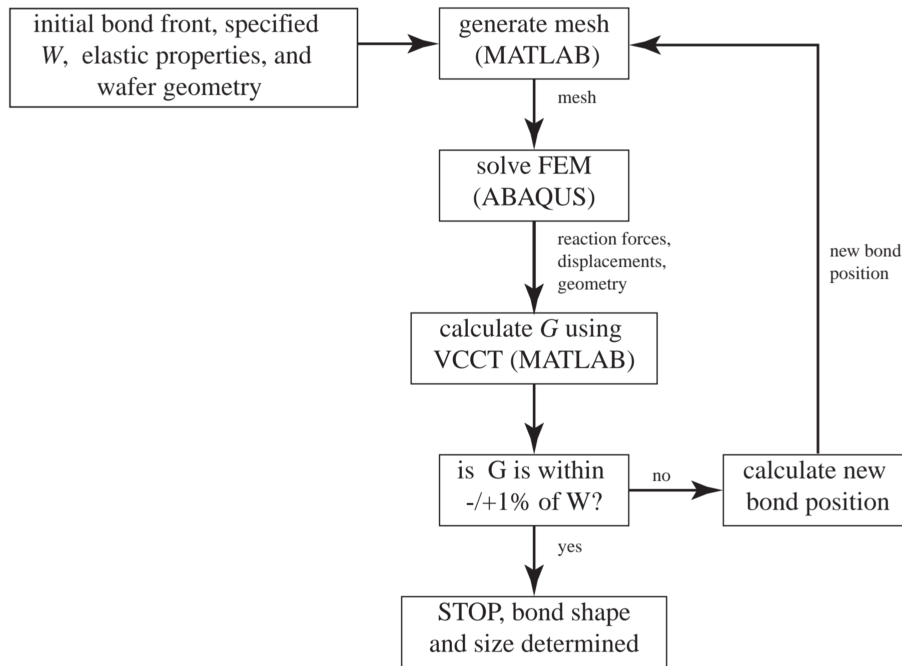

Figure 4-5: Overview of numerical model.

ensure that they do not exceed a specified value, ΔR_{lim}. Values for ΔR_{lim} from 3-5 mm were found to work well. If any of the shifts along the front did exceed the specified ΔR_{lim}, the shifts along the entire front were scaled by a factor, $\left(\frac{\Delta R_{lim}}{\max(\Delta \mathbf{R})}\right)$, such that the maximum shift at any node along the front was ΔR_{lim}. The bond front position was iterated until G was within 1% of the specified work of adhesion value along the entire front. Convergence was typically achieved in 20 to 50 iterations.

The integration of the iterative process with the other elements of the model is shown in Fig. 4-5. The mesh is initially generated in MATLAB™ and then exported to ABAQUS™ where it is solved. The reaction forces and displacements from the finite element solution are transferred to MATLAB™, where G is calculated and the convergence criterion is evaluated. If the convergence criterion is satisfied, the model is terminated and the current bond position is taken as the equilibrium position. If it is not satisfied, a new bond front is calculated using the method described above. A new mesh is generated based on this bond front and the process is repeated until convergence is achieved. The bonding behavior of a pair may be mapped out by running the model multiple times for different work of adhesion values.

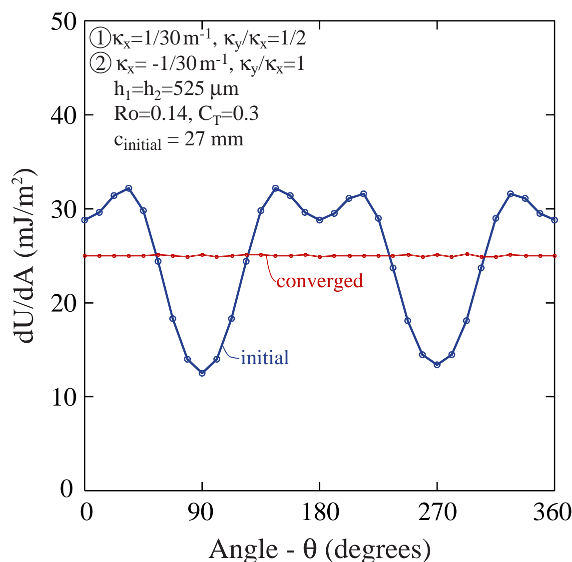

Figure 4-6: Distribution of G along initial circular bond front in an asymmetric wafer pair and the distribution of G along the converged bond front.

4.5 Results and Discussion

As an initial example to demonstrate the model, the bonding of wafers B and E that are shown in Fig. 4-4 is considered. The shapes of the wafers and a circular bond front with a 27 mm radius, as shown in Fig. 4-3(a), were used to construct the initial mesh. One finite element solution allows the distribution of the strain energy accumulation rate along the circular bond front to be calculated. The distribution of G along the front is shown in Fig. 4-6. The target work of adhesion value for this case was 25 mJ/m^2 and from Fig. 4-6 it is clear the circular front is not in equilibrium. Following 32 iterations, a bond front was determined such that $24.75 < G < 25.25$ along the entire front. The mesh after convergence is shown in Fig. 4-3(b) and the distribution of G along the front in Fig. 4-6. The shape of the front is seen to reflect the initial shapes of the wafers.

4.5.1 Elastic Anisotropy

A systematic study was performed to evaluate the effect of elastic anisotropy when bonding (100) silicon wafers. The bonding of three pairs with axisymmetric shape, but different thicknesses and curvatures were considered. Details regarding the three pairs along with work of adhesion values at which the bond fronts were calculated at are listed in Table 4.1. The work of adhesion values for each pair were selected such that the series are all the same when normalized by $h_1^{-3}(\kappa_2 - \kappa_1)^{-2}$. Given this normalization, if the plate theory scaling holds, the family of predicted bond fronts for each pair should match one another. The predicted bond fronts for the three anisotropic pairs are plotted in Fig. 4-7 along with fronts predicted using the analytical solution in Chapter 3 for a pair

Table 4.1: Geometry and work of adhesion values of predictions in Fig. 4-7.

Pair	h_1=h_2 (μm)	κ_1 (m^{-}1)	κ_2 (m^{-}1)	W (mJ/m^2)
1	525	1/30	-1/30	20, 25, 30, 35, 40 ,45, 50
2	525	1/30	0	6.25, 7.5, 8.75, 10, 11.25, 12.5
3	1050	1/30	0	40, 50, 60, 70, 80, 90, 100

with geometry and work of adhesion values identical to pair 1 in Table 4.1.

From Fig. 4-7 it is seen that the general scaling with thickness and curvature given by the plate theory solution hold, as all the predictions for the anisotropic pairs are the same. Furthermore, it is evident that the anisotropic finite element and plate theory solutions agree reasonably well and only the shape of the bond front varies slightly between the anisotropic and isotropic cases. The difference between the isotropic and anisotropic cases is not actually as large as might be expected given the significant variation in Young's modulus and Poisson's ratio that is shown in Fig. 4-2. At short bond lengths the effect of elastic anisotropy is not noticeable at all in the predicted bond fronts. At larger bond radii, the elastic anisotropy affects the shape slightly and the cubic symmetry of the material can clearly be seen in the predicted bond shapes.

A better appreciation of why the bond shapes appear as they do in the anisotropic pair may be gained by returning to the isotropic plate theory G given in Eq. (3.23). The elastic properties of the wafers in the equation for G can be grouped into one term,

$$E\frac{(1+\nu)}{(1-\nu)}\frac{1}{\left[(1+\nu)+R^2(1-\nu)\right]^2}, \tag{4.7}$$

which is function of the relative bond position, R. This term is plotted in Fig. 4-8 as function of direction in the (100) plane from the modulus and Poisson's ratio data in Fig. 4-2. The term is plotted for various bond positions, including R=0.34 and R=0.82, which approximately correspond to the shortest and longest bond radii plotted in Fig. 4-7. From Fig. 4-8 it is seen that the relevant elastic term in the bonding problem does not vary significantly in (100) plane even though the Young's modulus and Poisson's ratio do. At the shortest bond length in Fig. 4-7, R=0.34, it seen that the elastic term [Eq. (4.7)] in the plate theory solution is virtually axisymmetric and thus consistent with the axisymmetric bond fronts predicted at short bond radii from the anisotropic model. At the longest bond radii, R=0.82, Fig. 4-8 shows that the elastic term in the plate theory solution is largest in the [100] directions and smallest in the [110] directions. The bond front position is inversely proportional to the elastic term (i.e it is more difficult for the bond to propagate in the stiffer direction), thus it would be expected that the bond radii would be greatest in the [110] directions and smallest in [100] directions. The bond fronts predicted from the anisotropic model agree with this and thus are consistent with the plate theory solution.

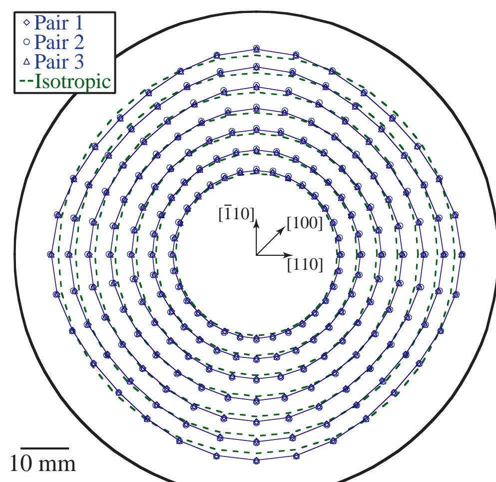

Figure 4-7: Predicted bond fronts for bonding axisymmetric anisotropic (100) silicon wafers as a function of work of adhesion. Details of the geometry are given in Table 4.1

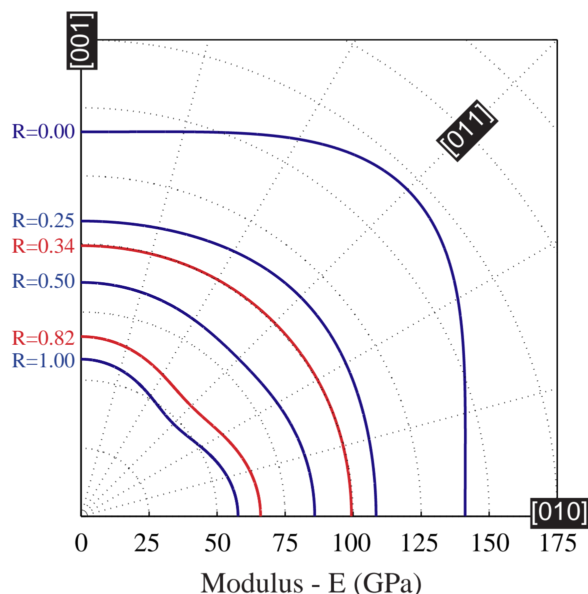

Figure 4-8: Effective bonding modulus in the (100) plane of silicon wafer as a function of direction.

4.5.2 Asymmetric Wafer Shape

To assess the ability of the model to predict asymmetric bond fronts resulting from asymmetries in the shapes of the wafers, the bonding of various combinations of wafers in Fig. 4-4 were considered. The predicted bond fronts for six different combinations of wafers in Fig. 4-4 are shown in Fig. 4-9. Each pair is labeled by a two letter combination which indicates the wafers (Fig. 4-4) in the bonded pair.

The first data set of interest is the three pairs shown in the top row of Fig. 4-9. These pairs correspond to wafers with different levels of asymmetry (A,B,C - Fig. 4-4) being bonded to a wafer with an axisymmetric negative curvature (E - Fig. 4-4). The pair on the left has the strongest asymmetry in wafer shape while the one on the right has the weakest. The predicted bond fronts show this change in wafer asymmetry and clearly reflect the shapes of the initial wafers. The wafers in all three pairs along the top row of Fig. 4-9 have the same curvature in the x-dir, but different curvatures in y-dir. By examining the size of the bonded area for a fixed work of adhesion of 20 mJ/m^2 in all three pairs, it is seen that the bond front is smallest for pair C-E, the wafer with the least asymmetry. Since all three pairs have the same maximum curvature, this result suggests that the bond prediction for the axisymmetric case would be a conservative estimate when assessing the bonding of wafers with asymmetries. As such, the plate theory solution presented in Chapter 3 may be used to establish an upper bound on bonding.

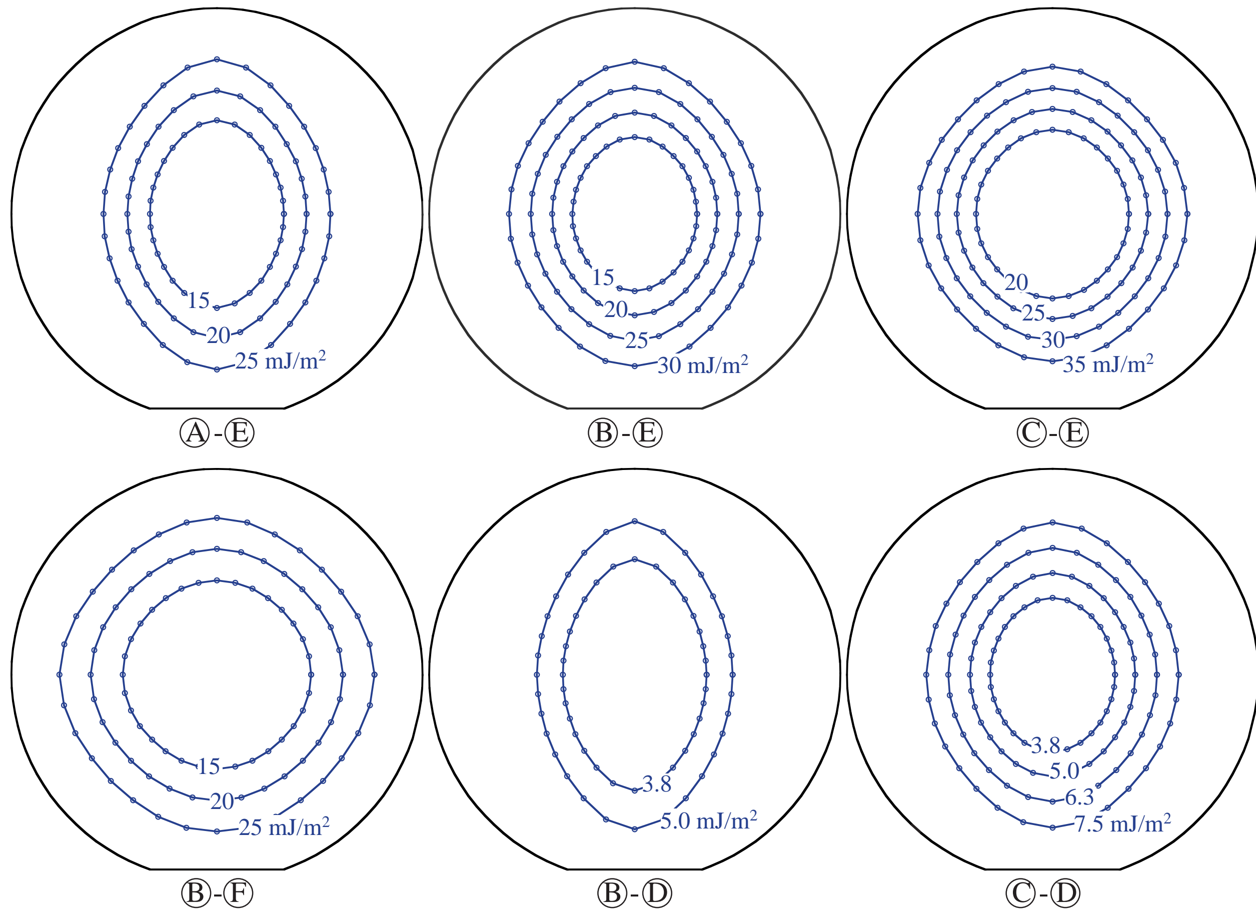

Figure 4-9: Predicted bond fronts for different combinations of the wafers shown in Fig. 4-4 for different values of work of adhesion. The labels on each plot correspond to the wafer labels given in Fig. 4-4

The second set of data of interest in Fig. 4-9 is the four plots in the second and third columns. In the second column, the asymmetric top wafer in pair B-E and B-D are both the same ($\kappa_x = 1/30\text{m}^{-1}$, $\kappa_y/\kappa_x = 1/2$), while the bottom wafers are different, B-E has a wafer with an axisymmetric curvature of $\kappa = -1/30$, while the bottom wafer in B-D is flat. The pairs in the third column, C-E and C-D, are similar, except for the fact that the top wafers in the pair have slightly less asymmetry ($\kappa_x = 1/30\text{m}^{-1}$, $\kappa_y/\kappa_x = 3/4$). By examining these two columns of data it is seen that the shapes of both wafers in the pair effect the final bond shape. The bond fronts in pair B-E have less asymmetry than B-D as a result of the bottom wafer in pair B-E having a larger axisymmetric shape variation. A similar result is seen when comparing pairs C-E and C-D.

The final plot in Fig. 4-9 that demonstrates an interesting result is pair B-F. Pair B-F shows predicted bond fronts for bonding two asymmetric wafers with their principle curvatures oriented 90° to one another. The shape of wafer B is given as,

$$w_o|_B = \frac{1}{240}[3 + \cos(2\theta)]r^2, \tag{4.8}$$

and wafer F is given as,

$$w_o|_F = -\frac{1}{240}[3 - \cos(2\theta)]r^2. \tag{4.9}$$

The predicted bond fronts shown for pair B-F in Fig. 4-9 appear similar to shapes predicted for the anisotropic axisymmetric case in Fig. 4-7. This occurs because even though the wafers are asymmetric, the gap at the interface, $w_o|_B - w_o|_F$, is axisymmetric,

$$w_o|_B - w_o|_F = 1/40r^2. \tag{4.10}$$

As a result, the bond front is axisymmetric. While this is true for this case, it is important to note that this would not be true if the wafers had different thickness and moduli, as the asymmetry of the stiffer wafer would be apparent in the bond front.

4.6 Summary and Limitations

The model that has been described in this chapter allows for the prediction of the size and shape of the bonded area for wafers with arbitrary geometries, etch patterns, and elastic anisotropy. The model has been demonstrated for several test cases and the results agree qualitatively with what would be expected based on the initial shape of the wafers and the elastic anisotropy. This model is employed in Chapter 6 as well and its ability to predict bond fronts for asymmetric wafers is verified through comparison to experiments. This model provides a powerful tool for assessing the bondability of wafers with real geometries and etch patterns and complements the analytical

solution in Chapter 3.

While the model described can accurately predict the shape and size of bonded areas, it should be recognized that some simplifications have been made in order to make the model feasible. The most significant simplification is the way in which the bonding of the wafers has been handled. In the analytical solution in the previous chapter and the finite element model reported here, bonding has been accomplished by closing the gap at the interface through the application of displacements in the z-direction. Thus, only tractions normal to the interface are applied during the bonding process. In reality, when the wafers bond, the interface carries tractions normal and parallel to the bonding surfaces. The tractions parallel to the interface are neglected here and taken as zero. This assumption is reasonable when the two wafers have thicknesses and moduli that are similar, as the in-plane displacements will be close to one another and there will be no significant shear stresses transferred at the interface. However, when one layer is much stiffer than the other, some caution should be used as the shear stresses transferred at the interface may be significant. These effects are neglected here and are typically ignored in adhesion analyses, because they significantly complicate the formulation of the problem and are viewed as second order effects. If effects such as these, as well as more complicated etch patterns are included in the model, a more advanced numerical scheme that propagates the bond front from an initial point, rather than simply iterates the shape to find the equilibrium front, will be required. A natural extension of the finite element model reported here would account for these shear stresses at the interface and include a propagation scheme.

Chapter 5

Clamping

In the previous chapters, the effect of flatness variations and etch patterns on bonding has been examined. An equally important effect in direct bonding is that of the bonding tool and how the wafers are mounted and loaded during the bonding process. While this is an important factor that must be understood for proper tool design, there has been very little work reported on this. One of the few reports on clamping is that by Feijoo et al. [76], which proposed the idea of introducing curvature by deforming the wafers during bonding to increase the strain and hence the mobility of the device layer in SOI substrates. A curvature was introduced in the bonded pair by applying a load at the center during bonding and a model for the stress relaxation that occurs as one layer is thinned was presented. With the exception of that work, the interactions between the bonding tool and the bonded pair have been largely ignored.

The current work seeks to address this by providing a model that permits the effect of basic clamping configurations to be understood. Specifically, a model is developed that provides a relationship between the initial geometry and elastic properties of the wafers, and the final shape of the bonded pair and the strain energy release rate at the interface. Understanding the final shape of a bonded wafer pair is critical when the pair will undergo subsequent bonding steps or processing and handling. Furthermore, it is necessary to assess the effect that clamping may have on bonding failure, this is done by comparing the strain energy release rate to the bond toughness.

The two basic bonding configurations considered in this work are shown in Fig. 5-1. The first, which will be referred to as the free configuration, Fig. 5-1(a), is the traditional arrangement that is employed in direct and anodic bonding, in which surface forces (direct) or electrostatic forces (anodic) pull the wafers into contact. In this configuration, the wafers are initially contacted at a point, from which the bond spreads. No external loads are applied with the exception of the initial point contact. The other case considered, the clamped configuration, is shown in Fig. 5-1(b). This type of setup, which is common to many interlayer techniques, but may be used in direct and anodic

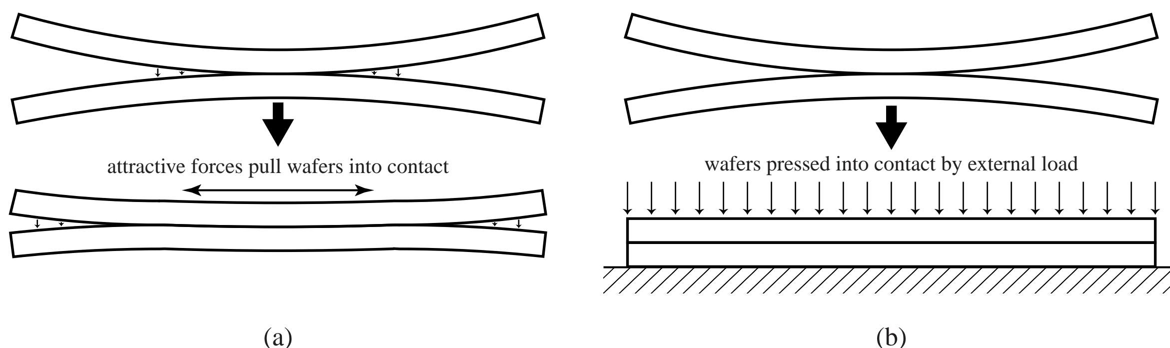

Figure 5-1: Schematic of two types of clamping configurations considered. (a) Free configuration: wafers are contacted at a point from which surface or electrostatic forces pull the wafers into contact. (b) Clamped configuration: wafers are pressed into contact by the application of an external load.

bonding processes as well, presses the wafers into contact through the application of an external load. In the case considered here, the wafer pair is assumed to be supported by a chuck that defines the curvature during bonding. These two arrangements represent two bounding cases and serve as good models for understanding the basic effects of clamping in wafer bonding processes.

The structure of this chapter is as follows. First, the models for the two cases are developed. The derivation is explained and expressions are developed for the final curvature of the bonded pair and the strain energy release rate at the interface. Next, the model is employed to understand how clamping may be used to improve the final shape of the bonded pair. Results from the free case and clamped case are compared and process implications highlighted. Then, the strain energy release rate results for the two cases are examined and compared. Finally, practical considerations are discussed and the results summarized.

5.1 Free Configuration

The model system that is used to examine the free case, is illustrated schematically in Fig. 5-2. Two wafers, with geometry defined in terms of their curvatures, κ_1, κ_2, their thicknesses, h_1, h_2, and radius, b, are bonded by initially making contact at the center, from which the bond front propagates. A curvature that is concave up is defined as positive, as shown Fig. 5-2, a negative curvature indicates the wafer is concave down. The analysis for the free configuration is restricted to cases where $\kappa_1 \geq \kappa_2$, as this is required in order to guarantee initial contact at the center of the wafers. The wafers are taken to be elastic and isotropic, with Young's moduli, E_1, E_2, and Poisson's ratios, ν_1, ν_2. The bond radii is defined as c and the crack length, which is measured from the edge of the wafer, is defined as a.

As the wafers bond, each wafer is deformed from its initial curvature to a common final curva-

ture, κ_f, in the bonded region. The deflection of each wafer from their initial curvature, κ_i in the bonded section ($0 \leq r \leq c$), section A, is,

$$\bar{w}_A = \frac{1}{2}(\kappa_f - \kappa_i)r^2. \tag{5.1}$$

In the unbonded section ($c \leq r \leq b$), section B, there is no shear force, thus the governing equation for the plate is,

$$\frac{d}{dr}\left[\frac{1}{r}\frac{d}{dr}\left(r\frac{dw}{dr}\right)\right] = 0. \tag{5.2}$$

Integrating the above equation and solving subject to the three boundary conditions,

$$\begin{array}{rcl} w_A|_{r=c} & = & w_B|_{r=c} \\ \left.\frac{dw_A}{dr}\right|_{r=c} & = & \left.\frac{dw_B}{dr}\right|_{r=c} \\ M_A|_{r=b} & = & 0 \end{array}, \tag{5.3}$$

the deflection in section B can be determined. Using the deflections, the radial moment in each section may be determined,

$$M = -\frac{Eh^3}{12(1-\nu^2)}\left(\frac{d^2w}{dr^2} + \frac{\nu}{r}\frac{dw}{dr}\right). \tag{5.4}$$

At $r = c$, equilibrium must be satisfied, thus the moment acting on each layer after bonding, M_i, is,

$$M_i = -M_B + M_A. \tag{5.5}$$

The moment acting on each layer after bonding, which represents the residual stress in each layer after bonding is,

$$M_i = \frac{1}{6}\bar{E}_i h_i^3(\kappa_i - \kappa_f)N_i(R) \tag{5.6}$$

where the subscript i denotes the wafer, either 1 or 2, and $\bar{E}_i$ is the plane strain modulus, $\bar{E}_i = \frac{E_i}{(1-\nu_i^2)}$. The quantity, $N_i(R)$, is a non-dimensional parameter that depends on the relative radius of the bonded area, $R = c/b$, and the Poisson's ratio,

$$N_i(R) = \frac{(1+\nu_i)}{(1+\nu_i) + (1-\nu_i)(R)^2} \tag{5.7}$$

Counterclockwise bending moments on rightward facing sections, as shown in Fig. 5-2, are defined as positive. It is important to note that while the preceding derivation and the following analyses are concerned with the radial component of the moment there is a tangential component in the bonded section that is equal in magnitude to the radial component.

In the free case, no external loads are applied, thus at any radial position, equilibrium must be satisfied through a balance of moments on the two wafers,

$$M_1 + M_2 = 0. \tag{5.8}$$

Using Eq. (5.6) with the equilibrium condition given by Eq. (5.8), the final curvature of the bonded pair can be determined,

$$\kappa_f = \frac{\Sigma\eta^3\lambda\kappa_1 + \kappa_2}{\Sigma\eta^3\lambda + 1}. \tag{5.9}$$

Three non-dimensional parameters have been defined to simplify the result, $\Sigma = \bar{E}_1/\bar{E}_2$, $\eta = h_1/h_2$, and $\lambda = N_1(R)/N_2(R)$. The final curvature, in general, depends on the bonded radius because of the dependence on λ. However, when $\nu_1 = \nu_2$, $\lambda = 1$ and the final curvature is independent of the bond radius.

The residual stress that is present after bonding is stored elastic strain energy that may drive fracture processes, such as delamination, in the bonded pair. The strain energy release rate, G, at the interface may be expressed in terms of the moments and radial loads at the crack tip using the framework reported by Suo and Hutchinson [77]. In the case under consideration here, where the only loads acting on the layers are the two moments M_1 and M_2, [78],

$$G = \frac{6}{\bar{E}_1 h_1^3}(M_1^2 + \Sigma\eta^3 M_2^2) \tag{5.10}$$

Substitution into Eq. (5.10) of the moments, given by Eq. (5.6) with the final curvature defined by Eq. (5.9), yields the strain energy release rate,

$$G = \frac{1}{6}\bar{E}_1 h_1^3 \frac{(1+\Sigma\eta^3)}{(1+\Sigma\eta^3\lambda)^2}(\kappa_2 - \kappa_1)^2 N_1(R)^2. \tag{5.11}$$

When the wafers have the same Poisson's ratio ($\nu_1 = \nu_2 = \nu$), the expression for strain energy release rate reduce to,

$$G = \frac{1}{6}\frac{E_1 h_1^3}{1+\Sigma\eta^3}(\kappa_2 - \kappa_1)^2 \frac{(1+\nu)}{(1-\nu)} \frac{1}{[(1+\nu)+(1-\nu)R^2]^2}. \tag{5.12}$$

It should be noted that the expressions for final curvature and energy release rate of the free configuration derived in this analysis agree with those obtained in Chapter 3. In Chapter 3, bond propagation was examined, thus the strain energy accumulation rate was calculated. As noted in Chapter 2 this quantity is equivalent to the strain energy release rate, which is the quantity derived in this chapter. In Chapter 3, the strain energy was calculated using plate theory and the final curvature and strain energy accumulation rate were determined through energy minimization

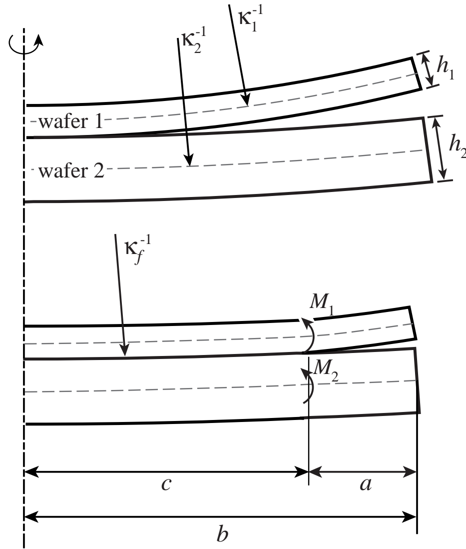

Figure 5-2: Geometry and loading in the free case. Wafers with two different curvatures, which may be positive (concave up, as shown) or negative (concave down) are bonded and deform to a common curvature κ_f. The residual stress that results from the wafers being deformed from their initial curvatures to the final curvature may be treated as effective moments acting on each wafer.

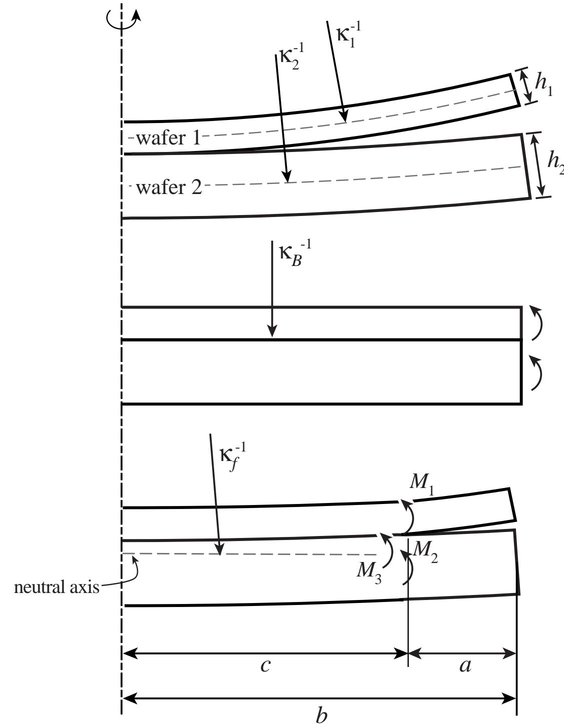

Figure 5-3: Geometry and loading in the clamped case. Two wafers are deformed to a common curvature, κ_B, by external moments and then bonded. The external loads are then removed and the bonded stack relaxes to curvature κ_f.

and energy accounting, respectively. In the present analysis, effective moments on each layer are determined and the Suo and Hutchinson analysis for fracture in layered materials is employed. This alternative approach was used here as it provides a more direct means of examining the clamped configuration. For the free case, there is no particular benefit to one analysis method over the other.

5.2 Clamped Configuration

The second bonding scenario considered, the clamped case, is illustrated in Fig. 5-3. The two wafers are deformed to a common bonding curvature, κ_B, by the application of external loads. While held at κ_B, the wafers are bonded. Following bonding, the clamping loads are removed and the wafer pair relaxes to its final curvature, κ_f. The analysis of this case is restricted to instances

where, $\nu_1 = \nu_2 = \nu$, as it does not affect the results significantly, but does allow for considerable simplification in the derivation. Under this constraint the moduli ratio reduces to, $\Sigma = E_1/E_2$.

The final curvature of the bonded pair once the loads are removed can be determined by considering the moments in the wafers. While the wafers are held at κ_B there is a moment in each wafer,

$$M_i = \frac{1}{6}\bar{E}_i h_i^3(\kappa_i - \kappa_B)N(R). \tag{5.13}$$

These internal moments in wafers 1 and 2 are initially balanced by the external loads. Once the wafers are bonded and the external loads are removed, the moments must be balanced by a moment in the bonded pair, M_3. Equilibrium requires,

$$M_1 + M_2 + M_3 = 0. \tag{5.14}$$

The moment acting on the bonded stack, M_3, causes the bonded pair to deform from κ_B to κ_f. The bonded section can be treated as a composite plate, the moment-curvature relation for the bonded section is,

$$M_3 = \frac{1}{6}\bar{E}_1 h_1^3(\kappa_B - \kappa_f)\frac{(\Sigma^2\eta^4 + 4\Sigma\eta^3 + 6\Sigma\eta^2 + 4\Sigma\eta + 1)}{(1+\Sigma\eta)\Sigma\eta^3}N(R). \tag{5.15}$$

The final curvature of the stack is determined by calculating M_3 from Eq. (5.14) by substituting for M_1 and M_2, which are given by Eq. (5.13),

$$M_3 = -\frac{1}{6}\bar{E}_1 h_1^3 \frac{1}{\Sigma\eta^3}[\Sigma\eta^3\kappa_1 + \kappa_2 - (\Sigma\eta^3 + 1)\kappa_B]N(R). \tag{5.16}$$

then solving for the final curvature using Eqs. (5.15) and (5.16),

$$\kappa_f = \frac{(\Sigma\eta + 1)(\Sigma\eta^3\kappa_1 + \kappa_2) + 3\Sigma\eta(\eta+1)^2\kappa_B}{\Sigma^2\eta^4 + 4\Sigma\eta^3 + 6\Sigma\eta^2 + 4\Sigma\eta + 1}. \tag{5.17}$$

As for the free case, the strain energy release rate at the interface can be determined using the Suo and Hutchinson analysis for cracks in layered materials [77]. In the current case, there are three moments applied at the crack tip, one on each layer and one that acts on the bonded section as shown in Fig. 5-3. The strain energy release rate for this case can be expressed as, [78],

$$G = \frac{6}{\bar{E}_1 h_1^3}(M_1^2 + \Sigma\eta^3 M_2^2 - \frac{\Sigma}{12I}M_3^2), \tag{5.18}$$

where I is the non-dimensional moment of inertia given by,

$$I = \frac{1}{12}\frac{\Sigma^2\eta^4 + 4\Sigma\eta^3 + 6\Sigma\eta^2 + 4\Sigma\eta + 1}{\eta^3(\Sigma\eta + 1)}. \tag{5.19}$$

Substitution for M_1 and M_2, given by Eq. (5.13), and M_3, given by Eq. (5.16) into Eq. (5.18) yields the strain energy release rate at the interface for the clamped case,

$$G = \frac{1}{6}\bar{E}_1 h_1^3 \frac{1}{\Sigma\eta^3}\left[\Sigma\eta^3(\kappa_1 - \kappa_B)^2 + (\kappa_2 - \kappa_B)^2 - \frac{(\Sigma\eta + 1)(\Sigma\eta^3\kappa_1 + \kappa_2 - (\Sigma\eta^3 + 1)\kappa_B)^2}{\Sigma^2\eta^4 + 4\Sigma\eta^3 + 6\Sigma\eta^2 + 4\Sigma\eta + 1}\right] N(R)^2. \tag{5.20}$$

This expression for strain energy release rate is valid assuming that after crack growth no contact occurs between the crack faces. Contact between the crack faces may occur when $\kappa_1 < \kappa_2$.

5.3 Results and Discussion

When examining the effect of wafer geometry and mounting on bonded wafer pairs there are two primary concerns: 1) the final shape of the bonded pair and 2) whether or not the bond will fail through delamination at the interface. The former is particularly important in devices that require the bonding of multiple wafers, since a large curvature in a bonded pair may lead to failure in subsequent bonding processes. Delamination is obviously always a concern in bonded structures and may be avoided by ensuring the interfacial strain energy release rate is less than the bond toughness. In this section, the results from the analysis above are used to examine both of these issues to provide practical guidance in process and equipment design.

5.3.1 Final Shape

The final shape of the bonded stack is described by the final curvature, κ_f, which is given by Eq. (5.9) for the free case and Eq. (5.17) for the clamped case. When the wafers have equal Poisson's ratios, the final curvature of the free case is a function of the initial curvatures of the wafers, and the thickness and modulus ratio of the two wafers. For the clamped case, the final shape depends on one additional parameter, the bonding curvature. While the bonding curvature can be changed through different clamping configurations, typically a nominally flat chuck, corresponding to $\kappa_B = 0$, is used.

The relative importance of the thickness and modulus ratio on the final curvature can be seen in Fig. 5-4. Figure 5-4 plots the final curvature for bonding an initially bowed wafer with curvature, κ_1 to a nominally flat wafer, $\kappa_2 = 0$, for the free and clamped case. From Fig. 5-4 it is clear that the relative thickness of the wafers is more important than the moduli ratio in determining the final curvature of the bonded pair. In the free case, when one layer is more than three times

the thickness of the other, the final curvature is essentially determined by the initial curvature of the thick wafer. This strong dependence on thickness is due to the fact that the deformation of the wafers is dominated by bending and thus has a cubic dependence on the thickness. When the wafers are clamped, then bonded, the thickness ratio also plays an important role in determining the final shape, but the effect is less pronounced because of the influence of the clamping curvature.

Perhaps more importantly, Fig. 5-4 demonstrates that clamping can make a significant difference in the final shape of the bonded pair. When the wafers have equal thickness and moduli ($\eta = 1$, $\Sigma = 1$) and the wafers are bonded in the free configuration, $\kappa_f = \frac{1}{2}\kappa_1$. However, when the wafers are clamped flat and then bonded, $\kappa_f = \frac{1}{8}\kappa_1$. This is a significant reduction in the curvature of the bonded pair solely due to the arrangement in which the wafers are mounted and this result demonstrates the potential for the use of clamping to control the shape of bonded pairs.

The results in Fig. 5-4 are for the specific case of $\kappa_B = 0$, which reduces the final curvature, but in general does not result in a flat bonded pair. From Eq. (5.17), it is clear that if the initial geometry and elastic properties of the wafers are known, it is possible to select a bonding curvature that will yield a flat bonded pair. This concept is explored in Fig. 5-5, which plots the bonding curvature that is required to obtain a flat pair, $\kappa_f = 0$, for various thickness and initial curvature ratios. The curvature ratio is defined as $\chi = \kappa_1/\kappa_2$, with $|\kappa_1| \leq |\kappa_2|$ (the flatter of the two wafers is wafer 1). With this definition, the range of $\chi = -1.0$ to $\chi = 1.0$, which corresponds to wafers that have equal but opposite curvature to wafers that have the same curvature, covers the full range of possibilities. As seen in Fig. 5-5, the bonding curvatures required to achieve a flat bonded pair are on the order of the initial curvatures of the wafers, thus in most cases it should be reasonable to achieve these through clamping. It is important to note though that as one wafer becomes much thinner than the other, the required bonding curvatures increase significantly suggesting that it may be difficult to employ this method of curvature reduction in cases where one layer is very thin.

From the previous discussion, it is evident that clamping can be advantageous by reducing curvature in bonded pairs. There are situations however, in which poor clamping configurations may add curvature to a bonded pair. Figure 5-6 shows the final curvature when two initially flat wafers are bonded while deformed to curvature κ_B. When the wafers have equal thickness and modulus, the final curvature is $\kappa_f = \frac{3}{4}\kappa_B$. It is clear that a significant portion of the bonding curvature is retained after bonding. The bonded pair relaxes more as one of the wafers becomes thinner than the other. While this case may seem obscure, it is actually an important scenario and demonstrates the importance of using a flat chuck when bonding initially flat wafers in a clamped configuration. This type of effect has been observed in practice, as reported in [79]. Wafers, which were nominally flat, were bonded in a clamped configuration using two different chucks. In one case a steel chuck was used and in the other a teflon chuck. Wafer pairs bonded using the teflon chuck had significant curvature while those bonded on the steel chuck were nominally flat. The

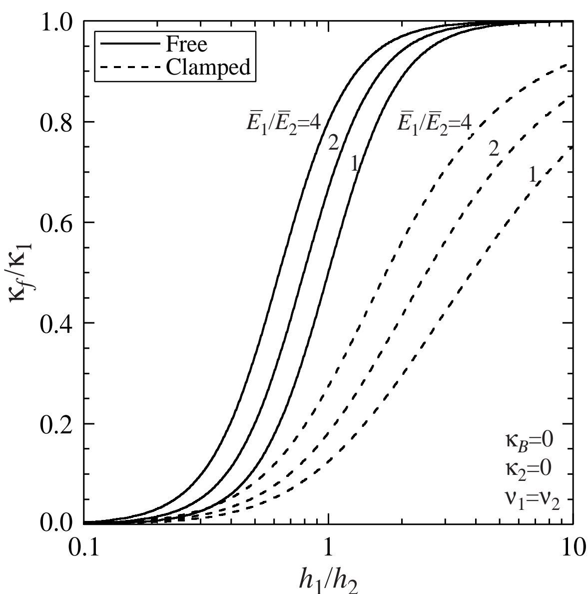

Figure 5-4: Final curvature of a bonded wafer pair for the two different mounting configurations. Plotted for various thickness and modulus ratios for the case where $\kappa_2 = 0$. For the clamped case, the bonding curvature is $\kappa_B = 0$.

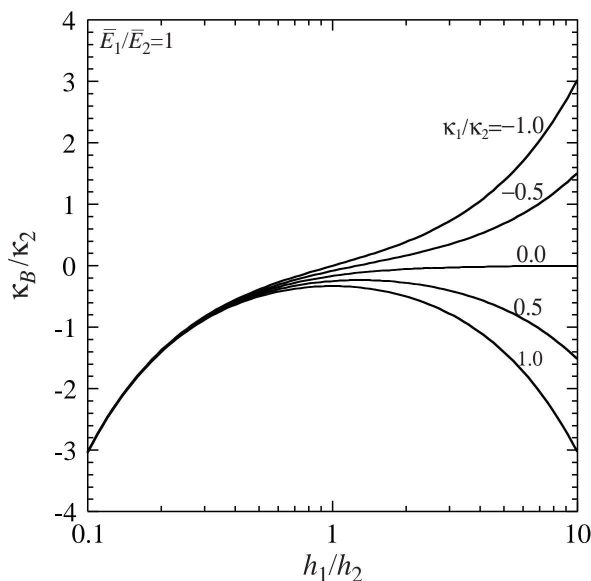

Figure 5-5: The bonding curvature that will yield a flat bonded pair, $\kappa_f = 0$, for various initial curvature ratios as a function of thickness ratio.

teflon chuck was not initially as flat as the steel chuck and was also thought to be deforming more than the steel chuck under the applied loads, due to its low relative stiffness. As a result, the wafers bonded using the teflon chuck were being bonded in a curved state and retained significant shape after bonding, similar to the case plotted in Fig. 5-6. The model results along with this experimental example, demonstrate the need to use a sufficiently flat and stiff chuck when bonding flat wafers in a clamped configuration.

5.3.2 Strain Energy Release Rate

As demonstrated above, the final curvature of a wafer-bonded pair may be controlled through appropriate clamping and mounting during the bonding process. However, the clamping arrangement also influences the residual stresses in the bonded pair. If there is sufficient residual stress following bonding the wafers may delaminate. As such, when considering different clamping configurations it is critical not only to consider the final shape, but the interfacial strain energy release rate as well.

The strain energy release rate for the free and clamped configuration are given by Eq. (5.11) and Eq. (5.20), respectively. While the two have different dependencies on the moduli and thicknesses of the wafers, they both have the same dependence on crack length. The variation of the strain energy

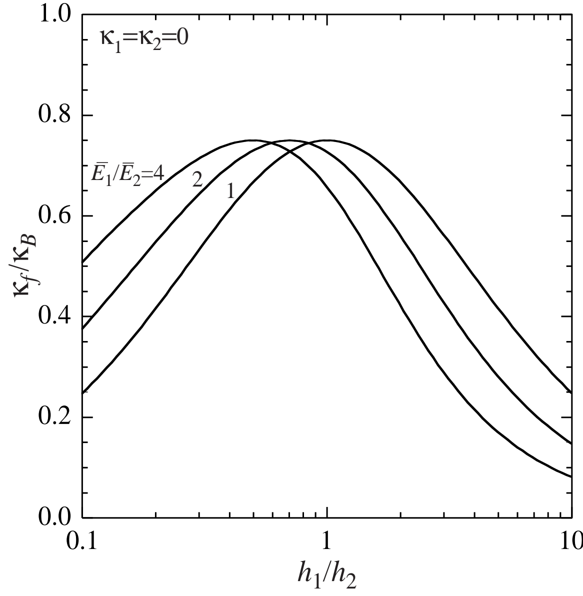

Figure 5-6: The final curvature of pair bonded at curvature κ_B when both wafers are initially flat ($\kappa_1 = \kappa_2 = 0$) for different modulus ratios as a function of thickness ratio.

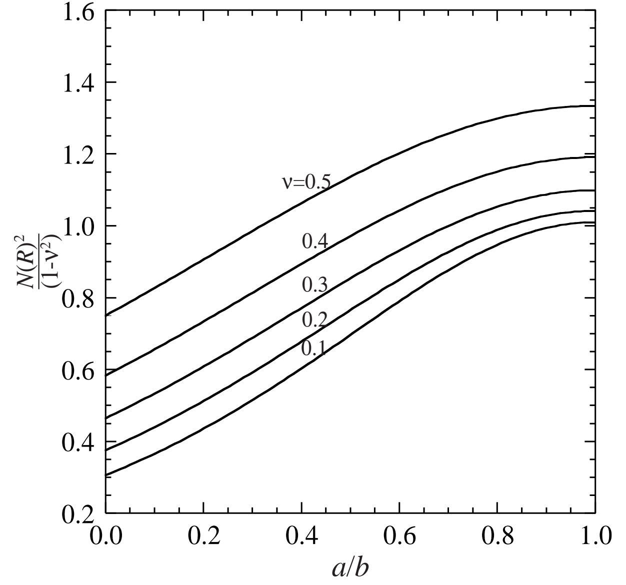

Figure 5-7: Dependence of strain energy release rate on crack length for different values of Poisson's ratio. The free and clamped configurations have the same dependence on crack length, but have different magnitudes.

release rate with crack length is a function of the Poisson's ratio. The dependence on crack length is plotted for various values of Poisson's ratio in Fig. 5-7. The strain energy release rate increases with crack length suggesting that if a crack initiates, it will propagate unstably and the wafers will delaminate completely. It should be noted that the expressions for strain energy release rate given are not valid at very short crack lengths, $a \to 0$, or at short ligament lengths, $a \to b$, when the characteristic dimension controlling the energy release rate ceases to be the plate thickness.

To assess the potential for delamination, the strain energy release rate must be compared to the interface toughness, Γ. Given that the crack will propagate unstably if a crack initiates at the edge, a delamination criterion may be written by comparing the interface toughness to the strain energy release rate at $R = 1$. When the wafers have the same elastic properties, the delamination criterion for the free case is,

$$\Gamma \leq \frac{1}{24} E h_1^3 \frac{1+\nu}{1-\nu} \left[\frac{(\kappa_2 - \kappa_1)^2}{1+\eta^3} \right], \tag{5.21}$$

and for the clamped case (with $\kappa_B = 0$) is,

$$\Gamma \leq \frac{1}{24} E h_1^3 \frac{1+\nu}{1-\nu} \left[\frac{\eta^3 \kappa_1^2 + \kappa_2^2}{\eta^3} - \frac{(\eta^3 \kappa_1 + \kappa_2)^2}{\eta^3 (1+\eta)^3} \right]. \tag{5.22}$$

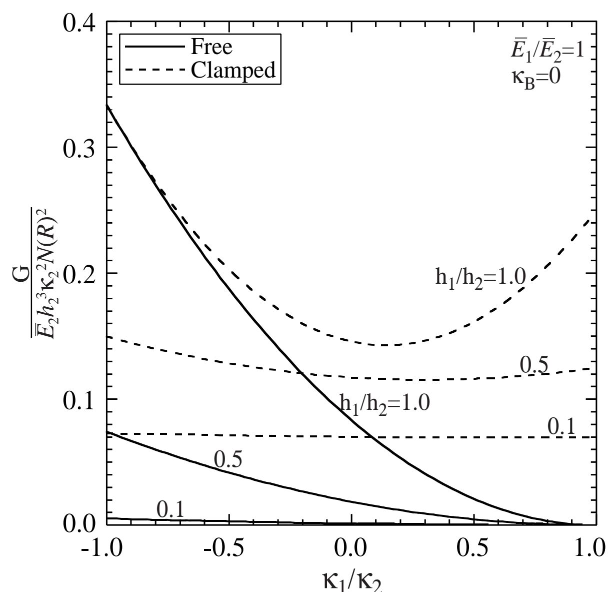

Figure 5-8: Normalized strain energy release rate as a function of curvature ratio for the clamped and free case at several different thickness ratios. The wafers are taken to have the same elastic properties and the bonding curvature is fixed at $\kappa_B = 0$.

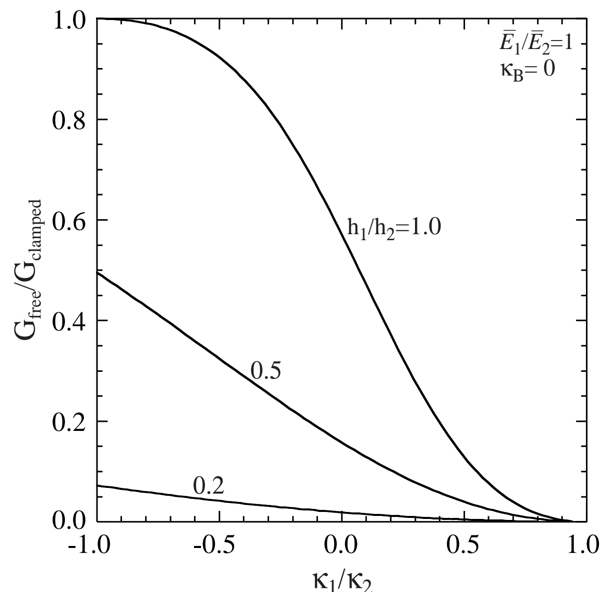

Figure 5-9: Ratio between the strain energy release rate of the free and clamped cases plotted in Fig. 5-8.

From Eqs. (5.21) and (5.22) it is clear that the strain energy release rate for the clamped and free case are markedly different. Figures 5-8 and 5-9 compare the strain energy release rate for the free and clamped (with $\kappa_B = 0$) configuration. Figure 5-8 plots the normalized values of strain energy release rate, while Fig. 5-9 plots the ratio of the strain energy release rate for the free case to that of the clamped case. From Fig. 5-9 it is seen that the strain energy release rate in a pair bonded in the free configuration is always less than or equal to that of a pair bonded in a clamped configuration. The only situation in which the strain energy release rate for the two cases are equal for a given pair of wafers is when the final curvature of the free case is equal to the bonding curvature in the clamped case. As seen in Fig. 5-9, the largest penalty is paid for clamping when the wafers have similar curvatures ($\kappa_1/\kappa_2 \rightarrow 1$). In the free case, the strain energy release rate is very low because the final curvature will be close to the initial curvature and the residual stresses in the wafers are small. However, in the clamped configuration, the bonding curvature may be far from the initial curvatures of the wafers, thus requiring more deformation of the wafers, resulting in a higher strain energy release rate.

These results suggest that care should be taken in selecting the clamping configuration for bonding processes. The fact that clamping the wafers during bonding tends to increase the strain energy release rates demonstrates that for processes such as anodic and direct bonding where

clamping is not required, using applied clamping loads may result in an increase in bonding failure. There are processes however, such as thermocompression bonding, which require clamping pressure in order to form a bond, where the use of applied loads is unavoidable. It is clear though that the way in which these loads are applied (i.e selecting the bonding curvature) can be chosen to minimize the residual stresses and hence the strain energy release rate of the wafer pair.

A final important point to note is that the strain energy release rate that results due to clamping and flatness variations of the type described for a typical silicon wafer (h=0.5-1.0 mm, κ=0.01-0.1 m^{-1}, E=150 GPa) are on the order of 1 to 100 mJ/m^2. This is rather small, and well below the interface toughness values of most bonding techniques, thus in many cases clamping can be used to flatten bonded wafers as described in Section 5.3.1 without concern of introducing sufficient residual stress to cause delamination. Notably, the one technique where strain energy release rates of this magnitude may be significant is direct wafer bonding. In direct bonding, wafers are initially joined at room temperature and the bond toughness prior to annealing for a typical silicon-silicon pair is on the order of 10-100 mJ/m^2, [6] thus instances may occur where poor clamping arrangements lead to bonding failure.

5.4 Summary

A mechanics analysis has been presented which describes the effect of two different clamping configurations during the bonding process. Given the initial geometry and elastic properties of the wafers as well as the bonding configuration, the final shape and strain energy release rate at the interface may be determined using the model presented. The results of the model demonstrate that the bonding curvature can influence the final shape of the bonded pair significantly. Using specific mounting configurations may permit bonded pairs to be engineered flat when the starting wafers are initially curved. The tooling required to achieve this is not standard at the present time, but the benefits of producing flat bonded pairs for subsequent bonding and processing may outweigh the effort required to develop it. The strain energy release rate results show that a pair bonded in the clamped configuration is usually more likely to delaminate than a pair bonded in the free configuration. The clamping process results in a larger amount of residual stress and hence a higher strain energy release rate at the interface. With the exception of room-temperature direct bonding though, the magnitude of the strain energy release rate is typically well below the interface toughness achieved in most wafer bonding processes. Thus clamping can often be employed to flatten wafers without a significant penalty.

The analysis and results presented here are for the case where the flatness variations of the wafers are axisymmetric. While flatness variations resulting from manufacturing are rarely axisymmetric, as discussed in Chapter 4, the model presented here can still be used to provide insight into the

basic effects of clamping in direct bonding. The general modeling approach that was described in this chapter may be extended to asymmetric cases through the use of numerical modeling similar to that in Chapter 4. The closed form axisymmetric models presented in this chapter can be used in first order calculations and to highlight future directions for bonding tool design, while more advanced numerical models should be developed for detailed process design.

Chapter 6

Experiments

In Chapters 2 through 5 a bonding criterion and a series of models for the effect of wafer-scale shape variations and clamping in direct bonding were presented. In this chapter, two series of experiments that were performed to validate the models in the previous chapters are described. The first set of experiments focuses on the ability of the model to predict the extent of bond propagation and compares the results to the models described in Chapters 3 and 4. The second set of experiments examines the final shape of the wafer pair and compares the results to model predictions based on the work described in Chapters 4 and 5. The objective of the experiments reported here are to validate the basic mechanics framework and modeling approach proposed in this work.

In this chapter, the overall approach for both sets of experiments is first outlined. The basic experimental configurations are described and metrics for model-experiment comparison identified. Then, the experimental details, analysis, and results of the bond propagation experiments are presented. Next, the final wafer shape experiments are described and results reported. Finally, the results from both sets of experiments are summarized.

6.1 Approach

The goal of the bond propagation experiments was to assess the ability of the models described to predict the size and shape of the bonded area. The general configuration of the bond propagation experiments is shown in Fig. 6-1. An unpatterned wafer with a tensile residually stressed nitride film on the back surface was bonded to a wafer with a shallow etched spoke pattern on the bonding surface. The spoke pattern that was used is shown in Fig. 6-2(b), and was selected as it makes the bond propagation stable (i.e. increasing G with increasing bond radius) and thus allows the bond to arrest when $G = W$. Achieving stable propagation in the experiments is essential as it allows partially bonded wafer pairs with measurable bonded areas to be obtained. As discussed in Chapter 3, propagation in bond pairs, in which the wafers are unpatterned and have wafer-scale

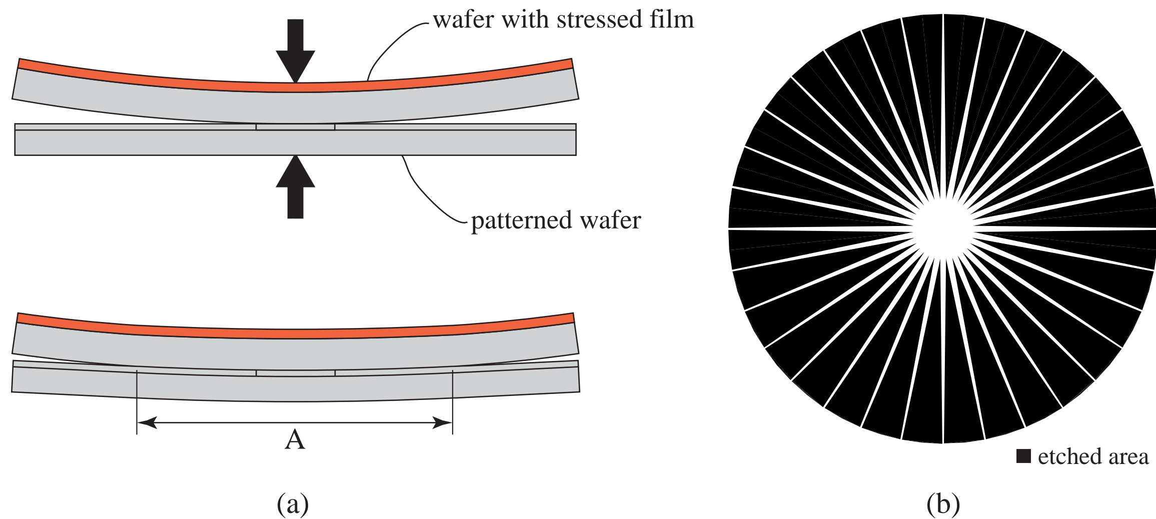

Figure 6-1: Schematic of bond propagation experiments. (a) The shape of one wafer in the pair is increased through the deposition of a residually stressed film on the wafer back surface. The second wafer in the pair has a spoke pattern, which is shown in (b), that is shallow etched on the bonding surface. The wafers are bonded while supported at the center and the bond area, A, is measured.

curvature, is unstable and as such would be expected to either bond completely or not at all.

The size of the bonded area that results is a function of the wafer geometry, elastic properties, etch pattern, and work of adhesion. The elastic properties of the single crystal silicon wafers used in the experiments are well known and the geometry (thickness and shape) of each wafer was measured in the experiments. The work of adhesion was not known and could not readily be measured independently. However, the work of adhesion could be determined for each bonded pair in the experiments by measuring the size of the bonded area and using the model to calculate the work of adhesion required to achieve that bonded area for the given geometry, elastic properties, and etch pattern. The work of adhesion that is calculated via this method is a lumped parameter that includes the effect of surface chemistry and smaller-scale flatness variations (waviness and roughness). The surface chemistry and smaller-scale flatness variations of all the wafers used in the experiments should be the same and as such the work of adhesion values extracted from all the wafer pairs should be the same. The wafer pairs used in the experiments have a range of different wafer scale geometries and thus the calculated work of adhesion values will only be constant across multiple pairs if the model properly accounts for the effects of the wafer-scale shape variations. In addition to comparing the extracted work of adhesion values across the wafer pairs, the ability of the model to predict the shape of the bond front in asymmetric cases may also be assessed in these experiments. This may be done by comparing the shape of the bonded area predicted by the numerical model (Chapter 4) to that observed experimentally. Comparison of the work of adhesion values across the experimental set and the predicted and observed shapes of the bond front provide

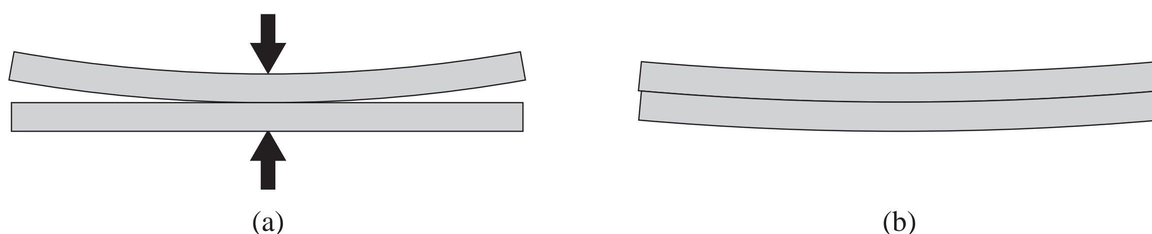

Figure 6-2: Schematic of bond shape experiments. Two wafers are bonded while supported at the center (free configuration). The wafers deform to a common final shape that is subsequently measured. The measured shape of the bonded pair is compared to the shape predicted based on the shape measurements of the individual wafers.

a good assessment of the capability of the model.

The second set of experiments, the final shape experiments, was designed to assess the ability of the model to predict the final shape of the wafer pair. In these experiments, two wafers with different initial shapes were bonded at room temperature while supported at the center, Fig. 6-2(a). The interfaces were unpatterned and the wafer-scale shape variations were sufficiently small such that complete bonding was achieved, Fig. 6-2(b). The geometry of the individual wafers and the bonded pair were measured. The shape of the bonded pair was predicted based on the measurements of the individual wafers and compared to the measured shape of the bonded pair. Pairs with a range of wafer shapes were bonded to validate that the model can predict the final shape across a range of different geometries.

These two series of experiments provide a route to assess the validity of the bonding criterion and models described in Chapters 2-5. The details and results of these experiments are described in the subsequent experiments.

6.2 Bond Propagation Study

6.2.1 Experimental Details

All wafers used in the bond propagation study were 100 mm (100) silicon wafers. The wafers were single side polished and all were taken from the same manufacturing lot. The fabrication process shown in Fig. 6-3 was used to produce the specimens. A tensile residual stressed nitride film was placed on the back surface of one wafer in the pair to add controlled wafer-scale shape variations. The thickness of the film was varied from 0.2 to 0.6 μm to achieve a range of wafer shapes. These wafers were fabricated by initially growing a 500 nm thermal oxide, then LPCVD of stoichiometric silicon nitride (high stress $\sigma \approx 0.7$-1.0 GPa). The silicon nitride was removed from the bonding surface by masking the back with a deposited low temperature oxide, and etching the nitride from the front in a standard hot-phosphoric etch solution (H_3PO_4 (85 %) at 165°C). The mask oxide

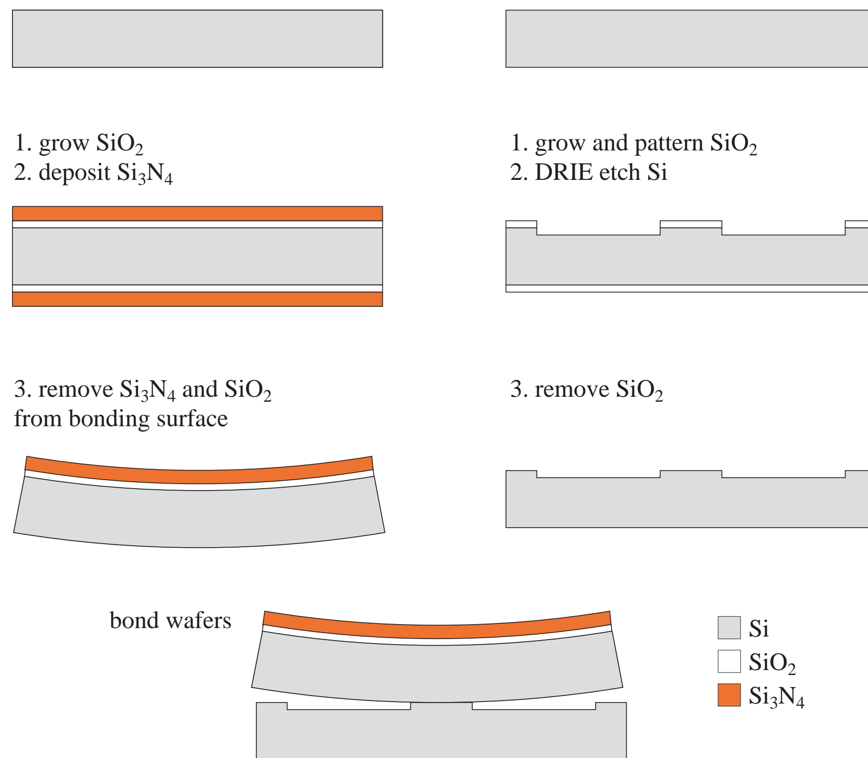

Figure 6-3: Fabrication process for bond propagation study.

on the back surface and the 500 nm thermal oxide on the bonding surface were removed using a buffered oxide etch (7:1 NH_4F(40%):HF(49%)). The spoke patterned wafers were fabricated by first growing a 1000 nm thermal oxide, then patterning the oxide using standard photolithography followed by a wet oxide etch. The pattern was transferred to the silicon using deep reactive ion etching (DRIE). The etch depth on all wafers was between 2 and 3 μm, which is deep enough to prevent bonding, but sufficiently shallow not to alter the stiffness of the wafer. Following etching, the oxide mask was removed using a buffered oxide etch. A standard RCA™ clean was used immediately prior to bonding to ensure a hydrophilic surface and consistent surface chemistry in all tests.

The wafers were supported at the center on a 3 mm diameter pin. The wafers were pressed into contact with another pin at the center to initiate the bond. All experiments were performed at room temperature and pressure in a class 100 clean room, the relative humidity was ≈40%. The bond front propagation was monitored using infrared (IR) transmission imaging and the bonded areas were measured directly from the IR transmission images. After bonding, the pairs were separated and the geometry of each wafer was measured using an ADE 9900 capacitance gage [80]. The gage has a 2 mm square capacitance probe that is scanned across the wafer to obtain full wafer maps of the thickness and shape.

6.2.2 Analysis

The work of adhesion for each bonded pair was calculated based on the wafer geometry, elastic properties, etch pattern, and measured bond area using the axisymmetric model described in Chapter 3 and the finite element based model presented in Chapter 4. Employing the axisymmetric model [Eq. (3.23)] was not straightforward as the shapes of the wafers and the bonded areas tended to not be axisymmetric and thus made defining a single bond radius and wafer curvature difference for each pair difficult. As a result, for each pair, a minimum, average, and maximum bond radius and curvature difference were determined from the experiments and a minimum, average, and maximum W for each wafer pair were calculated using Eq. (3.23). The finite element model presented a more direct route to calculate work of adhesion values for the pairs as their asymmetric geometries could be accounted for properly in the model. For each pair, the measured shapes and thicknesses of the individual wafers were imported into the model described in Chapter 4 and the bonding behavior was mapped out as a function of work of adhesion. Figure 6-4 shows an example of this process for one of the pairs in the experiment. The measured shapes of the individual wafers that are imported into the model are shown in Fig. 6-4(a)-(b) and the bond fronts predicted using the finite element model for a range of work of adhesion values are shown in Fig. 6-4(c). The work of adhesion for each pair may be determined by selecting the predicted bond front that fits the experimentally observed front the best. It is important to note that this may only be done if the shape of the predicted front matches that of the experimentally observed front reasonably well. In most cases, the shape of the predicted and experimental bond areas matched and the work of adhesion values could be determined using this approach.

6.2.3 Results and Discussion

Six wafer pairs were bonded in the bond propagation study. The shapes of the individual wafers in each pair and the resulting bond radii are summarized in Table 6.1. The wafer shape has been expressed as the peak-to-valley shape difference (P-V) across the center 90 mm of the wafer. The sign indicated next to the P-V values indicates if the wafer shape was concave up (+) or down (−). The signed P-V value clearly does not fully describe the wafer shape, but is given as it provides an understanding of the relative shapes of the wafers in the six pairs in the experiment. All of wafers in the experiment were nominally 525 μm thick. Measurements of the wafer thickness showed that the mean thicknesses of the wafers in the set ranged from 523-528 μm and that the total thickness variation of each wafer was less than 4 μm.

The bond radii listed in Table 6.1 were all measured from IR transmission images of the bonded pairs recorded 10 minutes after bonding. The bond front position (and hence the work of adhesion) was observed in the experiments to be time dependent. The bond front was observed typically to

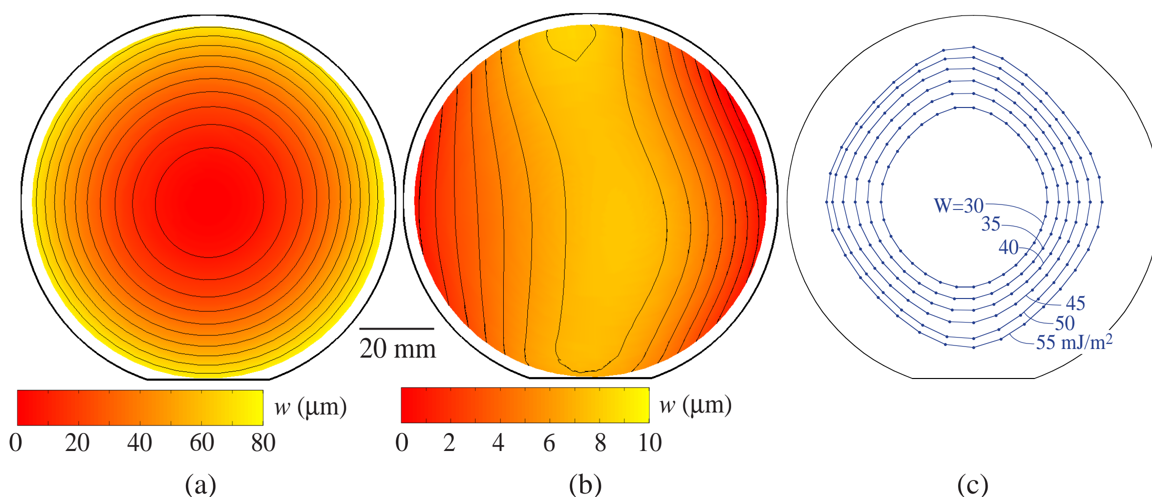

Figure 6-4: Example of data reduction in the propagation experiments. The shape measurements of the individual wafers, (a) and (b), are imported into the model described in Chapter 4 and bond fronts are mapped out for different values of work of adhesion, (c). The predicted bond fronts shown in (c) are for the bonding of the wafers shown in (a) and (b). The data shown is that of pair P4.

advance at a rate of several millimeters per second in the first few seconds after contact. After this initial short period of fast advance, the bonded area would continue to grow at a much slower rate for hours after contact. An example of the time dependence is shown in Fig. 6-5 for pair P4. This time dependence is presumably associated with the dynamics of bond formation at the interface as well as the adsorption of molecules (i.e water) on the surface and is likely a function of various factors such as temperature and humidity. No attempt was made to characterize this dependence fully or to further understand its origin as it is outside the focus of validating the mechanics models in this work. However, the fact that the work of adhesion changes with time means that all work of adhesion values must be determined from bond images recorded at the same time after bonding. All results reported in this work were obtained from measurements recorded 10 min after bonding. A period of 10 minutes was selected as the rate of bond advance was relatively slow at this point and

Table 6.1: Wafer pairs in bond propagation study.

	Wafer Shape		Bond Radius	
Pair	P-V 1 (μm)	P-V 2 (μm)	c_{min} (mm)	c_{max} (mm)
P1	52 (+)	7 (+)	31.7	41.9
P2	72 (+)	7 (+)	26.5	31.2
P3	63 (+)	7 (+)	32.2	37.4
P4	71 (+)	8 (−)	27.6	34.5
P5	31 (+)	7 (+)	41.8	46.3
P6	39 (+)	8 (−)	23.3	41.3

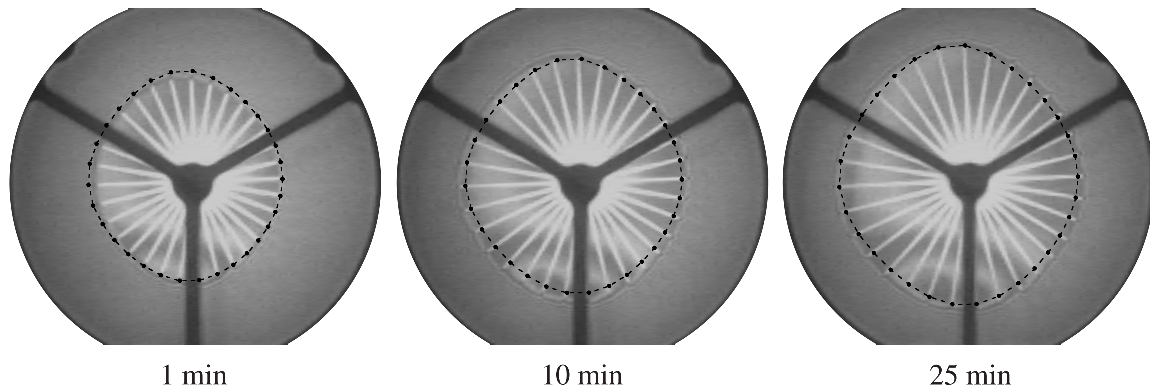

Figure 6-5: Time dependence in bond propagation experiments. IR transmission images of pair P4 recorded 1 min, 10 min, and 25 min after initial contact. The dashed black lines are model predictions and correspond to W=35 mJ/m^2 (1 min), W=40 mJ/m^2 (10 min), and W=45 mJ/m^2 (25 min). The three black lines separated by 120° in each of the images is an aluminum support that sits beneath the wafer pair.

the time period was short enough such that multiple pairs could be bonded sequentially without the ambient conditions (temperature and humidity) changing significantly.

The IR images of the six bonded pairs listed in Table 6.1 are shown in Fig. 6-6. Also shown in the images are the bond fronts predicted by the finite element model. In each image there are two predictions, in P1-P4 the smaller predicted bonded area corresponds to W=35 mJ/m^2 and the larger to W=40 mJ/m^2. In P6, the smaller prediction corresponds to W=25 mJ/m^2 and the larger to W=30 mJ/m^2. No prediction is shown for pair P5 because the bond front propagated to within 5 mm of the edge of the wafer and is considered to have bonded completely. In preliminary experiments it was observed, as in P5, that bonding across the outer 5 mm region rarely occurred for the current pattern even if the wafer-scale shape variations were small. It is believed that this a result of handling damage along the edge as well as 'edge roll-off'. Edge roll-off, refers to a decrease in thickness at the edge of the wafer and is an artifact of the polishing process. It is difficult feature to measure and is a topic that is currently under investigation by wafer manufacturers and metrology companies. In pairs P1-P4 the agreement between the predicted shape and the experiment is good and work of adhesion values may be extracted from the finite element results. The agreement in pair P6 is poor and a work of adhesion value cannot be determined. The poor agreement is believed to be a result of contamination on the wafer surfaces.

The work of adhesion values extracted from the pairs in the bond propagation study are summarized in Fig. 6-7. Work of adhesion values calculated via the axisymmetric model and the finite element model are both shown in the plot. For the axisymmetric analytical results, the markers in Fig. 6-7 correspond to the W calculated from the average bond radii and curvature difference of the pair and the limits of the error bars represent the W calculated from the minimum and maximum bond radii and curvature. Across pairs P1-P4 the average work of adhesion values extracted using

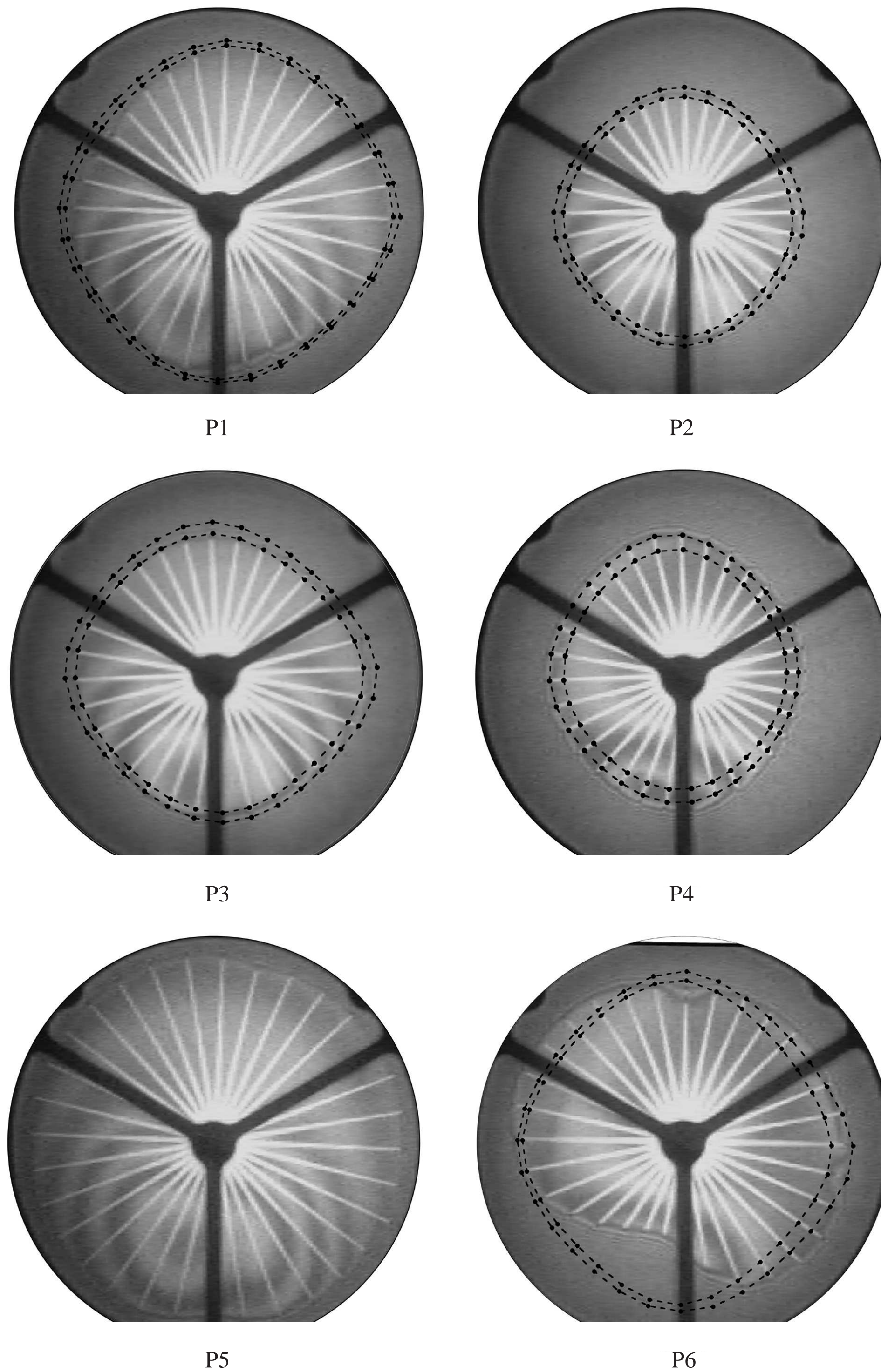

Figure 6-6: IR transmission images of the six bonded wafer pairs in the bond propagation study. The dashed black lines shown are the bond front positions predicted using the finite element model. In pairs P1-P4 the inner prediction corresponds to W=35 mJ/m^2 and the outer for W=40 mJ/m^2. In P5 no prediction is given as the bond front propagated nearly to the edge of the wafer. In P6 the inner prediction is for W=25 mJ/m^2 and the outer for W=30 mJ/m^2.

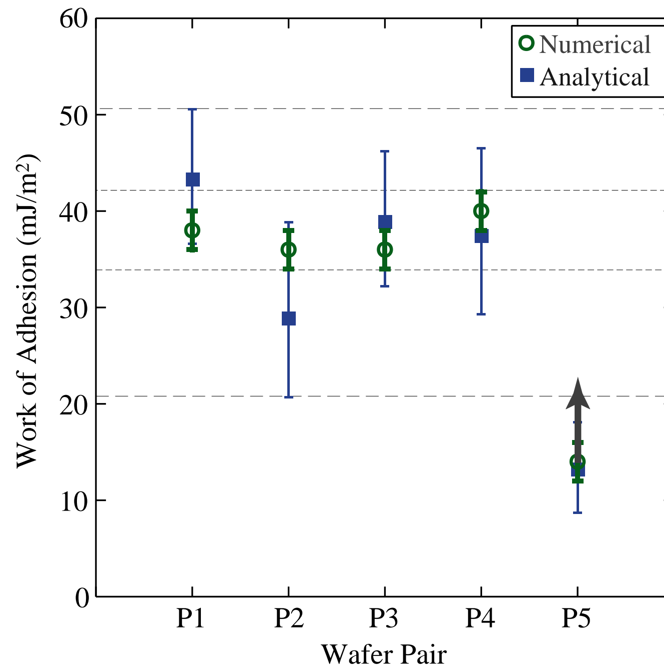

Figure 6-7: Summary of the work of adhesion values obtained in bond propagation study. The work of adhesion values were calculated for each pair from the experimental data using the analytical axisymmetric model described in Chapter 3 and the numerical model described in Chapter 4.

the axisymmetric model range from ≈29-43 mJ/m^2, while those extracted with the numerical model range from ≈36-40 mJ/m^2. The variability in the results extracted with the axisymmetric model is not surprising given that clear asymmetries are present in the wafer shapes and observed bond fronts. Pair P5 is the pair that bonded completely and as such only a lower bound on the work of adhesion may be calculated from the test. The lower bound calculated from P5 is consistent with the work of adhesion values of pairs P1-P4.

The excellent agreement between the predicted and observed bond shapes shown in Fig. 6-6 and the consistency in extracted work of adhesion values (numerical results) shown in Fig. 6-7 indicate that the proposed model accurately captures the mechanics of the bonding process and has the ability to model the effect of wafer scale shape variations in direct bonding. The small variation in the work of adhesion values that is present is reasonable given the time dependence discussed previously and the sensitivity of the work of adhesion to external factors such as temperature and humidity.

6.3 Bond Shape Experiments

6.3.1 Experimental Details

All wafers in the bond shape study were prime grade 150 mm (100) silicon wafers. A thermal silicon oxide with a small compressive residual stress (≈200-400 MPa) was grown on the bonding surface of some wafers in the experiment to introduce additional wafer-scale shape variations. Two different thickness oxide films, 0.25 and 0.50 μm, that added ≈12 μm and 24 μm, respectively, to the wafer-scale shape variations were used. The wafers were at the center, as shown in Fig. 6-2(a), and bonded at room temperature by initiating contact at the center. The bond propagation was monitored via IR transmission imaging. The shape variations were sufficiently small such that complete bonding was achieved in all pairs. Following bonding, the shape and thickness of the bonded pairs were measured using an ADE 9900 capacitance gage [80]. The wafer pairs were subsequently separated and the thickness and shape of the individual wafers were measured.

6.3.2 Analysis

The shape measurements obtained via the capacitance gage represent the wafer shape in a gravity free state. In these bonding experiments, the wafer was supported at the center in a horizontal configuration and thus deforms due to gravity. A general analysis of wafer deformation that occurs due to gravity for a range of support configurations is given in Appendix B. For the current experiments, in which 675 μm thick, 150 mm wafers are supported at the center, the deflection at the edge of wafer due to gravity is ≈12 μm. This is clearly significant as it is comparable to the initial shapes of the wafers. The loading applied to the wafer by gravity cannot be ignored as it is a load that will contribute to the final shape of the wafer analogous to the clamping effects discussed in Chapter 5. The deflection due to gravity that occurs during the bonding process results in additional shape in the final pair. Figure 6-8 details the effect that gravity deformation has on the final shape of the bonded pair and shows that bonding two wafers that are measured flat in a gravity-free state will result in a bonded pair with a gravity-free shape that has a peak to valley difference equal to 75 % of the deflection due to gravity during bonding. The reason for this retention of curvature is the change in bending stiffness that occurs when the wafers are bonded and is the same effect that allows the final shape to be controlled through clamping (Chapter 5).

The asymmetric nature of the wafers and the need to account for the effect of gravity required that a multi-step finite element model be used to predict the final shape of the bonded pair from the initial shapes of the individual wafers. An example of the analysis process used is shown in Fig. 6-9 for one of the bonded pairs in the experimental set. The measurements of the individual wafers, shown in Fig. 6-9(a)-(b), were imported into the finite element model. The deflection due to gravity was calculated through the application of an appropriate body force in the finite element

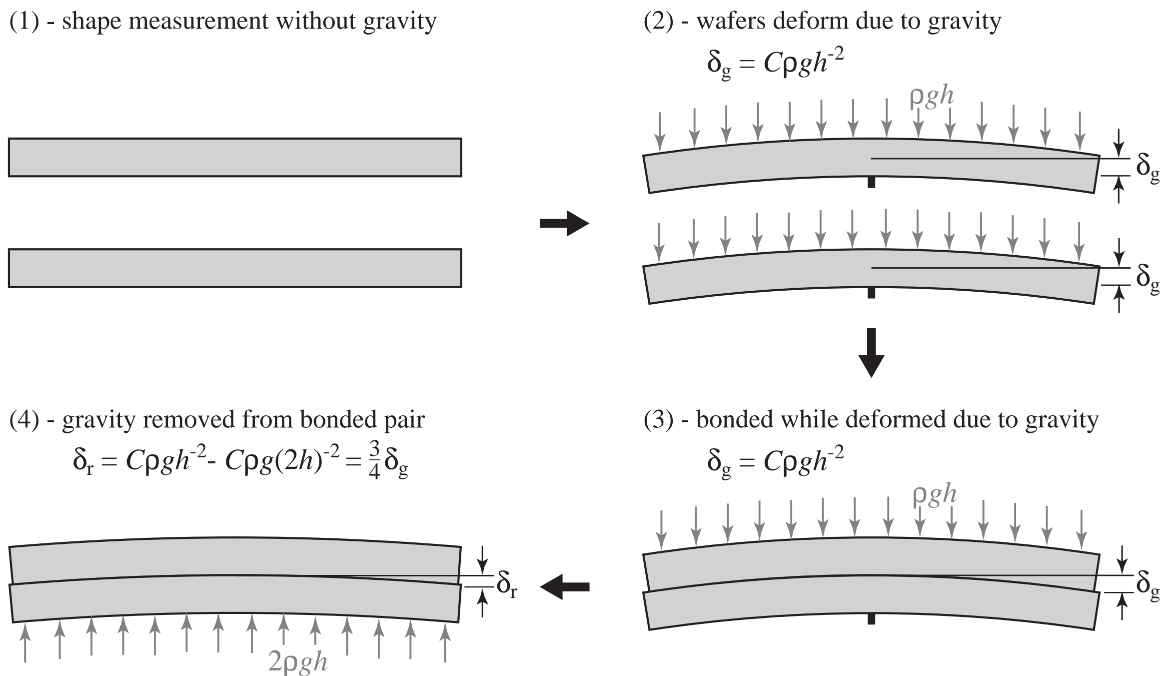

Figure 6-8: Effect of gravity in the shape experiments. The shape measurements of the wafers do not include deformation due to gravity, (1). The wafers are bonded while supported at the center in a horizontal configuration and as a result deform due to gravity, (2) and (3). The final shape is measured without gravity as well, but due to the change in bending stiffness that occurs as a result of bonding, a portion of the deformation due to gravity is retained in the pair, (4).

Table 6.2: Wafer pairs in final shape study.

Pair	Shape		Shape with Gravity		Least Squares Linear Fit	R^2
	P-V 1 (μm)	P-V 2 (μm)	P-V 1 (μm)	P-V 2 (μm)		
S1	4 (−)	4 (+)	14 (−)	11 (−)	0.898	0.984
S2	9 (+)	14 (−)	13 (−)	25 (−)	0.995	0.984
S3	5 (−)	15 (−)	14 (−)	26 (−)	1.028	0.993
S4	4 (−)	14 (−)	14 (−)	25 (−)	1.026	0.993
S5	23 (+)	5 (+)	13 (+)	13 (−)	0.489	0.076
S6	23 (+)	4 (+)	13 (+)	11 (−)	0.790	0.146

model and the shapes of the wafers with gravity while supported in the arrangement used in the bonding experiments was calculated, Fig. 6-9(c)-(d). The wafers were bonded in the finite element model by closing the gap at the interface through the application of displacements on the bonding surface, as described in Chapter 4. The predicted shape of the pair is shown in Fig. 6-9(e). The predicted shape of the pair can be compared to the measured the shape of the pair Fig. 6-9(f). To compare the predicted and measured shapes of the bond pair either gravity must be removed from the predicted shape of the bonded pair or gravity must be added to the measurement of the bonded pair. The latter was done here as the implementation was more straightforward, but there is no particular advantage to one approach over the other. The MATLAB™ script used to generate and run the ABAQUS™ models for this analysis are included in Appendix C.2.

6.3.3 Results and Discussion

Table 6.2 and Fig. 6-10 summarize the initial shapes of the wafers with and without gravity and the predicted and measured shapes of the bonded pairs. The shapes of the individual wafers in Table 6.2 and the bonded pairs in Fig. 6-10 are expressed as the difference between the peak and valley of the wafer shape over the center 140 mm of the wafer. The peak to valley values shown in Fig. 6-10 provide one metric for comparing the predicted shape to the measured shape, but do not provide a complete picture as they give no information about the agreement between the predicted and measured shape values as a function of spatial coordinate. An additional comparison between the predicted and measured shapes, that provides a comparison of the shape values at all the spatial coordinates, was obtained by calculating a factor via least squares that relates the predicted shape, w_{mod}, to the measured shape, w_{exp}, of the bonded pair. This factor may be thought of as the best fit slope if the w_{exp} for every spatial coordinate is plotted against the w_{mod} values at the corresponding spatial coordinates. A slope of 1 and an R^2 value of 1 would indicate perfect agreement between the predicted and measured bonded shape. The least squares factor and corresponding R^2 values for each pair are listed in Table 6.2.

The results in Fig. 6-10 and Table 6.2 show that the agreement between the measured and

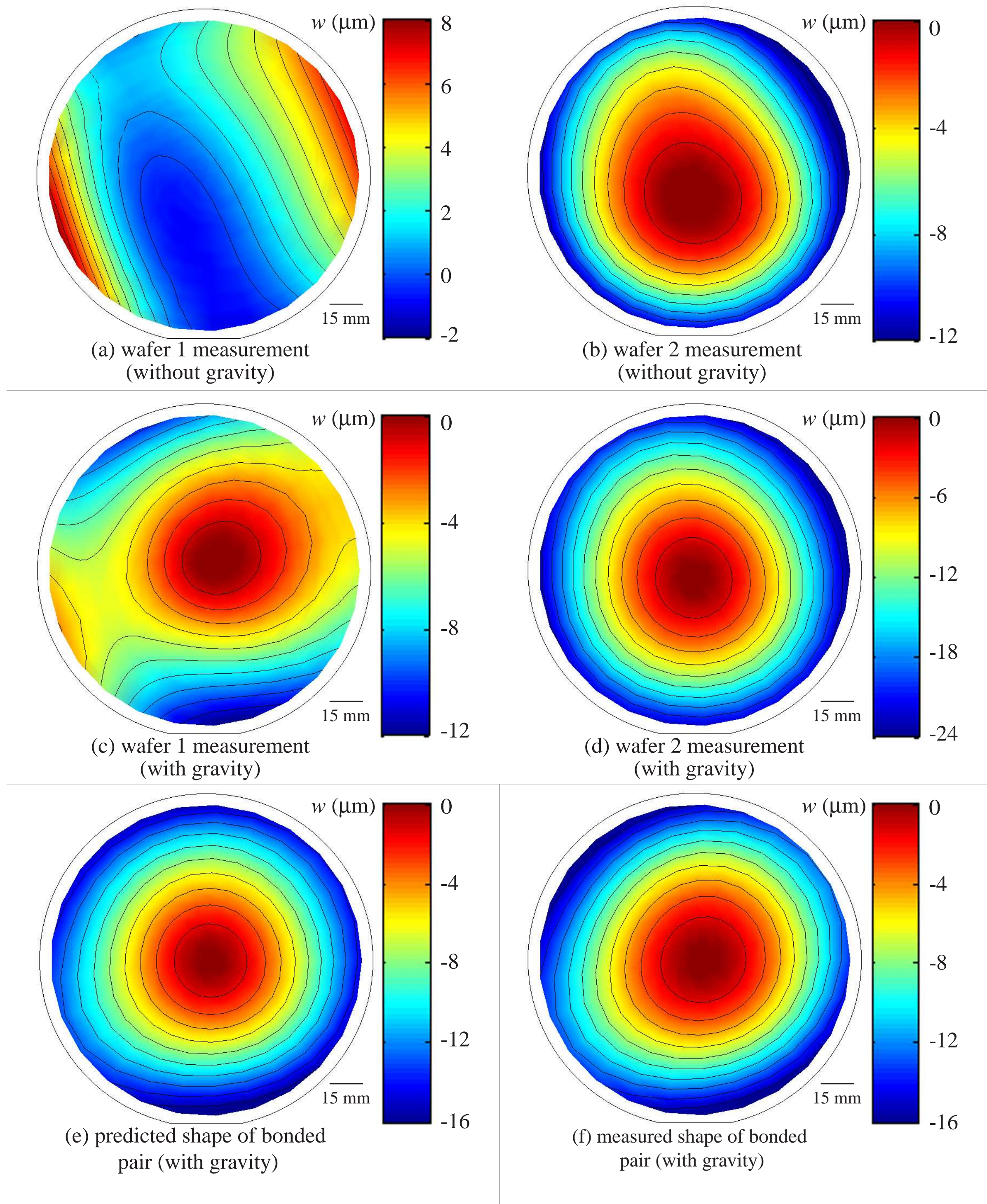

Figure 6-9: Example of analysis process used to predict the shape of the bonded wafer pairs. The measurements of the shapes of the initial wafers, (a) and (b), are imported into a finite element model and the shape of the wafers, while deformed due to gravity, is calculated, (c) and (d). The final shape of the wafer pair is predicted, (e), from the shapes of the two initial wafers with gravity and compared to the measured shape of the bonded pair, (f).

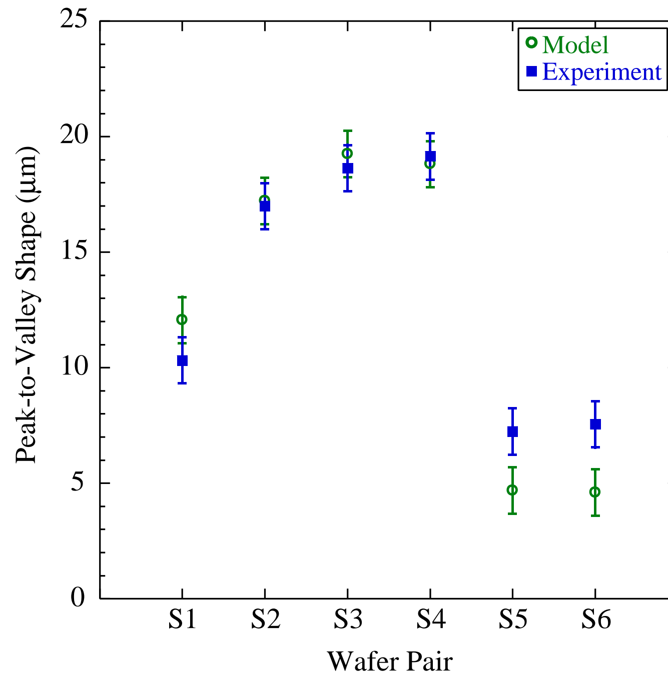

Figure 6-10: Summary of wafer shape experiments. The measured peak-to-valley deflection of the bonded pairs is compared to that predicted using the model.

predicted shapes of the bond pair is good in pairs S1-S4. The model and experiment peak to valley values are close and the least squares factor and the R^2 values are near 1 suggesting good agreement. The maps of the predicted and measured shape of pair S2 shown in Fig. 6-9(e)-(f) show that the shape magnitude and asymmetries in the bond pair are both predicted accurately. The agreement in pairs S5 and S6 appears reasonable in Fig. 6-10, but the least squares factors in Table 6.2 suggest the agreement is poorer.

The initial and final wafer shapes of pairs S5 and S6 are very similar to one another and insight into the differences between the predicted and the measured shape may be gained by looking at the analysis process for one of these pairs. Figure 6-11 shows radial cross sections of the individual wafers and the bonded pair of S6 at different points during the analysis process. As seen in Fig. 6-11 the key difference between the predicted and measured shape of the bond pair is that the measured shape increases monotonically with radial position, while the predicted shape initially decreases and then increases with radial position. This difference may be a result of discrepancies between the actual boundary conditions and those idealized in the finite element model as well as the method that was used to 'bond' the wafers in the finite element analysis. The method used to 'bond' the wafers is thought to have the greater effect. As discussed in Chapter 4, only normal tractions are transmitted across the bonded interface in the finite element model, while in reality tractions normal and parallel to the interface may be transferred. Neglecting the tractions parallel to the interface

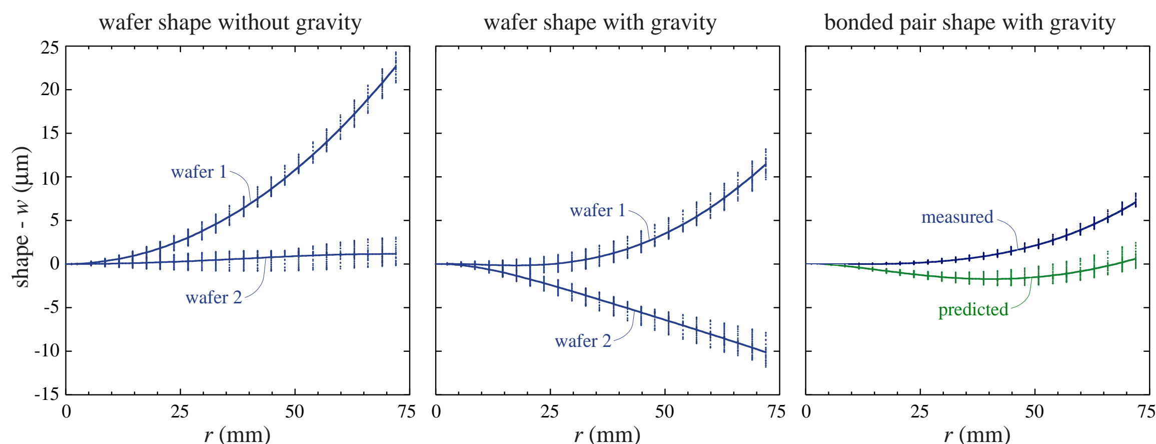

Figure 6-11: Detail of pair S6 in the shape experiments. Shown is a radial cross-section of the pair and different points in the analysis. The profile lines indicate the average shape at the specified radial positions while the vertical lines represent the total range of shape values (sweeping over 360 °) at the specified radial positions.

was important in realizing the model as it reduces the complexity of the model considerably and makes the full three-dimensional modeling of the bonding process feasible. Only accounting for tractions perpendicular to the interface results in the bending stiffness in the bonded region being underestimated. This is not important in most situations where the final shape is predicted to be monotonically increasing (i.e pairs S1-S4) but may play a role here because of the bi-modal predicted shape. It is important to note that while the agreement in pairs S5-S6 is not as good as that in S1-S4, the overall peak-to-valley of the wafer pair is still predicted within 30 %.

6.4 Summary

Overall, there is good agreement between the models that have been developed in the previous chapters and the experiments presented in this chapter. The bond propagation studies showed that the shape of the bond front could be predicted accurately and the effect of wafer scale shape variations in bonding can be accounted for. The bond shape studies illustrated that the shape of the bonded pair can be predicted based on the initial shapes of the wafers.

While the agreement was good overall, there were isolated cases in both sets of experiments where the model and experiment differed. In the propagation experiments in pair P6, the observed shape of the bonded area and that predicted by the model differed significantly. This is a not significant concern though as good agreement was obtained in the majority of the wafer pairs in the experimental set and a difference such as that observed in P6 can easily result from slight contamination of the wafer surfaces. In the shape experiments, differences were observed between the predicted and measured shapes of the bonded wafers in pairs S5 and S6. The difference between

the predicted and the measured shapes of the bonded pair in this case is believed to occur because of the fact the tractions parallel to the bonded interface were neglected in the model. While this simplification resulted in poorer agreement in pairs S5-S6 than in pairs S1-S4, the agreement was still reasonable and the peak to valley of the wafer pair was predicted within 30%.

The experiments reported in this chapter clearly demonstrate that the bonding criterion proposed and models that have been developed in Chapters 2–5 are effective in relating the initial wafer geometry to the bonded area and the shape of the bonded pair.

Chapter 7

Nanotopography

The primary focus of the work to this point has been the effect of wafer shape on direct bonding. As discussed in Chapter 2, wafer shape is only one segment of the large range of wafer geometry factors that may affect direct bonding. Nanotopography, which is defined in SEMI M43 as 'the non-planar deviation of the whole front wafer surface within a spatial wavelength range of approximately 0.2 to 20 mm' [46], is the next step down the spatial wavelength scale from wafer shape and is the focus of this chapter. In particular, this chapter will focus on assessing the impact of surface height variations with spatial wavelengths between 0.1 mm and 10 mm on direct bonding. As discussed in Chapter 2, these flatness variations are distinguished from those with smaller spatial wavelengths, such as roughness, based on the fact that these are accommodated during direct bonding though elastic deformation while those with smaller spatial wavelengths may not be. The specific range of spatial wavelengths examined in the current work was selected as it is consistent with the defined nanotopography range and measurements can be obtained across the range using a single metrology tool.

In this chapter, the relevant literature on nanotopography is first reviewed to provide an idea of the typical height variations observed, the origins of nanotopography, and the metrology available to measure it. Next, an elasticity solution that allows the strain energy required to bond two sinusoidally varying surfaces is reviewed. The solution is then used to develop bonding maps that provide an idea of the magnitude of nanotopography that would be significant in direct bonding. Then, nanotopography measurements conducted on three wafers manufactured using different polishing processes are detailed and results reported. The measurements from the wafers are analyzed and compared in terms of how the different topographies affect bonding. Finally, the strain energy required to bond the wafers is estimated and compared to typical values of work of adhesion to determine whether or not nanotopography is an important factor in direct bonding.

7.1 Background

Nanotopography has emerged as a significant factor in integrated circuit fabrication with the introduction of chemical mechanical polishing (CMP) processes for shallow trench isolation [81]. As a result, the metrology industry has introduced tools to measure it, wafer manufacturers have taken efforts to control it, and standards have been developed for reporting it. Furthermore, numerous research studies in which wafer nanotopography has been characterized, primarily motivated by the desire to understand its effect on CMP, have been carried out. As a result, an estimate of the typical height variations, an assessment of the tools available to measure it, and a qualitative explanation of the effects of different manufacturing processes on wafer nanotopography may be found in the literature.

Numerous studies have been performed in which the nanotopography of wafers have been characterized [82–87]. From these works it is evident that height variations between 10 and 100 nm across spatial wavelengths of 0.2 to 20 mm are common. Measurements on 200 mm wafers reported in [88] show that peak to valley variations over a 20 mm wavelength may be as large as 150 nm. Furthermore, results reported in [88] show that nanotopography amplitude and pattern depend to a large extent on the polishing configuration (single side or double side) as well as the details of the particular polishing process. Some discussion regarding the effects of different polishing methods as well as the effects of wafer mounting during polishing are discussed in [81, 85, 89, 90]. In general, double-side polished (DSP) wafers tend to have less nanotopography than single-side polished wafers (SSP). Single-side polishing processes result in a larger nanotopography because of the fact that the wafer is typically mounted to a flat reference chuck during the polishing process. This mounting scheme results in a portion of the topography of the wafer back surface being transmitted to the front surface. Wafers polished in a true double-side polishing process, where the wafers are free floating and both sides are polished simultaneously, tend to have significantly smaller height variations across spatial wavelengths between 0.2 and 20 mm [90].

Measuring nanotopography is a significant challenge in itself due to the large lateral areas that must be imaged while achieving sub-nanometer vertical resolution. As a result, several specialized systems have been developed and demonstrated for measuring nanotopography. Early measurements were performed using scanning laser systems, which could provide height maps of the surface, but were limited in terms of speed and data density by the line scan nature of the tools [91,92]. As a result, interferometric systems that use a white light halogen source have largely replaced the scanning laser systems for nanotopography measurements. In addition to speed, interferometric-based systems provide advantages over scanning systems including direct height mapping of the surface, large area acquisition, and the elimination of scan hardware that can cause vibration and measurement noise [91]. In the nanotopography studies discussed above, 200 and 300 mm wafers have

been measured using a commercial laser scanning system (ADE SQM), [93], as well as a commercial white light interferometric system (ADE Phase-Shift Nanomapper), [83,86–88]. Additional systems that use different measurement principles have also been reported, including scanning deflectometry [94] and a Schack-Hartman wavefront sensor [95]. While no specific measurement technique is specified in the relevant standards, interferometric systems appear to be the method of choice at the current time for characterizing full wafer nanotopography on 200 and 300 mm silicon wafers.

7.2 Modeling

If two wafers with nanotopography surface height variations are to be bonded, elastic deformation of the wafers is required. As discussed in Chapter 3, the critical consideration when assessing the effect of flatness variations that are accommodated through elastic deformation is the strain energy required per unit area of bond front advance, dU/dA, relative to the available work of adhesion. In the previous chapters, in which the effects of wafer shape were considered, a bond front was clearly defined and the problem of bonding was examined as a question of bond propagation. In the current situation, where the bonding of two surfaces with arbitrary topographies that may make contact at several points is considered, it is difficult, if not impossible, to define a single bond front for a similar calculation. For this reason, when examining the effect of nanotopography on bonding, the change in strain energy per change in bond area, $\Delta U/\Delta A$, over a specified area is considered rather than dU/dA. While this is an approximation that results in the averaging of the energy required to advance the bond front over some defined area, it may be put into a consistent framework with the wafer shape analysis by viewing the nanotopography contribution as an energy absorption term at the bond front.

In order to evaluate $\Delta U/\Delta A$ for nanotopography, the strain energy must be calculated as a function of the surface geometry. Yu and Suo [54] presented a model in the context of direct bonding that allowed the strain energy required to deform two wafers to close a sinusoidal gap at the interface (Fig. 7-1) to be calculated. The solution given by Yu and Suo is valid across the nanotopography range examined in the current work, assuming that the surface height variations are small compared to the wafer thickness (0.5-1 mm). This assumption certainly appears reasonable as the typical nanotopography (Sec. 7.1) height variations reported in the literature are the order of 10-100 nm. As such, the solution given in [54] is first used in this section to develop design maps that highlight the combinations of amplitude and wavelength that are important in direct bonding and then is employed in Sec. 7.4 to estimate the contribution of nanotopography to bonding by calculating $\Delta U/\Delta A$ for the surface geometry measurements obtained in this work.

A schematic of the cross-section of the geometry considered in [54] is shown in Fig. 7-1(a) and a three-dimensional map of the model surface is shown in Fig. 7-1(b). The gap at the interface that

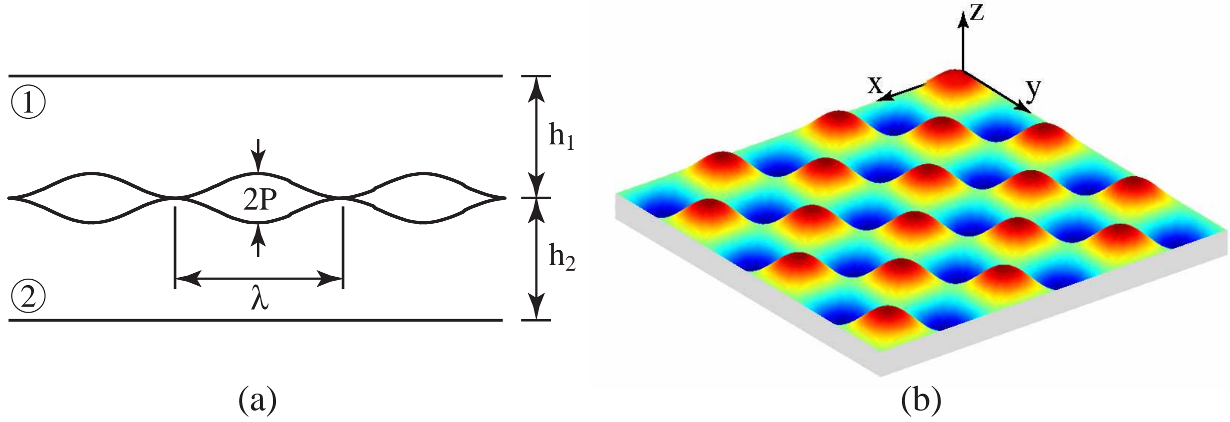

Figure 7-1: (a) A two-dimensional cross-section of the surface considered in the model. (b) Three-dimensional plot of surface examined in the analytical model.

must be closed through elastic deformation during bonding as a function of the spatial coordinates x and y is,

$$gap = 2P\left[1+\cos\left(2\pi\frac{x}{\lambda}\right)\cos\left(2\pi\frac{y}{\lambda}\right)\right]. \tag{7.1}$$

From the solution given in [54], the energy per unit area required to close this gap is,

$$\frac{\Delta U}{\Delta A} = \frac{\pi}{4\sqrt{2}}\frac{P^2}{\lambda}\left(\frac{1}{\bar{E}_1 I(2\pi h_1/\lambda)}+\frac{1}{\bar{E}_2 I(2\pi h_2/\lambda)}\right)^{-1}, \tag{7.2}$$

where h_1 and h_2 are the thicknesses of the layers, λ is the wavelength and P is the amplitude of the surface topography, $\bar{E}_1$ and $\bar{E}_2$ are the plane strain moduli of the wafers ($\bar{E}_i = E/(1-\nu_i^2)$), and the function $I(\alpha)$ is,

$$I(\alpha) = \frac{e^{2\sqrt{2}\alpha}+e^{-2\sqrt{2}\alpha}-2-8\alpha^2}{e^{2\sqrt{2}\alpha}-e^{-2\sqrt{2}\alpha}+4\sqrt{2}\alpha}. \tag{7.3}$$

In the case where the wafers have the same elastic properties ($\bar{E}_1 = \bar{E}_2$) and equal thickness ($h_1 = h_2$), Eq. (7.2) reduces to,

$$\frac{\Delta U}{\Delta A} = \frac{\pi}{8\sqrt{2}}\frac{\bar{E}_1 P^2}{\lambda} I\left(2\pi\frac{h_1}{\lambda}\right). \tag{7.4}$$

The effect of surface topography on bonding may be more clearly understood by creating bonding maps using Eq. (7.4) that show combinations of amplitude and wavelength that will bond (assuming no other flatness variations are present) given a work of adhesion. Figures 7-2 and 7-3 are two examples of such maps that may be used to understand the range of nanotopographies that are potentially detrimental to bonding. Figure 7-2 provides guidance on acceptable amplitudes at a range of wavelengths for various values of work of adhesion. The lines plotted in Figs. 7-

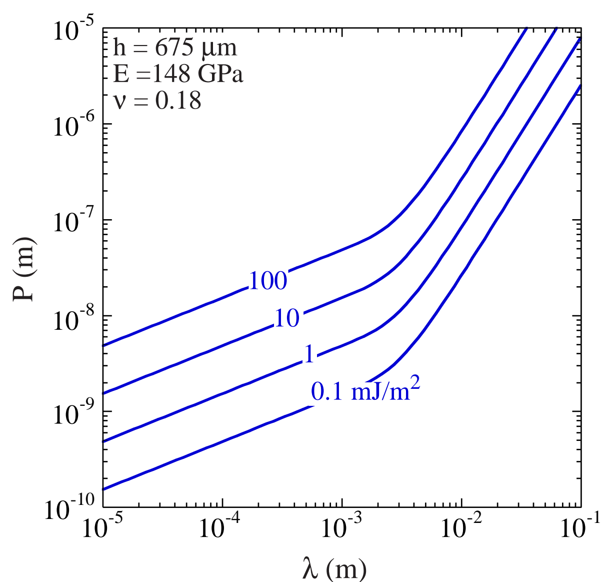

Figure 7-2: Map showing ΔU/ΔA as a function of wavelength and amplitude.

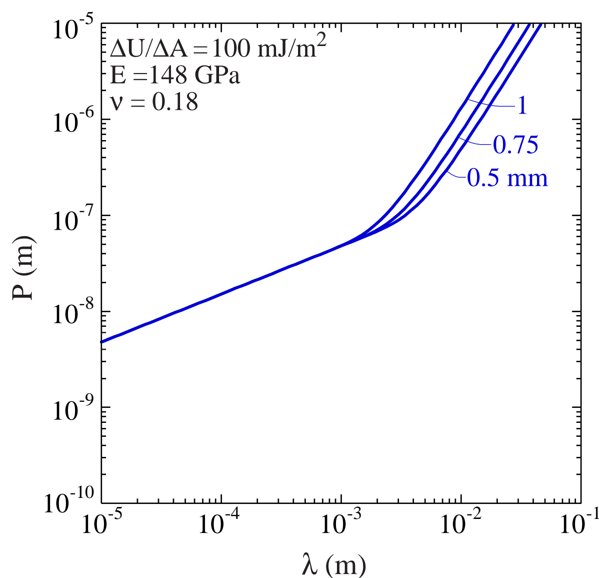

Figure 7-3: Map showing effect of wafer thickness on ΔU/ΔA as a function of misfit wavelength and amplitude.

2 and 7-3 should be interpreted as bounds - that is, combinations of wavelength and amplitude that fall below the lines are bondable while those that fall above are not. From Fig. 7-2, which is plotted for bonding two standard 150 mm silicon wafers (h_1=h_2=675 μm, E_1=E_2=148 GPa, ν_1=ν_2=0.18), the amplitudes of nanotopography that may play a significant role in bonding can be determined. Given that typical values of work of adhesion in silicon wafer bonding are between 1 and 100 mJ/m^2 (hydrophobic and hydrophilic bonding) and that wafer shape variations typically result in strain energy accumulation rates of 1-100 mJ/m^2, the 1 mJ/m^2 bound in Fig. 7-2 serves as a good reference to assess whether nanotopography may play a role in direct bonding. With this consideration, it is seen that at wavelengths of 1 and 10 mm, height variations of 5 and 90 nm, respectively, would be required for nanotopography to play a significant role in direct bonding. From this simple consideration and the typical values of nanotopography observed in previous work, it is reasonable to expect that nanotopography may be a contributing factor in direct bonding failures.

The map shown in Fig. 7-3 demonstrates the importance of wafer thickness when considering nanotopography effects in bonding. At the longer spatial wavelengths ($\approx$ 10mm) in the nanotopography range, bonding difficultly increases with the cube of thickness, the same scaling observed in wafer-scale shape variations. At spatial wavelengths less than 1 mm, the strain energy required to achieve bonding is independent of wafer thickness. This suggests that a portion of the nanotopography range is affected by wafer thickness and that there may be benefits to using thinner wafers and bonding with one ‘compliant’ layer as discussed in Chapter 3 with respect to wafer shape effects.

Table 7.1: Wafers in nanotopography experiments.

Wafer	Process	Thickness (μm)	TTV (μm)
(A)	single-side	630.2	1.7
(B)	double-side rough	523.7	2.6
(C)	double-side fine	523.3	1.8

7.3 Material and Measurements

The nanotopography of wafers that were manufactured using three different polishing processes were measured in this work. All of the wafers used were (100) 150 mm diameter silicon wafers. Three different polishing processes - (A) single side fine polish, (B) double side rough polish, and (C) double side fine polish, were used. The three different wafers are summarized in Table 7.1 along with their thickness and total thickness variation measured on an ADE 9900 capacitance gage [80].

The wafer size (150 mm) used in this work complicated the nanotopography measurement as the commercial systems discussed in Sec. 7.1 are production line systems designed to measure 200 and 300 mm wafers and cannot readily accommodate smaller diameter wafers. As such, nanotopography was measured using a large area Fizeau interferometer that provided comparable resolution to the specialized nanotopography metrology tools, while allowing more flexibility in wafer handling. Specifically, a vertically mounted (downward looking) Zygo Verifire AT™ Fizeau interferometer with a Ring of Fire™ illumination system [96] was used. The system had a 6-inch aperture with an adjustable zoom setting that allowed the size of the imaging area to be varied. The camera resolution on the system was fixed at 776x576 pixels. As a result, the zoom setting determined the size of measurement area as well as the spatial resolution. A low zoom setting allows a large area to be measured, but results in low spatial resolution, while a high zoom setting yields a high spatial resolution but limits the measurement area. Given that the aim of this work was to measure flatness variations with spatial wavelengths from approximately 0.1 to 10 mm, a zoom setting which resulted in a spatial resolution of 108.8 μm and a measurement area of 84.4 mm by 62.6 mm was used for all measurements. This setting allowed wavelengths down to $\approx$0.22 mm (based on a Nyquist consideration) to be measured while providing a sufficiently large measurement area after filtering to permit statistically significant information on longer wavelength height variations to be obtained.

The wafers were rested on a 6-inch diameter reference flat in a horizontal orientation during all measurements. The wafers were not clamped or mounted to a vacuum chuck. This arrangement results in the wafer resting on three points determined by the shape of the wafer and means that overall wafer shape may be affected by gravity. This is not a concern though, as the interest in these measurements is at spatial wavelengths shorter than 10 mm where deformations due to gravity should not affect the surface geometry. SEMI M43 [46], the nanotopography standard, makes

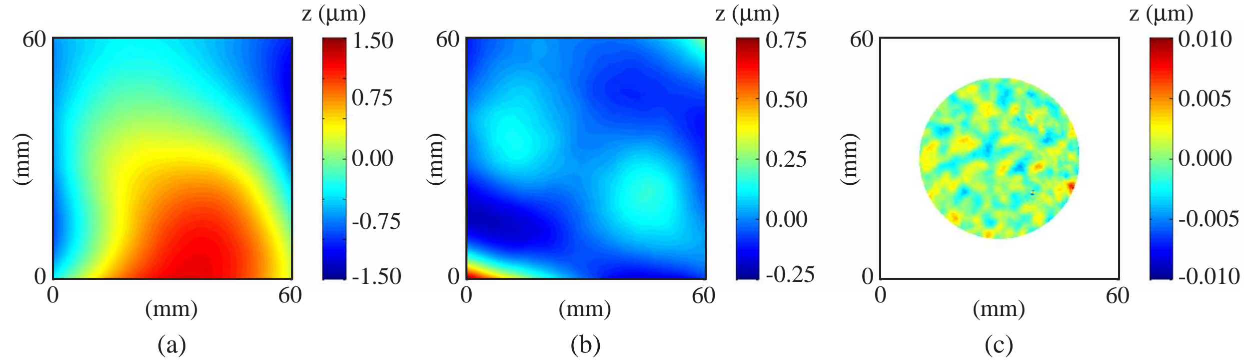

Figure 7-4: Process used to isolate the nanotopography features from the raw measurements (data shown is that for wafer (C)). (a) Raw measurement. (b) Surface after overall form was removed. (c) Final data after filtering with a 10 mm high-pass double Gaussian filter and cropping to remove edge effects.

no statement about how the wafer should be mounted during measurements. While mounting situations vary between commercial tools, most systems mount the wafer on a vacuum chuck as it removes wafer-scale shape variations that may limit the area over which nanotopography measurements can be obtained. Caution should be used however, given that certain chuck configurations may affect the measured nanotopography since pin and ring spacings on many chucks are similar to that of the wavelengths of interest. The wafers were not mounted on a chuck in this work to ensure that the nanotopography measurements obtained would be representative of the surface geometry during direct bonding, in which the wafers are typically not fixed to a chuck.

Regardless of mounting configuration, long spatial wavelength height variations typically obscure the nanotopography features of interest in raw measurements obtained via interferometric systems. A high-pass filtering routine is typically required to isolate the spatial wavelengths relevant to nanotopography. Filtering has been used in all nanotopography measurements reported and the selection of filtering techniques has been investigated [97]. The preferred method of filtering reported in [97] and specified in SEMI M43 [46] is a high-pass double gaussian filter. The double gaussian filter effectively removes the long wavelength variations without significantly attenuating the height of features in the range of interest.

In the current work, the nanotopography of the surfaces was isolated from the raw measurements through the process shown in Fig. 7-4. The raw measurement (84.4 mm by 62.6 mm), which was centered on the wafer, was first cropped to a 60 mm square analysis area (Fig. 7-4(a)). A third-order best fit polynomial was then removed from the measurement (Fig. 7-4(b)) and the resulting surface was filtered using a high-pass double gaussian filter with a 10 mm cutoff. The filtered data was cropped to a 40 mm circle (Fig. 7-4(c)) in order to remove non-physical edge effects that result from the filtering process. This post-processing was performed externally by importing the raw data in text format into MATLAB™.

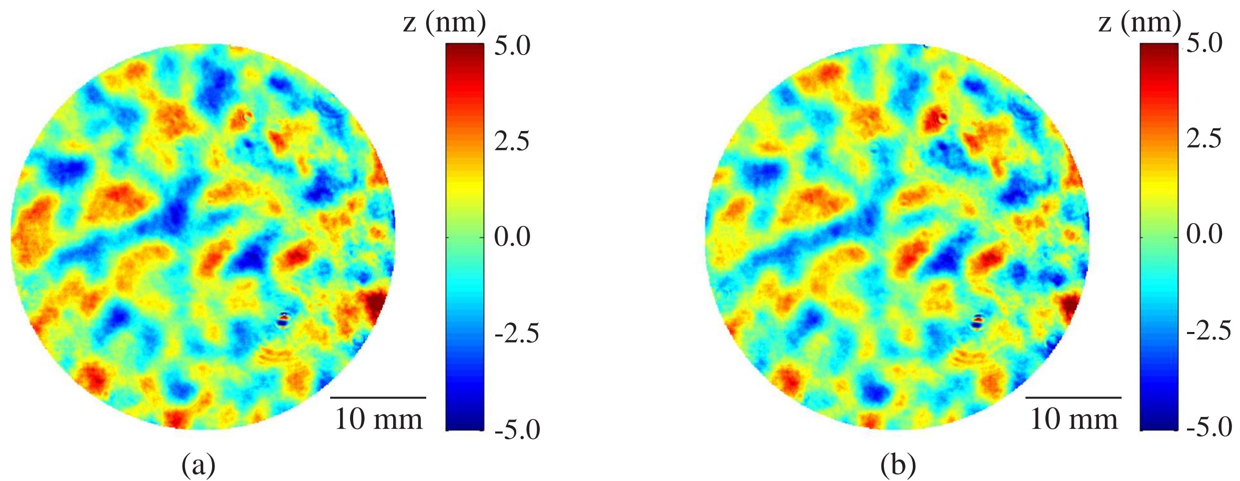

Figure 7-5: Comparison of the (a) double gaussian filter and the built-in Zygo MetroPro filtering functions (b) for wafer (C).

As a check on the data processing sequence described above, the data was also filtered using the measurement analysis features built-in to the Zygo MetroPro™ software [98]. A similar process was used in MetroPro™ , in which the overall form was first removed (using the piston, tilt, astigmatism, coma, and spherical aberration functions in MetroPro™), followed by filtering using the built-in high-pass FFT based filter with a fixed cutoff of 10 mm. A comparison between the results of both data processing routines is shown in Fig. 7-5. Similar features are seen in the final data obtained from both processing sequences, although, the amplitude of the height variations appear to attenuated slightly more in the MetroPro™ processing scheme.

7.4 Results and Discussion

Nanotopography measurements obtained for the three wafers listed in Table 7.1 are shown in Fig. 7-6. The nanotopography height variations observed are consistent with, but at the low end of the range of values reported in literature. This fact may be the result of the use of double-gaussian filter with a 10 mm rather than a 20 mm cutoff as well as not mounting the wafers to a chuck during measurement. When a wafer is mounted to a chuck, a portion of the back surface topography is transmitted to the front surface resulting in larger nanotopography values. Thus, it is reasonable that the amplitude of nanotopography measured in this work is less than that reported in the literature. In addition to providing an idea of the overall nanotopography variations, the maps shown in Fig. 7-6 allow clear differences between the three wafers to be identified. Wafer (C) has the smallest height variations on the surface, while those on wafers (A) and (B) are larger. Furthermore, the dominant wavelength of the height variations on the DSP wafers, wafers (B) and

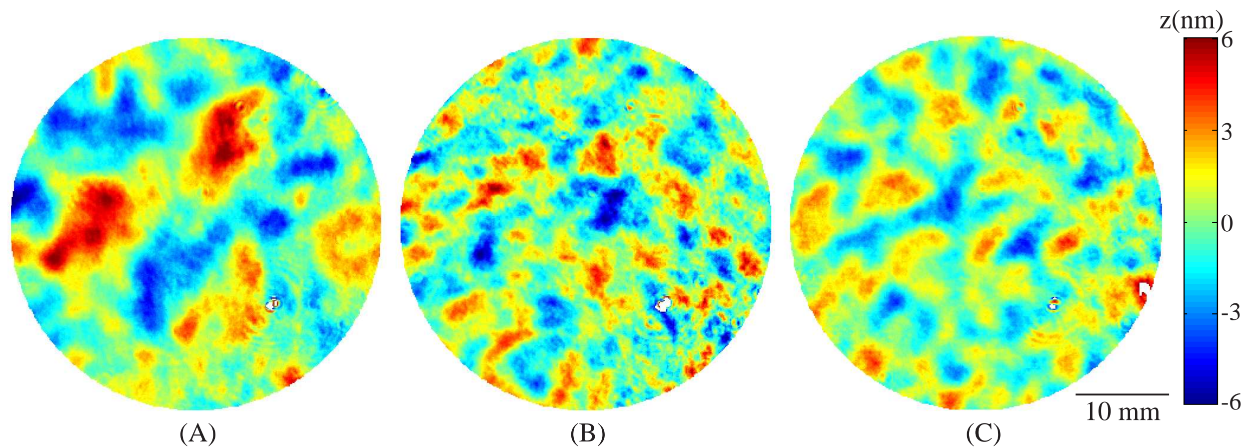

Figure 7-6: Nanotopography of the three different wafers - wafer (A) SSP fine polish, wafer (B) DSP rough polish, wafer (C) DSP fine polish. Each map shown is 40 mm in diameter.

(C), appear to be less than that of wafer (A).

A more quantitative comparison between the three wafers may be obtained by examining the power spectral densities (PSD) of the surfaces. The PSD is particularly relevant in the current context as it provides information about both the amplitude and wavelength of the height variations on the surfaces. The PSD for the three wafers are shown in Fig. 7-7. The PSD's shown were obtained by estimating the PSD using Welch's method [99] along line scans in the x and y directions (369 scans in x and y each) and then averaging. No significant differences were observed in the PSD's calculated in the x and y directions. Thus, the PSD's shown for each wafer are an average of the PSD's obtained from all the x and y scans for that wafer. The results shown in Fig. 7-7 show that wafer (B) has the largest power spectral density across the range of wavelengths of interest. Wafers (A) and (C) have PSD's with similar magnitudes, however at high spatial frequencies, the PSD's suggest that wafer (C) has smaller surface height variations. The amplitude of the different frequency components of the surface scale with the PSD, thus it can be concluded from Fig. 7-7 that wafer (B) would be the most difficult of the three to bond as it has the largest amplitude across the range of spatial wavelengths. However, it is not clear whether (A) or (C) has a better nanotopography in terms of bonding given the tradeoff between amplitude and wavelength and the fact that the PSD's of (A) and (C) cross at a spatial frequency of approximately 0.3 mm^{-1}. The PSD clearly provides a more quantitative assessment of surface topography in terms of bonding than simply inspecting the height maps of surfaces shown in Fig. 7-6.

The PSD's provide a good way to compare the three surfaces, although quantities that directly scale with the amplitude of the height variations at different wavelengths would provide a more direct route to connect the nanotopography measurements to bonding through the model presented in Sec. 7.2. By integrating the power spectral density, $S(f)$, across a specified frequency band (f_l

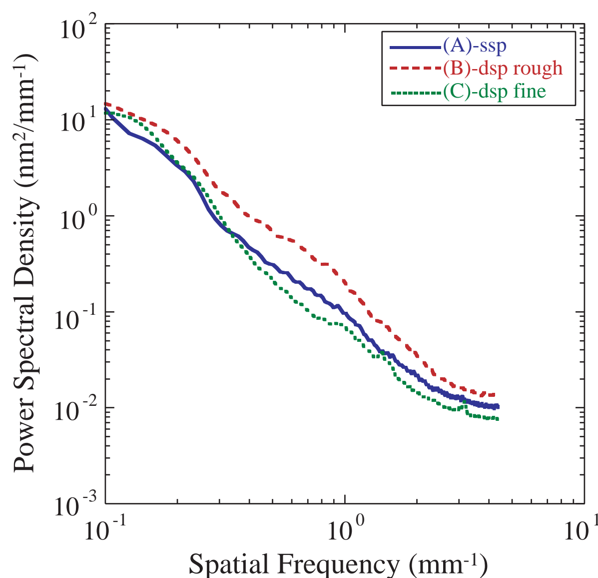

Figure 7-7: Power spectral densities of the nanotopography of three surfaces measured.

to f_h), the mean square value of the height variations, $\bar{z}^2$, within that frequency band may be estimated [100],

$$\bar{z}^2 = \int_{f_l}^{f_h} S(f)df. \tag{7.5}$$

Using Eq. (7.5), the root mean square of the height variations, $z_{rms} = \sqrt{\bar{z}^2}$, as a function of spatial wavelength was calculated from the PSD's shown in Fig. 7-7 by dividing the PSD's into adjacent frequency bands 0.09 mm^{-1} wide and integrating across each band. The root mean square values as a function of the mean frequency in each band are plotted in Fig. 7-8. Each point in Fig. 7-8 corresponds to the root mean square of the height variations across a band, 0.09 mm^{-1} wide, centered at the specified spatial frequency. As expected, the plot displays a similar trend to the PSD plot in Fig. 7-7. The real value of the plot, though, is that it provides a measure of how the amplitude of the height variations scale with spatial wavelength for the three wafers.

The measurements shown in Fig. 7-6 clearly reveal that the surface height variations of the wafers examined in this work are not sinusoidal in nature, as is assumed in the model discussed in Sec. 7.2. However, to obtain a better understanding of how the three surface topographies relate to bonding, it is reasonable to assume that the general scaling with spatial wavelength and amplitude given by the model will hold for these surfaces. Assuming that the amplitude of the height variations as a function of wavelength scale with the root mean square value of the surface height variations as a function of wavelength, shown in Fig. 7-8, the model presented in Sec. 7.2 may be used to assess the relative $\Delta U/\Delta A$ of the three wafers. Using Eq. (7.4) and taking the

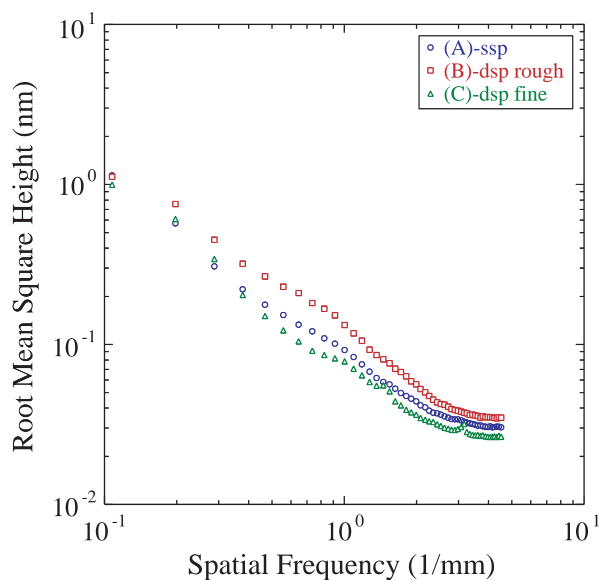

Figure 7-8: The root-mean square roughness across a frequency band 0.09 mm^{-1} plotted against the mean frequency in the band.

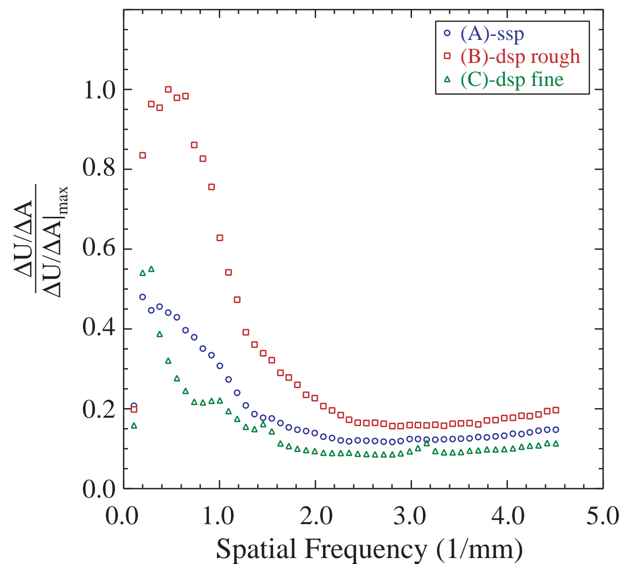

Figure 7-9: The normalized $\Delta U/\Delta A$ of the three surfaces considered.

thickness and elastic properties as h_1=h_2=675 μm, E_1=E_2=148 GPa, ν_1=ν_2=0.18, the $\Delta U/\Delta A$ for each point in Fig. 7-8 was calculated and normalized by the maximum value of $\Delta U/\Delta A$ observed across the three wafers. Figure 7-9 shows the results of this calculation and may be used to assess the relative bonding difficulty of the three wafers examined in this work.

The results in Fig. 7-9 show that wafer (B) has the highest $\Delta U/\Delta A$ and thus has the nanotopography that is the least desirable in terms of bonding. As was discussed previously, this conclusion could have also been made by inspecting the PSD's (Fig. 7-7) alone. The additional information that Fig. 7-9 provides is that it quantifies the difference in bonding difficulty. The difference in topography between wafer (B) and wafers (A) and (C) results in the $\Delta U/\Delta A$ of wafer (B) being more than twice that of the other wafers at low spatial frequencies. The plot also helps to elucidate the difference in terms of bonding between wafers (A) and (C), which was not clear from the PSD's shown in Fig. 7-7. Fig. 7-9 clearly shows that wafer (C) has superior topography to that of (A) in terms on bonding as the $\Delta U/\Delta A$ is lower.

The analysis to this point has allowed the three wafers to be compared to one another in terms of their topographies and the relative values of their $\Delta U/\Delta A$'s. It has not, however, permitted the importance of nanotopography to be assessed in relation to other flatness variations or typical values of work of adhesion. In order to do this, the $\Delta U/\Delta A$ of the surfaces must be calculated. This is not a trivial task, given that the model is for a sinusoidally varying surface with a single wavelength and the real surfaces have surface height variations at multiple wavelengths. An approach was

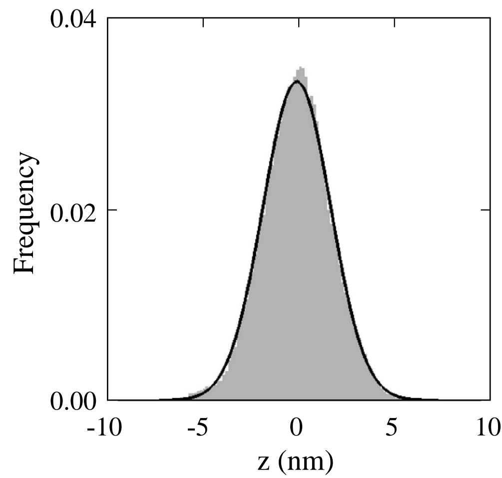

Figure 7-10: The distribution of surface heights on wafer (B) with a normal distribution fitted for reference.

considered in which the real surfaces could be represented as a summation of sinusoidal components using Fourier decomposition and then the $\Delta U/\Delta A$ could be calculated by linear superposition of the required displacements in the model as suggested in [54]. While this approach is reasonable, problems arise when attempting to implement it, as each term in the Fourier decomposition not only has a specific amplitude associated with it, but a phase as well. Accommodating the phase information in the superposition scheme is not straightforward and makes employing this approach difficult. As a result, an alternative approach in which the strain energy for a reference sinusoidal surface, which has an amplitude and wavelength similar to that of the actual surface, was used to obtain an estimate of the strain energy per unit area required to bond wafers with nanotopography.

The goal of the reference surface analysis was to establish an upper bound on $\Delta U/\Delta A$ for the nanotopography features observed. To accomplish this, wafer (B), which has the least desirable topography in terms of bonding, was used to determine the reference surface geometry. To ensure that the full spatial wavelength range was examined, reference surfaces were created from the data on wafer (B) that was processed with filters at three different cutoff wavelengths - λ_C= 1, 5, and 10 mm. This was done to ensure that small wavelength variations, which may present more of a problem for bonding than those with a higher amplitude and longer wavelength, were not ignored. The wavelengths for the reference surfaces were estimated by examining the nanotopography maps and measuring the distance between peaks on the surface. It was determined that a conservative estimate (i.e. a shorter wavelength that results in a higher $\Delta U/\Delta A$) of the dominant wavelength on the surface was approximately $0.75\lambda_C$. To estimate the amplitude of the reference surface, the distribution of height values, which fit a normal distribution well (Fig. 7-10), was considered. The mean of the surface was set to zero during the data reduction process through the application of an offset, thus the standard deviation provides a measure of the amplitude of the height variations on

Table 7.2: Properties of reference surfaces and corresponding $\Delta U/\Delta A$.

λ_C (mm)	σ (nm)	P=7.0σ (nm)	λ_R (mm)	$\Delta U/\Delta A$ (mJ/m^2)
10	1.8	12.6	7.50	0.07
5	1.0	7.0	3.75	0.22
1	0.3	2.1	0.75	0.25

the surface. The standard deviations, σ, of the height values for wafer (B) calculated from data sets filtered at the three different cutoff wavelengths are listed in Table 7.2. The peak to valley height, P, of the reference surface was set to 7σ, as 99.96% of the height values are expected to fall within $+/-3.5\sigma$. As a comparison, the reference surface determined from the data filtered with a 10 mm cutoff is shown with measurements from the three wafers in Fig. 7-11. The $\Delta U/\Delta A$ values were calculated for the reference surfaces using Eq. (7.4) (taking the thickness and elastic properties of standard 150 mm silicon wafers, h_1=h_2=675 μm, E_1=E_2=148 GPa, ν_1=ν_2=0.18). The amplitude and wavelengths of the three reference surfaces as well as the strain energies per unit area required to bond them are summarized in Table 7.2.

The $\Delta U/\Delta A$ values for the three reference surfaces listed in Table 7.2 are relatively small compared to typical values of work of adhesion. For example, in the experiments in Chapter 6, the effective work of adhesion values that were measured were 35-40 mJ/m^2 - considerably larger than the $\Delta U/\Delta A$ calculated for nanotopography here. These results suggest that nanotopography played a relatively small role in the bonding experiments performed in Chapter 6. If the effective work of adhesion is significantly lower (i.e. hydrophobic bonding or rough surfaces) or the nanotopography height variations are larger (i.e. materials with polishing processes that are less developed than those for silicon) nanotopography may be an important role in direct bonding.

The $\Delta U/\Delta A$ values given in Table 7.2 are clearly estimates, though it is believed that the reference surfaces were chosen conservatively such that the values provide an upper bound on the nanotopography effect in bonding. Given this and the comparisons outlined above, it appears that nanotopography will play a role in direct bonding, but in the common case of hydrophilic direct bonding of prime grade silicon wafers, such as those measured here, the effect will be minor. For processes with a low effective work of adhesion, such as hydrophobic bonding or when surfaces have a high roughness, it may be necessary to take specific steps to control and monitor nanotopography. However, if polishing processes that yield surfaces similar to those used to manufacture prime grade silicon wafers can be used to manufacture the wafers to be bonded, nanotopography should not be a significant concern.

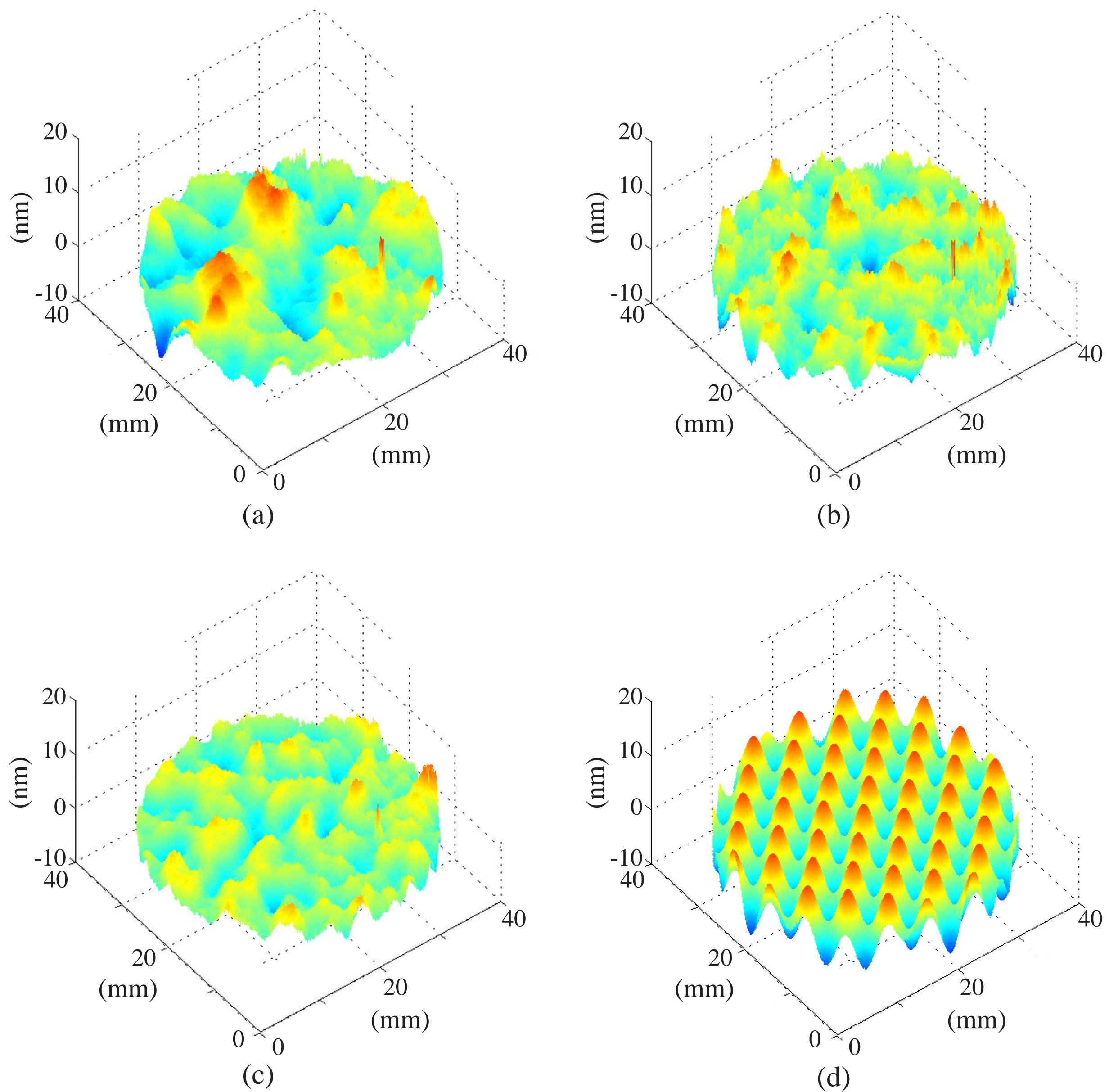

Figure 7-11: Comparison between the measurements from the wafers (a) - wafer (A), (b) - wafer (B), (c) - wafer (C); and (d) - the reference surface.

7.5 Summary

The effect of wafer nanotopography with spatial wavelengths from $\approx 0.2-10$ mm in direct bonding has been investigated. A model that can be used to predict the strain energy required to bond wafers with nanotopography height variations on the surface was reviewed and used to develop bonding maps. It was concluded from the maps that at wavelengths of 1 and 10 mm, height variations of 5 and 90 nm are required for nanotopography to have an influence in direct bonding. Silicon wafers, manufactured under three different polishing conditions that resulted in different nanotopographies, were measured. The height variations observed were relatively small - less than 20 nm from peak to valley across wavelengths of 10 mm. Spectral analysis was performed on the surfaces and coupled to the elasticity model which allowed the relative bondability of the three wafers to be assessed. Finally, an upper bound on $\Delta U/\Delta A$ was estimated based on the measurements from the wafers. The estimate suggests that in this case the contribution of nanotopography to the overall strain energy required to bond two wafers is relatively small.

While the nanotopography of the wafers measured in these experiments was determined to have a small effect on bonding, this may not be true for the nanotopography of wafers manufactured using other polishing processes. When developing polishing processes for wafers that will be bonded it is important to ensure that the nanotopography will not significantly affect the bondability, as observed here. The work reported in this chapter provides an example of how this may be done. The measurement and analysis techniques described are general and provide a route for characterizing nanotopography and relating the measurements to bondability.

Chapter 8

Double Cantilever Specimen

A key part of wafer bonding process development is the characterization of the mechanical integrity of the bond. The interfacial toughness is a key characteristic of the bond and is an input to process models such as that for clamping described in Chapter 5. The interface toughness is commonly measured using a wafer bonded double cantilever specimen. While the test is easy to perform, there are questions with regard to the accuracy of the method because of the fact that the test is typically performed on whole wafer pairs. The numerical modeling techniques developed in Chapter 4 are particularly well suited to examining the effect of this factor on the accuracy of the specimen. In this chapter, the mechanics of the wafer bonded double cantilever are investigated and recommendations for improving accuracy in these tests is provided.

The mechanics of the specimen are first reviewed and the traditional expressions used for data reduction are derived. Next, the effect of the circular wafer geometry on the accuracy of the traditional beam theory based expression used to calculate the interface toughness from the crack length is examined through finite element analysis. The finite element analysis is used to predict the shape of the crack front and to extract a relationship for the interface toughness as a function of crack length for whole wafer specimens. Finally, the finite element results are compared to experiments to validate the modeling approach employed.

8.1 Background

Numerous techniques have been employed for the task of characterizing the mechanical integrity of the bond, including pressure [24] and tensile tests [101] that yield a fractures stress, as well as fracture mechanics-based specimens that provide a measure of the interface toughness or surface energy. Fracture mechanics-based specimens that have been used include double cantilever [102], chevron-notch [103], and four-point bend specimens [104]. The chevron-notch and four point bend specimens have clear advantages in terms of testing and accuracy, but specimen preparation can

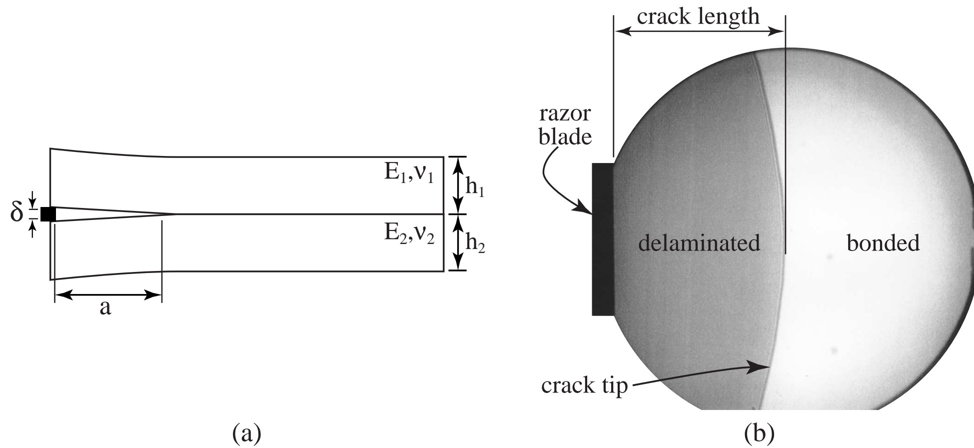

Figure 8-1: Overview of blade insertion test. (a) Cross-section of specimen. (b) Infrared transmission image of test.

be time consuming and particularly difficult for weakly bonded pairs. As a result, the double cantilever geometry or the 'crack opening method', which was initially introduced to the wafer bonding community by Maszara et al. [102], has become the most common method for evaluating the integrity of wafer bonds. The basic test, shown in Fig. 8-1, is conducted by inserting a thin blade of known thickness at the interface of a bonded pair and measuring the length of the resulting crack. The interface toughness or surface energy is related to the measured crack length through an expression that is a function of the blade thickness and the thicknesses and elastic properties of the wafers.

While the method has seen widespread use due to its simple implementation, there have been persistent questions with regard to its accuracy. The issues pertaining to the method that have been discussed previously may be grouped into two categories: 1) environmental effects and 2) specimen mechanics and geometry concerns. The previous work that addresses the environmental effects has examined the role of humidity and time on the measured interface toughness values [6, 105]. While these effects have been discussed in the wafer bonding literature as artifacts of the specimen, they are truly a result of the fact that the interface toughness, which may be thought of as a material property, is a function of these factors. As such, these effects will be observed regardless of the specimen and while they must be addressed when conducting tests using the double cantilever geometry they should not be viewed as problems specific to the specimen. The second set of concerns, and the one that is the focus of the current work, is associated with the mechanics of the specimen.

Maszara et al. [102] adopted the double cantilever specimen concept and the expression that is commonly used for data reduction from Gillis and Gillman [106]. The analysis presented in [106] that was employed by Maszara et al. was derived for the case where the two layers of the

double cantilever deform under the assumptions of beam theory (*layer width and thickness << crack length*). However, when the test is conducted on whole wafer bonded pairs, as has become standard practice, the arms of the double cantilever are not beams, as the crack length is typically comparable to the width of the specimen, Fig. 8-1(b). Bagdahn et al. [107] examined the effect of conducting the test on whole wafer pairs. They concluded that if the beam theory based expression for data reduction given by [102] is used to calculate interface toughness values from tests on whole wafer pairs, the non-beam like geometry may lead to errors of 10-30%. As a result, they recommended that the test should either be conducted on thin beam-like strips diced from whole wafer pairs or finite element analysis should be used to extract interface toughness values from tests conducted on whole wafer pairs. Despite these recommendations, researchers have continued routinely to conduct the test on whole wafer pairs and use the beam theory based expression for data reduction. While this is presumably because of the time and difficulty associated with dicing weakly bonded wafers or developing finite element models for data reduction, it is clearly not a good practice. In this work, the specimen is examined using finite element analysis and an improved expression for data reduction is given that allows accurate interface toughness values to be easily extracted from tests conducted on whole wafer pairs.

8.2 Specimen Mechanics

The basic geometry of the specimen is shown in Fig. 8-1(a). The specimen consists of two bonded layers with thickness, h_1,h_2, elastic properties, E_1,ν_1, E_2,ν_2, and a blade of thickness δ inserted at the interface that results in a crack of length a at the interface. A fracture mechanics framework, in which the crack driving force is expressed as the strain energy release rate, G, [108] is the most straightforward method to analyze the specimen and will be used throughout this work. The strain energy release rate is a function of the geometry and loading and is compared to the interface toughness, Γ to determine the equilibrium crack length. The crack is at stable equilibrium when $G = \Gamma$ and $dG/da < 0$. The term interface toughness that is used to describe the resistance of the interface to delamination is consistent with the surface energy, γ, term that is more commonly used in the wafer bonding literature, $\Gamma = 2\gamma$.

The strain energy release rate for the specimen may be determined from the moment per unit width acting on each layer at the crack tip, M, using the framework provided in [78]. If it is assumed that the two layers are beams ($h << a$, $width << a$), the moment at the crack tip for the double cantilever geometry shown in Fig. 8-1(b) may be expressed as,

$$M_{DCB} = \frac{1}{4}\frac{\bar{E}_1 h_1^3}{(1+\Sigma\eta^3)}\frac{\delta}{a^2}, \tag{8.1}$$

where $\bar{E}$ is the plane strain modulus, $\bar{E} = E/(1-\nu^2)$ and η and Σ are the thickness and modulus ratios, respectively, $\eta = h_1/h_2$, $\Sigma = \bar{E}_1/\bar{E}_2$. The strain energy release rate for the current case, where the two moments that act on each layer are equal and opposite, is [78],

$$G = \frac{6M^2}{\bar{E}_1 h_1^3}(1+\Sigma\eta^3). \tag{8.2}$$

Substitution of Eq. (8.1) into the above yields,

$$G_{DCB} = \frac{3}{8}\frac{\bar{E}_1 h_1^3}{(1+\Sigma\eta^3)}\frac{\delta^2}{a^4}. \tag{8.3}$$

This equation gives the strain energy release rate as a function of the loading, specimen geometry and crack length and may be used to determine the interface toughness from a test by recognizing that $G = \Gamma$ when the crack is at equilibrium. Assuming that the crack remains at the interface, crack propagation is stable for all crack lengths as $dG/da < 0$ for all a. The expression given in Eq. (8.3) agrees with that given by [102] for the case of $\Sigma = 1$, $\eta = 1$ and other data reduction expressions in the wafer bonding literature for the general case where $\Sigma \neq 1$ and $\eta \neq 1$ [6].

A point that is important, but is neglected in the wafer bonding literature, is that the loading at the interface in mixed-mode when $\Sigma \neq 1$ or $\eta \neq 1$. When the wafers have equal thicknesses and moduli, the loading at the interface is a pure mode I (opening). However, when the layers have different thicknesses or moduli, there is a mode II (sliding) component as well. The mode I and mode II components of the specimen may be determined from the moment per unit width given in Eq. (8.1) using expressions in [78]. The ratio of mode I and mode II loading at the interface is typically expressed as the phase angle, $\Psi = \tan^{-1}(K_{II}/K_I)$, where K_I and K_{II} are mode I and mode II stress intensity factors and are related to the strain energy release rate via, $G_I = K_I^2/\bar{E}$ and $G_{II} = K_{II}^2/\bar{E}$. The mode I and mode II components of strain energy release rate may be summed to give the total energy release rate, $G = G_I + G_{II}$, which is given by Eq. (8.3). The phase angle and the mode I and mode II strain energy release rates are plotted as a function of thickness ratio in Fig. 8-2 for the double cantilever beam.

The fact that the specimen is mixed-mode when the moduli or thicknesses of the layers are not equal is important as interface toughness may be a function of the phase angle. The dependence of interface toughness on phase angle is currently not fully understood and in general it is assumed that the relationship must be determined experimentally [78]. Given that the dependence on phase angle is often attributed to contact of asperities on the crack faces and plasticity it is not clear if there will be a dependence in wafer bonded specimens, which are typically elastic with smooth interfaces. However, there have been no systematic studies examining the effect of mixed-mode loading on wafer bond toughness and as such care should be taken when comparing toughness

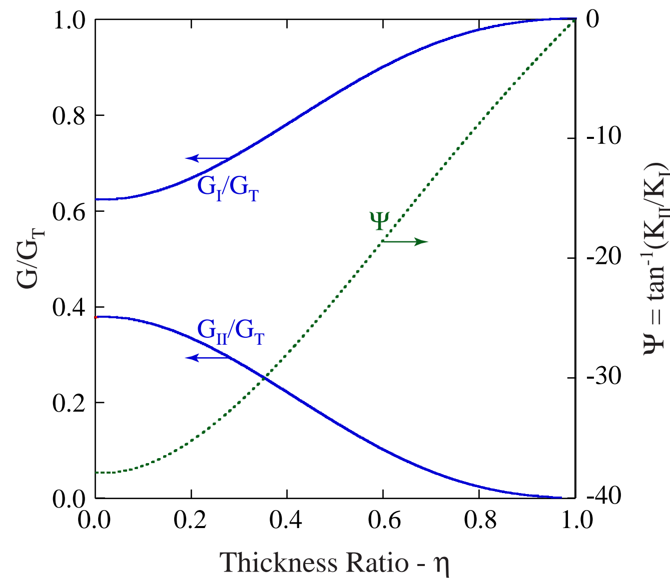

Figure 8-2: Mixed mode properties of double cantilever specimen as a function of the thickness ratio of the layers. The left hand axis shows the ratio of the mode I and II strain energy release rates to the total energy release rate. The right hand axis shows the phase angle.

values obtained from tests performed on specimens with different phase angles. In addition to this concern, mixed-mode loading may also lead to testing difficulties as crack deflection from the interface may occur. Under mixed-mode conditions the crack will only remain at the interface if the toughness of the interface is sufficiently less than that of the bulk material. The ratio of interface to bulk toughness at which crack deflection will occur may be predicted by assessing the strain energy release rate in the competing directions of crack advance [78, 109]. At high values of interface toughness and mixed-mode loading the crack will deflect from the interface resulting in fracture of the specimen and only allow a lower bound on bond toughness to be determined from the test.

8.3 Finite Element Model

Perhaps the most significant concern when employing the double cantilever geometry for evaluating bond toughness is the common practice of conducting the test on whole wafer pairs rather than dicing thin strips from the wafer to yield a specimen with a true beam geometry. This full wafer geometry results in a curved crack front as is observed in Fig. 8-1(b) and may lead to inaccurate toughness values being calculated from Eq. (8.3), which is based on beam theory. In this section, a three dimensional finite element model is used to predict the shape of the bond front as a function of crack length and to assess the accuracy of Eq. (8.3) for data reduction in tests performed on

whole wafer pairs.

The mesh and geometry of the wafer pair used in the finite element analysis are shown in Fig. 8-3. The test case investigated was a wafer pair comprised of two equal thickness 100 mm diameter silicon wafers, a common geometry used in wafer bonding process development work. The in-plane wafer geometry was based on that of a standard (100) 100 mm n-type wafer as specified in SEMI M1 [40]. The wafers have a 100 mm diameter and a major flat (32.5 mm long) and minor flat (18 mm long) oriented 180° from one another and aligned along the [110] direction. Single crystal silicon is elastic with cubic symmetry, the stiffness coefficients are, C_{11}=165.7 GPa, C_{12}=63.9 GPa, C_{44}=79.6 GPa [72]. Symmetry was employed such that only one half of one wafer in the pair was modeled. Appropriate boundary conditions were applied on all symmetry planes. A fixed displacement was applied in the z-dir along the line of nodes a distance $a_\circ$ from the minor flat to represent the blade loading. The crack length, a, is defined as the distance between the point where the displacement is applied and the center of the crack front. The model was meshed primarily with 20 node solid elements in the arrangement shown in Fig. 8-3. This mesh was used throughout the study and consisted of 21 elements across the crack front and 2 through the thickness of the wafer. The mesh was refined around the crack tip such that there were 16 elements across a 2.0 mm wide region perpendicular to the crack front. The mesh outside of the crack front region was adjusted as a function of the crack position to maintain approximately the same mesh density and element aspect ratio as that shown in Fig. 8-3.

The virtual crack closure technique (VCCT) was used to calculate the strain energy release rate locally along the crack front from the reaction forces and the displacements near the crack tip obtained from the finite element model. The expressions used for calculating G via the VCCT for 20-node solid elements can be found in [74]. The VCCT was employed as it allows accurate calculation of strain energy release rate values without significant mesh refinement at the crack tip. Convergence studies were used to select the mesh density shown in Fig. 8-3 to ensure accurate calculation of G.

The model was initially constructed with a straight crack front that was parallel to the line of prescribed displacements that represent the loading applied by the blade. Figure 8-4 shows the variation in G along a straight crack front at various crack lengths. The results show that at short crack lengths, the strain energy release rate has a maximum at the center and drops off quickly near the edge. At longer crack lengths, the opposite is true, there is a low strain energy release rate near the center and a higher value at the edge. This variation in energy release rate along the crack front is primarily due to the circular geometry of the wafer and suggests that the crack front will not be straight, as at equilibrium $G = \Gamma$ along the entire crack front. The variation in G shown in Fig. 8-4 suggests that the crack will have a negative curvature at short crack lengths and a positive curvature at longer crack lengths. This is consistent with what is routinely observed

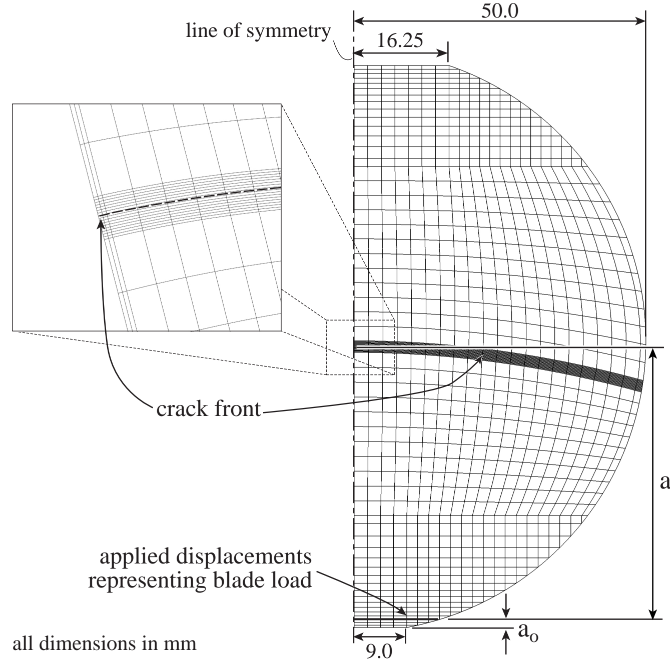

Figure 8-3: Geometry of wafer and finite element mesh.

in experiments and that shown in Fig. 8-1. These results, while providing an estimate of variation in G along the crack, do not allow the accuracy of Eq. (8.3) to be quantified as the G values are computed along a non-equilibrium front.

To address the issue of the applicability of Eq. (8.3) to whole wafer pairs, the strain energy release rate for a crack in equilibrium must be calculated. The difficulty in doing this is that the shape of the equilibrium crack is not known *a priori*. As such, the equilibrium crack shape and position must be determined through an iterative procedure in which the geometry that yields $G = \Gamma$ along the entire crack is found. The approach used in this work to accomplish this is similar to that used described in Chapter 4 and was adapted from [75].

The mesh shown in Fig. 8-3 was developed such that the position of the nodes along the crack front were specified solely by their y position (their x position is defined by their y position). In general, the strain energy release rate at each node along the crack depends on the position of all the nodes along the crack. Thus, the strain energy release rate at any node may be taken to be a non-linear function of the positions of all the nodes along the crack,

$$G_i = f(y_1, y_2, ...y_n), \tag{8.4}$$

where i is the node number and n is the total number of nodes along the crack. The equilibrium

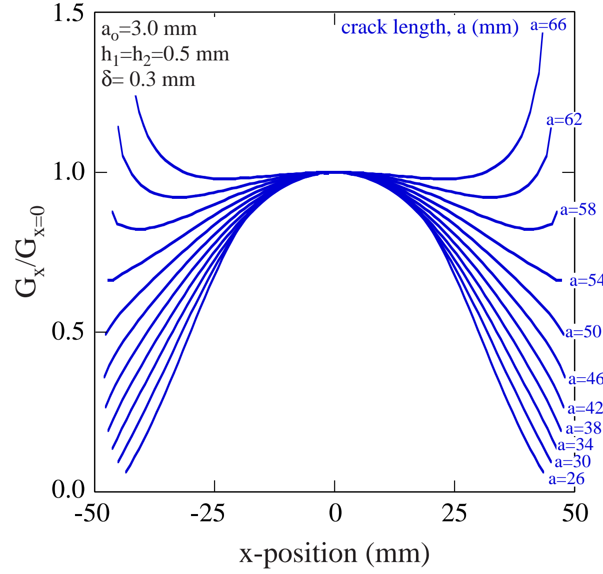

Figure 8-4: Variation in strain energy release rate across a straight crack for a range of crack lengths.

condition, $G_i = \Gamma$ for all i, is expressed as,

$$\mathbf{F} \equiv \begin{bmatrix} G_1(y_1, ..., y_n)/\Gamma - 1 \\ \vdots \\ G_n(y_1, ..., y_n)/\Gamma - 1 \end{bmatrix} = \begin{bmatrix} 0 \\ \vdots \\ 0 \end{bmatrix}. \tag{8.5}$$

The functions $G_1 ... G_n$ can be evaluated via a single finite element analysis for a given crack position, $\mathbf{Y}$, ($\mathbf{Y} = [y_1 ... y_n]^T$). The vector $\mathbf{Y}$ that satisfies Eq. (8.5) is determined using a quasi-Newton method, in which the position of the crack front is updated after each iteration according to,

$$\mathbf{Y}^{k+1} = \mathbf{Y}^k - (\mathbf{B}^k)^{-1}\mathbf{F}^k, \tag{8.6}$$

where k indicates the iteration number. An approximate Jacobian, $\mathbf{B}$, as was employed in [75], was used and updated after each iteration using the rank one Broyden update formula,

$$\mathbf{B}^{k+1} = \mathbf{B}^k + \frac{(\mathbf{dF}^k - \mathbf{B}^k\mathbf{dY}^k)(\mathbf{dY}^T)^k}{(\mathbf{dY}^T)^k(\mathbf{dY})^k} \tag{8.7}$$

where,

$$\begin{aligned} \mathbf{dY}^k &= \mathbf{Y}^{k+1} - \mathbf{Y}^k \\ \mathbf{dF}^k &= \mathbf{F}^{k+1} - \mathbf{F}^k \end{aligned} . \tag{8.8}$$

The magnitude of the shift calculated by Eq. (8.6) was checked after each iteration to ensure that it

would not result in significant mesh distortion. If any of the shifts along the crack exceeded a specified value, y_{lim}, the shifts at all the nodes along the front were scaled by a factor $\left(\frac{y_{lim}}{\max(\mathbf{Y}^{k+1}-\mathbf{Y}^{k})}\right)$, such that the relative shifts along the front were maintained and the maximum shift was equal to y_{lim}. A value of y_{lim} of 0.1 mm was found to work well for the current mesh. The shape of the crack was iterated using the above approach until the G values at all the nodes along the crack were within 1 % of the specified Γ.

The commercial finite element package ABAQUS™ was used in conjunction with a MATLAB™ script that was written to generate the mesh and post process the data. The mesh was generated in MATLAB™ based on a vector specifying the crack position, $\mathbf{Y}$, and exported to ABAQUS™. The model was solved in ABAQUS™, the reaction forces and displacements were exported to MATLAB™, and the strain energy release rate values were calculated in MATLAB™ using the VCCT. If the convergence criterion was not satisfied, a new crack front position was calculated using Eq. (8.6) and the process was repeated. The MATLAB™ scripts for this analysis are given in Appendix C.3.

8.4 Results and Discussion

The model was employed to examine the variation of crack shape as a function of length by solving the model for a range of specified Γ values. Figure 8-5 shows predicted crack fronts for a range of values of interface toughness in a bonded pair consisting of two silicon wafers ($h_1 = h_2 = 0.5$ mm), with a blade of thickness $\delta = 0.3$ mm inserted $a_o = 3.5$ mm in from the flat. As expected from the analysis with the straight crack, the crack has a negative curvature at short crack lengths, flattens out, and then adopts a positive curvature at long crack lengths. The shape of the crack front is primarily a result of the circular shape of the wafers and is affected only slightly by the silicon anisotropy. To assess the role of the elastic anisotropy, crack fronts were predicted for a pair with the same loading and geometry with isotropic elastic properties (E=148 GPa, ν=0.18 - the in-plane averages for a (100) silicon wafer). From Fig. 8-6 it is seen that the crack shapes are not significantly different from the anisotropic case and follow a similar trend in which the curvature of the front is largest at short crack lengths. The crack fronts predicted in the isotropic case have slightly shorter crack lengths than those predicted for the anisotropic case at the same values of interface toughness. This occurs because the stiffness in the direction perpendicular to the crack front, which is the dominant bending axis, is less in the isotropic case than it is in the anisotropic case examined ($\bar{E}_{isotropic} = 153$ GPa, $\bar{E}_{[110]} = 170$ GPa).

To assess the accuracy of Eq. (8.3), the strain energy release rate as a function of crack length for whole wafer pairs was evaluated for a range of different cases. The percent difference between the strain energy release rate calculated from the beam theory solution, Eq. (8.3), and the finite

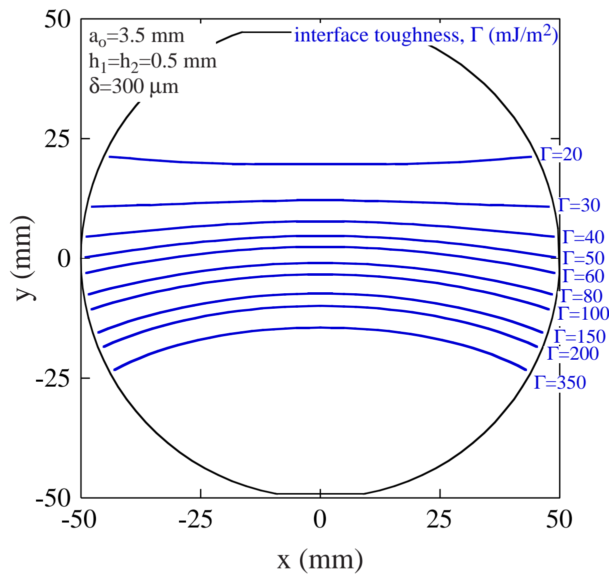

Figure 8-5: Predicted crack shapes as a function of interface toughness for a (100) bonded silicon wafer pair.

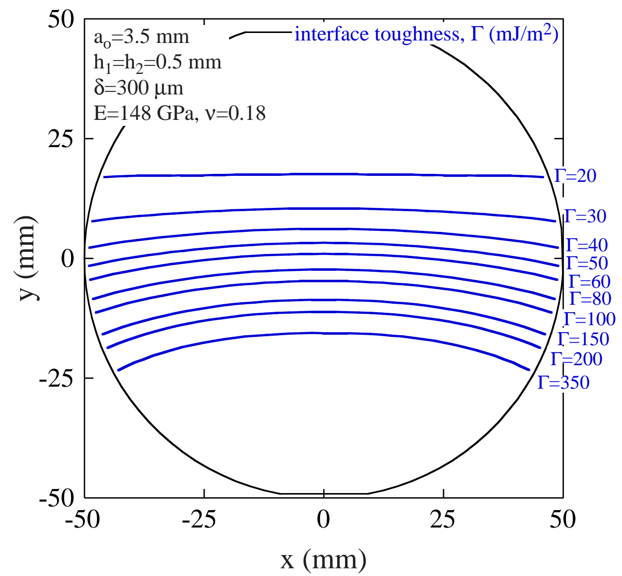

Figure 8-6: Predicted crack shapes as a function of interface toughness for a isotropic bonded pair with elastic properties, E=148 GPa, ν=0.18

element solution for various blade insertion lengths as a function of crack length is plotted in Fig. 8-7. In the beam theory solution, a plane strain modulus of $\bar{E}_{[110]} = 169.6$ GPa was used as this is the effective modulus in the direction of bending in a test performed on (100) wafers with the blade inserted at the flat. The first point of interest in Fig. 8-7 is that the error in the strain energy release rate changes with blade insertion length - a $\approx$ 5% difference is observed between an insertion length of 2.0 and 3.5 mm. This suggests that the insertion length affects the correct calculation of G and indicates that if values between tests are to be compared it is critical that the insertion length be kept constant. The second important point that is demonstrated in Fig. 8-7 is that the percent difference in G between the beam theory and the finite element solutions varies as a function of crack length. This suggests that the $1/a^4$ dependence of G predicted by beam theory is not valid when the test is conducted on whole wafer pairs.

An improved expression for data reduction that relates G to the crack length for 100 mm (100) silicon wafers was developed from the results of 135 finite element simulations in which the thickness of the wafers and blade were systematically varied from 0.4-0.7 mm and 0.1-0.5 mm, respectively, over crack lengths from 25 to 75 mm. For each simulation, the equilibrium crack shape and position were calculated for a specified Γ and the crack length, a, as defined in Fig. 8-3, was determined from the final position of the crack front. The results of these simulations are summarized in Fig. 8-8. The scaling with the wafer and blade thickness predicted by Eq. (8.3) was observed to hold across the range investigated, as all the simulation results collapsed to single curve when

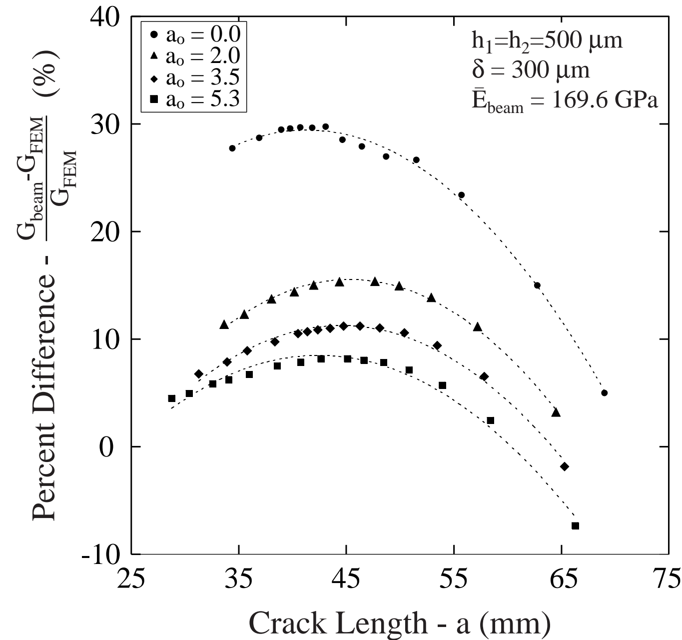

Figure 8-7: Percent difference between the strain energy release rate calculated via the finite element model and beam theory for four different blade insertion lengths.

normalized by $1/\delta^2 h^3$ as shown in Fig. 8-8. The beam theory solution, when plotted versus a using the normalization in Fig. 8-8 corresponds to a straight line of slope $(3/16)^{-1/4}$ and is shown in the figure for comparison. It is seen that the beam theory and finite element solutions agree well at points, but deviate at others. A second order polynomial fit through the finite element data was calculated and is shown in Fig. 8-8. The difference between the beam theory and the finite element data appears small, however this is deceiving and is a result of the normalization used. The difference in G values predicted by the two methods as a function of crack length is actually significant in certain situations. The dashed curve, which corresponds to the axis on the right, shows the percent difference between the beam theory solution and the fit to the finite element data. At a crack length of ≈45 mm the beam theory overpredicts the interface toughness by 15%, while at long crack lengths (≈75 mm) the beam theory underpredicts the interface toughness by as much as 10%. This implies that when comparing interface toughness values that are calculated using Eq. (8.3) errors up to 25% are possible over the range of crack lengths examined. At crack lengths that are shorter or longer than those examined here, the errors are expected to be larger.

The results clearly suggest that for accurate data reduction on tests conducted on whole wafer pairs, Eq. (8.3) should not be used. For (100) 100 mm pairs, in which the blade is inserted in 3.5 mm at the minor flat and the crack length is between 25 and 75 mm, the second order fit to

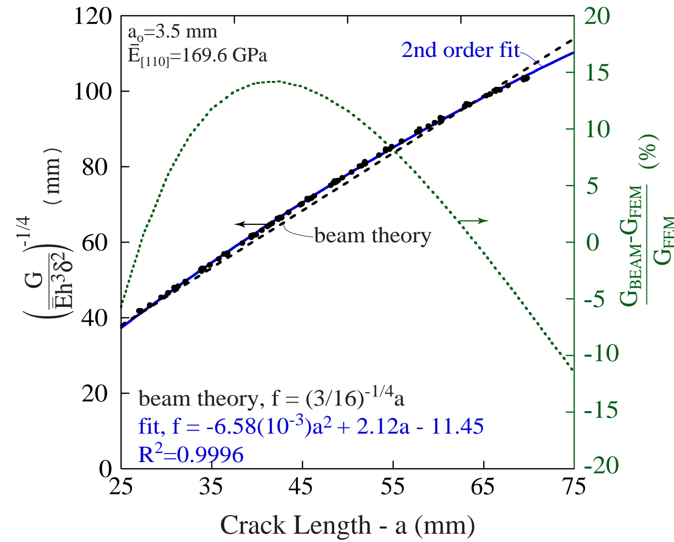

Figure 8-8: Strain energy release rate as a function of crack length determined from 135 finite element simulations compared to the traditional beam theory result.

the finite element solution given in Fig. 8-8 may be used for improved data reduction,

$$G_{FEM} = \bar{E}h^3\delta^2[-6.58(10^{-3})a^2 + 2.12a - 11.45]^{-4}. \quad (8.9)$$

It is critical that this fit only be used for specimen geometries and crack lengths in the specified range as there is no expectation that it should be valid outside of this range.

8.5 Experimental Validation

Experiments in which the predicted crack shapes were compared to actual crack shapes were performed to validate the finite element model used in this work. Specimens were fabricated by bonding 525 μm thick, (100), 100 mm silicon wafers at room temperature. In order to obtain different values of interface toughness, yielding different crack lengths, two different surface treatments were used prior to bonding. The wafers for one pair were cleaned using a standard ‘piranha’ clean (3:1 H_2SO_4:H_2O_2) resulting in a hydrophilic surface, while a hydrophobic HMDS (hexamethyldisilazane) coating was deposited on the wafers used in the second pair. A 240 μm thick blade was inserted at the interface and the resulting crack was imaged using an infrared transmission inspection system. Images of pairs recorded 2 min after insertion of the blade are shown in Fig. 8-9 along with the crack front shapes predicted by the finite element model. The predicted crack fronts shown in Fig. 8-9(a) and (b) correspond to interface toughness values of 133 and 25 mJ/m^2, respectively. The agreement between the experimental and predicted crack shapes is reasonable. The difference

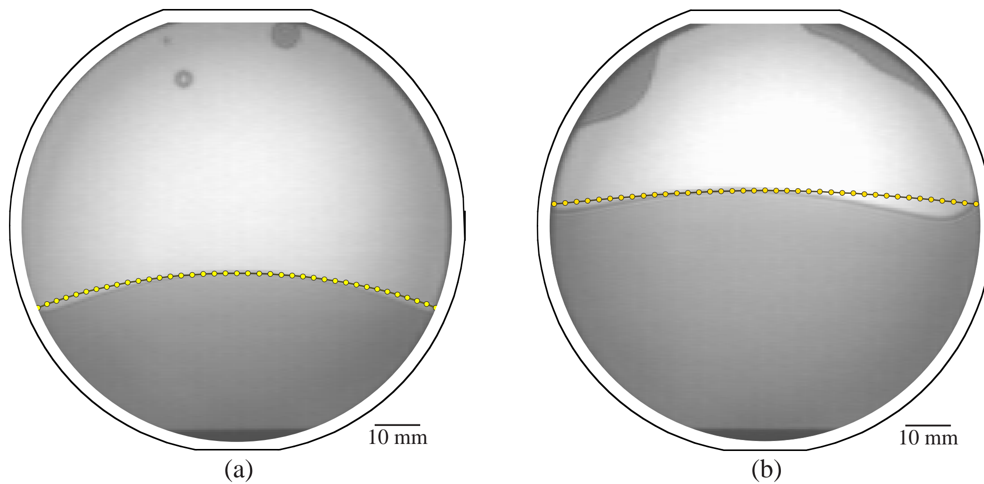

Figure 8-9: Comparison between the crack shape predicted via finite element analysis and experimental results for pairs with two different interface toughnesses. (a) Γ=135 mJ/m^2, (b) Γ=25 mJ/m^2

between the actual crack and predicted observed in (b) is believed to result from small wafer-scale shape variations as well non-uniformities in the hydrophobic coating that lead to a spatially varying work of adhesion. The shape of the wafers was measured prior to bonding to ensure the bow on the wafers was less than 10 μm, however small amplitude variations were present. In pair (b) the interface toughness is rather low and as such flatness variations would be expected to affect the shape of the crack more than in specimens with higher values of interface toughness. Overall, the agreement is good and suggests that the modeling approach employed accurately captures the relevant mechanics.

8.6 Summary

The mechanics of the wafer bonded double cantilever specimen have been investigated to assess accuracy of interface toughness values measured using the specimen. The effect of using a data reduction expression derived under the assumptions of beam theory [Eq. (8.3)] for a specimen in which the arms are whole wafers rather than beams was examined through finite element analysis. The finite element model permitted the shape of the crack to be predicted. The shape of the predicted cracks compared well with experiments suggesting that the modeling method used was effective. The finite element model was used to show that the expression that is commonly used in the data reduction during double cantilever tests conducted on whole wafer pairs may overpredict the interface toughness by 15% at crack lengths of 40 mm and underpredict the toughness by 10% at crack lengths of 75 mm in 100 mm diameter silicon pairs. A large number of finite element simulations were performed to determine an expression for calculating accurate interface toughness

values from tests performed on (100) 100 mm silicon wafer pairs.

This work clearly shows that the wafer bonded double cantilever specimen is prone to errors. Other techniques for evaluating interface toughness, such as the chevron-notch specimen [103], have been demonstrated to be effective and should be seriously considered when characterizing high-toughness bonds. The double cantilever specimen, while not ideal, has found widespread use and remains a straightforward and effective method for evaluating weak interfaces where the preparation of other specimens would be difficult. However, if the specimen is employed the factors discussed in this work should be considered.

Chapter 9

Conclusions and Recommendations

Mechanics-based models and experiments that demonstrate the connection between flatness variations, etch patterns, wafer mounting and bonding failure have been presented in this thesis. In this chapter, the various aspects of this work are summarized and discussed, key conclusions made, and recommendations for future work given. First, the thesis is summarized and general comments about the integration of the various parts of the work made. Then, the key conclusions that can be drawn from this work are identified and recommendations for future work itemized.

9.1 Summary and Discussion

The primary objective of this work was to develop quantitative models of the direct bonding process to enable more intelligent, process, device and tool design. In Chapter 2, a general framework and bonding criterion were introduced that related the strain energy that is accumulated in the wafers as they are bonded to the energy available to form the bond (work of adhesion). The criterion proposed examines bonding as a question of bond propagation and states the bond will advance if the change in strain energy per unit area of bond advance is less than the work of adhesion,

$$\frac{dU_E}{dA} < W. \tag{9.1}$$

In Chapters 3 and 4, analytical and numerical models were developed that apply the criterion given by Eq. (9.1) to assess the effect of wafer-scale shape variations and etch patterns. Analytical models for the bonding of wafers with axisymmetric curvature showed the basic scaling of bonding difficulty with wafer geometry and elastic properties. A finite element based model was developed and used to demonstrate the role that elastic anisotropy and asymmetric shape variations have in determining the shape of the bonded area. In Chapter 5, the analytical models developed in Chapter 3 were extended to show the effect of clamping in wafer bonding. The clamping models

demonstrated that the arrangement used to mount the wafers during the bonding process can be used to control the shape and residual stress state of the final bonded pair. The basic bonding criterion and the models that address the effect of wafer-scale shape variations and clamping in bonding were compared to experiments in Chapter 6. The model and experiments showed good agreement.

Chapter 7 examined the effect of mid-spatial wavelength surface height variations referred to as nanotopography. Measurements were performed on silicon wafers manufactured using three different polishing processes and the effect of the measured features on bonding was assessed through modeling. Comparing the surfaces and analyzing their bondability proved difficult as the measurements revealed that the surfaces had complicated topographies. Several different approaches were demonstrated for comparing the bondability of the surfaces and a method was proposed to estimate $\Delta U/\Delta A$ by defining a reference surface. While the calculations showed the nanotopography of the wafers used in this work would have little effect on bonding, the general measurement and analysis approach that was demonstrated can be used to assess wafer quality when developing manufacturing processes for wafers that will be bonded.

An analysis of the commonly used wafer bonded double cantilever specimen was presented in Chapter 8. The analysis examined the mechanics of the test and applied a variation of the numerical model introduced in Chapter 4 to develop an improved expression for reducing the data from the tests. While the modeling shared a common framework with other work in the thesis, the real motivation to examine the test was that the double cantilever is the method that is most frequently used to assess interface toughness of wafer bonds. Accurate values of interface toughness are essential in the development of bonding processes as it is a key input into models such as the clamping analysis presented in Chapter 5.

A point of confusion that exists in the wafer bonding literature and warrants further discussion here is the quantity that is actually measured in the blade insertion test and how it relates to the work of adhesion that is a key parameter in the models presented in this work. While the double cantilever test is a fracture test that provides a measure of the interface toughness, values obtained from the tests are often referred to as the work of adhesion or surface energy in the wafer bonding literature. In most cases, the values measured via the blade insertion test do not equal the work of adhesion. For pairs that have been annealed, it is obvious that the interface toughness should not be equated to the work of adhesion available to drive bonding, as during the fracture of annealed interfaces short-range primary bonds, which do not form when surfaces are contacted in atmospheric conditions at room temperature, are broken and contribute to the toughness. For pairs bonded at room temperature, the interface toughness measured via a fracture test and the work of adhesion responsible for driving the process might be expected to be equal given the same types of bonds are involved. The results in the literature and those presented here suggest that the

interface toughness of room temperature bonded pairs is not equal to the work of adhesion that drives the bonding process. Interface toughness values of hydrophilic room temperature bonded pairs reported in the wafer bonding literature range from $\Gamma = 100 - 200$ mJ/m^2 (also see Fig. 8-9, $\Gamma = 135$ mJ/m^2), while the work of adhesion values extracted from the bonding experiments reported in this work range from $W = 35 - 40$ mJ/m^2. The work of adhesion values obtained here are clearly lower than the interface toughness values commonly reported.

This difference in the work of adhesion and room temperature interface toughness values is not completely unexpected, as the energy associated with bond formation and disassociation are likely to be different. Hysteresis, such as this, is commonly observed in adhesion and fracture tests conducted in polymer systems [110]. In addition to the fundamental differences between adhesion and fracture, the systems from which the work of adhesion and interface toughness values are measured are clearly not completely equilibrated when the measurements are taken. This assertion is supported by the time dependence that is observed in the adhesion and fracture tests. The work of adhesion values measured in this work, were calculated from bond areas measured 10 min after bonding. While the bond front was not advancing fast at this point, the bonded area and hence the work of adhesion were certainly increasing with time. In fracture tests, the opposite behavior has been noted - after the insertion of the blade the crack is typically observed to increase in length with time meaning that the interface toughness decreases with time. If both specimens were held for a sufficiently long period of time in the same environment the difference between the interface toughness and work of adhesion values would likely decrease significantly. Unfortunately, no systematic experiments have yet been done to verify this, however the test geometry introduced in this work along with more traditional fracture specimens would permit such tests to be done. The chemistry of the interface and the mechanisms of the evolution with time are complicated and are not fully understood at the current time. Until this is understood better, it is essential that only work of adhesion values obtained from adhesion tests be used when evaluating whether or not wafers will bond with the models presented in this work.

The final topic which must be discussed is concerned with the factors that influence the work of adhesion and how the effects of the various flatness variations may be incorporated into a single framework. While it is clearly desirable to think of the work of adhesion as a material property that is only a function of the types and density of the bonds at the interface, the reality is that the values that are typically quoted also include information about smaller-scale flatness variations such as surface roughness and waviness. For example in determining the work of adhesion values in the experiments in this work, only wafer-scale shape variations were measured and accounted for, thus the work of adhesion values reported are truly effective quantities that represent information about the surface chemistry and smaller scale flatness variations. Similarly in the blade insertion test only the macroscale geometry is considered and thus the interface toughness values measured

are functions of small-scale geometry as well as surface chemistry. While this approach blurs the separation between the wafer geometry and the surface chemistry, the advantages of lumping small-scale geometry features into the work of adhesion are clear. The approach provides a practical way to incorporate the effects of the various flatness variations discussed in Chapter 2 into a single framework.

In particular, the approach of lumping small-scale flatness variations into the work of adhesion allows difficulties with accommodating flatness variations with length scales that span several orders of magnitude into a single model to be avoided. While it was easy to define a bond front when examining wafer scale shape variations, it was not clear how this would be for the case of nanotopography. As a result, the effect of nanotopography was expressed as a strain energy accumulated per unit area, $\Delta U/\Delta A$. This term can be viewed as an energy absorption term at the bond front and may be included in an effective work of adhesion. Similarly the effect of surface roughness can be included in the effective work of adhesion. With these considerations, the bonding criterion then appears as,

$$\frac{dU_E}{dA} < \bar{W}\left(W, \left.\frac{\Delta U}{\Delta A}\right|_{waviness}, roughness\right), \tag{9.2}$$

where the left hand side of the equation is the strain energy accumulation rate, which includes information about larger scale flatness variations and etch patterns, and the right hand side is an effective work of adhesion, $\bar{W}$, that is a function of the true work of adhesion, surface waviness, and roughness. This type of separation is analogous to the approach commonly used in interfacial fracture mechanics where the overall loading and geometry of the structure is related to the strain energy release rate which is compared to the interface toughness that is function of the strength and the micromechanics (i.e. mechanical interlocking, fiber pull-out etc.) of the interface. The key point that must be remembered though when including geometry effects in the work of adhesion is that the test specimen used to measure work of adhesion must incorporate the same geometric effects as are present in the situation in which the values will be used.

The integration scheme proposed above is one approach for integrating the various aspects of this work into a practical and consistent framework. As an improved understanding of the effect of smaller-scale flatness variations, surface chemistry, and methods to measure work of adhesion is developed alternative approaches for incorporating the models developed in this work with others will almost certainly emerge.

9.2 Conclusions

This thesis has made substantial contributions in the development of quantitative models for direct wafer bonding processes. The main achievements and conclusions of this work are:

- A general bonding criterion that allows the effect of flatness variations, etch patterns and work of adhesion in direct bonding processes to be modeled has been developed and experimentally validated.

- Analytical and numerical models that permit the effect of wafer-scale shape variations and etch patterns on direct bonding failure to be assessed have been developed. The analytical models provide first order estimates of bondability while the numerical model can be used to predicting bonding in specific cases. Comparison to experiments demonstrated that the models effectively capture the mechanics of the bonding process.

- Analytical models that demonstrate the effect of clamping and mounting on the residual stress and shape of the bonded pair have been developed. The results show that the mounting method is critical in determining the shape of the bond pair and that it is possible to design bonding tools to control the final shape of the bonded pair.

- The effect of nanotopography on bonding has been examined. A route for characterizing it and analyzing its effect on bonding has been demonstrated. The results show that for prime grade silicon wafers the effect of nanotopography on bonding is small, but suggest that small increases in nanotopography could result in bonding failures.

- The mechanics of the blade insertion test and validity of values extracted using it have been examined. A corrected expression for extracting interface toughness values from tests conducted on whole was wafer pairs was given to improve the accuracy of the test.

These achievements support the overall conclusion of the work that mechanics-based models can be used to assess the effects of different factors in direct bonding and provide guidance in process, device and tool design.

9.3 Recommendations for Future Work

The work that was performed in this thesis has demonstrated the applicability and effectiveness of mechanics-based models in predicting bonding failure. While this work has made significant advances, it has also highlighted several topics that require further work. These are itemized below:

- Development of improved techniques to measure the work of adhesion. The work of adhesion is a key input in the models and was extracted from the bond tests in this work. However, for further experimental validation, process development, and process control applications, a robust technique to measure work of adhesion is required.

- Improved understanding of the work of adhesion. It is known that the work of adhesion depends on surface chemistry as well as small-scale flatness variations, however the exact mechanisms that lead to the time and humidity dependence are not fully understood. A better understanding of the work of adhesion is essential for effective use of the models developed in this work.

- Improved numerical models for complex etch patterns. While the finite element model presented was effective in modeling the asymmetric shape variations and etch patterns in the experimental work, the technique becomes computationally expensive for wafers with a high density of small etch features that are common in actual mask layouts. Either improved modeling techniques or approaches that blend small features into larger effective features must be pursued to apply the modeling to real device layouts.

- Development of improved bonding tools. The current work demonstrated the importance of the interaction of the bonding tool and wafer pair and highlighted the ability to capitalize on this interaction to control the final shape of the wafer pair. The design of tools that allow these effects to be realized should be pursued.

9.4 Final Remarks

This thesis has shown that mechanics-based models can be used to improve the understanding of direct wafer bonding processes, indicate future directions for tool design, and provide a basis for setting tolerances on wafer geometry. The work has established a framework that will provide a basis for future work in understanding and modeling direct wafer bonding processes. It is believed that the general approach followed in this work of using mechanics models to improve process understanding has applications in a range of microfabrication processes beyond wafer bonding.

References

[1] G. K. Celler and S. Cristoloveanu. Fronteirs of silicon-on-insulator. *Journal of Applied Physics*, 93(9):4955–78, 2003.

[2] M. A. Schmidt. Wafer-to-wafer bonding for microstructure formation. *Proceedings of the IEEE*, 86(8):1575–1585, 1998.

[3] A. Plößl and G. Kräuter. Wafer direct bonding: Tailoring adhesion between brittle materials. *Materials Science and Engineering*, R25:1–88, 1999.

[4] G. Taraschi, A.J. Pitera, L.M. McGill, Z.-Y. Cheng, M.L. Lee, T.A Langdo, and E.A. Fitzgerald. Ultrathin strained Si-on-insulator and SiGe-on-insulator created using low temperature wafer bonding and metastable stop layers. *Journal of the Electrochemical Society*, 151:G47–G56, 2004.

[5] A. Mehra, A. Ayon, I.A. Waitz, and M.A. Schmidt. Microfabrication of high-temperature silicon devices using wafer bonding and deep reactive ion etching. *Journal of Microelectromechanical Systems*, 8:152, 1999.

[6] Q.-Y. Tong and U. Gosele. *Semiconductor wafer bonding : Science and technology*. Wiley, New York, 1999.

[7] G. Wallis and D.I. Pomerantz. Field assisted glass-metal sealing. *Journal of Applied Physics*, 40:3946–3949, 1969.

[8] A. Cozma and R. Puers. Characterization of the electrostatic bonding of silicon and pyrex glass. *Journal of Micromechanics and Microengineering*, 5:98–102, 1995.

[9] S. Weichel, Roger de Reus, and Michael Lindahl. Silicon-to-silicon wafer bonding using evaporated glass. *Sensors and Actuators*, A70:179–184, 1998.

[10] W.H. Ko. Packaging of microfabricated devices and systems. *Materials Chemistry and Physics*, 42:169–175, 1995.

[11] M.P. Helsel, J.D. Barger, D.W. Wine, and T.D. Orbson. Wafer scale packaging for a MEMS video scanner. In *Proceedings of SPIE - The International Society for Optical Engineering*, volume 4407, pages 214–220, 2001.

[12] R.F. Wolffenbuttel. Low-temperature intermediate Au-Si wafer bonding: Eutectic or silicide bonding. *Sensors and Actuators*, A62:680–686, 1997.

[13] G.S. Matijasevic, C.Y. Wang, and C.C. Lee. Void free bonding of large silicon dice using gold-tin alloys. *IEEE Transactions on Components, Hybrids, and Manufacturing Technology*, 13(4):1128–1134, 1990.

[14] C.H. Tsau, M.A. Schmidt, and S.M. Spearing. Fabrication of wafer-level thermocompression bonds. *Journal of Microelectromechanical Systems*, 11(6):641–647, 2002.

[15] W.P. Eaton and S.H. Risbud. Silicon wafer-to-wafer bonding at T<200°C with polymethylmethacrylate. *Applied Physics Letters*, 65(4):439–441, 1994.

[16] V.L. Spiering, J.W. Berenschot, M. Elwenspoek, and J.H.J. Fluitman. Sacrificial wafer bonding for planarization after very deep etching. *Journal of Microelectromechanical Systems*, 4(3):151–157, 1995.

[17] D. Lammers. Bonding twist takes chips 3-D. *Electronic Engineering Times*, page 1, November 4 2002.

[18] R. Khanna and N. Miki. MIT Microengine Program - personal communication, August 2002.

[19] K.T. Turner and S.M. Spearing. Modeling of direct wafer bonding: Effect of wafer bow and etch patterns. *Journal of Applied Physics*, 92(12):7658–7666, 2002.

[20] K.T. Turner, M.D. Thouless, and S.M. Spearing. Mechanics of wafer bonding: Effect of wafer bow and etch patterns. *Journal of Applied Physics*, 95(1):349–355, 2004.

[21] K.T. Turner and S.M. Spearing. Measurement of work of adhesion on wafers for direct bonding. In *Materials Research Society Symposium - Proceedings*, volume 782, pages A12.4.1–A12.4.6, 2003.

[22] K.T. Turner and S.M. Spearing. Role of wafer bow and etch patterns in direct bonding. In *Proceedings of the 7th International Symposium on Semiconductor Wafer Bonding: Science, Technology, and Applications*, pages 166–174, 2003.

[23] J.B. Lasky. Wafer bonding for silicon on insulator technologies. *Applied Physics Letters*, 48(1):78–80, 1986.

[24] M. Shimbo, K. Furukawa, K. Fukuda, and K. Tanzawa. Silicon-to-silicon direct bonding method. *Journal of Applied Physics*, 60(8):2987–2989, 1986.

[25] W.P. Maszara. Silicon-on-insulator by wafer bonding: A review. *Journal of the Electrochemical Society*, 138(1):341–347, 1991.

[26] S. Bengtsson. Semiconductor wafer bonding: A review of interfacial properties and applictaion. *Journal of Electronic Materials*, 21(8):841–862, 1992.

[27] K. Mitani and U. Gösele. Wafer bonding technology for silicon-on-insulator applications: A review. *Journal of Electronic Materials*, 21(7):669–676, 1992.

[28] J. Haisma, G.A.C.M. Spierings, U.K.P. Biermann, and A.A. van Gorkum. Diversity and feasibility of direct bonding: a survey of a dedicated optical technology. *Applied Optics*, 33(7):1154–1169, 1994.

[29] Q.-Y. Tong and U. Gösele. Semiconductor wafer bonding: Recent developments. *Materials Chemistry and Physics*, 37:101–127, 1994.

[30] U. Gösele and Q.-Y. Tong. Semiconductor wafer bonding. *Annual Review of Materials Science*, 28:215–241, 1998.

[31] Q.-Y. Tong and U. Gösele. Wafer bonding and layer splitting for microsystems. *Advanced Materials*, 11(17):1409–1425, 1999.

[32] U. Gösele, J. Haisma, M. Schmidt, and T. Abe, editors. *1st Int. Symp. on Semiconductor Wafer Bonding: Science, Technology, and Applications*, volume 92-7, Pennington, NJ, 1992. Electrochemical Society.

[33] H. Baumgart, C. Hunt, M. Schmidt, and T. Abe, editors. *2nd Int. Symp. on Semiconductor Wafer Bonding: Science, Technology, and Applications*, volume 93-29, Pennington, NJ, 1993. Electrochemical Society.

[34] H. Baumgart, C. Hunt, S. Iyer, U. Gösele, and T. Abe, editors. *3rd Int. Symp. on Semiconductor Wafer Bonding: Science, Technology, and Applications*, volume 95-97, Pennington, NJ, 1995. Electrochemical Society.

[35] U. Gösele, H. Baumgart, C. Hunt, and T. Abe, editors. *4th Int. Symp. on Semiconductor Wafer Bonding: Science, Technology, and Applications*, volume 97-36, Pennington, NJ, 1998. Electrochemical Society.

[36] U. Gösele, H. Baumgart, C. Hunt, and T. Abe, editors. *5th Int. Symp. on Semiconductor Wafer Bonding: Science, Technology, and Applications*, volume 99-35, Pennington, NJ, 2000. Electrochemical Society.

[37] H. Baumgart, C. Hunt, S. Bengtsson, and T. Abe, editors. *6th Int. Symp. on Semiconductor Wafer Bonding: Science, Technology, and Applications*, volume 2001-27, Pennington, NJ, 2002. Electrochemical Society.

[38] S. Bengtsson, C. Hunt, S. Bengtsson, and T. Suga, editors. *7th Int. Symp. on Semiconductor Wafer Bonding: Science, Technology, and Applications*, volume 2003-19, Pennington, NJ, 2004. Electrochemical Society.

[39] S.S. Iyer and A.J. Auberton-Herve. *Silicon wafer bonding technology: for VLSI and MEMS applications*. IEE, London, 2002.

[40] SEMI. SEMI M1-0302: Specifications for polished monocrystalline silicon wafers, 2002. (Semiconductor Equipment and Materials International).

[41] ASTM. ASTM F 1241-95: Standard terminology of silicon technology, 2000. (American Society for Testing and Materials).

[42] ASTM. ASTM F 534-97: Standard test method for bow of silicon wafers, 1997. (American Society for Testing and Materials).

[43] ASTM. ASTM F 1390-97: Standard test method for measuring warp of silicon wafers by automated noncontact scanning, 1997. (American Society for Testing and Materials).

[44] ASTM. ASTM F 1451-92: Standard test method for measuring sori on silicon wafers by automated noncontact scanning, 1999. (American Society for Testing and Materials).

[45] ASTM. ASTM F 533-96: Standard test method for thickness and thickness variation of silicon wafers, 1996. (American Society for Testing and Materials).

[46] SEMI. SEMI M43-0301: Guide for reporting wafer nanotopography, 2001. (Semiconductor Equipment and Materials International).

[47] SEMI. SEMI M40-2000: Guide for measurement of surface roughness of planar surface on silicon wafer, 2000. (Semiconductor Equipment and Materials International).

[48] Lord Rayleigh. A study of glass surfaces in optical contact. *Proceedings of the Royal Society of London. Series A, Mathematical and Physical Sciences*, 156(888):326–349, 1936.

[49] W.P. Maszara, B-L. Jiang, A. Yamada, G.A. Rozgonyi, H. Baumgart, and A.J.R. de Kock. Role of surface morphology in wafer bonding. *Journal of Applied Physics*, 69(1):257–260, 1991.

[50] R. Stengl, K. Mitani, V. Lehmann, and U. Gosele. Silicon wafer bonding: Chemistry, elasto-mechanics, and manufacturing. *Proceedings of the 1989 IEEE SOS/SOI Technology Conference*, page 123, 1989.

[51] U. Gösele and Q.-Y. Tong. Silicon layer transfer by wafer bonding. In *Proceedings of the Second International Symposium on Semiconductor Wafer Bonding: Science, Technology, and Applications*, volume 93-29, pages 395–409. The Electrochemical Society, 1993.

[52] Q.-Y. Tong and U. Gösele. Thickness considerations in direct silicon wafer bonding. *Journal of the Electrochemical Society*, 142(11):3975–3979, 1995.

[53] Q.-Y. Tong, S. Krasnicki, and U. Gösele. Thick wafer bonding. In *Proceedings of the Third International Symposium on Semiconductor Wafer Bonding: Science, Technology, and Applications*, volume 95-7, pages 155–162. The Electrochemical Society, 1995.

[54] H.H. Yu and Z. Suo. A model of wafer bonding by elastic accomodation. *Journal of the Mechanics and Physics of Solids*, 46(5):829–44, 1998.

[55] L.N. Hong and R.W. Bower. Comparison of experimental and theoretical curvature considerations for direct wafer bonding. In *Proceedings of the SPIE: Microelectronic packaging and laser processing*, volume 3184, pages 129–135, 1997.

[56] L.N. Hong and R.W. Bower. Radius of curvature considerations for direct wafer bonding. *Japanese Journal of Applied Physics, Part 1*, 37(11):5932–5936, 1998.

[57] R.W. Bower, W. Chan, L. Hong, and V.H.C. Watt. Mechanical considerations for direct bonding of semiconductor materials. In *Proceedings of the Third International Symposium on Semiconductor Wafer Bonding: Science, Technology, and Applications*, volume 95-7, pages 107–115. The Electrochemical Society, 1995.

[58] M. Bergh, S. Bengtsson, and M.O. Andersson. The influence of surface micro-roughness on bondability. In *Proceedings of the Third International Symposium on Semiconductor Wafer Bonding: Science, Technology, and Applications*, volume 95-7, pages 126–137. The Electrochemical Society, 1995.

[59] C. Gui, M. Elwenspoek, N. Tas, and J.G.E Gardeniers. The surface adhesion parameter: a measure for wafer bondability. In *Proceedings of the 1999 12th IEEE International Conference on Micro Electro Mechanical Systems*, pages 290–295, 1999.

[60] C. Gui, M. Elwenspoek, N. Tas, and J.G.E Gardeniers. The effect of surface roughness on direct wafer bonding. *Journal of Applied Physics*, 85(10):7448–7454, 1999.

[61] K.N.G. Fuller and D. Tabor. The effect of surface roughness on the adhesion of elastic solids. *Proceedings of the Royal Society of London. Series A, Mathematical and Physical Sciences*, 345:327–342, 1975.

[62] N. Miki and S.M. Spearing. Effect of nanoscale surface roughness on the bonding energy of direct-bonded silicon wafers. *Journal of Applied Physics*, 94(10):6800–6806, 2003.

[63] K.L. Johnson. Adhesion at the contact of solids. In W.T. Koiter, editor, *Theoretical and Applied Mechanics*. North Holland, 1976.

[64] A.A. Griffith. The phenomenon of rupture and flow in solids. *Philisophical Transactions of the Royal Society, London*, A221:163–197, 1921.

[65] K.L. Johnson, K. Kendall, and A.D. Roberts. Surface energy and the contact of elastic solids. *Proceedings of the Royal Society of London. Series A, Mathematical and Physical Sciences*, 324:301–313, 1971.

[66] G.R. Irwin. Onset of fast crack propagation in high strength steel and aluminium alloys. In *Proceedings of the Second Sagamore Conference*, volume II, pages 289–305, 1956.

[67] D. Maugis. *Contact, Adhesion and Rupture of Elastic Solids*. Springer, New York, 2000.

[68] S.P. Timoshenko and S. Woinowsky-Krieger. *Theory of Plates and Shells*. McGraw-Hill, London, 1959.

[69] Hibbitt, Karlsson, Sorensen, Inc. ABAQUS standard users manual, 2001. Pawtucket, RI.

[70] C. Gui, R.E. Oosterbroek, J.W. Berenschot, S. Schlautmann, T.S.J. Lammerink, A. van den Berg, and M. Elwenspoek. Selective wafer bonding by surface roughness control. *Journal of the Electrochemical Society*, 148:G225–8, 2001.

[71] A.P. Roberts and E.J. Garboczi. Computation of the linear elastic properties of random pourous materials with a wide variety of microstructure. *Proceedings of the Royal Society of London. Series A*, 458:1033, 2002.

[72] J.J. Wortman and R.A. Evans. Young's modulus, shear modulus, and Poisson's ratio in silicon and germanium. *Journal of Applied Physics*, 36(1):153–156, 1965.

[73] T.L. Anderson. *Fracture Mechanics: Fundamentals and Applications*. CRC Press, New York, 1995.

[74] R. Krueger. The virtual crack closure technique: History, approach, and applications. Technical report, NASA, 2002. ICASE 2002-10.

[75] D. Hitchings, P. Robinson, and F. Javidrad. A finite element model for delamination in propagation in constants. *Computers and Structures*, 60(6):1093–1104, 1996.

[76] D. Feijoó, I. Ong, K. Mitani, W.-S. Yang, S. Yu, and U. M. Gösele. Prestressing of bonded wafers. In *Proceedings of the First International Symposium on Semiconductor Wafer Bonding: Science, Technology, and Applications*, volume 92-7, pages 230–8. The Electrochemical Society, 1992.

[77] Z. Suo and J.W. Hutchinson. Interface crack between two elastic layers. *International Journal of Fracture*, 43:1–18, 1990.

[78] J. W. Hutchinson and Z. Suo. Mixed mode cracking in layered materials. *Advances in Applied Mechanics*, 29:63–191, 1992.

[79] N. Miki, X. Zhang, R. Khana, A. A. Ayón, D. Ward, and S. M. Spearing. Multi-stack silicon-direct wafer bonding for 3D MEMS manufacturing. *Sensors and Actuators, A*, 103:194–201, 2003.

[80] ADE Corporation, Westwood, MA. *9900 UltraGage Users Manual*, 2000.

[81] K.V. Ravi. Wafer flatness requirements for future technologies. *Future Fab International*, 7:207–212, 2000.

[82] D. Boning and B. Lee. Nanotopography issues in shallow trench isolation CMP. *MRS Bulletin*, 27(10):761–5, 2002.

[83] B. Lee, D.S. Boning, W. Baylies, N. Poduje, P. Hester, H. Xia, J. Valley, C. Koliopoulus, D. Hetherington, H. Sun, and M. Lacey. Wafer nanotopography effects on CMP: Experimental validation of modeling methods. In *Materials Research Society Symposium - Proceedings*, volume 671, pages M4.9.1–6, 2001.

[84] B. Lee, T. Gan, D. Boning, P. Hester, N. Poduje, and W. Baylies. Nanotopography effects on chemical mechanical polishing for shallow trench isolation. In *IEEE International Symposium on Semiconductor Manufacturing Conference, Proceedings*, pages 425–432, 2000.

[85] T. Katoh, J.-G. Park, W.-M. Lee, H. Jeon, U.-G. Paik, and H. Suga. The nanotopography effect of improved single-side polished wafer on oxide chemical mechanical polishing. *Japanese Journal of Applied Physics, Part 2: Letters*, 41:L443–L446, 2002.

[86] J.-G. Park, T. Katoh, H.-C. Yoo, and J.-H. Park. Spectral analyses of the impact of nanotopography of silicon wafers on oxide chemical mechanical polishing. *Japanese Journal of Applied Physics, Part 2: Letters*, 40:L857–L860, 2001.

[87] J.-G. Park, T. Katoh, H.-C. Yoo, D.-H. Lee, and U.-G. Paik. Spectral analyses on pad dependency of nanotopography impact on oxide chemical mechanical polishing. *Japanese Journal of Applied Physics, Part 2: Letters*, 41:L17–9, 2002.

[88] B. Lee, D.S. Boning, W. Baylies, N. Poduje, and J. Valley. Modeling and mapping of nanotopography interactions with CMP. In *Materials Research Society Symposium - Proceedings*, volume 732E, pages I1.1.1–12, 2002.

[89] G. Wenski, T. Altmann, W. Winkler, G. Heier, and G. Holker. Doubleside polishing - a technology for 300 mm wafer manufacturing. *Materials Science in Semiconductor Processing*, 5:375–80, 2003.

[90] MEMC. Application Note: AE-008, August 2001.

[91] J.F. Valley, C.L. Koliopoulos, and S. Tang. Interferometric metrology of wafer nanotopography for advanced CMOS process integration. In *Proceedings of SPIE - The International Society for Optical Engineering*, volume 4449, pages 160–8, 2001.

[92] J.F. Valley, T. Templeton, C.L. Koliopoulos, and M. Yoshise. Nanotopography metrology for leading edge 300-mm process integration. In *Proceedings of SPIE - The International Society for Optical Engineering*, volume 4689, pages 1027–36, 2001.

[93] R. Schmolke, R. Deters, P. Thieme, R. Pech, H. Schwenk, and G. Diakourakis. On the impact of nanotopography of silicon wafers on post-cmp oxide layers. *Journal of the Electrochemical Society*, 149(4):G257–G265, 2002.

[94] I. Weingaertner, M. Wurm, R.D. Geckeler, C. Elster, M. Schulz, E. Dumitrescu, S. Krey, and J. Heinisch. Novel scheme for the ultraprecise and fast measurement of the nanotopography of large wafers. In *Proceedings of SPIE - The International Society for Optical Engineering*, volume 4779, pages 13–22, 2002.

[95] T.D. Raymond, D.R. Neal, D.M. Topa, and T.L. Schmitz. High-speed noninterferometric nanotopographic characterization of Si wafer surfaces. In *Proceedings of SPIE - The International Society for Optical Engineering*, volume 4809, pages 208–16, 2002.

[96] Zygo Coroporation, Middlefield, CT. *VeriFire AT Interferometer System Operating Manual OMP-0480*, 2002.

[97] F. Reidel, H.-A. Gerber, and P. Wagner. Impact of filtering on nanotopography measurement of 300 mm silicon wafers. *Materials Science in Semiconductor Processing*, 5:465–72, 2003.

[98] Zygo Coroporation, Middlefield, CT. *MetroPro Reference Guide OMP-0347G*, 2002.

[99] The MathWorks, Natick, MA. *Signal Processing Toolbox: For use with MATLAB*, 2002.

[100] ASTM International. ASTM F1811-97: Standard practice for estimating the power spectral density function and related finish parameters from surface profile data, 1997.

[101] T. Abe, T. Takei, A. Uchiyama, K. Yoshizawa, and Y. Nakazato. Silicon wafer bonding mechanism for silicon-on-insulator structures. *Japanese Journal of Applied Physics*, 29(12):L2311–L2314, 1990.

[102] W.P. Maszara, G. Goetz, A. Caviglia, and B. McKitterick. Bonding of silicon wafers for silicon on insulator. *Journal of Applied Physics*, 64(10):4943–4950, 1988.

[103] M. Petzold, J. Bagdahn, and D. Katzer. Quality and mechanical reliability assessment of wafer-bonded micromechanical components. *Microelectronics reliability*, 39:1103–1108, 1999.

[104] K.T. Turner and S.M. Spearing. Characterization of silicon fusion bond using a four-point bend specimen. In *Materials Research Society Symposium - Proceedings*, volume 657, pages EE6.3.1–EE6.3.6, 2000.

[105] T. Martini, J. Steinkirchner, and U. Gösele. The crack opening method in silicon wafer bonding. *Journal of the Electrochemical Society*, 144(1):354–357, 1997.

[106] P.P. Gillis and J.J. Gilman. Double-cantilever clevage mode of crack propagation. *Journal of Applied Physics*, 35(3):647–658, 1964.

[107] J. Bagdahn, M. Petzold, M. Reiche, and K. Gutjahr. Characterization of directly bonded silicon wafers by means of the double cantilever crack opening method. In *Semiconductor Wafer Bonding IV: Science, Technology, and Applications*, volume PV 97-36, pages 291–298, 1997. Paris, France - September 1997.

[108] B. Lawn. *Fracture of Brittle Solids*. Cambridge University Press, Cambridge, UK, 2nd edition, 1993.

[109] M.-Y. He and J.W. Hutchinson. Kinking of a crack out of an interface. *Journal of Applied Mechanics*, 56:270–278, 1989.

[110] K.R. Shull. Contact mechanics and the adhesion of soft solids. *Materials Science and Engineering R*, 36:1–45, 2002.

[111] C.L. Dym and I.H. Shames. *Solid Mechanics: A Variational Approach*. McGraw-Hill, New York, 1973.

Appendix A

Mindlin Plate Analysis

A classical plate theory and finite element model were presented in Chapter 2 to calculate the strain energy accumulation rate for the bonding of two wafers with different initial curvatures. The finite element and classical plate theory solutions agreed well at large bond radii, but differed at short bond radii. In this appendix, an alternative derivation of the strain energy accumulation rate using Mindlin plate theory is presented.

Mindlin plate theory is a higher-order plate theory that includes deformations due to bending as well as transverse shear. The radial moment, M_r, tangential moment, M_θ, and the transverse shear force, Q, may be expressed in terms of the deflection, $\bar{w}$, and the line element rotation, Φ,

$$M_r = -D\left(\Phi' + \nu\frac{\Phi}{r}\right), \tag{A.1}$$

$$M_\theta = -D\left(\frac{\Phi}{r} + \nu\Phi'\right), \tag{A.2}$$

$$Q = -k_p\mu h(\Phi - \bar{w}'). \tag{A.3}$$

The $'$ denotes d/dr and k_p is the shear coefficient. For a solid isotropic plate of uniform thickness, $k_p = 4/3$, [111]. The shear modulus is μ and D is the plate rigidity, which was defined in Chapter 3. The equilibrium equations for the plate are,

$$M_r' + \frac{1}{r}(M_r - M_\theta) = Q, \tag{A.4}$$

$$\frac{1}{r}(rQ)' = -q \tag{A.5}$$

where q is a distributed load on the plate.

The geometry considered in this analysis is that shown in Fig. 3-1. The derivation shown here is for wafer 1, but is identical to that for wafer 2. The deflection in section A is known $[\bar{w}_A = \frac{1}{2}(\kappa_f -$

$\kappa_1)r^2]$ but Φ is not. Rewriting Eq. (A.4) in terms of $\bar{w}$ and Φ using Eqs. (A.1), (A.2), and (A.3) a differential equation that can be solved for Φ is obtained.

$$\Phi'' + \frac{1}{r}\Phi' - \left(\frac{1}{r^2} + \frac{k_pGh}{D}\right)\Phi = -\bar{w}'\frac{k_pGh}{D} \tag{A.6}$$

Substituting in $\bar{w}'_A = (\kappa_f - \kappa_1)r$, Φ_A is readily found,

$$\Phi_A = (\kappa_f - \kappa_1)r + C_3 I_1\left(r\sqrt{\frac{k_pGh}{D}}\right) + C_4 K_1\left(r\sqrt{\frac{k_pGh}{D}}\right) \tag{A.7}$$

where $I_1()$ and $K_1()$ are modified Bessel functions of the first and second kind, respectively. Due to symmetry in the plate, $\Phi_A|_{r=0} = 0$, to ensure this $C_4 = 0$ since $K_1(r\sqrt{\frac{k_pGh}{D}}) \to \infty$ as $r \to 0$. Thus, Eq. (A.7) reduces to

$$\Phi_A = (\kappa_f - \kappa_1)r + C_3 I_1\left(r\sqrt{\frac{k_pGh}{D}}\right). \tag{A.8}$$

This equation, combined with the deflection,

$$\bar{w}'_A = (\kappa_f - \kappa_1)r^2, \tag{A.9}$$

describes the deformation in the bonded section of the wafer. In section B of the plate there are no applied distributed loads or shear loads and as such the relevant governing equation is,

$$\left[\frac{1}{r}\left(r\bar{w}'_B\right)'\right]' = 0. \tag{A.10}$$

Integrating this, the general equation for the transverse deflection of the plate is section 2 is found,

$$\bar{w}_B = \frac{1}{4}C_5 r^2 + C_6 \ln(\frac{r}{c}) + C_7. \tag{A.11}$$

The fact that there are no applied transverse shear loads in section 2 also leads to:

$$\Phi_B = \bar{w}'_B. \tag{A.12}$$

The transverse deflection of the plate, Eqs (A.9) and (A.11), and the rotation of the line elements, Eqs. (A.8) and (A.12), fully describe the deformation of the plate and permit the calculation of strain energy in the plate. While these equations describe the deformation of the plate, four integration constants, C_3, C_5, C_6, C_7, remain in this set of equations. These integration constants

can be determined from the four remaining boundary conditions,

$$\begin{aligned} \bar{w}_A|_{r=c} &= \bar{w}_B|_{r=c} \\ \Phi_A|_{r=c} &= \Phi_B|_{r=c} \\ M_{rB}|_{r=b} &= 0 \\ M_{rA}|_{r=c} &= M_{rA}|_{r=c} \end{aligned} . \tag{A.13}$$

Using these four boundary conditions, the four constants can be solved for. The constants and final form of the equations for $\bar{w}$ and Φ are not shown here due to their complicated nature.

The strain energy in the plate can be calculated as,

$$U = \pi \int_0^b \int_{-h/2}^{h/2} (\sigma_{rr}\epsilon_{rr} + \sigma_{\theta\theta}\epsilon_{\theta\theta} + 2\sigma_{rz}\epsilon_{rz}) r dz dr. \tag{A.14}$$

This can be rewritten in terms of w and Φ as

$$U = \pi \int_0^b \left[D \left((\Phi')^2 + 2\frac{\nu}{r}\Phi\Phi' + \left(\frac{\Phi}{r}\right)^2 \right) + k_p G h (\bar{w}' - \Phi)^2 \right] r dr. \tag{A.15}$$

A closed form solution could not be found for the integral in Eq. (A.15). As such, the strain energy was evaluated by substituting Eqs. (A.9), (A.11), (A.8), and (A.12) into Eq. (A.15) and numerically integrating. The strain energy accumulation rate was then obtained through numerical differentiation of the strain energy. The results are shown in Fig. 3-5.

Appendix B

Gravity Deformation

In the bonding experiments that were performed, deformation of the wafers due to gravity was observed to have a significant effect on the wafer shape. This appendix summarizes an axisymmetric plate theory model that predicts the deflections due to gravity for several simple mounting configurations.

B.1 Model

The basic geometry considered is pictured in Fig. B-1. A wafer of radius b and thickness h is supported on an axisymmetric ring of radius s. A distributed load, q, resulting from gravity acts across the entire wafer. The distributed load due to gravity which has units of force/area is given by,

$$q = \rho g h, \tag{B.1}$$

where ρ is the density of the wafer and g is the gravitational acceleration ($g = -9.807$ m/s^2). To determine the deflection of the plate it is useful to divide the plate in two sections, A: $0 \geq r \geq s$ and B: $s \geq r \geq b$. The plate deflection is related to the distributed load by,

$$\frac{1}{r}\frac{d}{dr}\left\{r\frac{d}{dr}\left[\frac{1}{r}\frac{d}{dr}\left(r\frac{d\bar{w}_i}{dr}\right)\right]\right\} = \frac{q}{D}, \tag{B.2}$$

where $\bar{w}$ is the deflection and the subscript i denotes the section (A or B). The flexural rigidity, D, is defined in terms of the elastic modulus, E, Poisson's ratio, ν, and the plate thickness,

$$D = \frac{Eh^3}{12(1-\nu^2)}. \tag{B.3}$$

The deflection in each section of the plate can be determined by substituting Eq. (B.1) into

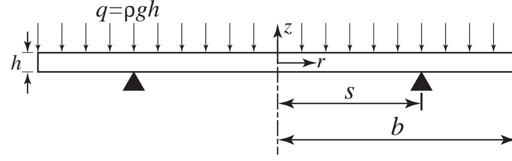

Figure B-1: Schematic of wafer loaded by gravity.

Eq. (B.2) and integrating. Four integrations are required to obtain an expression for $\bar{w}_i$, hence there are four integration constants for each section. The eight integration constants are determined by applying appropriate boundary conditions,

$$\begin{array}{cc} \bar{w}_A|_{r=s} = 0 & \bar{w}_B|_{r=s} = 0 \\ \left.\frac{d\bar{w}_A}{dr}\right|_{r=s} = \left.\frac{d\bar{w}_B}{dr}\right|_{r=s} & \left.\frac{d\bar{w}_A}{dr}\right|_{r=0} = 0 \\ M_{rA}|_{r=s} = M_{rB}|_{r=s} & M_{rB}|_{r=b} = 0 \\ Q_A|_{r=0} = 0 & Q_B|_{r=b} = 0 \end{array} . \tag{B.4}$$

The radial moment, M_{ri}, and the shear force, Q_i, are expressed in the terms of deflection by,

$$M_{ri} = -D\left(\frac{1}{r}\frac{d\bar{w}_i}{dr} + \nu\frac{d^2\bar{w}_i}{dr^2}\right) \tag{B.5}$$

$$Q_i = -D\left\{\frac{d}{dr}\left[\frac{1}{r}\frac{d}{dr}\left(r\frac{d\bar{w}_i}{dr}\right)\right]\right\}. \tag{B.6}$$

Solving subject to the boundary conditions, the deflections in section A and B are determined,

$$\bar{w}_A = \frac{3}{16}\frac{\rho g b^4}{\tilde{E}h^2}\left\{(\bar{r}^2 - \bar{s}^2)[\bar{r}^2 - 3\bar{s}^2 - 2 + \nu(\bar{r}^2 + 5\bar{s}^2 - 6) - 8(1+\nu)\ln(\bar{s})]\right\}, \tag{B.7}$$

$$\bar{w}_B = \frac{3}{16}\frac{\rho g b^4}{\tilde{E}h^2}\left\{(\bar{r}^2 - \bar{s}^2)[\bar{r}^2 - 3\bar{s}^2 + 6 + \nu(\bar{r}^2 + 5\bar{s}^2 + 2)] - 8(1+\nu)[(\bar{r}^2 + \bar{s}^2)\ln(\bar{r}) - 2\bar{s}^2\ln(\bar{s})]\right\}. \tag{B.8}$$

The expressions for deflection have been written in terms of the non-dimensional support radius, $\bar{s} = s/b$, non-dimensional radial position, $\bar{r} = r/b$, and the biaxial modulus, $\tilde{E} = E/(1-\nu)$.

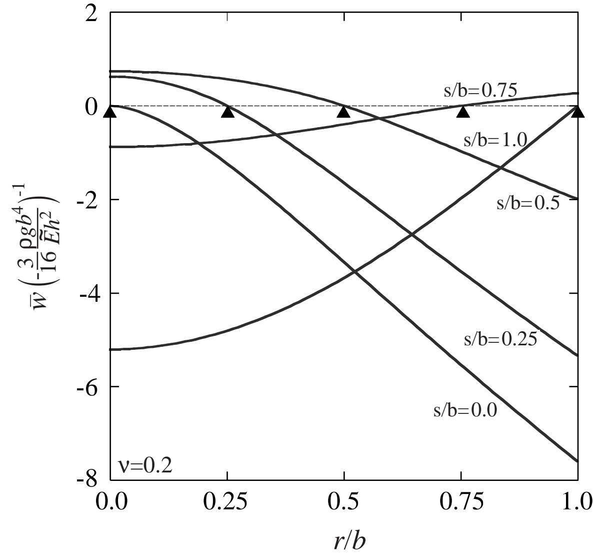

Figure B-2: Deflection profiles of a wafer loaded by gravity for different support radii.

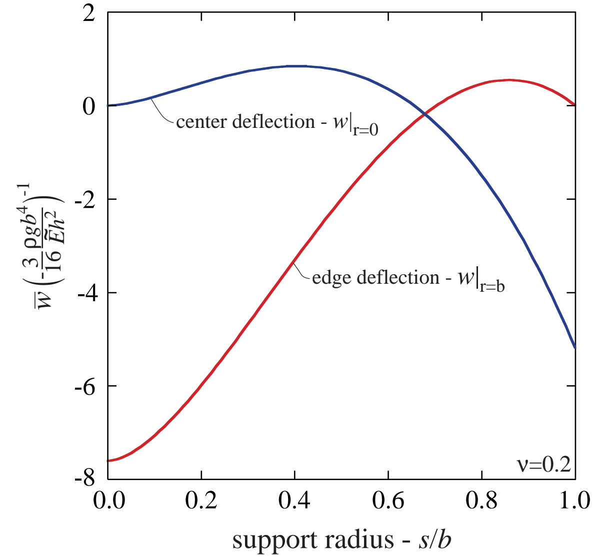

Figure B-3: Deflection at the center and edge of the wafer as a function of support radius.

B.2 Results

The deflection profiles calculated with Eqs. (B.7) and (B.8) for wafers with different support radii are plotted in Fig. B-2. The deflection and radial position are plotted as non-dimensional quantities. Values of the normalization constant, $(-\frac{3}{16}\frac{\rho g b^4}{\tilde{E}h^2})$, for different standard wafer sizes are given in Table B.1. As shown in Fig. B-2 the point of maximum deflection switches from the center ($\bar{r} = 0$) of the wafer to the edge ($\bar{r} = 1$) as the support radius is increased. The deflection at the edge and center of the wafer are plotted as function of support radius in Fig. B-3.

Two limiting cases of the above analysis that are of interest are: (1) the deflection at the edge of a center supported wafer, ($\bar{w}_{cs} = \bar{w}_B|_{\bar{s}=0,\bar{r}=1}$), and (2) the deflection at the center of an edge supported wafer, ($\bar{w}_{es} = \bar{w}_A|_{\bar{s}=1,\bar{r}=0}$). The deflection equations simplify considerably for these cases,

$$\bar{w}_{cs} = \frac{3}{16}\frac{\rho g b^4}{\tilde{E}h^2}(7 + 3\nu) \tag{B.9}$$

$$\bar{w}_{es} = \frac{3}{16}\frac{\rho g b^4}{\tilde{E}h^2}(5 + \nu) \tag{B.10}$$

Calculated deflections for these two cases for different standard wafer sizes are listed in Table B.1.

Table B.1: Deflections due to gravity for various standard wafer geometries.

Wafer Properties		Normalization	Center Supported	Edge Supported
Diameter (mm)	Thickness (μm)	$-\frac{3}{16}\frac{\rho g b^4}{\tilde{E}h^2}$ (μm)	$\bar{w}\|_{\bar{s}=0,\bar{r}=1}$ (μm)	$\bar{w}\|_{\bar{s}=1,\bar{r}=0}$ (μm)
100	525	0.54	-4.1	-2.8
150	625	1.92	-14.5	-10.0
200	725	4.51	-34.1	-23.4
300	775	19.99	-150.8	-103.6
results calculated assuming standard properties of silicon, $E = 148 GPa$, $\nu = 0.18$, $\rho = 2330 kg/m^3$				

Appendix C

Finite Element Code

C.1 Asymmetric Bond Prediction

Below are the MATLAB™ scripts that are used to generate and execute the finite element model used to calculate bonding in asymmetric wafer pairs (Chapter 4 and Chapter 6). The mesh is generated in MATLAB™, exported to ABAQUS™ and solved. The data is retrieved from the ABAQUS™ results file and post-processed in MATLAB™. The model is comprised of six m-files:

1. *vcct_06.m* - Script that is executed to run the model. It calls *spoke_06.m*, which generates the mesh, runs the model, and then post-processes the data. The VCCT calculation and iteration scheme are contained within this script.

2. *spoke_06.m* - Script used to generate mesh. The script writes a text file with the model that is read by ABAQUS™.

3. *geth1.m* - This function reads in the thickness of wafer 1. In the studies in this work, the thickness of the wafer was defined as being uniform, although a thickness variation across the wafer could be defined or imported from measurements by using a routine similar to that used *getz1.m*

4. *geth2.m* - This function does the same as geth1.m, but for wafer 2 (code not included).

5. *getz1.m* - This function reads in the shape of wafer 1. It reads a text file that includes the shape values and interpolates the data to the mesh. The text files of shape data were either generated artificially (for the systematic studies in Chapter 4) or were created from the measurements on the wafers (Chapter 6) by exporting the data from ADE Device Toolbox™ software.

6. *getz2.m* - This function does the same as getz1.m, but for wafer 2 (code not included).

vcct_06.m

```
clear;

% m-file designed to run spoke_06 multiple times
% reads data from results file
% calculates G at each spoke, then tries to adjust bond front to match G

%**Target G and tolerance**
GC = 0.020                  % target work of adhesion value
G_conv = 0.01*GC;           % convergence criterion
dr_lim = 3.0e-3;            % maximum distance nodes can move per iteration

%**Initial guess for bond front shape**
ns = 32;                    % number of spokes
b = 25.0e-3;                % initial bon radii
B = b*ones(ns,1);           % vector with bond front postion at each spoke

for i = 1:1000;

    %**Run ABAQUS code**

    % Create .inp file and run ABAQUS
    !del spoke_06.mdl
    [A(i,1), nq1] = spoke_06(B(:,i),ns);
    !abaqus job=spoke_06 interactive

    % Delete old test file, convert new results file to text
    !del filtotxt6.tur
    !abaqus filtotxt6

    %**Read in data**
    % Read in energy data
    es1 = 2;                        % first line of energy data of set 1
    ef1 = es1;                      % last line of energy data of set 1
    [U1(i,1)] = textread('filtotxt6.tur','%f',((ef1-es1)+1),'expchars','E','headerlines',(es1-1));

    % Read in displacement data for wafer 1
    es1 = ef1+2;                    % first line of displacement data at nodes 1 row ahead of crack tip
    ef1 = es1+((nq1+1)*ns-1);       % last line of displacement data at nodes 1 row ahead of crack tip
    [D1NODEA(:,i),D1A(:,i)] = textread('filtotxt6.tur','%u %*f %*f %f',((ef1-es1)+1),'expchars','E','headerlines',(es1-1));

    % Read in displacement data for wafer 1
    es1 = ef1+1;                    % first line of displacement data at nodes 2 rows ahead of crack tip
    ef1 = es1+((2*nq1+1)*ns-1);     % last line of displacement data at nodes 2 rows ahead of crack tip
    [D1NODEB(:,i),D1B(:,i)] = textread('filtotxt6.tur','%u %*f %*f %f',((ef1-es1)+1),'expchars','E','headerlines',(es1-1));

    % Read in displacement data for wafer 2
    es1 = ef1+1;                    % first line of displacement data at nodes 1 row ahead of crack tip
    ef1 = es1+((nq1+1)*ns-1);       % last line of displacement data at nodes 1 row ahead of crack tip
    [D2NODEA(:,i),D2A(:,i)] = textread('filtotxt6.tur','%u %*f %*f %f',((ef1-es1)+1),'expchars','E','headerlines',(es1-1));

    es1 = ef1+1;                    % first line of displacement data at nodes 2 rows ahead of crack tip
    ef1 = es1+((2*nq1+1)*ns-1);     % last line of displacement data at nodes 2 rows ahead of crack tip
    [D2NODEB(:,i),D2B(:,i)] = textread('filtotxt6.tur','%u %*f %*f %f',((ef1-es1)+1),'expchars','E','headerlines',(es1-1));

    % Read in reaction force data
    es1 = ef1+2;                    % first line of reaction force data at nodes behind tip
    ef1 = es1+((nq1+1)*ns-1);       % last line of reaction force data at nodes behind tip
    [RFNODEA(:,i),RFA(:,i)] = textread('filtotxt6.tur','%u %*f %*f %f',((ef1-es1)+1),'expchars','E','headerlines',(es1-1));

    es1 = ef1+1;                    % first line of reaction force data at nodes at crack tip
    ef1 = es1+((2*nq1+1)*ns-1);     % last line of reaction force data at nodes at crack tip
    [RFNODEB(:,i),RFB(:,i)] = textread('filtotxt6.tur','%u %*f %*f %f',((ef1-es1)+1),'expchars','E','headerlines',(es1-1));

    % Read in x-y nodal coordinates and initial gap ahead of tip
    es1 = ef1+2;                    % first line of nodal coordinates 1 node behind tip
    ef1 = es1+((nq1+1)*ns-1);       % last line of nodal coordinates 1 node behind tip
    [CTIP0(:,1),CTIP0(:,2),CTIP0(:,3)] = textread('filtotxt6.tur','%u %f %f %*f',((ef1-es1)+1),'expchars','E','headerlines',(es1-1));

    es1 = ef1+1;                    % first line of nodal coordinates at tip
    ef1 = es1+((2*nq1+1)*ns-1);     % first line of nodal coordinates at tip
    [CTIP1(:,1),CTIP1(:,2),CTIP1(:,3)] = textread('filtotxt6.tur','%u %f %f %*f',((ef1-es1)+1),'expchars','E','headerlines',(es1-1));

    es1 = ef1+1;                    % first line of nodal coordinates 1 node ahead of tip on wafer 1
    ef1 = es1+((nq1+1)*ns-1);       % last line of nodal coordinates 1 node ahead of tip on wafer 1
    [CTIP2(:,1),CTIP2(:,2),CTIP2(:,3),GAP2(:,2)] = textread('filtotxt6.tur','%u %f %f %f',((ef1-es1)+1),'expchars','E','headerlines',(es1-1));
    GAP2(:,1)=CTIP2(:,1);

    es1 = ef1+1;                    % first line of nodal coordinates 2 nodes behind tip on wafer 1
    ef1 = es1+((2*nq1+1)*ns-1);     % first line of nodal coordinates 2 nodes behind tip on wafer 1
    [CTIP3(:,1),CTIP3(:,2),CTIP3(:,3),GAP3(:,2)] = textread('filtotxt6.tur','%u %f %f %f',((ef1-es1)+1),'expchars','E','headerlines',(es1-1));
    GAP3(:,1)=CTIP3(:,1);

    es1 = ef1+1;                    % first line of nodal coordinates 1 node ahead of tip on wafer 2
    ef1 = es1+((nq1+1)*ns-1);       % last line of nodal coordinates 1 node ahead of tip on wafer 2
    [GAP2(:,3),GAP2(:,4)] = textread('filtotxt6.tur','%u %*f %*f %f',((ef1-es1)+1),'expchars','E','headerlines',(es1-1));
```

```
es1 = ef1+1;                    % first line of nodal coordinates 2 nodes behind tip on wafer 2
ef1 = es1+((2*nq1+1)*ns-1);     % first line of nodal coordinates 2 nodes behind tip on wafer 2
[GAP3(:,3),GAP3(:,4)] = textread('filtotxt6.tur','%u %*f %*f %f',((ef1-es1)+1),'expchars','E','headerlines',(es1-1));

GAP2(:,5) = GAP2(:,2)-GAP2(:,4);
GAP3(:,5) = GAP3(:,2)-GAP3(:,4);

%**CALCULATE G USING VCCT**
k=1;
for j=1:ns
    for m=1:(2*nq1+1)
        if m==1                 % node at spoke edge
            dA(k,i) = (1/2)*(det([CTIP1(k,2),CTIP3(k,2);CTIP1(k,3),CTIP3(k,3)])+det([CTIP3(k,2),CTIP3(k+1,2);CTIP3(k,3),CTIP3(k+1,3)])+
                        det([CTIP3(k+1,2),CTIP1(k+1,2);CTIP3(k+1,3),CTIP1(k+1,3)])+det([CTIP1(k+1,2),CTIP1(k,2);CTIP1(k+1,3),CTIP1(k,3)]));
            pt1 = k;
            pt2 = (nq1+1)*(j-1)+(m-1)/2+1;
            pt3 = k+1;

            G1 =       RFB(pt1,i)*(GAP3(pt1,5)+(D1B(pt1,i)-D2B(pt1,i)));
            G2 =       RFA(pt2,i)*(GAP2(pt2,5)+(D1A(pt2,i)-D2A(pt2,i)));
            G3 = (1/2)*RFB(pt3,i)*(GAP3(pt3,5)+(D1B(pt3,i)-D2B(pt3,i)));

            GVCCT(k,i) = 1/2/dA(k,i)*(G1+G2+G3);
            k=k+1;
        elseif m==2              % midside node 1 in from the spoke edge
            dA1 = (1/2)*(det([CTIP1(k,2),CTIP3(k,2);CTIP1(k,3),CTIP3(k,3)])+det([CTIP3(k,2),CTIP3(k+1,2);CTIP3(k,3),CTIP3(k+1,3)])+
                    det([CTIP3(k+1,2),CTIP1(k+1,2);CTIP3(k+1,3),CTIP1(k+1,3)])+det([CTIP1(k+1,2),CTIP1(k,2);CTIP1(k+1,3),CTIP1(k,3)]));
            dA2 = (1/2)*(det([CTIP1(k-1,2),CTIP3(k-1,2);CTIP1(k-1,3),CTIP3(k-1,3)])+det([CTIP3(k-1,2),CTIP3(k,2);CTIP3(k-1,3),CTIP3(k,3)])+
                    det([CTIP3(k,2),CTIP1(k,2);CTIP3(k,3),CTIP1(k,3)])+det([CTIP1(k,2),CTIP1(k-1,2);CTIP1(k,3),CTIP1(k-1,3)]));
            dA(k,i) = dA1+dA2;

            pt1 = k-1;
            pt2 = k;
            pt3 = k+1;
            pt4 = (nq1+1)*(j-1)+m/2;
            pt5 = (nq1+1)*(j-1)+m/2+1;

            G1 =       RFB(pt1,i)*(GAP3(pt1,5)+(D1B(pt1,i)-D2B(pt1,i)));
            G2 =       RFB(pt2,i)*(GAP3(pt2,5)+(D1B(pt2,i)-D2B(pt2,i)));
            G3 = (1/2)*RFB(pt3,i)*(GAP3(pt3,5)+(D1B(pt3,i)-D2B(pt3,i)));
            G4 =       RFA(pt4,i)*(GAP2(pt4,5)+(D1A(pt4,i)-D2A(pt4,i)));
            G5 = (1/2)*RFA(pt5,i)*(GAP2(pt5,5)+(D1A(pt5,i)-D2A(pt5,i)));

            GVCCT(k,i) = 1/2/dA(k,i)*(G1+G2+G3+G4+G5);
            k=k+1;
        elseif m<2*nq1
            if rem(m,2)==0      % midside nodes
                dA1 = (1/2)*(det([CTIP1(k,2),CTIP3(k,2);CTIP1(k,3),CTIP3(k,3)])+det([CTIP3(k,2),CTIP3(k+1,2);CTIP3(k,3),CTIP3(k+1,3)])+
                        det([CTIP3(k+1,2),CTIP1(k+1,2);CTIP3(k+1,3),CTIP1(k+1,3)])+det([CTIP1(k+1,2),CTIP1(k,2);CTIP1(k+1,3),CTIP1(k,3)]));
                dA2 = (1/2)*(det([CTIP1(k-1,2),CTIP3(k-1,2);CTIP1(k-1,3),CTIP3(k-1,3)])+det([CTIP3(k-1,2),CTIP3(k,2);CTIP3(k-1,3),CTIP3(k,3)])+
                        det([CTIP3(k,2),CTIP1(k,2);CTIP3(k,3),CTIP1(k,3)])+det([CTIP1(k,2),CTIP1(k-1,2);CTIP1(k,3),CTIP1(k-1,3)]));
                dA(k,i) = dA1+dA2;

                pt1 = k-1;
                pt2 = k;
                pt3 = k+1;
                pt4 = (nq1+1)*(j-1)+m/2;
                pt5 = (nq1+1)*(j-1)+m/2+1;

                G1 = (1/2)*RFB(pt1,i)*(GAP3(pt1,5)+(D1B(pt1,i)-D2B(pt1,i)));
                G2 =       RFB(pt2,i)*(GAP3(pt2,5)+(D1B(pt2,i)-D2B(pt2,i)));
                G3 = (1/2)*RFB(pt3,i)*(GAP3(pt3,5)+(D1B(pt3,i)-D2B(pt3,i)));
                G4 = (1/2)*RFA(pt4,i)*(GAP2(pt4,5)+(D1A(pt4,i)-D2A(pt4,i)));
                G5 = (1/2)*RFA(pt5,i)*(GAP2(pt5,5)+(D1A(pt5,i)-D2A(pt5,i)));
                GVCCT(k,i) = 1/2/dA(k,i)*(G1+G2+G3+G4+G5);
            else                % corner nodes
                dA1 = (1/2)*(det([CTIP1(k,2),CTIP3(k,2);CTIP1(k,3),CTIP3(k,3)])+det([CTIP3(k,2),CTIP3(k+1,2);CTIP3(k,3),CTIP3(k+1,3)])+
                        det([CTIP3(k+1,2),CTIP1(k+1,2);CTIP3(k+1,3),CTIP1(k+1,3)])+det([CTIP1(k+1,2),CTIP1(k,2);CTIP1(k+1,3),CTIP1(k,3)]));
                dA2 = (1/2)*(det([CTIP1(k-1,2),CTIP3(k-1,2);CTIP1(k-1,3),CTIP3(k-1,3)])+det([CTIP3(k-1,2),CTIP3(k,2);CTIP3(k-1,3),CTIP3(k,3)])+
                        det([CTIP3(k,2),CTIP1(k,2);CTIP3(k,3),CTIP1(k,3)])+det([CTIP1(k,2),CTIP1(k-1,2);CTIP1(k,3),CTIP1(k-1,3)]));
                dA(k,i) = dA1+dA2;

                pt1 = k-1;
                pt2 = k;
                pt3 = (nq1+1)*(j-1)+(m-1)/2+1;
                pt4 = k+1;

                G1 = (1/2)*RFB(pt1,i)*(GAP3(pt1,5)+(D1B(pt1,i)-D2B(pt1,i)));
                G2 =       RFB(pt2,i)*(GAP3(pt2,5)+(D1B(pt2,i)-D2B(pt2,i)));
                G3 =       RFA(pt3,i)*(GAP2(pt3,5)+(D1A(pt3,i)-D2A(pt3,i)));
                G4 = (1/2)*RFB(pt4,i)*(GAP3(pt4,5)+(D1B(pt4,i)-D2B(pt4,i)));

                GVCCT(k,i) = 1/2/dA(k,i)*(G1+G2+G3+G4);
            end
            k=k+1;
        elseif m<2*nq1+1        % midside node 1 from other spoke edge
```

```
            dA1 = (1/2)*(det([CTIP1(k,2),CTIP3(k,2);CTIP1(k,3),CTIP3(k,3)])+det([CTIP3(k,2),CTIP3(k+1,2);CTIP3(k,3),CTIP3(k+1,3)])+
                   det([CTIP3(k+1,2),CTIP1(k+1,2);CTIP3(k+1,3),CTIP1(k+1,3)])+det([CTIP1(k+1,2),CTIP1(k,2);CTIP1(k+1,3),CTIP1(k,3)]));
            dA2 = (1/2)*(det([CTIP1(k-1,2),CTIP3(k-1,2);CTIP1(k-1,3),CTIP3(k-1,3)])+det([CTIP3(k-1,2),CTIP3(k,2);CTIP3(k-1,3),CTIP3(k,3)])+
                   det([CTIP3(k,2),CTIP1(k,2);CTIP3(k,3),CTIP1(k,3)])+det([CTIP1(k,2),CTIP1(k-1,2);CTIP1(k,3),CTIP1(k-1,3)]));
            dA(k,i) = dA1+dA2;

            pt1 = k-1;
            pt2 = k;
            pt3 = k+1;
            pt4 = (nq1+1)*(j-1)+m/2;
            pt5 = (nq1+1)*(j-1)+m/2+1;

            G1 = (1/2)*RFB(pt1,i)*(GAP3(pt1,5)+(D1B(pt1,i)-D2B(pt1,i)));
            G2 =       RFB(pt2,i)*(GAP3(pt2,5)+(D1B(pt2,i)-D2B(pt2,i)));
            G3 =       RFB(pt3,i)*(GAP3(pt3,5)+(D1B(pt3,i)-D2B(pt3,i)));
            G4 = (1/2)*RFA(pt4,i)*(GAP2(pt4,5)+(D1A(pt4,i)-D2A(pt4,i)));
            G5 =       RFA(pt5,i)*(GAP2(pt5,5)+(D1A(pt5,i)-D2A(pt5,i)));

            GVCCT(k,i) = 1/2/dA(k,i)*(G1+G2+G3+G4+G5);
            k=k+1;
        else                    % node at other spoke edge
            dA(k,i) = (1/2)*(det([CTIP1(k-1,2),CTIP3(k-1,2);CTIP1(k-1,3),CTIP3(k-1,3)])+det([CTIP3(k-1,2),CTIP3(k,2);CTIP3(k-1,3),CTIP3(k,3)])+
                       det([CTIP3(k,2),CTIP1(k,2);CTIP3(k,3),CTIP1(k,3)])+det([CTIP1(k,2),CTIP1(k-1,2);CTIP1(k,3),CTIP1(k-1,3)]));
            pt1 = k;
            pt2 = (nq1+1)*(j-1)+(m-1)/2+1;
            pt3 = k-1;

            G1 =       RFB(pt1,i)*(GAP3(pt1,5)+(D1B(pt1,i)-D2B(pt1,i)));
            G2 =       RFA(pt2,i)*(GAP2(pt2,5)+(D1A(pt2,i)-D2A(pt2,i)));
            G3 = (1/2)*RFB(pt3,i)*(GAP3(pt3,5)+(D1B(pt3,i)-D2B(pt3,i)));

            GVCCT(k,i) = 1/2/dA(k,i)*(G1+G2+G3);
            k=k+1;
        end
    end
    %--area weighted average of G on each spoke--
    G(j,i) = sum(GVCCT((k-2*nq1-1):(k-1),i).*dA((k-2*nq1-1):(k-1),i))/sum(dA((k-2*nq1-1):(k-1),i));
end

%**Plot front shape and G variation
figure(3); clf;

subplot(2,2,1)
TPL=[0 : 2*pi/ns : 2*pi]';
BPL=[B(:,i); B(1,i)];
plot(BPL.*cos(TPL),BPL.*sin(TPL));
title('Bond front shape')
axis square

subplot(2,2,2)
plot((1:ns),G,(1:ns),G(:,i),'ro')
title('G variation')
xlabel('spoke number')
ylabel('G J/m^2')
axis square

%**Check Convergence Criterion**
dG(:,i) = G(:,i)-GC;                    % difference between actual and target G

if max(abs(dG(:,i)))<G_conv             % if convergence criterion satisfied, print results and pause
    FINAL = [B(:,i), G(:,i), dG(:,i)]
    pause
end

%**Predict new bond shape**
F(:,i) = (G(:,i)./GC)-1;                % residuals at each spoke
Favg(i,1) = mean(F(:,i))

subplot(2,2,3)
plot((1:ns),F,(1:ns),F(:,i),'ro')
title('Residuals')
xlabel('spoke number')
ylabel('F')
axis square

subplot(2,2,4)
plot((1:i)',Favg,'ro-')
title('Average Residuals')
xlabel('average residual')
ylabel('iteration')
axis square

if i==1
    for r=1:ns
        for s=1:ns
            if r==s
                J(r,s)=1;
```

```
                else
                    J(r,s)=0;
                end
            end
        end

        Bp = J;                             % Jacobian for this step
        Rinc = -J\F(:,i);                   % radial increment in bond front position

        if max(abs(Rinc))>dr_lim            % check if step size too big for mesh
            beta = dr_lim/max(abs(Rinc));   % scale so max Rinc will be dr_lim
        else
            beta=1;
        end
        B(:,i+1) = B(:,i)+Rinc*beta;        % new radial positions
    else
        dR(:,i-1) = B(:,i)-B(:,i-1);
        dF(:,i-1) = F(:,i)-F(:,i-1);

        BROY = Bp + ((dF(:,i-1)-Bp*dR(:,i-1))*dR(:,i-1)')/(dR(:,i-1)'*dR(:,i-1));   % update Jacobian
        Rinc = -BROY\F(:,i);

        if max(abs(Rinc))>dr_lim            % check if step size too big for mesh
            beta = dr_lim/max(abs(Rinc));   % scale so max Rinc will be dr_lim
        else
            beta=1;
        end
        B(:,i+1) = B(:,i)+Rinc*beta;        % new radial positions
        Bp=BROY;                            % store current Jacobian for next step
    end

end
```

spoke_06.m

```
function [AT, nq1] = spoke_06(B,ns)

% function reads in b which descibes the bond front position
% function outputs:
%  - AT is total bonded area
%  - nq1 is number of elements in each spoke
%  - ns is number of spokes

% This m-file generates a .inp file which contains an ABAQUS model of a the bonding of wafers
% The geometry is setup such that a spoke pattern is on the surface

% Kevin Turner
% Original: 18 October 2003
% Updated: 15 December 2003

%**DEFINE BASIC GEOMETRY**
c = 50.0e-3;                % wafer radius (m)
fl = 32.50e-3;              % flat length (m)

%**DEFINE ETCH PATTERN GEOMETRY**
Ro = 0.14;                  % non-dimensional diameter of initial unetched area
cT = 0.3;                   % taper ratio of spokes (non-dimensional)

%**ELASTIC PROPERTIES**
C11 = 166.2e9;              % 11 stiffness coefficient (Pa)
C12 = 64.4e9;               % 12 stiffness coefficient (Pa)
C44 = 79.8e9;               % 44 stiffness coefficient (Pa)
den = 2330;                 % density in kg/m^3

%**DEFINE MESH PARAMETERS**
nr1 = 1;                    % number of elements in radial direction in section 1 (has to be 1)
nr2 = 2;                    % number of elements in radial direction in section 2
nr34 = 1;                   % number of elements in radial direction in sections 3 and 4 (has to be 1)
nr78 = 4;                   % number of elements in radial direction in sections 7 and 8 (crack front region)
nr5690 = 8;                 % total number of elements in radial direction in sections 56 and 90

nq1 = 4;                    % number of elements in theta direction in each spoke (avoid odd numbers)
nq2 = 3;                    % number of elements in theta direction in sections between spoke

nz1 = 2;                    % number of elements through the thickness of wafer 1
nz2 = 2;                    % number of elements through the thickness of wafer 2

rs1 = 2.0e-3;               % radius of section 1 (mm)
rs34 = 3.0e-3;              % radius of sections 3 & 4 (mm)
wyc = 5.0e-3;               % width of refined zone near crack tip (mm)

B=B'; B(1,length(B)+1)=B(1,1);  % add extra point on B vector so it goes from 0 to 2pi

%--calculate number of elents in sections 56 and 90
bavg = mean(B); nr56 = ceil(((bavg-wyc/2-rs34-c*Ro)/(c*(1-Ro)-rs34-wyc))*nr5690); if nr56 < 1
```

```
    nr56 = 1;
elseif nr56 == nr5690;
    nr56 = nr5690-1;
end nr90 = nr5690-nr56;

nrinc = 1000;              % increment in node numbers from one radius to the next
nzinc = 100000;            % increment in node numbers from one layer of nodes to the next
nwinc = 1000000;           % increment in node numbers between wafers
ndinc = 9900000;           % increment in node numbers for dummy nodes

%**LAYOUT GRID**
%---Sections 1,2,3,4----
R1 = [0 : rs1/(2*nr1) : rs1]';                                % radial positions of nodes in section 1
R2 = [rs1 : (Ro*c-rs1)/(2*nr2) : Ro*c]';                      % radial positions of nodes in section 2
R34 = [Ro*c : rs34/(2*nr34) : Ro*c+rs34]';                    % radial positions of nodes in sections 3 and 4
Q12 = [0 : 2*pi/(2*nq1*ns) : 2*pi]';                          % theta positions of nodes in sections 1 and 2
QS = [0 : 2*pi/(ns) : 2*pi]';                                 % theta positions of line at center of each spoke
QSC = (QS(1:ns,1)+QS(2:ns+1,1))/2.0;                          % theta positions of line in the middle of the two spokes
S3 = (Ro/(Ro-1))*2*pi/ns*((1-cT)*(R34/c)+(Ro*cT-1))*c;       % arc length of each spoke at each radial position in section 3
%---Section 7---
k=1; for i=1:ns+1
    RS7(:,i) = [B(1,i)-wyc/2 : wyc/(2*nr78) : B(1,i)+wyc/2]';                        % radial positions for each spoke in section 7
    DQ7(:,i) = (Ro/(Ro-1))*2*pi/ns*((1-cT)*(RS7(:,i)/c)+(Ro*cT-1))*c./RS7(:,i);     % included angle at each radius in section 7
    for j=1:2*nq1+1;
        R7(:,k) = RS7(:,i);                                                          % radial positions in crack front region, section 7
        Q7(:,k) = QS(i,1)*ones(2*nr78+1,1)+DQ7(:,i)*(j-nq1-1)/(2*nq1);              % angular postions in crack front region
        k=k+1;
    end
end RS7(:,i+1) = RS7(:,1); DQ7(:,i+1) = DQ7(:,1);
%---Section 5---
k=1; for i=1:ns+1
    RS5(:,i) = [R34(nr34*2+1,1) : (RS7(1,i)-R34(nr34*2+1,1))/(nr56*2) : RS7(1,i)]'; % radial positions for each node at center of spoke in sec 5
    DQ5(:,i) = (Ro/(Ro-1))*2*pi/ns*((1-cT)*(RS5(:,i)/c)+(Ro*cT-1))*c./RS5(:,i);     % included angle at each radius in section 5
    for j=1:2*nq1+1
        R5(:,k) = RS5(:,i);
        Q5(:,k) = QS(i,1)*ones(2*nr56+1,1)+DQ5(:,i)*(j-nq1-1)/(2*nq1);              % angular postions in crack front region
        k=k+1;
    end
end
%---Section 9---
k=1; for i=1:ns+1
    if (QS(i,1) > (3*pi/2-asin(fl/2/c))) & (QS(i,1) < (3*pi/2+asin(fl/2/c)))
       cf = ((c^2-1/4*fl^2)^0.5)/cos(3*pi/2-QS(i,1));
       RS9(:,i) = [RS7(nr78*2+1,i) : (cf-RS7(nr78*2+1,i))/(nr90*2) : cf]';
       DQ9(:,i) = (Ro/(Ro-1))*2*pi/ns*((1-cT)*(RS9(:,i)/c)+(Ro*cT-1))*c./RS9(:,i);
       for j=1:2*nq1+1
           R9(:,k) = RS9(:,i);
           Q9(:,k) = QS(i,1)*ones(2*nr90+1,1)+DQ9(:,i)*(j-nq1-1)/(2*nq1);
           k=k+1;
       end
   else
       RS9(:,i) = [RS7(nr78*2+1,i) : (c-RS7(nr78*2+1,i))/(nr90*2) : c]';
       DQ9(:,i) = (Ro/(Ro-1))*2*pi/ns*((1-cT)*(RS9(:,i)/c)+(Ro*cT-1))*c./RS9(:,i);
       for j=1:2*nq1+1
           R9(:,k) = RS9(:,i);
           Q9(:,k) = QS(i,1)*ones(2*nr90+1,1)+DQ9(:,i)*(j-nq1-1)/(2*nq1);
           k=k+1;
       end
   end
end
%---Section 8---
k=1; for i=1:ns
    VA = [Ro*c*cos(QSC(i,1)) Ro*c*sin(QSC(i,1))];                                                    % local origin for mesh region
    VB = [R7(:,(2*nq1+1)*i).*cos(Q7(:,(2*nq1+1)*i)) , R7(:,(2*nq1+1)*i).*sin(Q7(:,(2*nq1+1)*i))];        % begin point for region for each radius
    VC = [R7(:,(2*nq1+1)*i+1).*cos(Q7(:,(2*nq1+1)*i+1)) , R7(:,(2*nq1+1)*i+1).*sin(Q7(:,(2*nq1+1)*i+1))]; % end point for region for each radius
    VAB = VB-[VA(1,1)*ones(length(VB),1), VA(1,2)*ones(length(VB),1)];                               % start point relative to local origin
    VAC = VC-[VA(1,1)*ones(length(VC),1), VA(1,2)*ones(length(VC),1)];                               % end point relative to local origin
    [LRB, LQB] = carttopolar(VAB(:,1),VAB(:,2));
    [LRC, LQC] = carttopolar(VAC(:,1),VAC(:,2));
    DQBC = acos(diag(VAB*VAC')./(diag(VAB*VAB').*diag(VAC*VAC')).^0.5);
    for j=2:2*nq2
        LR8 = LRB + (LRC-LRB)*(j-1)/(2*nq2);
        LQ8 = LQB + (DQBC)*(j-1)/(2*nq2);
        X8(:,k) = LR8.*cos(LQ8) + VA(1,1);
        Y8(:,k) = LR8.*sin(LQ8) + VA(1,2);
        k=k+1;
    end
end
%---Section 6---
k=1; for i=1:ns
    VA = [Ro*c*cos(QSC(i,1)) Ro*c*sin(QSC(i,1))];                                                    % local origin for mesh region
    VB = [R5(:,(2*nq1+1)*i).*cos(Q5(:,(2*nq1+1)*i)) , R5(:,(2*nq1+1)*i).*sin(Q5(:,(2*nq1+1)*i))];        % begin point for region for each radius
    VC = [R5(:,(2*nq1+1)*i+1).*cos(Q5(:,(2*nq1+1)*i+1)) , R5(:,(2*nq1+1)*i+1).*sin(Q5(:,(2*nq1+1)*i+1))]; % end point for region for each radius
    VAB = VB-[VA(1,1)*ones(length(VB),1), VA(1,2)*ones(length(VB),1)];                               % start point relative to local origin
    VAC = VC-[VA(1,1)*ones(length(VC),1), VA(1,2)*ones(length(VC),1)];                               % end point relative to local origin
    [LRB, LQB] = carttopolar(VAB(:,1),VAB(:,2));
    [LRC, LQC] = carttopolar(VAC(:,1),VAC(:,2));
```

```
    DQBC = acos(diag(VAB*VAC').(diag(VAB*VAB').*diag(VAC*VAC')).^0.5);
    for j=2:2*nq2
        LR6 = LRB + (LRC-LRB)*(j-1)/(2*nq2);
        LQ6 = LQB + (DQBC)*(j-1)/(2*nq2);
        X6(:,k) = LR6.*cos(LQ6) + VA(1,1);
        Y6(:,k) = LR6.*sin(LQ6) + VA(1,2);
        k=k+1;
    end
end
%---Section 10---
k=1; for i=1:ns
    VA = [Ro*c*cos(QSC(i,1)) Ro*c*sin(QSC(i,1))];                                                  % local origin for mesh region
    VB = [R9(:,(2*nq1+1)*i).*cos(Q9(:,(2*nq1+1)*i)) , R9(:,(2*nq1+1)*i).*sin(Q9(:,(2*nq1+1)*i))];         % begin point for region for each radius
    VC = [R9(:,(2*nq1+1)*i+1).*cos(Q9(:,(2*nq1+1)*i+1)) , R9(:,(2*nq1+1)*i+1).*sin(Q9(:,(2*nq1+1)*i+1))]; % end point for region for each radius
    VAB = VB-[VA(1,1)*ones(length(VB),1), VA(1,2)*ones(length(VB),1)];                                  % start point relative to local origin
    VAC = VC-[VA(1,1)*ones(length(VC),1), VA(1,2)*ones(length(VC),1)];                                  % end point relative to local origin
    [LRB, LQB] = carttopolar(VAB(:,1),VAB(:,2));
    [LRC, LQC] = carttopolar(VAC(:,1),VAC(:,2));
    DQBC = acos(diag(VAB*VAC').(diag(VAB*VAB').*diag(VAC*VAC')).^0.5);
    for j=2:2*nq2
        LR10 = LRB + (LRC-LRB)*(j-1)/(2*nq2);
        LQ10 = LQB + (DQBC)*(j-1)/(2*nq2);
        X10(:,k) = LR10.*cos(LQ10) + VA(1,1);
        Y10(:,k) = LR10.*sin(LQ10) + VA(1,2);
        k=k+1;
    end
end
for i=1:ns*(2*nq2-1)                                        % this loop adjusts positions of nodes on perimeter
    [RE TE] = carttopolar(X10(nr90*2+1,i),Y10(nr90*2+1,i));
    if (TE > (3*pi/2-asin(fl/2/c))) & (TE < (3*pi/2+asin(fl/2/c)))
        Y10(nr90*2+1,i) = -(c^2-(fl/2)^2)^0.5;
        X10(nr90*2+1,i) = -Y10(nr90*2+1,i)*tan(TE-3*pi/2);
    else
        X10(nr90*2+1,i) = c*cos(TE);
        Y10(nr90*2+1,i) = c*sin(TE);
    end
end

%**GENERATE X-Y GRID**
%---Section 1---
N1(1,:) = [1, 0.0, 0.0]; k = 2; for i=1:(2*nr1)
    for j=1:(2*nq1*ns)
        N1(k,1) = nrinc*i+j;
        N1(k,2) = R1(i+1,1)*cos(Q12(j,1));
        N1(k,3) = R1(i+1,1)*sin(Q12(j,1));
        k=k+1;
        nrt1 = nrinc*i;
    end
end
%---Section 2---
k=1; for i=1:(2*nr2)
    for j=1:(2*nq1*ns)
        N2(k,1) = nrt1+nrinc*(i)+j;
        N2(k,2) = R2(i+1,1)*cos(Q12(j,1));
        N2(k,3) = R2(i+1,1)*sin(Q12(j,1));
        k=k+1;
        nrt2 = nrt1+nrinc*i;
    end
end
%---Sections 3&4---
k=1; p=1; for i=2:(2*nr34)
    r=1;
    for j=1:ns
        for m=1:(nq1*2+1)
            Q3(k,1) = (QS(j,1)+S3(i,1)/R34(i,1)*(m-nq1-1)/(nq1*2));
            N3(k,1) = nrt2+nrinc*(i-1)+r;
            N3(k,2) = R34(i,1)*cos(Q3(k,1));
            N3(k,3) = R34(i,1)*sin(Q3(k,1));
            k=k+1; r=r+1;
        end
        for m=2:(nq2*2)
            Q4(p,1) = ((QS(j+1,1)-S3(i,1)/R34(i,1)/2)-(QS(j,1)+S3(i,1)/R34(i,1)/2))*(m-1)/(nq2*2)+(QS(j,1)+S3(i,1)/R34(i,1)/2);
            N4(p,1) = nrt2+nrinc*(i-1)+r;
            N4(p,2) = R34(i,1)*cos(Q4(p,1));
            N4(p,3) = R34(i,1)*sin(Q4(p,1));
            p=p+1; r=r+1;
            nrt34 = nrt2+nrinc*(i-1);
        end
    end
end
%---Sections 5&6---
k=1; p=1; r=1; for i=1:(2*nr56)
    r=1;
    for m=1:ns
        for j=1:(2*nq1+1)
            N5(k,1) = nrt34+nrinc*i+r;
            N5(k,2) = R5(i,((m-1)*(2*nq1+1)+j))*cos(Q5(i,((m-1)*(2*nq1+1)+j)));
```

```
            N5(k,3) = R5(i,((m-1)*(2*nq1+1)+j))*sin(Q5(i,((m-1)*(2*nq1+1)+j)));
            k=k+1; r=r+1;
        end
        for j=1:(2*nq2-1)
            N6(p,1) = nrt34+nrinc*i+r;
            N6(p,2) = X6(i,((m-1)*(2*nq2-1)+j));
            N6(p,3) = Y6(i,((m-1)*(2*nq2-1)+j));
            p=p+1; r=r+1;
            nrt56 = nrt34+nrinc*i;
        end
    end
end
%---Sections 7&8---
k=1; p=1; for i=1:(2*nr78+1)
    r=1;
    for m=1:ns
        for j=1:(2*nq1+1)
            N7(k,1) = nrt56+nrinc*i+r;
            N7(k,2) = R7(i,((m-1)*(2*nq1+1)+j))*cos(Q7(i,((m-1)*(2*nq1+1)+j)));
            N7(k,3) = R7(i,((m-1)*(2*nq1+1)+j))*sin(Q7(i,((m-1)*(2*nq1+1)+j)));
            k=k+1; r=r+1;
        end
        for j=1:(2*nq2-1)
            N8(p,1) = nrt56+nrinc*i+r;
            N8(p,2) = X8(i,((m-1)*(2*nq2-1)+j));
            N8(p,3) = Y8(i,((m-1)*(2*nq2-1)+j));
            p=p+1; r=r+1;
            nrt78 = nrt56+nrinc*i;
        end
    end
end
%---Sections 9&10---
k=1; p=1; for i=2:(2*nr90+1)
    r=1;
    for m=1:ns
        for j=1:((2*nq1+1))
            N9(k,1) = nrt78+nrinc*(i-1)+r;
            N9(k,2) = R9(i,((m-1)*(2*nq1+1)+j))*cos(Q9(i,((m-1)*(2*nq1+1)+j)));
            N9(k,3) = R9(i,((m-1)*(2*nq1+1)+j))*sin(Q9(i,((m-1)*(2*nq1+1)+j)));
            k=k+1; r=r+1;
        end
        for j=1:((2*nq2-1))
            N10(p,1) = nrt78+nrinc*(i-1)+r;
            N10(p,2) = X10(i,((m-1)*(2*nq2-1)+j));
            N10(p,3) = Y10(i,((m-1)*(2*nq2-1)+j));
            p=p+1; r=r+1;
        end
    end
end

%**PLOT GRID**
wout = wafer_outline(2*c,fl); figure(1); clf;
plot(N1(:,2),N1(:,3),'k.',N2(:,2),N2(:,3),'r.',N3(:,2),N3(:,3),'b.',N4(:,2),N4(:,3),'g.',N5(:,2),N5(:,3),'m.',N6(:,2),N6(:,3),'k.',N7(:,2),
     N7(:,3),'c.',N8(:,2),N8(:,3),'y.',N9(:,2),N9(:,3),'k.',N10(:,2),N10(:,3),'g.',wout(:,1),wout(:,2),'r-')
axis square axis([-c c -c c])

%***GET Z AND H VALUES***
NA = [N1; N2; N3; N4; N5; N6; N7; N8; N9; N10];                       % matrix containing [node number, X, Y] of all nodes in first layer

figure(2); clf;
%--wafer 1 (top wafer)---
Z1 = [getz1(NA(:,2),NA(:,3))];                                        % position of center plane of wafer 1
H1 = [geth1(NA(:,2),NA(:,3))];                                        % thickness of wafer 1
for i=1:nz1*2+1
    NZ1(:,i) = Z1+H1./(2.*nz1).*(i-nz1-1);                            % z positions of each node in layer1
end
NZ1 = NZ1-ones(size(NZ1))*NZ1(1,1);                                   % adjust layer 1 data so x=0, y=0 is z=0 at bonding surface
%--wafer 2 (bottom wafer)---
Z2 = [getz2(NA(:,2),NA(:,3))];                                        % position of center plane of wafer 2
H2 = [geth2(NA(:,2),NA(:,3))];                                        % thickness of wafer 2
for i=1:nz2*2+1
    NZ2(:,i) = Z2+H2./(2.*nz2).*(i-nz2-1);                            % z positions of each node in layer2
end
NZ2 = NZ2-ones(size(NZ2))*(NZ2(1,1))-H2(1,1);                         % adjust layer 1 data so x=0, y=0 is z=0 at bonding surface

%***MAKE NODE SETS FOR INTERFACE AND LOADING***
NINT1 = [N1; N2; N3; N5; N7(1:(2*nq1+1)*ns*(nr78+1),:)];              % nodes to be bonded on wafer 1
NINT1 = NINT1(2:length(NINT1),:);                                     % eliminate node 1 from data set - NINT1 is a vector with
                                                                      % [node #, x-pos, y-pos] of nodes at interface to be bonded

%--get distance between nodes at interface--
wtbar = waitbar(0,'Please wait...'); for i=1:length(NZ1)
    for j=1:length(NINT1)
        if NINT1(j,1) == NA(i,1)
            DELTA(j,1) = NZ1(i,1)-NZ2(i,2*nz2+1);
        end
    end
```

```
    waitbar(i/length(NZ1),wtbar)
end close(wtbar)

%--create loading and equation vectors-- (use loop to eliminate constraints on nodes in middle of elements)
k=1; p=1; for i=1:((nr1+nr2+nr34+nr56+nr78/2)*2)
    if i <= (nr1+nr2)*2
        for j=1:((nq1*2*ns))
            if (rem(i,2)~=0)&(rem(j,2)==0)
                p=p+1;
            else
                NEQ(k,:) = [NINT1(p,1), 3, -1.0, (NINT1(p,1)+nwinc+2*nz2*nzinc), 3, 1.0, NINT1(p,1)+ndinc,3,-1.0];
                NLOAD(k,:) = [NINT1(p,1)+ndinc, 3, DELTA(p,1)];
                k=k+1; p=p+1;
            end
        end
    else
        for j=1:ns
            for m=1:2*nq1+1
                if (rem(i,2)~=0)&(rem(m,2)==0)
                    p=p+1;
                else
                    NEQ(k,:) = [NINT1(p,1), 3, -1.0, (NINT1(p,1)+nwinc+2*nz2*nzinc), 3, 1.0, NINT1(p,1)+ndinc,3,-1.0];
                    NLOAD(k,:) = [NINT1(p,1)+ndinc, 3, DELTA(p,1)];
                    k=k+1; p=p+1;
                end
            end
        end
    end
end

%***GENERATE ELEMENT VECTORS
%---section 1---
k=1; p=1; for i=1:nr1
    for j=1:nq1*ns
        EL1(k,1) = p;
        EL1(k,2) = N1(1,1);
        EL1(k,3) = (2*i)*nrinc+(2*j-1);
        if j~=nq1*ns
            EL1(k,4) = EL1(k,3)+2;
        else
            EL1(k,4) = EL1(1,3);
        end
        EL1(k,5) = EL1(k,2)+2*nzinc;
        EL1(k,6) = EL1(k,3)+2*nzinc;
        EL1(k,7) = EL1(k,4)+2*nzinc;
        EL1(k,8) = EL1(k,3)-nrinc;
        EL1(k,9) = EL1(k,3)+1;
        EL1(k,10) = EL1(k,4)-nrinc;
        EL1(k,11) = EL1(k,8)+2*nzinc;
        EL1(k,12) = EL1(k,9)+2*nzinc;
        EL1(k,13) = EL1(k,10)+2*nzinc;
        EL1(k,14) = EL1(k,2)+nzinc;
        EL1(k,15) = EL1(k,3)+nzinc;
        EL1(k,16) = EL1(k,4)+nzinc;
        k=k+1; p=p+1;
    end
end
%---section 2---
k=1; for i=1:nr2
    for j=1:nq1*ns
        EL2(k,1) = p;
        EL2(k,2) = N2(1,1)+nrinc*(2*(i-1)-1)+2*(j-1);
        EL2(k,3) = EL2(k,2)+nrinc*2;
        if j~=nq1*ns
            EL2(k,4) = EL2(k,3)+2;
        else
            EL2(k,4) = N2(1,1)+nrinc*(2*(i-1)+1);
        end
        EL2(k,5) = EL2(k,4)-nrinc*2;
        EL2(k,6) = EL2(k,2)+2*nzinc;
        EL2(k,7) = EL2(k,3)+2*nzinc;
        EL2(k,8) = EL2(k,4)+2*nzinc;
        EL2(k,9) = EL2(k,5)+2*nzinc;
        EL2(k,10) = EL2(k,2)+nrinc;
        EL2(k,11) = EL2(k,3)+1;
        EL2(k,12) = EL2(k,4)-nrinc;
        EL2(k,13) = EL2(k,2)+1;
        EL2(k,14) = EL2(k,10)+2*nzinc;
        EL2(k,15) = EL2(k,11)+2*nzinc;
        EL2(k,16) = EL2(k,12)+2*nzinc;
        EL2(k,17) = EL2(k,13)+2*nzinc;
        EL2(k,18) = EL2(k,2)+nzinc;
        EL2(k,19) = EL2(k,3)+nzinc;
        EL2(k,20) = EL2(k,4)+nzinc;
        EL2(k,21) = EL2(k,5)+nzinc;
        k=k+1; p=p+1;
    end
```

```
end
%---section 3 and 4---
k=1; k1=1; for i=1:ns
    for j=1:nq1
        EL3(k,1) = p;
        if i == 1
            if j <= nq1/2-1
                EL3(k,2) = N3(1,1)-nrinc+2*nq1*ns-nq1+2*(j-1);
                EL3(k,5) = EL3(k,2)+2;
            elseif j<=nq1/2
                EL3(k,2) = N3(1,1)-nrinc+2*nq1*ns-nq1+2*(j-1);
                EL3(k,5) = N3(1,1)-nrinc;
            else
                EL3(k,2) = N3(1,1)-nrinc+nq1+2*nq1*(i-2)+2*(j-1);
                EL3(k,5) = EL3(k,2)+2;
            end
        else
            EL3(k,2) = N3(1,1)-nrinc+nq1+2*nq1*(i-2)+2*(j-1);
            EL3(k,5) = EL3(k,2)+2;
        end
        EL3(k,3) = N3(1,1)+nrinc+2*(j-1)+2*(nq1+nq2)*(i-1);
        EL3(k,4) = EL3(k,3)+2;
        EL3(k,6) = EL3(k,2)+2*nzinc;
        EL3(k,7) = EL3(k,3)+2*nzinc;
        EL3(k,8) = EL3(k,4)+2*nzinc;
        EL3(k,9) = EL3(k,5)+2*nzinc;
        EL3(k,10) = EL3(k,3)-nrinc;
        EL3(k,11) = EL3(k,3)+1;
        EL3(k,12) = EL3(k,4)-nrinc;
        EL3(k,13) = EL3(k,2)+1;
        EL3(k,14) = EL3(k,10)+2*nzinc;
        EL3(k,15) = EL3(k,11)+2*nzinc;
        EL3(k,16) = EL3(k,12)+2*nzinc;
        EL3(k,17) = EL3(k,13)+2*nzinc;
        EL3(k,18) = EL3(k,2)+nzinc;
        EL3(k,19) = EL3(k,3)+nzinc;
        EL3(k,20) = EL3(k,4)+nzinc;
        EL3(k,21) = EL3(k,5)+nzinc;
        k=k+1; p=p+1;
    end
    for j=1:nq2
        EL4(k1,1) = p;
        EL4(k1,2) = N2(1,1)+(2*nr2-1)*nrinc+(nq1*2)*(i-1)+nq1;
        EL4(k1,3) = N4(1,1)-1+nrinc+(i-1)*(nq1*2+nq2*2)+2*(j-1);
        if i==ns & j==nq2
            EL4(k1,4) = N3(1,1)+nrinc;
        else
            EL4(k1,4) = EL4(k1,3)+2;
        end
        EL4(k1,5) = EL4(k1,2)+2*nzinc;
        EL4(k1,6) = EL4(k1,3)+2*nzinc;
        EL4(k1,7) = EL4(k1,4)+2*nzinc;
        EL4(k1,8) = EL4(k1,3)-nrinc;
        EL4(k1,9) = EL4(k1,3)+1;
        EL4(k1,10) = EL4(k1,4)-nrinc;
        EL4(k1,11) = EL4(k1,8)+2*nzinc;
        EL4(k1,12) = EL4(k1,9)+2*nzinc;
        EL4(k1,13) = EL4(k1,10)+2*nzinc;
        EL4(k1,14) = EL4(k1,2)+nzinc;
        EL4(k1,15) = EL4(k1,3)+nzinc;
        EL4(k1,16) = EL4(k1,4)+nzinc;
        k1=k1+1; p=p+1;
    end
end
%---sections 5 and 6---
k=1; k1=1; for m=1:nr56
    for i=1:1:ns
        for j=1:nq1
            EL5(k,1) = p;
            EL5(k,2) = N5(1,1)+2*nrinc*(m-1)+(2*(nq1+nq2))*(i-1)+2*(j-1);
            EL5(k,3) = EL5(k,2)+2*nrinc;
            EL5(k,4) = EL5(k,3)+2;
            EL5(k,5) = EL5(k,2)+2;
            EL5(k,6) = EL5(k,2)+2*nzinc;
            EL5(k,7) = EL5(k,3)+2*nzinc;
            EL5(k,8) = EL5(k,4)+2*nzinc;
            EL5(k,9) = EL5(k,5)+2*nzinc;
            EL5(k,10) = EL5(k,2)+nrinc;
            EL5(k,11) = EL5(k,3)+1;
            EL5(k,12) = EL5(k,5)+nrinc;
            EL5(k,13) = EL5(k,2)+1;
            EL5(k,14) = EL5(k,10)+2*nzinc;
            EL5(k,15) = EL5(k,11)+2*nzinc;
            EL5(k,16) = EL5(k,12)+2*nzinc;
            EL5(k,17) = EL5(k,13)+2*nzinc;
            EL5(k,18) = EL5(k,2)+nzinc;
            EL5(k,19) = EL5(k,3)+nzinc;
```

```
            EL5(k,20) = EL5(k,4)+nzinc;
            EL5(k,21) = EL5(k,5)+nzinc;
            k=k+1; p=p+1;
        end
        for j=1:nq2
            EL6(k1,1) = p;
            EL6(k1,2) = N6(1,1)+2*nrinc*(m-1)+(2*(nq1+nq2))*(i-1)+2*(j-1)-1;
            EL6(k1,3) = EL6(k1,2)+2*nrinc;
            if i==ns & j==nq2
                EL6(k1,4) = N5(1,1)+2*nrinc*(m);
            else
                EL6(k1,4) = EL6(k1,3)+2;
            end
            EL6(k1,5) = EL6(k1,4)-nrinc*2;
            EL6(k1,6) = EL6(k1,2)+2*nzinc;
            EL6(k1,7) = EL6(k1,3)+2*nzinc;
            EL6(k1,8) = EL6(k1,4)+2*nzinc;
            EL6(k1,9) = EL6(k1,5)+2*nzinc;
            EL6(k1,10) = EL6(k1,2)+nrinc;
            EL6(k1,11) = EL6(k1,3)+1;
            EL6(k1,12) = EL6(k1,5)+nrinc;
            EL6(k1,13) = EL6(k1,2)+1;
            EL6(k1,14) = EL6(k1,10)+2*nzinc;
            EL6(k1,15) = EL6(k1,11)+2*nzinc;
            EL6(k1,16) = EL6(k1,12)+2*nzinc;
            EL6(k1,17) = EL6(k1,13)+2*nzinc;
            EL6(k1,18) = EL6(k1,2)+nzinc;
            EL6(k1,19) = EL6(k1,3)+nzinc;
            EL6(k1,20) = EL6(k1,4)+nzinc;
            EL6(k1,21) = EL6(k1,5)+nzinc;
            k1=k1+1; p=p+1;
        end
    end
end
%---sections 7 and 8---
k=1; k1=1; for m=1:nr78
    for i=1:1:ns
        for j=1:nq1
            EL7(k,1) = p;
            EL7(k,2) = N7(1,1)+2*nrinc*(m-1)+(2*(nq1+nq2))*(i-1)+2*(j-1);
            EL7(k,3) = EL7(k,2)+2*nrinc;
            EL7(k,4) = EL7(k,3)+2;
            EL7(k,5) = EL7(k,2)+2;
            EL7(k,6) = EL7(k,2)+2*nzinc;
            EL7(k,7) = EL7(k,3)+2*nzinc;
            EL7(k,8) = EL7(k,4)+2*nzinc;
            EL7(k,9) = EL7(k,5)+2*nzinc;
            EL7(k,10) = EL7(k,2)+nrinc;
            EL7(k,11) = EL7(k,3)+1;
            EL7(k,12) = EL7(k,5)+nrinc;
            EL7(k,13) = EL7(k,2)+1;
            EL7(k,14) = EL7(k,10)+2*nzinc;
            EL7(k,15) = EL7(k,11)+2*nzinc;
            EL7(k,16) = EL7(k,12)+2*nzinc;
            EL7(k,17) = EL7(k,13)+2*nzinc;
            EL7(k,18) = EL7(k,2)+nzinc;
            EL7(k,19) = EL7(k,3)+nzinc;
            EL7(k,20) = EL7(k,4)+nzinc;
            EL7(k,21) = EL7(k,5)+nzinc;
            k=k+1; p=p+1;
        end
        for j=1:nq2
            EL8(k1,1) = p;
            EL8(k1,2) = N8(1,1)+2*nrinc*(m-1)+(2*(nq1+nq2))*(i-1)+2*(j-1)-1;
            EL8(k1,3) = EL8(k1,2)+2*nrinc;
            if i==ns & j==nq2
                EL8(k1,4) = N7(1,1)+2*nrinc*(m);
            else
                EL8(k1,4) = EL8(k1,3)+2;
            end
            EL8(k1,5) = EL8(k1,4)-nrinc*2;
            EL8(k1,6) = EL8(k1,2)+2*nzinc;
            EL8(k1,7) = EL8(k1,3)+2*nzinc;
            EL8(k1,8) = EL8(k1,4)+2*nzinc;
            EL8(k1,9) = EL8(k1,5)+2*nzinc;
            EL8(k1,10) = EL8(k1,2)+nrinc;
            EL8(k1,11) = EL8(k1,3)+1;
            EL8(k1,12) = EL8(k1,5)+nrinc;
            EL8(k1,13) = EL8(k1,2)+1;
            EL8(k1,14) = EL8(k1,10)+2*nzinc;
            EL8(k1,15) = EL8(k1,11)+2*nzinc;
            EL8(k1,16) = EL8(k1,12)+2*nzinc;
            EL8(k1,17) = EL8(k1,13)+2*nzinc;
            EL8(k1,18) = EL8(k1,2)+nzinc;
            EL8(k1,19) = EL8(k1,3)+nzinc;
            EL8(k1,20) = EL8(k1,4)+nzinc;
            EL8(k1,21) = EL8(k1,5)+nzinc;
```

```
            k1=k1+1; p=p+1;
        end
    end
end
%---sections 9 and 10---
k=1; k1=1; for m=1:nr90
    for i=1:1:ns
        for j=1:nq1
            EL9(k,1) = p;
            EL9(k,2) = N9(1,1)+2*nrinc*(m-1)-nrinc+(2*(nq1+nq2))*(i-1)+2*(j-1);
            EL9(k,3) = EL9(k,2)+2*nrinc;
            EL9(k,4) = EL9(k,3)+2;
            EL9(k,5) = EL9(k,2)+2;
            EL9(k,6) = EL9(k,2)+2*nzinc;
            EL9(k,7) = EL9(k,3)+2*nzinc;
            EL9(k,8) = EL9(k,4)+2*nzinc;
            EL9(k,9) = EL9(k,5)+2*nzinc;
            EL9(k,10) = EL9(k,2)+nrinc;
            EL9(k,11) = EL9(k,3)+1;
            EL9(k,12) = EL9(k,5)+nrinc;
            EL9(k,13) = EL9(k,2)+1;
            EL9(k,14) = EL9(k,10)+2*nzinc;
            EL9(k,15) = EL9(k,11)+2*nzinc;
            EL9(k,16) = EL9(k,12)+2*nzinc;
            EL9(k,17) = EL9(k,13)+2*nzinc;
            EL9(k,18) = EL9(k,2)+nzinc;
            EL9(k,19) = EL9(k,3)+nzinc;
            EL9(k,20) = EL9(k,4)+nzinc;
            EL9(k,21) = EL9(k,5)+nzinc;
            k=k+1; p=p+1;
        end
        for j=1:nq2
            EL10(k1,1) = p;
            EL10(k1,2) = N10(1,1)+2*nrinc*(m-1)-nrinc+(2*(nq1+nq2))*(i-1)+2*(j-1)-1;
            EL10(k1,3) = EL10(k1,2)+2*nrinc;
            if i==ns & j==nq2
                EL10(k1,4) = N9(1,1)+2*nrinc*(m-1)+nrinc;
            else
                EL10(k1,4) = EL10(k1,3)+2;
            end
            EL10(k1,5) = EL10(k1,4)-nrinc*2;
            EL10(k1,6) = EL10(k1,2)+2*nzinc;
            EL10(k1,7) = EL10(k1,3)+2*nzinc;
            EL10(k1,8) = EL10(k1,4)+2*nzinc;
            EL10(k1,9) = EL10(k1,5)+2*nzinc;
            EL10(k1,10) = EL10(k1,2)+nrinc;
            EL10(k1,11) = EL10(k1,3)+1;
            EL10(k1,12) = EL10(k1,5)+nrinc;
            EL10(k1,13) = EL10(k1,2)+1;
            EL10(k1,14) = EL10(k1,10)+2*nzinc;
            EL10(k1,15) = EL10(k1,11)+2*nzinc;
            EL10(k1,16) = EL10(k1,12)+2*nzinc;
            EL10(k1,17) = EL10(k1,13)+2*nzinc;
            EL10(k1,18) = EL10(k1,2)+nzinc;
            EL10(k1,19) = EL10(k1,3)+nzinc;
            EL10(k1,20) = EL10(k1,4)+nzinc;
            EL10(k1,21) = EL10(k1,5)+nzinc;
            k1=k1+1; p=p+1;
        end
    end
end

%---Calculate Total Bonded Area---
AT = pi*(c*Ro).^2;                  % area of unpatterned center section

NTEMP = [N5; N7]; k=1;              % area of elements in sections 5 and 8
for i=1:nr56+nr78/2.0
    for m=1:ns
        for j=1:nq1
          pt1 = (i-1)*2*ns*(2*nq1+1)+(m-1)*(2*nq1+1)+(j-1)*2+1;
          pt2 = pt1+1;
          pt3 = pt2+1;
          pt4 = (i)*2*ns*(2*nq1+1)+(m-1)*(2*nq1+1)+(j-1)*2+1;
          pt5 = pt4+1;
          pt6 = pt5+1;
          pt7 = (2*i-1)*ns*(2*nq1+1)+(m-1)*(2*nq1+1)+(j-1)*2+1;
          pt8 = pt7+2;
          A1=abs(1/2*(NTEMP(pt1,2)*(NTEMP(pt7,3)-NTEMP(pt2,3))+NTEMP(pt2,2)*(NTEMP(pt1,3)-NTEMP(pt7,3))+NTEMP(pt7,2)*(NTEMP(pt2,3)-NTEMP(pt1,3))));
          A2=abs(1/2*(NTEMP(pt2,2)*(NTEMP(pt8,3)-NTEMP(pt7,3))+NTEMP(pt7,2)*(NTEMP(pt2,3)-NTEMP(pt8,3))+NTEMP(pt8,2)*(NTEMP(pt7,3)-NTEMP(pt2,3))));
          A3=abs(1/2*(NTEMP(pt2,2)*(NTEMP(pt8,3)-NTEMP(pt3,3))+NTEMP(pt3,2)*(NTEMP(pt2,3)-NTEMP(pt8,3))+NTEMP(pt8,2)*(NTEMP(pt3,3)-NTEMP(pt2,3))));
          A4=abs(1/2*(NTEMP(pt4,2)*(NTEMP(pt5,3)-NTEMP(pt7,3))+NTEMP(pt7,2)*(NTEMP(pt4,3)-NTEMP(pt5,3))+NTEMP(pt5,2)*(NTEMP(pt7,3)-NTEMP(pt4,3))));
          A5=abs(1/2*(NTEMP(pt7,2)*(NTEMP(pt8,3)-NTEMP(pt5,3))+NTEMP(pt5,2)*(NTEMP(pt7,3)-NTEMP(pt8,3))+NTEMP(pt8,2)*(NTEMP(pt5,3)-NTEMP(pt7,3))));
          A6=abs(1/2*(NTEMP(pt5,2)*(NTEMP(pt8,3)-NTEMP(pt6,3))+NTEMP(pt6,2)*(NTEMP(pt5,3)-NTEMP(pt8,3))+NTEMP(pt8,2)*(NTEMP(pt6,3)-NTEMP(pt5,3))));
            AT = AT+A1+A2+A3+A4+A5+A6;
        end
    end
end
```

```
NTEMP2 = [N2((2*nr2)*(nq1*ns*2)-1,:); N2((2*nr2)*(nq1*ns*2),:);N2(((2*nr2-1)*(nq1*ns*2)+1):((2*nr2)*(nq1*ns*2)-1),:)];  % area of elements in section 3
NTEMP3 = [N3]; NTEMP5 = [N5(1:ns*(2*nq1+1),:)]; k=1; for i=1:ns
    for j=1:nq1
        pt1 = 2*k-1;
        pt2 = pt1+1;
        pt3 = pt2+1;
        pt4 = (2*nq1+1)*(i-1)+2*(j-1)+1;
        pt5 = pt4+1;
        pt6 = pt5+1;
        pt7 = pt4;
        pt8 = pt7+2;
        A1=abs(1/2*(NTEMP2(pt1,2)*(NTEMP3(pt7,3)-NTEMP2(pt2,3))+NTEMP2(pt2,2)*(NTEMP2(pt1,3)-NTEMP3(pt7,3))+NTEMP3(pt7,2)*(NTEMP2(pt2,3)-
           NTEMP2(pt1,3))));
        A2=abs(1/2*(NTEMP2(pt2,2)*(NTEMP3(pt8,3)-NTEMP3(pt7,3))+NTEMP3(pt7,2)*(NTEMP2(pt2,3)-NTEMP3(pt8,3))+NTEMP3(pt8,2)*(NTEMP3(pt7,3)-
           NTEMP2(pt2,3))));
        A3=abs(1/2*(NTEMP2(pt2,2)*(NTEMP3(pt8,3)-NTEMP2(pt3,3))+NTEMP2(pt3,2)*(NTEMP2(pt2,3)-NTEMP3(pt8,3))+NTEMP3(pt8,2)*(NTEMP2(pt3,3)-
           NTEMP2(pt2,3))));
        A4=abs(1/2*(NTEMP5(pt4,2)*(NTEMP5(pt5,3)-NTEMP3(pt7,3))+NTEMP3(pt7,2)*(NTEMP5(pt4,3)-NTEMP5(pt5,3))+NTEMP5(pt5,2)*(NTEMP3(pt7,3)-
           NTEMP5(pt4,3))))
        A5=abs(1/2*(NTEMP3(pt7,2)*(NTEMP3(pt8,3)-NTEMP5(pt5,3))+NTEMP5(pt5,2)*(NTEMP3(pt7,3)-NTEMP3(pt8,3))+NTEMP3(pt8,2)*(NTEMP5(pt5,3)-
           NTEMP3(pt7,3))))
        A6=abs(1/2*(NTEMP5(pt5,2)*(NTEMP3(pt8,3)-NTEMP5(pt6,3))+NTEMP5(pt6,2)*(NTEMP5(pt5,3)-NTEMP3(pt8,3))+NTEMP3(pt8,2)*(NTEMP5(pt6,3)-
           NTEMP5(pt5,3))));
        AT=AT+A1+A2+A3+A4+A5+A6;
        k=k+1;
    end
end

clear pt1 pt2 pt3 pt4 pt5 pt6 pt7 pt8 NTEMP NTEMP2 NTEMP3 NTEMP4 A1 A2 A3 A4 A5


%***Write output to data file***
file = 'spoke_06.inp';
fid = fopen(file,'w');

fprintf(fid,'*HEADING\n'); fprintf(fid,'**\n'); fprintf(fid,'** Model Definition\n');
fprintf(fid,'**\n');

fprintf(fid,'*PREPRINT,HISTORY=NO,MODEL=NO\n'); fprintf(fid,'**\n');

%---Nodes---
fprintf(fid,'*NODE, NSET=N1\n'); for i=1:2*nz1+1
    fprintf(fid,'%8.0f,%20.12E,%20.12E,%20.12E\n',[NA(:,1)+(ones(length(NA),1)*nzinc*(i-1)), NA(:,2:3), NZ1(:,i)]');
end

fprintf(fid,'*NODE, NSET=N2\n'); for i=1:2*nz2+1
    fprintf(fid,'%8.0f,%20.12E,%20.12E,%20.12E\n',[NA(:,1)+(ones(length(NA),1)*nzinc*(i-1)+nwinc), NA(:,2:3), NZ2(:,i)]');
end

fprintf(fid,'*NODE, NSET=NDUM\n');
fprintf(fid,'%8.0f,%20.12E,%20.12E,%20.12E\n',[NA(:,1)+ndinc, NA(:,2:3), ones(length(NA),1)*10.0e-3]');

fprintf(fid,'*NSET, NSET=CENT1\n');
fprintf(fid,'%8.0f,%8.0f,%8.0f,%8.0f,%8.0f,%8.0f,%8.0f,%8.0f\n',N1(:,1)');
fprintf(fid,'\n');

fprintf(fid,'*NSET, NSET=CENT2BOT\n');
fprintf(fid,'%8.0f,%8.0f,%8.0f,%8.0f,%8.0f,%8.0f,%8.0f,%8.0f\n',(N1(:,1)+nwinc)');
fprintf(fid,'\n');

fprintf(fid,'*NSET, NSET=CENT2\n');
fprintf(fid,'%8.0f,%8.0f,%8.0f,%8.0f,%8.0f,%8.0f,%8.0f,%8.0f\n',(N1(:,1)+nwinc+2*nz2*nzinc)');
fprintf(fid,'\n');

fprintf(fid,'*NSET, NSET=WAFER1_INT\n');
fprintf(fid,'%8.0f,%8.0f,%8.0f,%8.0f,%8.0f,%8.0f,%8.0f,%8.0f\n',(NA(:,1))');
fprintf(fid,'\n');

fprintf(fid,'*NSET, NSET=WAFER2_INT\n');
fprintf(fid,'%8.0f,%8.0f,%8.0f,%8.0f,%8.0f,%8.0f,%8.0f,%8.0f\n',(NA(:,1)+nwinc+2*nz2*nzinc)');
fprintf(fid,'\n');

fprintf(fid,'*NSET, NSET=CTIPLD\n');
fprintf(fid,'%8.0f,%8.0f,%8.0f,%8.0f,%8.0f,%8.0f,%8.0f,%8.0f\n',(N7(((2*nq1+1)*ns)*(nr78-1)+1:((2*nq1+1)*ns)*(nr78+1),1)+ndinc)');
fprintf(fid,'\n');

fprintf(fid,'*NSET, NSET=CTIPU1\n');
fprintf(fid,'%8.0f,%8.0f,%8.0f,%8.0f,%8.0f,%8.0f,%8.0f,%8.0f\n',(N7(((2*nq1+1)*ns)*(nr78+1)+1:((2*nq1+1)*ns)*(nr78+3),1))');
fprintf(fid,'\n');

fprintf(fid,'*NSET, NSET=CTIPU2\n');
fprintf(fid,'%8.0f,%8.0f,%8.0f,%8.0f,%8.0f,%8.0f,%8.0f,%8.0f\n',(N7(((2*nq1+1)*ns)*(nr78+1)+1:((2*nq1+1)*ns)*(nr78+3),1)+nwinc+2*nz2*nzinc)');
fprintf(fid,'\n');

%---ELEMENTS---
fprintf(fid,'**\n'); fprintf(fid,'** Elements\n'); fprintf(fid,'**\n');
```

```
fprintf(fid,'*ELEMENT, TYPE=C3D15, ELSET=SEC1\n');
fprintf(fid,'%8.0f,%8.0f,%8.0f,%8.0f,%8.0f,%8.0f,%8.0f,%8.0f,\n%8.0f,%8.0f,%8.0f,%8.0f,%8.0f,%8.0f,%8.0f,%8.0f\n',EL1');

fprintf(fid,'*ELEMENT, TYPE=C3D20, ELSET=SEC2\n');
fprintf(fid,'%8.0f,%8.0f,%8.0f,%8.0f,%8.0f,%8.0f,%8.0f,%8.0f,\n%8.0f,%8.0f,%8.0f,%8.0f,%8.0f,%8.0f,%8.0f,%8.0f,\n%8.0f,%8.0f,%8.0f,%8.0f,
            %8.0f\n',EL2');

fprintf(fid,'*ELEMENT, TYPE=C3D20, ELSET=SEC3\n');
fprintf(fid,'%8.0f,%8.0f,%8.0f,%8.0f,%8.0f,%8.0f,%8.0f,%8.0f,\n%8.0f,%8.0f,%8.0f,%8.0f,%8.0f,%8.0f,%8.0f,%8.0f,\n%8.0f,%8.0f,%8.0f,%8.0f,
            %8.0f\n',EL3');

fprintf(fid,'*ELEMENT, TYPE=C3D15, ELSET=SEC4\n');
fprintf(fid,'%8.0f,%8.0f,%8.0f,%8.0f,%8.0f,%8.0f,%8.0f,%8.0f,\n%8.0f,%8.0f,%8.0f,%8.0f,%8.0f,%8.0f,%8.0f,%8.0f\n',EL4');

fprintf(fid,'*ELEMENT, TYPE=C3D20, ELSET=SEC5\n');
fprintf(fid,'%8.0f,%8.0f,%8.0f,%8.0f,%8.0f,%8.0f,%8.0f,%8.0f,\n%8.0f,%8.0f,%8.0f,%8.0f,%8.0f,%8.0f,%8.0f,%8.0f,\n%8.0f,%8.0f,%8.0f,%8.0f,
            %8.0f\n',EL5');

fprintf(fid,'*ELEMENT, TYPE=C3D20, ELSET=SEC6\n');
fprintf(fid,'%8.0f,%8.0f,%8.0f,%8.0f,%8.0f,%8.0f,%8.0f,%8.0f,\n%8.0f,%8.0f,%8.0f,%8.0f,%8.0f,%8.0f,%8.0f,%8.0f,\n%8.0f,%8.0f,%8.0f,%8.0f,
            %8.0f\n',EL6');

fprintf(fid,'*ELEMENT, TYPE=C3D20, ELSET=SEC7\n');
fprintf(fid,'%8.0f,%8.0f,%8.0f,%8.0f,%8.0f,%8.0f,%8.0f,%8.0f,\n%8.0f,%8.0f,%8.0f,%8.0f,%8.0f,%8.0f,%8.0f,%8.0f,\n%8.0f,%8.0f,%8.0f,%8.0f,
            %8.0f\n',EL7');

fprintf(fid,'*ELEMENT, TYPE=C3D20, ELSET=SEC8\n');
fprintf(fid,'%8.0f,%8.0f,%8.0f,%8.0f,%8.0f,%8.0f,%8.0f,%8.0f,\n%8.0f,%8.0f,%8.0f,%8.0f,%8.0f,%8.0f,%8.0f,%8.0f,\n%8.0f,%8.0f,%8.0f,%8.0f,
            %8.0f\n',EL8');

fprintf(fid,'*ELEMENT, TYPE=C3D20, ELSET=SEC9\n');
fprintf(fid,'%8.0f,%8.0f,%8.0f,%8.0f,%8.0f,%8.0f,%8.0f,%8.0f,\n%8.0f,%8.0f,%8.0f,%8.0f,%8.0f,%8.0f,%8.0f,%8.0f,\n%8.0f,%8.0f,%8.0f,%8.0f,
            %8.0f\n',EL9');

fprintf(fid,'*ELEMENT, TYPE=C3D20, ELSET=SEC10\n');
fprintf(fid,'%8.0f,%8.0f,%8.0f,%8.0f,%8.0f,%8.0f,%8.0f,%8.0f,\n%8.0f,%8.0f,%8.0f,%8.0f,%8.0f,%8.0f,%8.0f,%8.0f,\n%8.0f,%8.0f,%8.0f,%8.0f,
            %8.0f\n',EL10');

fprintf(fid,'*ELSET, ELSET=W1L1\n SEC1, SEC2, SEC3, SEC4, SEC5, SEC6, SEC7, SEC8, SEC9, SEC10 \n');

for i=1:(nz1-1)
    fprintf(fid,'*ELCOPY, ELEMENT SHIFT=%6.0f, OLD SET=W1L1, SHIFT NODES=%6.0f, NEW SET=WAFER1\n',nzinc*i,nzinc*i*2);
end

fprintf(fid,'*ELCOPY, ELEMENT SHIFT=%6.0f, OLD SET=W1L1, SHIFT NODES=%6.0f, NEW SET=W2L2\n',nwinc,nwinc);

for i=1:(nz2-1)
    fprintf(fid,'*ELCOPY, ELEMENT SHIFT=%6.0f, OLD SET=W2L2, SHIFT NODES=%6.0f, NEW SET=WAFER2\n',nzinc*i,nzinc*i*2);
end

fprintf(fid,'*ELSET, ELSET=ALL\n W1L1, WAFER1, W2L2, WAFER2 \n');

%-----Equation Constraint-----
k=2; for i=1:length(NEQ)
        fprintf(fid,'*EQUATION\n %8.0f\n',3);
        fprintf(fid,'%12.0f,%4.0f,%4.0f,%12.0f,%4.0f,%4.0f,%12.0f,%4.0f,%4.0f\n',NEQ(i,:));
end

%---MATERTIAL PROPS---
fprintf(fid,'**\n'); fprintf(fid,'** Material Properties\n'); fprintf(fid,'**\n');

fprintf(fid,'*ORIENTATION, NAME=CS1, SYSTEM=RECTANGULAR, DEFINITION=COORDINATES\n');
fprintf(fid,'1.0, 1.0, 0.0, -1.0, 1.0, 0.0\n 3, 0.0\n');

fprintf(fid,'*SOLID SECTION, ELSET=ALL, MATERIAL=M1, ORIENTATION=CS1\n');

fprintf(fid,'*MATERIAL, NAME=M1\n');
fprintf(fid,'*DENSITY\n %10.6E,\n',den);
fprintf(fid,'*ELASTIC, TYPE=ORTHOTROPIC\n');
fprintf(fid,'%10.4E, %10.4E, %10.4E, %10.4E, %10.4E, %10.4E,%10.4E, %10.4E\n',C11,C12,C11,C12,C12,C11,C44,C44);
fprintf(fid,'%10.4E,\n',C44);

fprintf(fid,'*MATERIAL, NAME=M2\n');
fprintf(fid,'*DENSITY\n %10.6E,\n',den);
fprintf(fid,'*ELASTIC, TYPE=ISOTROPIC\n');
fprintf(fid,'%10.4E, %10.4E\n',150e9,0.18);

%---HISTORY DEFINITION---
fprintf(fid,'**\n'); fprintf(fid,'** History Definition\n'); fprintf(fid,'**\n');

fprintf(fid,'*STEP, PERTURBATION\n'); fprintf(fid,'*STATIC\n');

%---BOUNDARY CONDITIONS---
fprintf(fid,'**\n'); fprintf(fid,'** Boundary Conditions\n'); fprintf(fid,'**\n');

%-----BC at center------
```

```
fprintf(fid,'*BOUNDARY\n %8.0f, ENCASTRE\n',N1(1,1));

fprintf(fid,'*BOUNDARY\n %8.0f, ENCASTRE\n',(N1(1,1)+nwinc+2*nz2*nzinc));
fprintf(fid,'*BOUNDARY\n CENT2BOT, 3\n');

%---LOADING---
fprintf(fid,'**\n'); fprintf(fid,'** Loads\n'); fprintf(fid,'**\n');

fprintf(fid,'*BOUNDARY, TYPE=DISPLACEMENT\n');
fprintf(fid,'%10.0f, %10.0f, ,%20.12E\n',NLOAD');

%---Solver---
fprintf(fid,'*RESTART, WRITE\n');

%---Output---
fprintf(fid,'*NODE FILE, NSET=CTIPLD\n');          % reaction forces at crack tip
fprintf(fid,'RF\n');
fprintf(fid,'*NODE FILE, NSET=CTIPU1\n');          % displacements on wafer 1 near crack tip
fprintf(fid,'U\n');
fprintf(fid,'*NODE FILE, NSET=CTIPU2\n');          % displacements on wafer 2 near crack tip
fprintf(fid,'U\n');
fprintf(fid,'*NODE FILE, NSET=CTIPLD\n');          % coordinates of node at crack tip and behind
fprintf(fid,'COORD\n');
fprintf(fid,'*NODE FILE, NSET=CTIPU1\n');          % coordinates of node at crack tip and behind
fprintf(fid,'COORD\n');
fprintf(fid,'*NODE FILE, NSET=CTIPU2\n');          % coordinates of node at crack tip and behind
fprintf(fid,'COORD\n'); fprintf(fid,'*ENERGY FILE\n'); fprintf(fid,'*ENERGY PRINT\n');

fprintf(fid,'*END STEP'); fclose(fid);
```

geth1.m

```
function [H] = geth1(X,Y)
h1 = 675.0e-6;
%--uniform thickness
H = h1*ones(length(X),1);
```

getz1.m

```
function [Z] = getz1(X,Y)

% top wafer - wafer 1
% function reads in x and y coordinate and returns vector z with height positions

file = '.\150_shape\split_02.txt';      % text file with shape data

% Read in displacement data for wafer 1 from text file
[THETA(:,1),R(:,1),ZRAW(:,1)] = textread(file,'%*u %f %f %f %*s');

% Convert imported data to cartesian coordinates and meters
XR = (R.*cos(THETA*pi/180-pi/2))/10^3; YR = (R.*sin(THETA*pi/180-pi/2))/10^3;

% Make z=0 at x=0,y=0 and convert to meters
ZR = (ZRAW-ZRAW(1,1))/10^6;

% Is this wafer bonded in the same configuration as it is measured?
% if yes => flip=0, if no => flip=1
flip=1; if flip==1
    XR = -1.0*XR;
    ZR = -1.0*ZR;
end

% Vector for plot
n = 30; m = 30; k=1; for i=1:n+1
    for j=1:m+1
        r = ((i-1)/n)*50e-3;
        q = ((j-1)/m)*2*pi;
        XP(i,j) = r*cos(q);
        YP(i,j) = r*sin(q);
        k=k+1;
    end
end
% Interpolate data for plot
ZP = griddata(XR,YR,ZR,XP,YP,'v4');

% Interpolate data to return to FEA code
Z = griddata(XR,YR,ZR,X,Y,'v4');

% plot data
figure(2)
subplot(1,2,1)
surf(XP,YP,ZP)
title('wafer 1 shape')
hold on shading
interp
```

```
contour3(XP,YP,ZP+1,10,'k-')
view(2)
axis square
```

C.2 Bond Pair Shape Prediction

Below are the MATLAB™ scripts that are used to generate and execute the model used to calculate the shape of the bonded pair from the initial shapes of the wafers (Chapter 6). The model was developed to include the effect of gravity in the calculations. The mesh is generated in MATLAB™, exported to ABAQUS™ and solved. The model is comprised of the following m-files:

1. *shape_run.m* - Script used to run the model and post process the data. All geometry and wafer information is entered in this script and this is the file that is run in MATLAB™. The files below are all called from this script.
2. *shape_01_gravity.m* - Function to generate the ABAQUS™ model used to calculate the shape of the wafers with gravity when mounted in the bonding configuration.
3. *shape_01_bond.m* - Function to generate the ABAQUS™ model that is used to model the bonding of the wafers.
4. *shape_01_pair_gravity.m* - Function reads the measured shape of the bonded pair and calculates the deformations due to gravity such that it can be compared with the shape of the pair predicted using the model.
5. *geth1b.m and geth2b.m* - These functions are used to specify the thickness of the wafers. The code is not shown as it is similar to that in the previous section.
6. *getz1b.m and getz2b.m* - These functions are used to import the shape data of the wafers. The code is not shown as it is similar to that in the previous section.

shape_run.m

```
clear;

% -m-file designed to run the three ABAQUS files required to calculate the final
%  shape of a wafer pair

%****Test Data****

%--individual wafers--
bot_wafer = '..\split_Shape_Processed\2GS_S09_mn.mat';       % file with shape data for bot wafer (wafer 2)
top_wafer = '..\split_Shape_Processed\2GS_S10_mn.mat';       % file with shape data for top wafer (wafer 1)
flip_bot = 0;                                                % was wafer measured in same orientation as it was bonded? If yes set =0,
                                                             %  if no data must be flipped =1
flip_top = 1;                                                % was wafer measured in same orientation as it was bonded? If yes set =0
%--bonded pair--
bnd_wafer = '..\Bonded_Shape_Processed\2GS_B05_mn.mat';      % file with shape data for bonded wafer
flip_bnd = 0;                                                % was wafer measured in same orientation as it was bonded? If yes set =0

c = 75.0e-3;                                                % wafer diameter
fl = 32.5e-3;                                               % major flat length
ee = 5.0e-3;                                                % edge exclusion
PT3_rad = 50.0e-3;                                          % radius of 3-pts in fir

%****1st ABAQUS run - calculate gravity deformation on un bonded wafers****

% Create 1st .inp file and run ABAQUS to calculate wafer shape with gravity
!del shape_01_gravity.mdl shape_01_gravity(bot_wafer,top_wafer,flip_bot,flip_top); !abaqus
job=shape_01_gravity interactive

% Read results from file
!del filtotxt_grav.tur !abaqus filtotxt_grav
```

```
% Read in the number of data points
es1 = 2;                  % first line of displacement data
ef1 = es1;                % last line of displacement data
[num] = textread('filtotxt_grav.tur','%u',((ef1-es1)+1),'headerlines',(es1-1));

% Read in displacement data for top wafer (wafer 1)
es1 = 4;                  % first line of displacement data
ef1 = es1+num/2-1;        % last line of displacement data
[UNODE1(:,1),U1(:,1),U1(:,2),U1(:,3)] = textread('filtotxt_grav.tur','%u %f %f %f',((ef1-es1)+1),'expchars','E','headerlines',(es1-1));

% Read in displacement data for bot wafer (wafer 2)
es1 = ef1+1;              % first line of displacement data
ef1 = es1+num/2-1;        % last line of displacement data
[UNODE2(:,1),U2(:,1),U2(:,2),U2(:,3)] = textread('filtotxt_grav.tur','%u %f %f %f',((ef1-es1)+1),'expchars','E','headerlines',(es1-1));

% Read in nodal coordinates for top wafer (wafer 1)
es1 = ef1+2;              % first line of coordinate data
ef1 = es1+num/2-1;        % last line of coordinate data
[CNODE1(:,1),C1(:,1),C1(:,2),C1(:,3)] = textread('filtotxt_grav.tur','%u %f %f %f',((ef1-es1)+1),'expchars','E','headerlines',(es1-1));

% Read in nodal coordinates for bot wafer (wafer 2)
es1 = ef1+1;              % first line of coordinate data
ef1 = es1+num/2-1;        % last line of coordinate data
[CNODE2(:,1),C2(:,1),C2(:,2),C2(:,3)] = textread('filtotxt_grav.tur','%u %f %f %f',((ef1-es1)+1),'expchars','E','headerlines',(es1-1));

% Calculate coordinates of deformed wafer
CF1 = C1+U1;              % wafer 1
CF2 = C2+U2;              % wafer 2

% Plot initial shapes and final shape
figure(3);clf;

subplot(3,2,1)
C13PT = threept(C1(:,1),C1(:,2),C1(:,3),PT3_rad,c,ee);  % fit to three point plane
wafer_plot(C13PT(:,1),C13PT(:,2),C13PT(:,3),c,fl,ee) title('measured shape of wafer 1')

subplot(3,2,2)
C23PT = threept(C2(:,1),C2(:,2),C2(:,3),PT3_rad,c,ee);  % fit to three point plane
wafer_plot(C23PT(:,1),C23PT(:,2),C23PT(:,3),c,fl,ee) title('measured shape of wafer 2')

subplot(3,2,3)
CF13PT = threept(CF1(:,1),CF1(:,2),CF1(:,3),PT3_rad,c,ee);  % fit to three point plane
wafer_plot(CF13PT(:,1),CF13PT(:,2),CF13PT(:,3),c,fl,ee) title('wafer 1 with gravity')

subplot(3,2,4)
CF23PT = threept(CF2(:,1),CF2(:,2),CF2(:,3),PT3_rad,c,ee);  % fit to three point plane
wafer_plot(CF23PT(:,1),CF23PT(:,2),CF23PT(:,3),c,fl,ee) title('wafer 2 with gravity')

%****2nd ABAQUS run - bond wafers****

% Create 2nd .inp file and run ABAQUS to calculate wafer shape with gravity
!del shape_01_bond.mdl shape_01_bond(CF1,CF2); !abaqus job=shape_01_bond interactive

% Read results from file
!del filtotxt_bond.tur !abaqus filtotxt_bond

% Read in the number of data points
es1 = 2;                  % first line of displacement data
ef1 = es1;                % last line of displacement data
[num] = textread('filtotxt_bond.tur','%u',((ef1-es1)+1),'headerlines',(es1-1));

% Read in displacement data for top wafer (wafer 1)
es1 = 4;                  % first line of displacement data
ef1 = es1+num/2-1;        % last line of displacement data
[UNODE1B(:,1),U1B(:,1),U1(:,2),U1B(:,3)] = textread('filtotxt_bond.tur','%u %f %f %f',((ef1-es1)+1),'expchars','E','headerlines',(es1-1));

% Read in displacement data for bot wafer 1 (wafer 2)
es1 = ef1+1;              % first line of displacement data
ef1 = es1+num/2-1;        % last line of displacement data
[UNODE2B(:,1),U2B(:,1),U2B(:,2),U2B(:,3)] = textread('filtotxt_bond.tur','%u %f %f %f',((ef1-es1)+1),'expchars','E','headerlines',(es1-1));

% Read in nodal coordinates for top wafer (wafer 1)
es1 = ef1+2;              % first line of coordinate data
ef1 = es1+num/2-1;        % last line of coordinate data
[CNODE1B(:,1),C1B(:,1),C1B(:,2),C1B(:,3)] = textread('filtotxt_bond.tur','%u %f %f %f',((ef1-es1)+1),'expchars','E','headerlines',(es1-1));

% Read in nodal coordinates for bot wafer (wafer 2)
es1 = ef1+1;              % first line of coordinate data
ef1 = es1+num/2-1;        % last line of coordinate data
[CNODE2B(:,1),C2B(:,1),C2B(:,2),C2B(:,3)] = textread('filtotxt_bond.tur','%u %f %f %f',((ef1-es1)+1),'expchars','E','headerlines',(es1-1));

% Calculate coordinates of deformed wafer
CF1B = C1B+U1B;              % wafer 1
CF2B = C2B+U2B;              % wafer 2

% Plot final shape
figure(3); CF1BR = threept(CF1B(:,1),CF1B(:,2),CF1B(:,3),PT3_rad,c,ee);
```

```
% CF1BR(:,3) = CF1BR(:,3)-CF1BR(1,3);
subplot(3,2,5) wafer_plot(CF1BR(:,1),CF1BR(:,2),CF1BR(:,3),c,fl,ee) title('predicted shape after
bonding (w/ g)')

%****3rd ABAQUS run - add gravity to bonded pair****

% Create 3rd .inp file and run ABAQUS to calculate wafer shape with gravity
!del shape_01_pair_gravity.mdl shape_01_pair_gravity(bnd_wafer,flip_bnd); !abaqus
job=shape_01_pair_gravity interactive

% Read results from file
!del filtotxt_pair_grav.tur !abaqus filtotxt_pair_grav

% Read in the number of data points
es1 = 2;                  % first line of displacement data
ef1 = es1;                % last line of displacement data
[num] = textread('filtotxt_pair_grav.tur','%u',((ef1-es1)+1),'headerlines',(es1-1));

% Read in displacement data
es1 = 4;                  % first line of displacement data
ef1 = es1+num-1;          % last line of displacement data
[UNODE1P(:,1),U1P(:,1),U1P(:,2),U1P(:,3)] = textread('filtotxt_pair_grav.tur','%u %f %f %f',((ef1-es1)+1),'expchars','E','headerlines',(es1-1));

% Read in nodal coordinates
es1 = ef1+2;              % first line of coordinate data
ef1 = es1+num-1;        % last line of coordinate data
[CNODE1P(:,1),C1P(:,1),C1P(:,2),C1P(:,3)] = textread('filtotxt_pair_grav.tur','%u %f %f %f',((ef1-es1)+1),'expchars','E','headerlines',(es1-1));

% Calculate coordinates of deformed wafer
CF1P = C1P+U1P;              % bonded pair

% Plot final shape
figure(3);
CF1PR = threept(CF1P(:,1),CF1P(:,2),CF1P(:,3),PT3_rad,c,ee);  % fit to three point plane
%CF1PR(:,3) = CF1PR(:,3)-CF1PR(1,3);
subplot(3,2,6) wafer_plot(CF1PR(:,1),CF1PR(:,2),CF1PR(:,3),c,fl,ee) title('measured shape after
bonding (w/ g)')

% Error Analysis
n=50; m=40; for i=1:n
    for j=1:m
        r = (i-1)/(n-1)*(c-ee);
        T = (j-1)/(m-1)*2*pi;
        XGR(i,j) = r*cos(T);
        YGR(i,j) = r*sin(T);
    end
end

% R and Z-values on a common grid
RGR = (XGR.^2+YGR.^2).^.5;

ZMOD = griddata(CF1BR(:,1),CF1BR(:,2),CF1BR(:,3),XGR,YGR,'v4'); ZEXP =
griddata(CF1PR(:,1),CF1PR(:,2),CF1PR(:,3),XGR,YGR,'v4');

zMOD = CF1BR(:,3);      % column vector with model data
zEXP = CF1PR(:,3);      % column vector with experiment data

RGR2 = (mean(RGR'));

RN = RGR2(2:length(RGR2))'/c; grav =
(3/16)*(2330*9.8*2*(50.0e-3^4))/(180.5e9*(2*675.e-6)^2)*(RN.^2.*(RN.^2+6+0.18*(RN.^2+2))-8.*(1+.18).*(RN.^2.*log(RN)));

% Max, min, mean z as a fcn of r
ZMOD_mean = mean(ZMOD'); ZMOD_max = max(ZMOD'); ZMOD_min = min(ZMOD'); ZEXP_mean = mean(ZEXP');
ZEXP_max = max(ZEXP'); ZEXP_min = min(ZEXP');

ZMOD_mean = ZMOD_mean-ZMOD_mean(1,1); ZMOD_max = ZMOD_max-ZMOD_max(1,1); ZMOD_min =
ZMOD_min-ZMOD_min(1,1); ZEXP_mean = ZEXP_mean-ZEXP_mean(1,1); ZEXP_max = ZEXP_max-ZEXP_max(1,1);
ZEXP_min = ZEXP_min-ZEXP_min(1,1);

figure(4) clf subplot(1,2,1)
plot(RGR2,ZMOD_mean,'b.-',RGR2,ZMOD_min,'b-',RGR2,ZMOD_max,'b-',RGR2,ZEXP_mean,'r.-',RGR2,ZEXP_min,'r-',RGR2,ZEXP_max,'r-')
axis square

LSDATA = [RGR2',ZMOD_mean',ZMOD_min',ZMOD_max',ZEXP_mean',ZEXP_min',ZEXP_max']

[zMOD,zEXP]

subplot(1,2,2)
wafer_plot(CF1PR(:,1),CF1PR(:,2),(CF1BR(:,3)-CF1BR(1,3))-(CF1PR(:,3)-CF1PR(1,3)),c,fl,ee);
title('z_{model} - z_{experiment}');

scale_fact = (zMOD'*zMOD)\(zMOD'*zEXP)

save(['fem_out_',bnd_wafer(27:34)])
```

shape_01_gravity.m

```
function [] = shape_01_gravity(bot_wafer,top_wafer,flip_bot,flip_top)

% -This m-file generates a .inp file for ABAQUS
% -This is 1 of 3 files used to calculate the final shape of bonded pair
% -This file imports the data from the ADE measurements and calculates
%  the shape of the wafers when loaded by gravity
% -USAGE: [] = shape_01_gravity(bot_wafer,top_wafer,flip_bot,flip_top)
% -variables to be read: bot_wafer = filename of bottom wafer
%                        top_wafer = filename of top wafer
%                        flip_bot and flip-top = 1 or 0 denoting whether wafer data should be flipped

% Kevin Turner
% Original: 01 January 2004
% Modified: 20 February 2004

%**DEFINE BASIC GEOMETRY**
c = 75.0e-3;                % wafer radius (m)
fl = 32.50e-3;              % flat length (m)

%**ELASTIC PROPERTIES**
C11 = 166.2e9;              % 11 stiffness coefficient (Pa)
C12 = 64.4e9;               % 12 stiffness coefficient (Pa)
C44 = 79.8e9;               % 44 stiffness coefficient (Pa)
den = 2330;                 % density in kg/m^3

%**DEFINE MESH PARAMETERS**
nr1 = 1;                    % number of elements in radial direction in section 1 (has to be 1)
nr2 = 12;                   % number of elements in radial direction in section 2
nq1 = 32;                   % number of elements in theta direction
nz1 = 2;                    % number of elements through the thickness of wafer 1
nz2 = 2;                    % number of elements through the thickness of wafer 2

rs1 = 2.5e-3;               % radius of section 1 (mm)

nrinc = 1000;               % increment in node numbers from one radius to the next
nzinc = 100000;             % increment in node numbers from one layer of nodes to the next
nwinc = 1000000;            % increment in node numbers between wafers
ndinc = 9900000;            % increment in node numbers for dummy nodes

%**LAYOUT GRID**
%---Sections 1 and 2----
R1 = [0 : rs1/(2*nr1) : rs1]';          % radial positions of nodes in section 1
R2 = [rs1 : (c-rs1)/(2*nr2) : c]';      % radial positions of nodes in section 2
Q1 = [0 : 2*pi/(2*nq1) : 2*pi]';        % theta positions of nodes in sections 1 and 2

%**GENERATE X-Y GRID**
%---Section 1---
N1(1,:) = [1, 0.0, 0.0]; k = 2; for i=1:(2*nr1)
    for j=1:(2*nq1)
        N1(k,1) = nrinc*i+j;
        N1(k,2) = R1(i+1,1)*cos(Q1(j,1));
        N1(k,3) = R1(i+1,1)*sin(Q1(j,1));
        k=k+1;
        nrt1 = nrinc*i;
    end
end
%---Section 2---
k=1; for i=2:(2*nr2+1)
    for j=1:(2*nq1)
        N2(k,1) = nrt1+nrinc*(i-1)+j;
        N2(k,2) = R2(i,1)*cos(Q1(j,1));
        N2(k,3) = R2(i,1)*sin(Q1(j,1));
        k=k+1;
        nrt2 = nrt1+nrinc*i;
    end
end

% %**PLOT GRID**
% figure(1); clf;
% plot(N1(:,2),N1(:,3),'k.',N2(:,2),N2(:,3),'r.')
% axis square
% axis([-c c -c c])

%***GET Z AND H VALUES***
NA = [N1; N2];                  % matrix containing [node number, X, Y] of all nodes in first layer

figure(2); clf;
%--wafer 1 (top wafer)---
Z1 = [getz1b(NA(:,2),NA(:,3),top_wafer,flip_top)];   % position of center plane of wafer 1
H1 = [geth1b(NA(:,2),NA(:,3))];                      % thickness of wafer 1
for i=1:nz1*2+1
    NZ1(:,i) = Z1+H1./(2.*nz1).*(i-nz1-1);           % z positions of each node in layer1
end
NZ1 = NZ1-ones(size(NZ1))*NZ1(1,1);                  % adjust layer 1 data so x=0, y=0 is z=0 at bonding surface
%--wafer 2 (bottom wafer)---
Z2 = [getz2b(NA(:,2),NA(:,3),bot_wafer,flip_bot)];   % position of center plane of wafer 2
H2 = [geth2b(NA(:,2),NA(:,3))];                       % thickness of wafer 2
```

```
for i=1:nz2*2+1
    NZ2(:,i) = Z2+H2./(2.*nz2).*(i-nz2-1);           % z positions of each node in layer2
end
NZ2 = NZ2-ones(size(NZ2))*(NZ2(1,1))-H2(1,1);        % adjust layer 2 data so x=0, y=0 is z=0 at bonding surface

%***GENERATE ELEMENT VECTORS
%---section 1---
k=1; p=1; for i=1:nr1
    for j=1:nq1
        EL1(k,1) = p;
        EL1(k,2) = N1(1,1);
        EL1(k,3) = (2*i)*nrinc+(2*j-1);
        if j~=nq1
            EL1(k,4) = EL1(k,3)+2;
        else
            EL1(k,4) = EL1(1,3);
        end
        EL1(k,5) = EL1(k,2)+2*nzinc;
        EL1(k,6) = EL1(k,3)+2*nzinc;
        EL1(k,7) = EL1(k,4)+2*nzinc;
        EL1(k,8) = EL1(k,3)-nrinc;
        EL1(k,9) = EL1(k,3)+1;
        EL1(k,10) = EL1(k,4)-nrinc;
        EL1(k,11) = EL1(k,8)+2*nzinc;
        EL1(k,12) = EL1(k,9)+2*nzinc;
        EL1(k,13) = EL1(k,10)+2*nzinc;
        EL1(k,14) = EL1(k,2)+nzinc;
        EL1(k,15) = EL1(k,3)+nzinc;
        EL1(k,16) = EL1(k,4)+nzinc;
        k=k+1; p=p+1;
    end
end
%---section 2---
k=1; for i=1:nr2
    for j=1:nq1
        EL2(k,1) = p;
        EL2(k,2) = N2(1,1)+nrinc*(2*(i-1)-1)+2*(j-1);
        EL2(k,3) = EL2(k,2)+nrinc*2;
        if j~=nq1
            EL2(k,4) = EL2(k,3)+2;
        else
            EL2(k,4) = N2(1,1)+nrinc*(2*(i-1)+1);
        end
        EL2(k,5) = EL2(k,4)-nrinc*2;
        EL2(k,6) = EL2(k,2)+2*nzinc;
        EL2(k,7) = EL2(k,3)+2*nzinc;
        EL2(k,8) = EL2(k,4)+2*nzinc;
        EL2(k,9) = EL2(k,5)+2*nzinc;
        EL2(k,10) = EL2(k,2)+nrinc;
        EL2(k,11) = EL2(k,3)+1;
        EL2(k,12) = EL2(k,4)-nrinc;
        EL2(k,13) = EL2(k,2)+1;
        EL2(k,14) = EL2(k,10)+2*nzinc;
        EL2(k,15) = EL2(k,11)+2*nzinc;
        EL2(k,16) = EL2(k,12)+2*nzinc;
        EL2(k,17) = EL2(k,13)+2*nzinc;
        EL2(k,18) = EL2(k,2)+nzinc;
        EL2(k,19) = EL2(k,3)+nzinc;
        EL2(k,20) = EL2(k,4)+nzinc;
        EL2(k,21) = EL2(k,5)+nzinc;
        k=k+1; p=p+1;
    end
end

file = 'shape_01_gravity.inp';
% Write .inp file
fid = fopen(file,'w');

fprintf(fid,'*HEADING\n'); fprintf(fid,'**\n'); fprintf(fid,'** Model Definition\n');
fprintf(fid,'**\n');

fprintf(fid,'*PREPRINT,HISTORY=NO,MODEL=NO\n'); fprintf(fid,'**\n');

%***NODES***
%---Nodes---
fprintf(fid,'*NODE, NSET=N1\n'); for i=1:2*nz1+1
    fprintf(fid,'%8.0f,%20.12E,%20.12E,%20.12E\n',[NA(:,1)+(ones(length(NA),1)*nzinc*(i-1)), NA(:,2:3), NZ1(:,i)]');
end

fprintf(fid,'*NODE, NSET=N2\n'); for i=1:2*nz2+1
    fprintf(fid,'%8.0f,%20.12E,%20.12E,%20.12E\n',[NA(:,1)+(ones(length(NA),1)*nzinc*(i-1)+nwinc), NA(:,2:3), NZ2(:,i)]');
end

fprintf(fid,'*NSET, NSET=CENT1\n');
fprintf(fid,'%8.0f,%8.0f,%8.0f,%8.0f,%8.0f,%8.0f,%8.0f,%8.0f\n',N1(:,1)');
fprintf(fid,'\n');
```

```
fprintf(fid,'*NSET, NSET=CENT1BOT\n');
fprintf(fid,'%8.0f,%8.0f,%8.0f,%8.0f,%8.0f,%8.0f,%8.0f,%8.0f\n',N1(:,1)');
fprintf(fid,'\n');

fprintf(fid,'*NSET, NSET=CENT2BOT\n');
fprintf(fid,'%8.0f,%8.0f,%8.0f,%8.0f,%8.0f,%8.0f,%8.0f,%8.0f\n',(N1(:,1)+nwinc)');
fprintf(fid,'\n');

fprintf(fid,'*NSET, NSET=CENT2\n');
fprintf(fid,'%8.0f,%8.0f,%8.0f,%8.0f,%8.0f,%8.0f,%8.0f,%8.0f\n',(N1(:,1)+nwinc+2*nz2*nzinc)');
fprintf(fid,'\n');

fprintf(fid,'*NSET, NSET=WAFER1_INT\n');
fprintf(fid,'%8.0f,%8.0f,%8.0f,%8.0f,%8.0f,%8.0f,%8.0f,%8.0f\n',(NA(:,1))');
fprintf(fid,'\n');

fprintf(fid,'*NSET, NSET=WAFER2_INT\n');
fprintf(fid,'%8.0f,%8.0f,%8.0f,%8.0f,%8.0f,%8.0f,%8.0f,%8.0f\n',(NA(:,1)+nwinc+2*nz2*nzinc)');
fprintf(fid,'\n');

%***ELEMENTS***
fprintf(fid,'**\n'); fprintf(fid,'** Elements\n'); fprintf(fid,'**\n');

fprintf(fid,'*ELEMENT, TYPE=C3D15, ELSET=SEC1\n');
fprintf(fid,'%8.0f,%8.0f,%8.0f,%8.0f,%8.0f,%8.0f,%8.0f,%8.0f,\n%8.0f,%8.0f,%8.0f,%8.0f,%8.0f,%8.0f,%8.0f,%8.0f\n',EL1');

fprintf(fid,'*ELEMENT, TYPE=C3D20, ELSET=SEC2\n');
fprintf(fid,'%8.0f,%8.0f,%8.0f,%8.0f,%8.0f,%8.0f,%8.0f,%8.0f,\n%8.0f,%8.0f,%8.0f,%8.0f,%8.0f,%8.0f,%8.0f,%8.0f,\n%8.0f,%8.0f,%8.0f,%8.0f,
            %8.0f\n',EL2');

fprintf(fid,'*ELSET, ELSET=W1L1\n SEC1, SEC2\n');

for i=1:(nz1-1)
    fprintf(fid,'*ELCOPY, ELEMENT SHIFT=%6.0f, OLD SET=W1L1, SHIFT NODES=%6.0f, NEW SET=WAFER1E\n',nzinc*i,nzinc*i*2);
end

fprintf(fid,'*ELCOPY, ELEMENT SHIFT=%6.0f, OLD SET=W1L1, SHIFT NODES=%6.0f, NEW SET=W2L2\n',nwinc,nwinc);

for i=1:(nz2-1)
    fprintf(fid,'*ELCOPY, ELEMENT SHIFT=%6.0f, OLD SET=W2L2, SHIFT NODES=%6.0f, NEW SET=WAFER2E\n',nzinc*i,nzinc*i*2);
end

fprintf(fid,'*ELSET, ELSET=WAFER1\n W1L1, WAFER1E\n'); fprintf(fid,'*ELSET, ELSET=WAFER2\n W2L2,
WAFER2E\n');

fprintf(fid,'*ELSET, ELSET=ALL\n WAFER1, WAFER2 \n');

%***MATERTIAL PROPS***
fprintf(fid,'**\n'); fprintf(fid,'** Material Properties\n'); fprintf(fid,'**\n');

fprintf(fid,'*ORIENTATION, NAME=CS1, SYSTEM=RECTANGULAR, DEFINITION=COORDINATES\n');
fprintf(fid,'1.0, 1.0, 0.0, -1.0, 1.0, 0.0\n 3, 0.0\n');

fprintf(fid,'*SOLID SECTION, ELSET=ALL, MATERIAL=M1, ORIENTATION=CS1\n');

fprintf(fid,'*MATERIAL, NAME=M1\n');
fprintf(fid,'*DENSITY\n %10.6E,\n',den);
fprintf(fid,'*ELASTIC, TYPE=ORTHOTROPIC\n');
fprintf(fid,'%10.4E, %10.4E, %10.4E, %10.4E, %10.4E, %10.4E,%10.4E, %10.4E\n',C11,C12,C11,C12,C12,C11,C44,C44);
fprintf(fid,'%10.4E,\n',C44);

fprintf(fid,'*MATERIAL, NAME=M2\n');
fprintf(fid,'*DENSITY\n %10.6E,\n',den);
fprintf(fid,'*ELASTIC, TYPE=ISOTROPIC\n');
fprintf(fid,'%10.4E, %10.4E\n',150e9,0.18);

%***HISTORY DEFINITION***
fprintf(fid,'**\n'); fprintf(fid,'** History Definition\n'); fprintf(fid,'**\n');

fprintf(fid,'*STEP, PERTURBATION\n'); fprintf(fid,'*STATIC\n');

%---BOUNDARY CONDITIONS---
fprintf(fid,'**\n'); fprintf(fid,'** Boundary Conditions\n'); fprintf(fid,'**\n');

%-----BC at center------
fprintf(fid,'*BOUNDARY\n %8.0f, ENCASTRE\n',N1(1,1));
fprintf(fid,'*BOUNDARY\n %8.0f, ENCASTRE\n',(N1(1,1)+nwinc+2*nz2*nzinc));
fprintf(fid,'*BOUNDARY\n CENT2BOT, 3\n'); fprintf(fid,'*BOUNDARY\n CENT1BOT, 3\n');

%---LOADING---
fprintf(fid,'**\n'); fprintf(fid,'** Loads\n'); fprintf(fid,'**\n');

%-----Gravity Load----
fprintf(fid,'*DLOAD\n'); fprintf(fid,'ALL, GRAV, 9.8, 0, 0, -1\n');

%---Solver---
fprintf(fid,'*RESTART, WRITE\n');
```

```
fprintf(fid,'*NODE FILE, NSET=WAFER1_INT\n');      % coordinates at interface of wafer 1
fprintf(fid,'COORD\n');

fprintf(fid,'*NODE FILE, NSET=WAFER2_INT\n');      % coordinates at interface of wafer 2
fprintf(fid,'COORD\n');

fprintf(fid,'*NODE PRINT, NSET=WAFER1_INT\n');      % coordinates at interface of wafer 1
fprintf(fid,'COORD\n');

fprintf(fid,'*NODE PRINT, NSET=WAFER2_INT\n');      % coordinates at interface of wafer 2
fprintf(fid,'COORD\n');

fprintf(fid,'*NODE FILE, NSET=WAFER1_INT\n');      % displacements at interface of wafer 1
fprintf(fid,'U\n');

fprintf(fid,'*NODE FILE, NSET=WAFER2_INT\n');      % displacements at interface of wafer 2
fprintf(fid,'U\n');

fprintf(fid,'*END STEP'); fclose(fid);
```

shape_01_bond.m

```
function [] = shape_01_bond(CF1,CF2)

% -This m-file generates a .inp file for ABAQUS
% -This is 1 of 3 files used to calculate the final shape of bonded pair
% -This file bonds the wafer
% -USAGE: [] = shape_01_bond(CF1,CF2)
% -variables - CF1 = n x 3 matrix that contains x,y,z shape of wafer 1 interface
%              CF2 = n x 3 matrix that contains x,y,z shape of wafer 2 interface

% Kevin Turner
% Original: 01 January 2004

%**DEFINE BASIC GEOMETRY**
c = 75.0e-3;                % wafer radius (m)
fl = 32.50e-3;              % flat length (m)

%**ELASTIC PROPERTIES**
C11 = 166.2e9;              % 11 stiffness coefficient (Pa)
C12 = 64.4e9;               % 12 stiffness coefficient (Pa)
C44 = 79.8e9;               % 44 stiffness coefficient (Pa)
den = 2330;                 % density in kg/m^3

%**DEFINE MESH PARAMETERS**
nr1 = 1;                    % number of elements in radial direction in section 1 (has to be 1)
nr2 = 12;                   % number of elements in radial direction in section 2
nq1 = 32;                   % number of elements in theta direction
nz1 = 2;                    % number of elements through the thickness of wafer 1
nz2 = 2;                    % number of elements through the thickness of wafer 2

rs1 = 2.5e-3;               % radius of section 1 (mm)

nrinc = 1000;               % increment in node numbers from one radius to the next
nzinc = 100000;             % increment in node numbers from one layer of nodes to the next
nwinc = 1000000;            % increment in node numbers between wafers
ndinc = 9900000;            % increment in node numbers for dummy nodes

%**LAYOUT GRID**
%---Sections 1 and 2----
R1 = [0 : rs1/(2*nr1) : rs1]';          % radial positions of nodes in section 1
R2 = [rs1 : (c-rs1)/(2*nr2) : c]';      % radial positions of nodes in section 2
Q1 = [0 : 2*pi/(2*nq1) : 2*pi]';        % theta positions of nodes in sections 1 and 2

%**GENERATE X-Y GRID**
%---Section 1---
N1(1,:) = [1, 0.0, 0.0]; k = 2; for i=1:(2*nr1)
    for j=1:(2*nq1)
        N1(k,1) = nrinc*i+j;
        N1(k,2) = R1(i+1,1)*cos(Q1(j,1));
        N1(k,3) = R1(i+1,1)*sin(Q1(j,1));
        k=k+1;
        nrt1 = nrinc*i;
    end
end
%---Section 2---
k=1; for i=2:(2*nr2+1)
    for j=1:(2*nq1)
        N2(k,1) = nrt1+nrinc*(i-1)+j;
        N2(k,2) = R2(i,1)*cos(Q1(j,1));
        N2(k,3) = R2(i,1)*sin(Q1(j,1));
        k=k+1;
        nrt2 = nrt1+nrinc*i;
    end
end
```

```
%**PLOT GRID**
% figure(1); clf;
% plot(N1(:,2),N1(:,3),'k.',N2(:,2),N2(:,3),'r.')
% axis square
% axis([-c c -c c])

%***GET Z AND H VALUES***
NA = [N1; N2];                  % matrix containing [node number, X, Y] of all nodes in first layer

%--wafer 1 (top wafer)---
Z1 = griddata(CF1(:,1),CF1(:,2),CF1(:,3),NA(:,2),NA(:,3),'v4');     % position of interface of wafer 1
H1 = [geth1b(NA(:,2),NA(:,3))];                                     % thickness of wafer 1
for i=1:nz1*2+1
    NZ1(:,i) = Z1+H1./(2.*nz1).*(i-nz1-1);                          % z positions of each node in layer1
end
NZ1 = NZ1-ones(size(NZ1))*NZ1(1,1);                                 % adjust layer 1 data so x=0, y=0 is z=0 at bonding surface
%--wafer 2 (bottom wafer)---
Z2 = griddata(CF2(:,1),CF2(:,2),CF2(:,3),NA(:,2),NA(:,3),'v4');     % position of interface of wafer 2
H2 = [geth2b(NA(:,2),NA(:,3))];                                     % thickness of wafer 2
for i=1:nz2*2+1
    NZ2(:,i) = Z2+H2./(2.*nz2).*(i-nz2-1);                          % z positions of each node in layer2
end
NZ2 = NZ2-ones(size(NZ2))*(NZ2(1,1))-H2(1,1);                       % adjust layer 2 data so x=0, y=0 is z=0 at bonding surface

%***MAKE NODE SETS FOR INTERFACE AND LOADING***
NINT1 = [N1; N2];                                                   % nodes to be bonded on wafer 1
NINT1 = NINT1(2:length(NINT1),:);                                   % eliminate node 1 from data set - NINT1 is a vector with
                                                                    %  [node #, x-pos, y-pos] of nodes at interface to be bonded

%--get distance between nodes at interface--
wtbar = waitbar(0,'Please wait...'); for i=1:length(NZ1)
    for j=1:length(NINT1)
        if NINT1(j,1) == NA(i,1)
            DELTA(j,1) = NZ1(i,1)-NZ2(i,2*nz2+1);
        end
    end
    waitbar(i/length(NZ1),wtbar)
end close(wtbar)

%--create loading and equation vectors-- (use loop to eliminate constraints on nodes in middle of elements)
k=1; p=1; for i=1:((nr1+nr2)*2)
    if i <= (nr1+nr2)*2
        for j=1:(nq1*2)
            if (rem(i,2)~=0)&(rem(j,2)==0)
                p=p+1;
            else
                NEQ(k,:) = [NINT1(p,1), 3, -1.0, (NINT1(p,1)+nwinc+2*nz2*nzinc), 3, 1.0, NINT1(p,1)+ndinc,3,-1.0];
                NLOAD(k,:) = [NINT1(p,1)+ndinc, 3, DELTA(p,1)];
                k=k+1; p=p+1;
            end
        end
    end
end

%***GENERATE ELEMENT VECTORS
%---section 1---
k=1; p=1; for i=1:nr1
    for j=1:nq1
        EL1(k,1) = p;
        EL1(k,2) = N1(1,1);
        EL1(k,3) = (2*i)*nrinc+(2*j-1);
        if j~=nq1
            EL1(k,4) = EL1(k,3)+2;
        else
            EL1(k,4) = EL1(1,3);
        end
        EL1(k,5) = EL1(k,2)+2*nzinc;
        EL1(k,6) = EL1(k,3)+2*nzinc;
        EL1(k,7) = EL1(k,4)+2*nzinc;
        EL1(k,8) = EL1(k,3)-nrinc;
        EL1(k,9) = EL1(k,3)+1;
        EL1(k,10) = EL1(k,4)-nrinc;
        EL1(k,11) = EL1(k,8)+2*nzinc;
        EL1(k,12) = EL1(k,9)+2*nzinc;
        EL1(k,13) = EL1(k,10)+2*nzinc;
        EL1(k,14) = EL1(k,2)+nzinc;
        EL1(k,15) = EL1(k,3)+nzinc;
        EL1(k,16) = EL1(k,4)+nzinc;
        k=k+1; p=p+1;
    end
end
%---section 2---
k=1; for i=1:nr2
    for j=1:nq1
        EL2(k,1) = p;
        EL2(k,2) = N2(1,1)+nrinc*(2*(i-1)-1)+2*(j-1);
```

```
        EL2(k,3) = EL2(k,2)+nrinc*2;
        if j~=nq1
            EL2(k,4) = EL2(k,3)+2;
        else
            EL2(k,4) = N2(1,1)+nrinc*(2*(i-1)+1);
        end
        EL2(k,5) = EL2(k,4)-nrinc*2;
        EL2(k,6) = EL2(k,2)+2*nzinc;
        EL2(k,7) = EL2(k,3)+2*nzinc;
        EL2(k,8) = EL2(k,4)+2*nzinc;
        EL2(k,9) = EL2(k,5)+2*nzinc;
        EL2(k,10) = EL2(k,2)+nrinc;
        EL2(k,11) = EL2(k,3)+1;
        EL2(k,12) = EL2(k,4)-nrinc;
        EL2(k,13) = EL2(k,2)+1;
        EL2(k,14) = EL2(k,10)+2*nzinc;
        EL2(k,15) = EL2(k,11)+2*nzinc;
        EL2(k,16) = EL2(k,12)+2*nzinc;
        EL2(k,17) = EL2(k,13)+2*nzinc;
        EL2(k,18) = EL2(k,2)+nzinc;
        EL2(k,19) = EL2(k,3)+nzinc;
        EL2(k,20) = EL2(k,4)+nzinc;
        EL2(k,21) = EL2(k,5)+nzinc;
        k=k+1; p=p+1;
    end
end

file = 'shape_01_bond.inp';
% Write .inp file
fid = fopen(file,'w');

fprintf(fid,'*HEADING\n'); fprintf(fid,'**\n'); fprintf(fid,'** Model Definition\n');
fprintf(fid,'**\n');

fprintf(fid,'*PREPRINT,HISTORY=NO,MODEL=NO\n'); fprintf(fid,'**\n');

%***NODES***
%---Nodes---
fprintf(fid,'*NODE, NSET=N1\n'); for i=1:2*nz1+1
    fprintf(fid,'%8.0f,%20.12E,%20.12E,%20.12E\n',[NA(:,1)+(ones(length(NA),1)*nzinc*(i-1)), NA(:,2:3), NZ1(:,i)]');
end

fprintf(fid,'*NODE, NSET=N2\n'); for i=1:2*nz2+1
    fprintf(fid,'%8.0f,%20.12E,%20.12E,%20.12E\n',[NA(:,1)+(ones(length(NA),1)*nzinc*(i-1)+nwinc), NA(:,2:3), NZ2(:,i)]');
end

fprintf(fid,'*NODE, NSET=NDUM\n');
fprintf(fid,'%8.0f,%20.12E,%20.12E,%20.12E\n',[NA(:,1)+ndinc, NA(:,2:3), ones(length(NA),1)*10.0e-3]');

fprintf(fid,'*NSET, NSET=CENT1\n');
fprintf(fid,'%8.0f,%8.0f,%8.0f,%8.0f,%8.0f,%8.0f,%8.0f,%8.0f\n',N1(:,1)');
fprintf(fid,'\n');

fprintf(fid,'*NSET, NSET=CENT1BOT\n');
fprintf(fid,'%8.0f,%8.0f,%8.0f,%8.0f,%8.0f,%8.0f,%8.0f,%8.0f\n',N1(:,1)');
fprintf(fid,'\n');

fprintf(fid,'*NSET, NSET=CENT2BOT\n');
fprintf(fid,'%8.0f,%8.0f,%8.0f,%8.0f,%8.0f,%8.0f,%8.0f,%8.0f\n',(N1(:,1)+nwinc)');
fprintf(fid,'\n');

fprintf(fid,'*NSET, NSET=CENT2\n');
fprintf(fid,'%8.0f,%8.0f,%8.0f,%8.0f,%8.0f,%8.0f,%8.0f,%8.0f\n',(N1(:,1)+nwinc+2*nz2*nzinc)');
fprintf(fid,'\n');

fprintf(fid,'*NSET, NSET=WAFER1_INT\n');
fprintf(fid,'%8.0f,%8.0f,%8.0f,%8.0f,%8.0f,%8.0f,%8.0f,%8.0f\n',(NA(:,1))');
fprintf(fid,'\n');

fprintf(fid,'*NSET, NSET=WAFER2_INT\n');
fprintf(fid,'%8.0f,%8.0f,%8.0f,%8.0f,%8.0f,%8.0f,%8.0f,%8.0f\n',(NA(:,1)+nwinc+2*nz2*nzinc)');
fprintf(fid,'\n');

%***ELEMENTS***
fprintf(fid,'**\n'); fprintf(fid,'** Elements\n'); fprintf(fid,'**\n');

fprintf(fid,'*ELEMENT, TYPE=C3D15, ELSET=SEC1\n');
fprintf(fid,'%8.0f,%8.0f,%8.0f,%8.0f,%8.0f,%8.0f,%8.0f,%8.0f,\n%8.0f,%8.0f,%8.0f,%8.0f,%8.0f,%8.0f,%8.0f,%8.0f\n',EL1');

fprintf(fid,'*ELEMENT, TYPE=C3D20, ELSET=SEC2\n');
fprintf(fid,'%8.0f,%8.0f,%8.0f,%8.0f,%8.0f,%8.0f,%8.0f,%8.0f,\n%8.0f,%8.0f,%8.0f,%8.0f,%8.0f,%8.0f,%8.0f,%8.0f,\n%8.0f,%8.0f,%8.0f,%8.0f,%8.0f\n',
        EL2');

fprintf(fid,'*ELSET, ELSET=W1L1\n SEC1, SEC2\n');

for i=1:(nz1-1)
    fprintf(fid,'*ELCOPY, ELEMENT SHIFT=%6.0f, OLD SET=W1L1, SHIFT NODES=%6.0f, NEW SET=WAFER1E\n',nzinc*i,nzinc*i*2);
```

```
end

fprintf(fid,'*ELCOPY, ELEMENT SHIFT=%6.0f, OLD SET=W1L1, SHIFT NODES=%6.0f, NEW SET=W2L2\n',nwinc,nwinc);

for i=1:(nz2-1)
    fprintf(fid,'*ELCOPY, ELEMENT SHIFT=%6.0f, OLD SET=W2L2, SHIFT NODES=%6.0f, NEW SET=WAFER2E\n',nzinc*i,nzinc*i*2);
end

fprintf(fid,'*ELSET, ELSET=WAFER1\n W1L1, WAFER1E\n'); fprintf(fid,'*ELSET, ELSET=WAFER2\n W2L2,
WAFER2E\n');

fprintf(fid,'*ELSET, ELSET=ALL\n WAFER1, WAFER2 \n');

%-----Equation Constraint-----
k=2; for i=1:length(NEQ)
        fprintf(fid,'*EQUATION\n %8.0f\n',3);
        fprintf(fid,'%12.0f,%4.0f,%4.0f,%12.0f,%4.0f,%4.0f,%12.0f,%4.0f,%4.0f\n',NEQ(i,:));
end

%***MATERTIAL PROPS***
fprintf(fid,'**\n'); fprintf(fid,'** Material Properties\n'); fprintf(fid,'**\n');

fprintf(fid,'*ORIENTATION, NAME=CS1, SYSTEM=RECTANGULAR, DEFINITION=COORDINATES\n');
fprintf(fid,'1.0, 1.0, 0.0, -1.0, 1.0, 0.0\n 3, 0.0\n');

fprintf(fid,'*SOLID SECTION, ELSET=ALL, MATERIAL=M1, ORIENTATION=CS1\n');

fprintf(fid,'*MATERIAL, NAME=M1\n');
fprintf(fid,'*DENSITY\n %10.6E,\n',den);
fprintf(fid,'*ELASTIC, TYPE=ORTHOTROPIC\n');
fprintf(fid,'%10.4E, %10.4E, %10.4E, %10.4E, %10.4E, %10.4E,%10.4E, %10.4E\n',C11,C12,C11,C12,C12,C11,C44,C44);
fprintf(fid,'%10.4E,\n',C44);

fprintf(fid,'*MATERIAL, NAME=M2\n');
fprintf(fid,'*DENSITY\n %10.6E,\n',den);
fprintf(fid,'*ELASTIC, TYPE=ISOTROPIC\n');
fprintf(fid,'%10.4E, %10.4E\n',150e9,0.18);

%***HISTORY DEFINITION***
fprintf(fid,'**\n'); fprintf(fid,'** History Definition\n'); fprintf(fid,'**\n');

fprintf(fid,'*STEP, PERTURBATION\n'); fprintf(fid,'*STATIC\n');

%---BOUNDARY CONDITIONS---
fprintf(fid,'**\n'); fprintf(fid,'** Boundary Conditions\n'); fprintf(fid,'**\n');

%-----BC at center------
fprintf(fid,'*BOUNDARY\n %8.0f, ENCASTRE\n',N1(1,1));

fprintf(fid,'*BOUNDARY\n %8.0f, ENCASTRE\n',(N1(1,1)+nwinc+2*nz2*nzinc));
fprintf(fid,'*BOUNDARY\n CENT2BOT, 3\n');

%---LOADING---
fprintf(fid,'**\n'); fprintf(fid,'** Loads\n'); fprintf(fid,'**\n');

%------close interface gap-------
fprintf(fid,'*BOUNDARY, TYPE=DISPLACEMENT\n');
fprintf(fid,'%10.0f, %10.0f, ,%20.12E\n',NLOAD');

%---Solver---
fprintf(fid,'*RESTART, WRITE\n');

fprintf(fid,'*NODE FILE, NSET=WAFER1_INT\n');      % coordinates at interface of wafer 1
fprintf(fid,'COORD\n');

fprintf(fid,'*NODE FILE, NSET=WAFER2_INT\n');      % coordinates at interface of wafer 2
fprintf(fid,'COORD\n');

fprintf(fid,'*NODE PRINT, NSET=WAFER1_INT\n');      % coordinates at interface of wafer 1
fprintf(fid,'COORD\n');

fprintf(fid,'*NODE PRINT, NSET=WAFER2_INT\n');      % coordinates at interface of wafer 2
fprintf(fid,'COORD\n');


fprintf(fid,'*NODE FILE, NSET=WAFER1_INT\n');      % displacements at interface of wafer 1
fprintf(fid,'U\n');

fprintf(fid,'*NODE FILE, NSET=WAFER2_INT\n');      % displacements at interface of wafer 2
fprintf(fid,'U\n');

fprintf(fid,'*END STEP'); fclose(fid);
```

shape_01_pair_gravity.m

```
function [] = shape_01_pair_gravity(bnd_wafer,flip_bnd)
```

```
% -This m-file generates a .inp file for ABAQUS
% -This is the 3rd of 3 files used to calculate the final shape of bonded pair
% -This file imports the data from the ADE measurements and calculates
%  the shape of the bonded pair when loaded by gravity
% -USAGE: [] = shape_01_pair_gravity(bnd_wafer,flip_bnd)

% Kevin Turner
% Original: 01 January 2004

%**DEFINE BASIC GEOMETRY**
c = 75.0e-3;                % wafer radius (m)
fl = 32.50e-3;              % flat length (m)

%**ELASTIC PROPERTIES**
C11 = 166.2e9;              % 11 stiffness coefficient (Pa)
C12 = 64.4e9;               % 12 stiffness coefficient (Pa)
C44 = 79.8e9;               % 44 stiffness coefficient (Pa)
den = 2330;                 % density in kg/m^3

%**DEFINE MESH PARAMETERS**
nr1 = 1;                    % number of elements in radial direction in section 1 (has to be 1)
nr2 = 12;                   % number of elements in radial direction in section 2
nq1 = 32;                   % number of elements in theta direction
nz1 = 2;                    % number of elements through the thickness of wafer 1

rs1 = 2.5e-3;               % radius of section 1 (mm)

nrinc = 1000;               % increment in node numbers from one radius to the next
nzinc = 100000;             % increment in node numbers from one layer of nodes to the next
nwinc = 1000000;            % increment in node numbers between wafers
ndinc = 9900000;            % increment in node numbers for dummy nodes

%**LAYOUT GRID**
%---Sections 1 and 2----
R1 = [0 : rs1/(2*nr1) : rs1]';          % radial positions of nodes in section 1
R2 = [rs1 : (c-rs1)/(2*nr2) : c]';      % radial positions of nodes in section 2
Q1 = [0 : 2*pi/(2*nq1) : 2*pi]';        % theta positions of nodes in sections 1 and 2

%**GENERATE X-Y GRID**
%---Section 1---
N1(1,:) = [1, 0.0, 0.0]; k = 2; for i=1:(2*nr1)
    for j=1:(2*nq1)
        N1(k,1) = nrinc*i+j;
        N1(k,2) = R1(i+1,1)*cos(Q1(j,1));
        N1(k,3) = R1(i+1,1)*sin(Q1(j,1));
        k=k+1;
        nrt1 = nrinc*i;
    end
end
%---Section 2---
k=1; for i=2:(2*nr2+1)
    for j=1:(2*nq1)
        N2(k,1) = nrt1+nrinc*(i-1)+j;
        N2(k,2) = R2(i,1)*cos(Q1(j,1));
        N2(k,3) = R2(i,1)*sin(Q1(j,1));
        k=k+1;
        nrt2 = nrt1+nrinc*i;
    end
end

%**PLOT GRID**
% figure(1); clf;
% plot(N1(:,2),N1(:,3),'k.',N2(:,2),N2(:,3),'r.')
% axis square
% axis([-c c -c c])

%***GET Z AND H VALUES***
NA = [N1; N2];                  % matrix containing [node number, X, Y] of all nodes in first layer

figure(2); clf;
%--wafer 1 ---
Z1 = [getz1b(NA(:,2),NA(:,3),bnd_wafer,flip_bnd)];      % position of center plane of wafer 1
H1 = [geth1b(NA(:,2),NA(:,3))+geth2b(NA(:,2),NA(:,3))];  % thickness of wafer 1
for i=1:nz1*2+1
    NZ1(:,i) = Z1+H1./(2.*nz1).*(i-nz1-1);          % z positions of each node in layer1
end
NZ1 = NZ1-ones(size(NZ1))*NZ1(1,1);                 % adjust layer 1 data so x=0, y=0 is z=0 at bonding surface

%***GENERATE ELEMENT VECTORS
%---section 1---
k=1; p=1; for i=1:nr1
    for j=1:nq1
        EL1(k,1) = p;
        EL1(k,2) = N1(1,1);
        EL1(k,3) = (2*i)*nrinc+(2*j-1);
        if j~=nq1
```

```
            EL1(k,4) = EL1(k,3)+2;
        else
            EL1(k,4) = EL1(1,3);
        end
        EL1(k,5) = EL1(k,2)+2*nzinc;
        EL1(k,6) = EL1(k,3)+2*nzinc;
        EL1(k,7) = EL1(k,4)+2*nzinc;
        EL1(k,8) = EL1(k,3)-nrinc;
        EL1(k,9) = EL1(k,3)+1;
        EL1(k,10) = EL1(k,4)-nrinc;
        EL1(k,11) = EL1(k,8)+2*nzinc;
        EL1(k,12) = EL1(k,9)+2*nzinc;
        EL1(k,13) = EL1(k,10)+2*nzinc;
        EL1(k,14) = EL1(k,2)+nzinc;
        EL1(k,15) = EL1(k,3)+nzinc;
        EL1(k,16) = EL1(k,4)+nzinc;
        k=k+1; p=p+1;
    end
end
%---section 2---
k=1; for i=1:nr2
    for j=1:nq1
        EL2(k,1) = p;
        EL2(k,2) = N2(1,1)+nrinc*(2*(i-1)-1)+2*(j-1);
        EL2(k,3) = EL2(k,2)+nrinc*2;
        if j~=nq1
            EL2(k,4) = EL2(k,3)+2;
        else
            EL2(k,4) = N2(1,1)+nrinc*(2*(i-1)+1);
        end
        EL2(k,5) = EL2(k,4)-nrinc*2;
        EL2(k,6) = EL2(k,2)+2*nzinc;
        EL2(k,7) = EL2(k,3)+2*nzinc;
        EL2(k,8) = EL2(k,4)+2*nzinc;
        EL2(k,9) = EL2(k,5)+2*nzinc;
        EL2(k,10) = EL2(k,2)+nrinc;
        EL2(k,11) = EL2(k,3)+1;
        EL2(k,12) = EL2(k,4)-nrinc;
        EL2(k,13) = EL2(k,2)+1;
        EL2(k,14) = EL2(k,10)+2*nzinc;
        EL2(k,15) = EL2(k,11)+2*nzinc;
        EL2(k,16) = EL2(k,12)+2*nzinc;
        EL2(k,17) = EL2(k,13)+2*nzinc;
        EL2(k,18) = EL2(k,2)+nzinc;
        EL2(k,19) = EL2(k,3)+nzinc;
        EL2(k,20) = EL2(k,4)+nzinc;
        EL2(k,21) = EL2(k,5)+nzinc;
        k=k+1; p=p+1;
    end
end

file = 'shape_01_pair_gravity.inp';
% Write .inp file
fid = fopen(file,'w');

fprintf(fid,'*HEADING\n'); fprintf(fid,'**\n'); fprintf(fid,'** Model Definition\n');
fprintf(fid,'**\n');

fprintf(fid,'*PREPRINT,HISTORY=NO,MODEL=NO\n'); fprintf(fid,'**\n');

%***NODES***
%---Nodes---
fprintf(fid,'*NODE, NSET=N1\n'); for i=1:2*nz1+1
    fprintf(fid,'%8.0f,%20.12E,%20.12E,%20.12E\n',[NA(:,1)+(ones(length(NA),1)*nzinc*(i-1)), NA(:,2:3), NZ1(:,i)]');
end

fprintf(fid,'*NSET, NSET=CENT1\n');
fprintf(fid,'%8.0f,%8.0f,%8.0f,%8.0f,%8.0f,%8.0f,%8.0f,%8.0f\n',N1(:,1)');
fprintf(fid,'\n');

fprintf(fid,'*NSET, NSET=CENT1BOT\n');
fprintf(fid,'%8.0f,%8.0f,%8.0f,%8.0f,%8.0f,%8.0f,%8.0f,%8.0f\n',N1(:,1)');
fprintf(fid,'\n');

fprintf(fid,'*NSET, NSET=WAFER1_INT\n');
fprintf(fid,'%8.0f,%8.0f,%8.0f,%8.0f,%8.0f,%8.0f,%8.0f,%8.0f\n',(NA(:,1))');
fprintf(fid,'\n');

%***ELEMENTS***
fprintf(fid,'**\n'); fprintf(fid,'** Elements\n'); fprintf(fid,'**\n');

fprintf(fid,'*ELEMENT, TYPE=C3D15, ELSET=SEC1\n');
fprintf(fid,'%8.0f,%8.0f,%8.0f,%8.0f,%8.0f,%8.0f,%8.0f,%8.0f,\n%8.0f,%8.0f,%8.0f,%8.0f,%8.0f,%8.0f,%8.0f,%8.0f\n',EL1');

fprintf(fid,'*ELEMENT, TYPE=C3D20, ELSET=SEC2\n');
fprintf(fid,'%8.0f,%8.0f,%8.0f,%8.0f,%8.0f,%8.0f,%8.0f,%8.0f,\n%8.0f,%8.0f,%8.0f,%8.0f,%8.0f,%8.0f,%8.0f,%8.0f,\n%8.0f,%8.0f,%8.0f,%8.0f,%8.0f\n',
        EL2');
```

```
fprintf(fid,'*ELSET, ELSET=W1L1\n SEC1, SEC2\n');

for i=1:(nz1-1)
    fprintf(fid,'*ELCOPY, ELEMENT SHIFT=%6.0f, OLD SET=W1L1, SHIFT NODES=%6.0f, NEW SET=WAFER1E\n',nzinc*i,nzinc*i*2);
end

fprintf(fid,'*ELSET, ELSET=WAFER1\n W1L1, WAFER1E\n');

fprintf(fid,'*ELSET, ELSET=ALL\n WAFER1\n');

%***MATERTIAL PROPS***
fprintf(fid,'**\n'); fprintf(fid,'** Material Properties\n'); fprintf(fid,'**\n');

fprintf(fid,'*ORIENTATION, NAME=CS1, SYSTEM=RECTANGULAR, DEFINITION=COORDINATES\n');
fprintf(fid,'1.0, 1.0, 0.0, -1.0, 1.0, 0.0\n 3, 0.0\n');

fprintf(fid,'*SOLID SECTION, ELSET=ALL, MATERIAL=M1, ORIENTATION=CS1\n');

fprintf(fid,'*MATERIAL, NAME=M1\n');
fprintf(fid,'*DENSITY\n %10.6E,\n',den);
fprintf(fid,'*ELASTIC, TYPE=ORTHOTROPIC\n');
fprintf(fid,'%10.4E, %10.4E, %10.4E, %10.4E, %10.4E, %10.4E,%10.4E, %10.4E\n',C11,C12,C11,C12,C12,C11,C44,C44);
fprintf(fid,'%10.4E,\n',C44);

fprintf(fid,'*MATERIAL, NAME=M2\n');
fprintf(fid,'*DENSITY\n %10.6E,\n',den);
fprintf(fid,'*ELASTIC, TYPE=ISOTROPIC\n');
fprintf(fid,'%10.4E, %10.4E\n',150e9,0.18);

%***HISTORY DEFINITION***
fprintf(fid,'**\n'); fprintf(fid,'** History Definition\n'); fprintf(fid,'**\n');

fprintf(fid,'*STEP, PERTURBATION\n'); fprintf(fid,'*STATIC\n');

%---BOUNDARY CONDITIONS---
fprintf(fid,'**\n'); fprintf(fid,'** Boundary Conditions\n'); fprintf(fid,'**\n');

%-----BC at center------
fprintf(fid,'*BOUNDARY\n %8.0f, ENCASTRE\n',N1(1,1));
fprintf(fid,'*BOUNDARY\n CENT1BOT, 3\n');

%---LOADING---
fprintf(fid,'**\n'); fprintf(fid,'** Loads\n'); fprintf(fid,'**\n');

%-----Gravity Load----
fprintf(fid,'*DLOAD\n'); fprintf(fid,'ALL, GRAV, 9.8, 0, 0, -1\n');

%---Solver---
fprintf(fid,'*RESTART, WRITE\n');

fprintf(fid,'*NODE FILE, NSET=WAFER1_INT\n');      % coordinates at interface of wafer 1
fprintf(fid,'COORD\n');

fprintf(fid,'*NODE PRINT, NSET=WAFER1_INT\n');     % coordinates at interface of wafer 1
fprintf(fid,'COORD\n');

fprintf(fid,'*NODE FILE, NSET=WAFER1_INT\n');      % displacements at interface of wafer 1
fprintf(fid,'U\n');

fprintf(fid,'*END STEP'); fclose(fid);
```

C.3 Wafer Bonded Double Cantilever

Below are the MATLAB™ scripts to generate and execute the model to predict the crack shape and calculate G in the wafer bonded double cantilever specimen. A MATLAB™ script is used to generate a mesh that is exported to ABAQUS™ and solved. The data finite element data is post-processed in MATLAB™.

1. *sequence_ntype_10.m* - Script used to run the model and post process the data. The iteration scheme to determine the shape of the crack is in this script.

2. *ntype_10.m* - Function to generate the ABAQUS™ model of the double cantilever specimen.

sequence_ntype_10.m

```
% solves ntype_10 multiple times to find equilibrium crack front
% initial guess for crack front defined by second order polynomial with coefficients A1,A2,A3
% can set dimensions of wafer and mesh density

% Kevin Turner
% 09 April 2003

clear; figure(2); clf;

% Setup runs
eps = 1e-12;                                          % tolerance
GC = 350.0;                                           % target strain energy release rate value along front in mJ/m^2
G_conv = 0.001*GC;                                    % maximum variation along converged crack front in mJ/m^2

% Wafer Geometry
b = 50.0e-3;
w1 = 18.00e-3/2.0;                                   % bottom flat half length (m)
w2 = 32.500e-3/2.0;                                  % top flat half length (m)
h1 = 500.0e-6;                                       % thickness of wafers, code only set up for symmetric problems
ube = 1.0e-3;                                        % width of nodes at wafer edge

GEOM = [b; w1; w2; h1; ube];                        % vector that gets passed to n_type_10d

% Mesh properties
nx1 = 10; ef=2;
dy_lim = 0.1e-3;                                    % maximum movement of node in y-dir during iteration

% Nodes at which to calculate G at, nodes in between are determined from spline fit, there are 2*nx1+3 nodes across crack front,
%  however G calculations only at the first 2*nx1+1 nodes
spline_nodes = [ 1 : 2 : 2*nx1+1]';                 % all corner nodes of elements

% Initial guess - defined as second order polynomial of the form y=A1*x^2+A2*x+A3, fit units should be in m
A1 = (-4.3e-3)*10^3; A2 = (0.00); A3 = (-13)/10^3;

% Convert initial guess to y-positions at spline nodes - mesh info that is needed, same info calculated in n_type_10d
nxf1 = ceil(nx1*(w1-ube)/(b-ube));                      % number of elements along bottom flat
nxf2 = ceil(nx1*(w2-ube)/(b-ube));                      % number of elements along top flat
y1 = 30.0e-3;                                           % +/- upper/lower position of center mesh section
x1 = (b^2-y1^2)^0.5;                                    % length of horizontal at top and bottom of center mesh section
X1a = [0 : w1/(nxf1*ef) : w1]';                         % x-position of nodes along line at y=-y1 within bottom flat
X2a = [0 : w2/(nxf2*ef) : w2]';                         % x-position of nodes along line at y=+y1 within top flat
X1b = [w1 : (x1-ube-w1)/((nx1-nxf1)*ef) : x1-ube]';     % x-position of nodes along line at y=-y1 outside bottom flat
X2b = [w2 : (x1-ube-w2)/((nx1-nxf2)*ef) : x1-ube]';     % x-position of nodes along line at y=+y1 outside top flat
X1c = [x1-ube : ube/2 : x1]'; X2c = [x1-ube : ube/2 : x1]'; X1d = [X1b(1:length(X1b)-1) ; X1c ];
X2d = [X2b(1:length(X2b)-1) ; X2c ]; X1 = [X1a(1:length(X1a)-1); X1d ]; X2 = [X2a(1:length(X2a)-1);
X2d ];
Xcent1 = [0 : (b-ube)/(nx1*ef) : b-ube]';               % x-position of nodes at center
Xcent2 = [b-ube/2 : ube/2 : b]'; Xcent = [Xcent1; Xcent2];

for j=1:length(spline_nodes)                            % equivalent data for spline nodes only
    for r=1:nx1*ef+3
        if r == spline_nodes(j,1)
            X1S(j,1) = X1(r,1);
            X2S(j,1) = X2(r,1);
            XcentS(j,1) = Xcent(r,1);
        end
    end
end

% Map initial crack shape onto crack front nodes
for i=1:length(Xcent)
    X = X1(i); g=1;
    while abs(g) > eps
        g  = 1/2*(X2(i)+X1(i)-2*Xcent(i))*(A1*X^2+A2*X+A3)^2/(y1^2)-1/2*(-X2(i)+X1(i))*(A1*X^2+A2*X+A3)/y1+Xcent(i)-X;
        dg = (X2(i)+X1(i)-2*Xcent(i))*(A1*X^2+A2*X+A3)*(2*A1*X+A2)/(y1^2)-1/2*(-X2(i)+X1(i))*(2*A1*X+A2)/y1-1;
        X = -g/dg + X;
    end
    X3(i,1) = X;                                        % x-position of crack front nodes
    Y3(i,1) = A1*X^2+A2*X+A3;                           % y-position of crack front nodes
end

n=1000; for i = 1:n;

    %***Determine y-position of all of nodes along front using spline
    if i==1
        XC(:,i) = X3(:,1);
        YC(:,i) = Y3(:,1);
        for j=1:length(spline_nodes)                            % equivalent data for spline nodes only
            for r=1:nx1*ef+3
                if r == spline_nodes(j,1)
                    XS(j,1) = XC(r,1);
                    YS(j,1) = YC(r,1);
                end
            end
        end
    else
        XS(:,i) = (1/2).*(X2S+X1S-2.*XcentS).*(YS(:,i)./y1).^2-(1/2).*(-X2S+X1S).*(YS(:,i)./y1)+XcentS;
```

```
        XC(:,i) = XC(:,i-1); g1=1;                                          % inital guess for Xc
        while max(abs(g1)) > eps
            YC(:,i) = spline(XS(:,i),YS(:,i),XC(:,i));
            g1 = (1/2)*(X2+X1-2*Xcent).*(YC(:,i)./y1).^2-(1/2).*(-X2+X1).*(YC(:,i)./y1)+Xcent - XC(:,i);
            for r=1:length(YC(:,i))
                dx = zeros(length(YC(:,i)),1);
                dx(r,1) = 1.0e-9;
                YC2(:,i) = spline(XS(:,i),YS(:,i),(XC(:,i)+dx));
                gd2 = (1/2)*(X2+X1-2*Xcent).*(YC2(:,i)./y1).^2-(1/2).*(-X2+X1).*(YC2(:,i)./y1)+Xcent - (XC(:,i)+dx);
                JC(:,r) = (gd2-g1)/dx(r,1);
            end
            XC(:,i) = XC(:,i)-JC\g1;
        end
    end

%     for j=1:length(spline_nodes)
%         for r=1:nx1*ef+3
%             if r == spline_nodes(j,1)
%                 YS(j,i+1) = YC(r,i)+1.0e-3;
%             end
%         end
%     end

    %***Run Finite Element Model***
    !del n_type_10d.mdl
    !del n_type_10d.odb
    !del n_type_10d.dat
    !del n_type_10d.sta
    !del n_type_10d.log
    !del n_type_10d.prt
    !del n_type_10d.msg
    !del n_type_10d.res
    !del n_type_10d.stt
    !del n_type_10d.com

    [CTIP0,CTIP2, a] = ntype_10(nx1,YC(:,i),GEOM);

    figure(2)
    subplot(2,2,1)
    plot(XS(:,i),YS(:,i),'ro',XC,YC)

    !abaqus job=n_type_10d interactive

    %***Read FEM data***

    es1 = 367;               % first line of reaction force data (at the crack tip)
    ef1 = es1+nx1*ef+2;      % first line of reaction force data (at the crack tip)
    [RF0(:,i)] = textread('n_type_10d.dat','%*u %*f %*f %f %*f %*f %*f',((ef1-es1)+1),'expchars','E','headerlines',(es1-1));

    es2 = ef1+15;            % first line of reaction force data (ahead of crack tip)
    ef2 = es2+nx1+1;         % first line of reaction force data (ahead of crack tip)
    [RF3(:,i)] = textread('n_type_10d.dat','%*u %*f %*f %f %*f %*f %*f',((ef2-es2)+1),'expchars','E','headerlines',(es2-1));

    es3 = ef2+15;            % first line of displacement data (one node behind tip)
    ef3 = es3+nx1+1;         % first line of displacement data (one node behind tip)
    [U1(:,i)] = textread('n_type_10.dat','%*u %*f %*f %f %*f %*f %*f',((ef3-es3)+1),'expchars','E','headerlines',(es3-1));

    es4 = ef3+15;            % first line of displacement data (two nodes behind tip)
    ef4 = es4+nx1*ef+2;      % first line of displacement data (two nodes behind tip)
    [U2(:,i)] = textread('n_type_10.dat','%*u %*f %*f %f %*f %*f %*f',((ef4-es4)+1),'expchars','E','headerlines',(es4-1));

    %***Calculate G***

    % at corner nodes
    k=1;
    for j=1:((length(CTIP0)-1)/2)
        if k==1
            dA1(k,i) = 0.0;
            dA2(k,i) = 0.50*(det([CTIP2(k,2),CTIP2(k+2,2);CTIP2(k,3),CTIP2(k+2,3)])+det([CTIP2(k+2,2),CTIP0(k+2,2);CTIP2(k+2,3),CTIP0(k+2,3)])
            +det([CTIP0(k+2,2),CTIP0(k,2);CTIP0(k+2,3),CTIP0(k,3)])+det([CTIP0(k,2),CTIP2(k,2);CTIP0(k,3),CTIP2(k,3)]));
            dA(k,i) = 1/2*(dA1(k,i)+dA2(k,i));
            G(k,i) = -10^3*(1/2/dA(k,i))*(2*RF0(k,i)*U2(k,i) + 2*RF3((k+1)/2,i)*U1((k+1)/2,i) + RF0(k+1,i)*U2(k+1,i));
        else
            dA1(k,i) = 0.50*(det([CTIP2(k-2,2),CTIP2(k,2);CTIP2(k-2,3),CTIP2(k,3)])+det([CTIP2(k,2),CTIP0(k,2);CTIP2(k,3),CTIP0(k,3)])
            +det([CTIP0(k,2),CTIP0(k-2,2);CTIP0(k,3),CTIP0(k-2,3)])+det([CTIP0(k-2,2),CTIP2(k-2,2);CTIP0(k-2,3),CTIP2(k-2,3)]));
            dA2(k,i) = 0.50*(det([CTIP2(k,2),CTIP2(k+2,2);CTIP2(k,3),CTIP2(k+2,3)])+det([CTIP2(k+2,2),CTIP0(k+2,2);CTIP2(k+2,3),CTIP0(k+2,3)])
            +det([CTIP0(k+2,2),CTIP0(k,2);CTIP0(k+2,3),CTIP0(k,3)])+det([CTIP0(k,2),CTIP2(k,2);CTIP0(k,3),CTIP2(k,3)]));
            dA(k,i) = 1/2*(dA1(k,i)+dA2(k,i));
            G(k,i) = -10^3*(1/2/dA(k,i))*(RF0(k-1,i)*U2(k-1,i) + 2*RF0(k,i)*U2(k,i) + 2*RF3((k+1)/2,i)*U1((k+1)/2,i) + RF0(k+1,i)*U2(k+1,i));
        end
        XPOS(k,i) = CTIP0(k,2)*10^3;
        YPOS(k,i) = CTIP0(k,3)*10^3;
        k=k+2;
    end

    % at midside nodes
    k=2;
```

```
for j=2:((length(CTIP0)-1)/2)
    if k==2
        dA(k,i) = 0.50*(det([CTIP2(k-1,2),CTIP2(k+1,2);CTIP2(k-1,3),CTIP2(k+1,3)])+det([CTIP2(k+1,2),CTIP0(k+1,2);CTIP2(k+1,3),CTIP0(k+1,3)])
        +det([CTIP0(k+1,2),CTIP0(k-1,2);CTIP0(k+1,3),CTIP0(k-1,3)])+det([CTIP0(k-1,2),CTIP2(k-1,2);CTIP0(k-1,3),CTIP2(k-1,3)]));
        G(k,i) = -10^3*(1/2/dA(k,i))*(2*RF0(k-1,i)*U2(k-1,i) + 2*RF3(k/2,i)*U1(k/2,i) + 2*RF0(k,i)*U2(k,i) + RF0(k+1,i)*U2(k+1,i)
        + RF3(k/2+1,i)*U1(k/2+1,i));
     else
        dA(k,i) = 0.50*(det([CTIP2(k-1,2),CTIP2(k+1,2);CTIP2(k-1,3),CTIP2(k+1,3)])+det([CTIP2(k+1,2),CTIP0(k+1,2);CTIP2(k+1,3),CTIP0(k+1,3)])
        +det([CTIP0(k+1,2),CTIP0(k-1,2);CTIP0(k+1,3),CTIP0(k-1,3)])+det([CTIP0(k-1,2),CTIP2(k-1,2);CTIP0(k-1,3),CTIP2(k-1,3)]));
        G(k,i) = -10^3*(1/2/dA(k,i))*(RF0(k-1,i)*U2(k-1,i) + RF3(k/2,i)*U1(k/2,i) + 2*RF0(k,i)*U2(k,i) + RF0(k+1,i)*U2(k+1,i)
        + RF3(k/2+1,i)*U1(k/2+1,i));
    end
    XPOS(k,i) = CTIP0(k,2)*10^3;
    YPOS(k,i) = CTIP0(k,3)*10^3;
    k=k+2;
end

% vector G lists G at each node along crack front with exception of the two nodes closet to the edge
% vectors XPOS and YPOS give coordinates of each node along crack front except for two nodes closet to the edge

% plot G as function of x-pos on wafer
figure(2)
subplot(2,2,2)
plot(XPOS,G,XPOS(:,i),G(:,i),'r.');
title('G variation along crack front')
xlabel('x-pos (mm)')
ylabel('G (mJ/m^2)')

% plot crack front shape
subplot(2,2,3)
plot(XPOS,YPOS,XPOS(:,i),YPOS(:,i),'r.');
title('Crack Front Shape')
xlabel('x-pos (mm)')
ylabel('y-pos (mm)')

%***Check Convergence Criterion***
dG(:,i) = (G(:,i)-GC);                  % dG at all nodes along crack front

for j=1:length(spline_nodes)
    for r=1:nx1*ef+1
        if r == spline_nodes(j,1)
            dG2(r,i) = dG(r,i);         % dG at spline nodes only
        end
    end
end

if max(abs(dG2(:,i))) < G_conv          % if convergence criterion satisifed, print results and pause
    FINAL = [XPOS(:,i) , XPOS(:,i).^2 , YPOS(:,i) ,  YPOS(:,i)-YPOS(1,i) , G(:,i) , dG(:,i)]
    pause
end

for j=1:length(spline_nodes)            % form GS and XPOSS which contain G and XPOS at the spline nodes only
    for r=1:nx1*ef+1
        if r == spline_nodes(j,1)
            GS(j,i) = G(r,i);
            XPOSS(j,i) = XPOS(r,i);
        end
    end
end

F(:,i) = (GS(:,i)./GC)-1;               % residual at spline nodes, =0 when fracture criterion is G=Gc, i is the solution number

subplot(2,2,4)
plot(XPOSS,F,XPOSS(:,i),F(:,i),'r.');
title('Residuals')
ylabel('F')
xlabel('XPOS (mm)')

if i==1

    for r=1:length(spline_nodes)
        for s=1:length(spline_nodes)
            if r==s
                J(r,s) = -1;
            else
                J(r,s) = 0;
            end
        end
    end

    Bp = J;                                 % jacobian for this step
    Yinc = -J\F(:,i);                       % solve for increment in y-dir

    if max(abs(Yinc)) > dy_lim              % check if step size too big physically for mesh
        beta = dy_lim/max(abs(Yinc));
    else
        beta=1;
```

```
        end
        YS(:,i+1) = YS(:,i) + Yinc*beta;        % create new vecor of node front positions

    else

        dY(:,i-1) = YS(:,i)-YS(:,i-1);
        dF(:,i-1) = F(:,i)-F(:,i-1);

        B = Bp + ((dF(:,i-1) - Bp*dY(:,i-1))*dY(:,i-1)')/(dY(:,i-1)'*dY(:,i-1));        % update jacobian
        Yinc = -B\F(:,i);

        if max(abs(Yinc)) > dy_lim              % check if step size too big physically for mesh
            beta = dy_lim/max(abs(Yinc));
        else
            beta=1;
        end

        YS(:,i+1) = YS(:,i) + Yinc*beta;        % create new vector of node front positions
        Bp = B;                                 % store current Jacobian for next step
    end

    f(i,1)=1/2*F(:,i)'*F(:,i)

end
```

ntype_10.m

```
function [CTIP0, CTIP2, a] = ntype_10(nx1,y_r,GEOM)

% nx1 is number of nodes in x in center section, y_r is vector of length nx1*ef+1
% uses 20-node solid elements

% K.T. Turner
% Original: 01 February 2003
% Modified: 21 March 2003

figure(1); clf;
file = 'n_type_10d.inp';

%--Geometry--
b = GEOM(1,1);                          % radius of wafer (m)
w1 = GEOM(2,1);                         % bottom flat half length (m)
w2 = GEOM(3,1);                         % top flat half length (m)
h1 = GEOM(4,1);                         % thickness of wafers, code only set up for symmetric problems
ube = GEOM(5,1);                        % unbonded edge region

yflat1 = -1*(b^2-(w1)^2)^0.5;           % y-position of minor flat
yflat2 = (b^2-(w2)^2)^0.5;              % y-position of major flat

%---Define Anisotropic Material Properties---
C11 = 165.7e9;                          % stiffness, C11
C12 = 63.9e9;                           % stiffness, C12
C44 = 79.56e9;                          % stiffness, C44

%--Loading--
delta = 150.0e-6;                       % half thickness of razor blade
nadv = 7;                               % line of nodes which blade is inserted to

%--Mesh parameters--
ef = 2;                                 % element factor, ef=2 when using 20-node elements

%nx1 = 10;                              % number of elements in x-direction along horizontal at +/- y1 % orig 25
nxf1 = ceil(nx1*(w1-ube)/(b-ube));      % number of elements along bottom flat
nxf2 = ceil(nx1*(w2-ube)/(b-ube));      % number of elements along top flat

wyc = 0.125e-3;                         % length of elements in crack front in y-dir      orig 0.125e-3
nyc = 16;                               % number of elements in crack front in y-dir (make even)   orig 16

nz1 = 2;                                % number of elements through the thickness

ar45 = 1.0;                             % aspect ratio control of elements in center section

y_inc = 100;                            % increment in node numbers when moving in y-dir
z_inc = 100000;                         % increment in node numbers when moving in z-dir

%--Calculate Nodal Positions in Sections 1 and 2--
y1 = 30.0e-3;                           % +/- upper/lower position of center mesh section
x1 = (b^2-y1^2)^0.5;                    % length of horizontal at top and bottom of center mesh section
X1a = [0 : w1/(nxf1*ef) : w1]';         % x-position of nodes along line at y=-y1 within bottom flat
X2a = [0 : w2/(nxf2*ef) : w2]';         % x-position of nodes along line at y=+y1 within top flat
X1b = [w1 : (x1-ube-w1)/((nx1-nxf1)*ef) : x1-ube]';     % x-position of nodes along line at y=-y1 outside bottom flat
X2b = [w2 : (x1-ube-w2)/((nx1-nxf2)*ef) : x1-ube]';     % x-position of nodes along line at y=+y1 outside top flat
X1c = [x1-ube : ube/2 : x1]'; X2c = [x1-ube : ube/2 : x1]';
X1d = [X1b(1:length(X1b)-1) ; X1c ];
X2d = [X2b(1:length(X2b)-1) ; X2c ];
```

```
for i=1:((nx1-nxf1)*ef+3)
    Y1(i,1) = -1*(b^2-(X1d(i,1))^2)^0.5;        % y-postion of node rows in section 1
    NX1(i,1) = i;                               % number of nodes in each row
end
for i=1:((nx1-nxf2)*ef+3)
    Y2(i,1) = (b^2-(X2d(i,1))^2)^0.5;           % y-position of node rows in section 2
    NX2(i,1) = i;                               % number of nodes in each row
end

X1 = [X1a(1:length(X1a)-1); X1d ]; X2 = [X2a(1:length(X2a)-1); X2d ];

%--Calculate Nodal Positions in Section 3--
Xcent1 = [0 : (b-ube)/(nx1*ef) : b-ube]';                  % x-position of nodes at center
Xcent2 = [b-ube/2 : ube/2 : b]'; Xcent = [Xcent1; Xcent2];

%--Plot lines that crack front moves on--
YLINE = [-y1 : 2*y1/20 : y1]';
for i=1:nx1*ef+3
    XLINE(:,i) = 1/2.*(-2.*Xcent(i,1)+X1(i,1)+X2(i,1)).*YLINE.^2/(y1.^2)-1/2.*(X1(i,1)-X2(i,1)).*YLINE./y1+Xcent(i,1);
    plot(XLINE(:,i),YLINE)
    hold on
end

%--Define nodes at crack front--
Y_C = y_r;                                                                                       % y-position of nodes at crack front
X_C = 1/2.*(-2.*Xcent+X1+X2).*Y_C.^2/(y1.^2)-1/2.*(X1-X2).*Y_C./y1+Xcent;                       % x-position of nodes at crack front
X_C(length(X_C),1) = sqrt(b^2-Y_C(length(X_C),1)^2);                                             % do not use parabolic estimation for edge node
X_C(length(X_C)-1,1) = (X_C(length(X_C),1)+X_C(length(X_C)-2,1))/2.0;

%--Define nodes ahead of and behind crack tip--
THETA(1,1) = 0;                % angle of local x coordinate relative to global x
for i=2:nx1*ef+1
    THETA(i,1) = atan((Y_C(i-1,1)-Y_C(i+1,1))/(X_C(i+1,1)-X_C(i-1,1)));
end

k_ind = [-nyc*ef/2 : 1 : nyc*ef/2]'; for i=1:nyc*ef+1
    for j=1:nx1*ef+1
        X3(i,j) = X_C(j,1) + wyc/2.0*k_ind(i,1)*sin(THETA(j,1));
        Y3(i,j) = Y_C(j,1) + wyc/2.0*k_ind(i,1)*cos(THETA(j,1));
    end
end

for i=1:nyc*ef+1
    Y3(i,nx1*ef+3) = Y_C(nx1*ef+3,1) + wyc/2.0*k_ind(i,1);
    X3(i,nx1*ef+3) = (b^2 - (Y3(i,nx1*ef+3))^2)^0.5;
end

for i=1:nyc*ef+1
    Y3(i,nx1*ef+2) = (Y3(i,nx1*ef+3) + Y3(i,nx1*ef+1))/2.0;
    X3(i,nx1*ef+2) = (X3(i,nx1*ef+3) + X3(i,nx1*ef+1))/2.0;
end

plot(X_C,Y_C,'go')

%--Calculate Nodal Positions in Sections 4 and 5--

ny4 = round((Y3(1,1)+y1)/(b*ar45/nx1)); ny5 = round((y1-Y3(nyc*ef+1,1))/(b*ar45/nx1));

if ny4 < 1
    ny4 = 1;
end if ny5 < 1
    ny5 = 1;
end

% Section 4

for j=1:(nx1*ef+3)
    for i=1:(ny4*ef+1)
        Y4(i,j) = (Y3(1,j)+y1)*((i-1)/(ny4*ef))-y1;
    end
    YM = (Y4(1,j)+Y4(ny4*ef+1,j))/2.0;
    XM  = 1/2*(-2*Xcent(j,1)+X1(j,1)+X2(j,1))*YM^2/(y1^2)-1/2*(X1(j,1)-X2(j,1))*YM/y1+Xcent(j,1);
    for i=1:(ny4*ef+1)
        y = Y4(i,j);
        X4(i,j) = (y^2*YM*X3(1,j)+y^2*Y3(1,j)*X1(j,1)-y^2*y1*XM-y^2*YM*X1(j,1)-y^2*Y3(1,j)*XM+y^2*y1*X3(1,j)-y*Y3(1,j)^2*X1(j,1)+y*Y3(1,j)^2*XM+
        y*YM^2*X1(j,1)+y*X3(1,j)*y1^2-y*XM*y1^2-y*X3(1,j)*YM^2+Y3(1,j)^2*y1*XM+Y3(1,j)^2*YM*X1(j,1)-YM^2*Y3(1,j)*X1(j,1)+XM*Y3(1,j)*y1^2
        -X3(1,j)*YM*y1^2-YM^2*y1*X3(1,j))/(Y3(1,j)*y1^2-YM*y1^2+YM*Y3(1,j)^2-y1*YM^2+y1*Y3(1,j)^2-Y3(1,j)*YM^2);
    end
end

for i=1:(ny4*ef+1)
    X4(i,nx1*ef+3) = (b^2-Y4(i,nx1*ef+3)^2)^0.5;
end

% Section 5
for j=1:(nx1*ef+3)
    for i=1:(ny5*ef+1)
```

```
        Y5(i,j) = (y1-Y3(nyc*ef+1,j))*((i-1)/(ny5*ef))+Y3(nyc*ef+1,j);
    end
    YM = (Y5(1,j)+Y5(ny5*ef+1,j))/2.0;
    XM  = 1/2*(-2*Xcent(j,1)+X1(j,1)+X2(j,1))*YM^2/(y1^2)-1/2*(X1(j,1)-X2(j,1))*YM/y1+Xcent(j,1);
    for i=1:(ny5*ef+1)
        y = Y5(i,j);
        X5(i,j) = -(y^2*YM*X2(j,1)-y^2*y1*XM-y^2*Y3(nyc*ef+1,j)*X2(j,1)+y^2*Y3(nyc*ef+1,j)*XM-y^2*YM*X3(nyc*ef+1,j)+y^2*y1*X3(nyc*ef+1,j)+
        y*y1^2*XM-y*y1^2*X3(nyc*ef+1,j)-y*Y3(nyc*ef+1,j)^2*XM+y*X2(j,1)*Y3(nyc*ef+1,j)^2-y*X2(j,1)*YM^2+y*X3(nyc*ef+1,j)*YM^2-
        y1^2*Y3(nyc*ef+1,j)*XM+y1^2*YM*X3(nyc*ef+1,j)+Y3(nyc*ef+1,j)^2*y1*XM-X3(nyc*ef+1,j)*y1*YM^2+X2(j,1)*Y3(nyc*ef+1,j)*YM^2-
        Y3(nyc*ef+1,j)^2*YM*X2(j,1))/(-Y3(nyc*ef+1,j)*YM^2+Y3(nyc*ef+1,j)*y1^2+y1*YM^2-YM*y1^2+YM*Y3(nyc*ef+1,j)^2-y1*Y3(nyc*ef+1,j)^2);
    end
end

for i=1:(ny5*ef+1)
    X5(i,nx1*ef+3) = (b^2-Y5(i,nx1*ef+3)^2)^0.5;
end

%--Define nodes in Section 1--
k=1; for i=1:length(Y1)
    for j=1:(nxf1*ef+NX1(i,1))
        N1(k,1) = y_inc*(i-1)+j;
        N1(k,2) = X1(j,1);
        N1(k,3) = Y1(i,1);
        N1(k,4) = 0.0;
        k = k+1;
        n_row1 = y_inc*(i-1);                    % number of last row of nodes
    end
end

%--Define nodes in Section 4--
k=1; for i=2:(ny4*ef)
    for j=1:(nx1*ef+3)
        N4(k,1) = n_row1+y_inc*(i-1)+j;
        N4(k,2) = X4(i,j);
        N4(k,3) = Y4(i,j);
        N4(k,4) = 0.0;
        k = k+1;
        n_row4 = n_row1+y_inc*(i-1);            % number of last row of nodes
    end
end

%--Define nodes in Section 3--
k=1; for i=1:(nyc*ef+1)
    for j=1:(nx1*ef+3)
        N3(k,1) = n_row4+y_inc*(i)+j;
        N3(k,2) = X3(i,j);
        N3(k,3) = Y3(i,j);
        N3(k,4) = 0.0;
        k = k+1;
        n_row3 = n_row4+y_inc*(i);            % number of last row of nodes
    end
end

%--Define nodes in Section 5--
k=1; for i=2:(ny5*ef)
    for j=1:(nx1*ef+3)
        N5(k,1) = n_row3+y_inc*(i-1)+j;
        N5(k,2) = X5(i,j);
        N5(k,3) = Y5(i,j);
        N5(k,4) = 0.0;
        k = k+1;
        n_row5 = n_row3+y_inc*(i-1);            % number of last row of nodes
    end
end

%--Define nodes in Section 2--
k=1; for i=1:length(Y2)
    for j=1:(nxf2*ef+NX2(i,1))
        N2(k,1) = n_row5 + y_inc*(length(Y2)-i+1)+j;
        N2(k,2) = X2(j,1);
        N2(k,3) = Y2(i,1);
        N2(k,4) = 0.0;
        k = k+1;
        n_row2 = n_row5+y_inc*(i-1);            % number of last row of nodes
    end
end

plot(N1(:,2),N1(:,3),'b.',N2(:,2),N2(:,3),'r.',N3(:,2),N3(:,3),'k.',N4(:,2),N4(:,3),'g.',N5(:,2),N5(:,3),'m.')
axis square axis([-b b -b b])

%--Elements--
%---Section 1---
k=1;
for i=1:(length(Y1)-1)/2                                    % y
    for j=1:((nxf1*ef+NX1((2*i-1),1)-1)/2);                 % x
        EL1(k,1)  = k;
        EL1(k,2)  = N1(1,1) + y_inc*(2*i-2) + (2*j-2);          % 1
```

```
        EL1(k,3)  = N1(1,1) + y_inc*(2*i-2) + (2*j);           % 2
        EL1(k,4)  = N1(1,1) + y_inc*(2*i) + (2*j);             % 3
        EL1(k,5)  = N1(1,1) + y_inc*(2*i) + (2*j-2);           % 4
        EL1(k,6)  = EL1(k,2) + z_inc*2;                        % 5
        EL1(k,7)  = EL1(k,3) + z_inc*2;                        % 6
        EL1(k,8)  = EL1(k,4) + z_inc*2;                        % 7
        EL1(k,9)  = EL1(k,5) + z_inc*2;                        % 8
        EL1(k,10) = N1(1,1) + y_inc*(2*i-2) + (2*j-1);         % 9
        EL1(k,11) = N1(1,1) + y_inc*(2*i-1) + (2*j);           % 10
        EL1(k,12) = N1(1,1) + y_inc*(2*i) + (2*j-1);           % 11
        EL1(k,13) = N1(1,1) + y_inc*(2*i-1) + (2*j-2);         % 12
        EL1(k,14) = EL1(k,10) + z_inc*2;                       % 13
        EL1(k,15) = EL1(k,11) + z_inc*2;                       % 14
        EL1(k,16) = EL1(k,12) + z_inc*2;                       % 15
        EL1(k,17) = EL1(k,13) + z_inc*2;                       % 16
        EL1(k,18) = EL1(k,2) + z_inc;                          % 17
        EL1(k,19) = EL1(k,3) + z_inc;                          % 18
        EL1(k,20) = EL1(k,4) + z_inc;                          % 19
        EL1(k,21) = EL1(k,5) + z_inc;                          % 20
        NT1(i,1)  = EL1(k,3);                                  % reference node for definition of 15 node elements
        k=k+1;
    end
end

q=1;
for i=1:(length(Y1)-1)/2                                       % 15 node elements
    EL1T(q,1)  = k;
    EL1T(q,2)  = NT1(i,1);
    EL1T(q,3)  = NT1(i,1) + y_inc*2 + 2;
    EL1T(q,4)  = NT1(i,1) + y_inc*2;
    EL1T(q,5)  = EL1T(q,2) + z_inc*2;
    EL1T(q,6)  = EL1T(q,3) + z_inc*2;
    EL1T(q,7)  = EL1T(q,4) + z_inc*2;
    EL1T(q,8)  = NT1(i,1) + y_inc + 1;
    EL1T(q,9)  = NT1(i,1) + y_inc*2 + 1;
    EL1T(q,10) = NT1(i,1) + y_inc;
    EL1T(q,11) = EL1T(q,8) + z_inc*2;
    EL1T(q,12) = EL1T(q,9) + z_inc*2;
    EL1T(q,13) = EL1T(q,10) + z_inc*2;
    EL1T(q,14) = EL1T(q,2) + z_inc;
    EL1T(q,15) = EL1T(q,3) + z_inc;
    EL1T(q,16) = EL1T(q,4) + z_inc;
    k=k+1;
    q=q+1;
end

%---Section 2---
q=1; N2S = n_row5+y_inc+1;
for i=1:(length(Y2)-1)/2                                       % y
    for j=1:((nxf2*ef+NX2((length(NX2)-2*i+1),1)-1)/2);        % x
        EL2(q,1)  = k;
        EL2(q,2)  = N2S + y_inc*(2*i-2) + (2*j-2);             % 1
        EL2(q,3)  = N2S + y_inc*(2*i-2) + (2*j);               % 2
        EL2(q,4)  = N2S + y_inc*(2*i) + (2*j);                 % 3
        EL2(q,5)  = N2S + y_inc*(2*i) + (2*j-2);               % 4
        EL2(q,6)  = EL2(q,2) + z_inc*2;                        % 5
        EL2(q,7)  = EL2(q,3) + z_inc*2;                        % 6
        EL2(q,8)  = EL2(q,4) + z_inc*2;                        % 7
        EL2(q,9)  = EL2(q,5) + z_inc*2;                        % 8
        EL2(q,10) = N2S + y_inc*(2*i-2) + (2*j-1);             % 9
        EL2(q,11) = N2S + y_inc*(2*i-1) + (2*j);               % 10
        EL2(q,12) = N2S + y_inc*(2*i) + (2*j-1);               % 11
        EL2(q,13) = N2S + y_inc*(2*i-1) + (2*j-2);             % 12
        EL2(q,14) = EL2(q,10) + z_inc*2;                       % 13
        EL2(q,15) = EL2(q,11) + z_inc*2;                       % 14
        EL2(q,16) = EL2(q,12) + z_inc*2;                       % 15
        EL2(q,17) = EL2(q,13) + z_inc*2;                       % 16
        EL2(q,18) = EL2(q,2) + z_inc;                          % 17
        EL2(q,19) = EL2(q,3) + z_inc;                          % 18
        EL2(q,20) = EL2(q,4) + z_inc;                          % 19
        EL2(q,21) = EL2(q,5) + z_inc;                          % 20
        NT2(i,1)  = EL2(q,3);                                  % reference node for deifnition of 15 node elements
        k=k+1;
        q=q+1;
    end
end

q=1;                                                           % 15 node elements
for i=1:(length(Y2)-1)/2
    EL2T(q,1)  = k;
    EL2T(q,2)  = NT2(i,1);
    EL2T(q,3)  = NT2(i,1) + 2;
    EL2T(q,4)  = NT2(i,1) + y_inc*2;
    EL2T(q,5)  = EL2T(q,2) + z_inc*2;
    EL2T(q,6)  = EL2T(q,3) + z_inc*2;
    EL2T(q,7)  = EL2T(q,4) + z_inc*2;
    EL2T(q,8)  = NT2(i,1) + 1;
```

```
    EL2T(q,9)  = NT2(i,1) + y_inc + 1;
    EL2T(q,10) = NT2(i,1) + y_inc;
    EL2T(q,11) = EL2T(q,8) + z_inc*2;
    EL2T(q,12) = EL2T(q,9) + z_inc*2;
    EL2T(q,13) = EL2T(q,10) + z_inc*2;
    EL2T(q,14) = EL2T(q,2) + z_inc;
    EL2T(q,15) = EL2T(q,3) + z_inc;
    EL2T(q,16) = EL2T(q,4) + z_inc;
    k=k+1;
    q=q+1;
end

%---Sections 3, 4, and 5---
q=1; N345S = n_row1+1;
for i=1:(nyc+ny4+ny5)                                           % y
    for j=1:(nx1+1);                                            % x
        EL345(q,1)  = k;
        EL345(q,2)  = N345S + y_inc*(2*i-2) + (2*j-2);          % 1
        EL345(q,3)  = N345S + y_inc*(2*i-2) + (2*j);            % 2
        EL345(q,4)  = N345S + y_inc*(2*i) + (2*j);              % 3
        EL345(q,5)  = N345S + y_inc*(2*i) + (2*j-2);            % 4
        EL345(q,6)  = EL345(q,2) + z_inc*2;                     % 5
        EL345(q,7)  = EL345(q,3) + z_inc*2;                     % 6
        EL345(q,8)  = EL345(q,4) + z_inc*2;                     % 7
        EL345(q,9)  = EL345(q,5) + z_inc*2;                     % 8
        EL345(q,10) = N345S + y_inc*(2*i-2) + (2*j-1);          % 9
        EL345(q,11) = N345S + y_inc*(2*i-1) + (2*j);            % 10
        EL345(q,12) = N345S + y_inc*(2*i) + (2*j-1);            % 11
        EL345(q,13) = N345S + y_inc*(2*i-1) + (2*j-2);          % 12
        EL345(q,14) = EL345(q,10) + z_inc*2;                    % 13
        EL345(q,15) = EL345(q,11) + z_inc*2;                    % 14
        EL345(q,16) = EL345(q,12) + z_inc*2;                    % 15
        EL345(q,17) = EL345(q,13) + z_inc*2;                    % 16
        EL345(q,18) = EL345(q,2) + z_inc;                       % 17
        EL345(q,19) = EL345(q,3) + z_inc;                       % 18
        EL345(q,20) = EL345(q,4) + z_inc;                       % 19
        EL345(q,21) = EL345(q,5) + z_inc;                       % 20
        k=k+1; q=q+1;
    end
end


%--Define Node Sets--
NTC = N2(1,1);                                  % Node at top corner for BC
NCENT1 = [N1(1,1) : y_inc : N2(1,1)]';          % Nodes in layer 1 along center symmetry plane
NCENT = NCENT1;
for i=1:(nz1*ef)
    NCENT = [NCENT; NCENT1+(i)*z_inc];          % All nodes along center symmetry plane
end

k=1;
for i=(nyc*ef/2):(nyc*ef)                       % Nodes along the interface in section 3 for symmetry plane
    for j=1:nx1*ef+3
        NINT3(k,1) = N3(1,1)+y_inc*i+j-1;
        k=k+1;
    end
end

for j=1:nx1*ef+3
    CTIP4(j,1:3) = N3((nx1*ef+3)*(nyc*ef/2+2)+j,1:3);      % Nodes one row ahead of crack tip and x-y coordinates
    CTIP3(j,1:3) = N3((nx1*ef+3)*(nyc*ef/2+1)+j,1:3);      % Nodes one row ahead of crack tip and x-y coordinates
    CTIP0(j,1:3) = N3((nx1*ef+3)*(nyc*ef/2)+j,1:3);        % Nodes at crack tip and x-y coordinates
    CTIP1(j,1:3) = N3((nx1*ef+3)*(nyc*ef/2-1)+j,1:3);      % Nodes one row behind crack tip and x-y coordinates
    CTIP2(j,1:3) = N3((nx1*ef+3)*(nyc*ef/2-2)+j,1:3);      % Nodes two rows behind crack tip and x-y coordinates
end

%--Define Loading--

k=1; for i=1:length(N1)
    if N1(i,3) == Y1(nadv,1)
        LD1(k,1) = N1(i,1);
        LD1(k,2) = 3;
        LD1(k,3) = delta;
        k=k+1;
    end
end

a = (CTIP0(1,3) - Y1(nadv,1))*10^3;         % crack length

% Write output to data file
fid = fopen(file,'w');

fprintf(fid,'*HEADING\n'); fprintf(fid,'**\n'); fprintf(fid,'** Model Definition\n');
fprintf(fid,'**\n');

fprintf(fid,'*PREPRINT,HISTORY=NO,MODEL=NO\n'); fprintf(fid,'**\n');
```

```
%***NODES***

%---Nodes---
fprintf(fid,'*NODE, NSET=N1\n');
fprintf(fid,'%8.0f,%20.12E,%20.12E,%20.12E\n',N1');
fprintf(fid,'*NODE, NSET=N2\n');
fprintf(fid,'%8.0f,%20.12E,%20.12E,%20.12E\n',N2');
fprintf(fid,'*NODE, NSET=N3\n');
fprintf(fid,'%8.0f,%20.12E,%20.12E,%20.12E\n',N3');
fprintf(fid,'*NODE, NSET=N4\n');
fprintf(fid,'%8.0f,%20.12E,%20.12E,%20.12E\n',N4');
fprintf(fid,'*NODE, NSET=N5\n');
fprintf(fid,'%8.0f,%20.12E,%20.12E,%20.12E\n',N5');

%---Node Sets---
fprintf(fid,'*NSET, NSET=NTC\n');
fprintf(fid,'%8.0f\n',NTC');
fprintf(fid,'*NSET, NSET=CTIP0\n');
fprintf(fid,'%8.0f\n',CTIP0(:,1)');
fprintf(fid,'*NSET, NSET=CTIP1\n');
fprintf(fid,'%8.0f\n',CTIP1(:,1)');
fprintf(fid,'*NSET, NSET=CTIP2\n');
fprintf(fid,'%8.0f\n',CTIP2(:,1)');
fprintf(fid,'*NSET, NSET=CTIP3\n');
fprintf(fid,'%8.0f\n',CTIP3(:,1)');
fprintf(fid,'*NSET, NSET=NCENT\n');
fprintf(fid,'%8.0f\n',NCENT');
fprintf(fid,'*NSET, NSET=NINT3\n');
fprintf(fid,'%8.0f\n',NINT3');
fprintf(fid,'*NSET, NSET=LOAD\n');
fprintf(fid,'%8.0f\n',LD1(:,1)');
fprintf(fid,'*NSET, NSET=INTERFACE\n N2, N5, NINT3\n'); fprintf(fid,'*NSET, NSET=MASTER\n N1, N2,
N3, N4, N5\n');

for i=1:nz1*ef
    fprintf(fid,'*NCOPY, CHANGE NUMBER=%6.0f, OLD SET=MASTER, SHIFT\n',z_inc*i);
    fprintf(fid,'0.00, 0.00, %20.12E\n', (h1/(nz1*ef))*i);
    fprintf(fid,'0.00, 0.00, 0.00, 0.00, 0.00, 0.00, 0.00\n');
end

%***ELEMENTS***
fprintf(fid,'**\n'); fprintf(fid,'** Elements\n'); fprintf(fid,'**\n');

fprintf(fid,'*ELEMENT, TYPE=C3D20, ELSET=SEC1\n');
fprintf(fid,'%8.0f,%8.0f,%8.0f,%8.0f,%8.0f,%8.0f,%8.0f,%8.0f,\n%8.0f,%8.0f,%8.0f,%8.0f,%8.0f,%8.0f,%8.0f,%8.0f,\n%8.0f,%8.0f,%8.0f,%8.0f,%8.0f\n',
        EL1');

fprintf(fid,'*ELEMENT, TYPE=C3D15, ELSET=SEC1T\n');
fprintf(fid,'%8.0f,%8.0f,%8.0f,%8.0f,%8.0f,%8.0f,%8.0f,%8.0f,\n%8.0f,%8.0f,%8.0f,%8.0f,%8.0f,%8.0f,%8.0f,%8.0f\n',EL1T');

fprintf(fid,'*ELEMENT, TYPE=C3D20, ELSET=SEC2\n');
fprintf(fid,'%8.0f,%8.0f,%8.0f,%8.0f,%8.0f,%8.0f,%8.0f,%8.0f,\n%8.0f,%8.0f,%8.0f,%8.0f,%8.0f,%8.0f,%8.0f,%8.0f,\n%8.0f,%8.0f,%8.0f,%8.0f,%8.0f\n',
        EL2');

fprintf(fid,'*ELEMENT, TYPE=C3D15, ELSET=SEC2T\n');
fprintf(fid,'%8.0f,%8.0f,%8.0f,%8.0f,%8.0f,%8.0f,%8.0f,%8.0f,\n%8.0f,%8.0f,%8.0f,%8.0f,%8.0f,%8.0f,%8.0f,%8.0f\n',EL2T');

fprintf(fid,'*ELEMENT, TYPE=C3D20, ELSET=SEC345\n');
fprintf(fid,'%8.0f,%8.0f,%8.0f,%8.0f,%8.0f,%8.0f,%8.0f,%8.0f,\n%8.0f,%8.0f,%8.0f,%8.0f,%8.0f,%8.0f,%8.0f,%8.0f,\n%8.0f,%8.0f,%8.0f,%8.0f,%8.0f\n',
        EL345');

fprintf(fid,'*ELSET, ELSET=LAYER1\n SEC1, SEC1T, SEC2, SEC2T, SEC345\n');

for i=1:(nz1-1)
    fprintf(fid,'*ELCOPY, ELEMENT SHIFT=%6.0f, OLD SET=LAYER1, SHIFT NODES=%6.0f, NEW SET=CLAYERS\n',z_inc*i,z_inc*i*ef);
end

fprintf(fid,'*ELSET, ELSET=ALL\n LAYER1, CLAYERS\n');

%***MATERTIAL PROPS***

fprintf(fid,'**\n'); fprintf(fid,'** Material Properties\n'); fprintf(fid,'**\n');

fprintf(fid,'*ORIENTATION, NAME=CS1, SYSTEM=RECTANGULAR, DEFINITION=COORDINATES\n');
fprintf(fid,'1.0, 1.0, 0.0, -1.0, 1.0, 0.0\n 3, 0.0\n');

fprintf(fid,'*SOLID SECTION, ELSET=ALL, MATERIAL=M1, ORIENTATION=CS1\n %10.6E, 5\n',h1);

fprintf(fid,'*MATERIAL, NAME=M1\n'); fprintf(fid,'*ELASTIC, TYPE=ORTHOTROPIC\n');
fprintf(fid,'%10.4E, %10.4E, %10.4E, %10.4E, %10.4E, %10.4E,%10.4E, %10.4E\n',C11,C12,C11,C12,C12,C11,C44,C44);
fprintf(fid,'%10.4E,\n',C44);

fprintf(fid,'*MATERIAL, NAME=M2\n'); fprintf(fid,'*ELASTIC, TYPE=ISOTROPIC\n');
fprintf(fid,'%10.4E, %10.4E\n',148e9,0.18);

%***HISTORY DEFINITION***
fprintf(fid,'**\n'); fprintf(fid,'** History Definition\n'); fprintf(fid,'**\n');
```

```
fprintf(fid,'*STEP, PERTURBATION\n'); fprintf(fid,'*STATIC\n');

%---BOUNDARY CONDITIONS---
fprintf(fid,'**\n'); fprintf(fid,'** Boundary Conditions\n'); fprintf(fid,'**\n');

%-----BC at edge------
fprintf(fid,'*BOUNDARY\n NTC, ENCASTRE\n'); fprintf(fid,'*BOUNDARY\n NCENT, XSYMM\n');

%-----BC at interface (symmetric)------
fprintf(fid,'*BOUNDARY\n INTERFACE, ZSYMM\n');

%---LOADING---
fprintf(fid,'**\n'); fprintf(fid,'** Loads\n'); fprintf(fid,'**\n');

fprintf(fid,'*BOUNDARY, TYPE=DISPLACEMENT\n');
fprintf(fid,'%10.0f, %10.0f, ,%20.12E\n',LD1');

%---Solver---
fprintf(fid,'*RESTART, WRITE\n');

fprintf(fid,'*NODE PRINT, NSET=LOAD\n');        % reaction forcese at load
fprintf(fid,'RF\n');

fprintf(fid,'*NODE PRINT, NSET=CTIP0\n');        % reaction forcese at crack tip
fprintf(fid,'RF\n');

fprintf(fid,'*NODE PRINT, NSET=CTIP3\n');        % reaction forcese at crack tip
fprintf(fid,'RF\n');

fprintf(fid,'*NODE PRINT, NSET=CTIP1\n');       % displacements behind crack tip
fprintf(fid,'U\n');

fprintf(fid,'*NODE PRINT, NSET=CTIP2\n');       % displacements behind crack tip
fprintf(fid,'U\n');

fprintf(fid,'*ENERGY PRINT\n');

fprintf(fid,'*END STEP'); fclose(fid);
```